

On Continuous Magnetically Enhanced Centrifugation in Large Scale Downstream Processing of Bioproducts

Submitted in fulfillment of the requirements for the degree of
DOKTOR DER INGENIEURWISSENSCHAFTEN (Dr.-Ing.)

at the
Department of Chemical and Process Engineering
Karlsruhe Institute of Technology (KIT)

APPROVED DISSERTATION

of
Dipl.-Ing. Johannes Lindner
Karlsruhe

Referee: Prof. Dr.-Ing. Hermann Nirschl

Second Reviewer: Prof. Dr. Matthias Franzreb

Day of oral exam: 11.07.2014

For my parents

Acknowledgements

First and foremost I would like to thank Prof. Dr. Nirschl for giving me the chance to do a PhD thesis in his workgroup, for his guidance and advice throughout the PhD thesis.

I also thank the MagPro²LIFE consortium for the good cooperation and mutual support. We owe acknowledgements to the EU for funding our research in the project MagPro²LIFE.

My special thanks go to Gunnar Grim and Johannes Feller from Andritz KMPT, who supported me in the design and set-up of two centrifuges, and who built a centrifuge for the process which we were thankfully allowed to test and publish. Thanks go to Karsten Keller and his crew at Solae Denmark Ltd., where those tests were conducted. Thanks go as well to Karl Holschuh and Johannes Bauer from Merck AG, who provided functionalized magnetic particles for tests. I would also like to express my gratitude to Ms. Aymée Michel from Evonik, who provided magnetic particles for tests.

I would like to thank the people whom I had the opportunity and pleasure to work with at the Institute of Mechanical Process Engineering and Mechanics. My deepest gratitude goes to my co-workers for the great working atmosphere. I enjoyed the group very much. Thanks for all the technical and kind support in difficult times.

I am very grateful for the students whom I worked well together with, notably Martina Kinna, Manuel Franz, Annika Hodapp, Miroslav Dimov, Christian Schäfer, Sonja von Lieres, Maximilian Kurtz and Daniel Markthaler.

Thanks to the technicians, who made the work just possible, notably Hans Guigas, who supported me in the design of the devices and with whom I had many discussions on technical realization. Thanks go to Thomas Reutter, Olaf Jörg and his crew who tirelessly manufactured parts. Thanks go to Klaus Hirsch, Thomas Lebe and their colleagues for particle measurements, and thanks to Bernhard Schweigler and his crew in the electric workshop. Thanks as well to Peter Krolla-Siedenstein who supported me in rheological tests at KIT-IFG.

Special thanks go to Prof. Dr. Matthias Franzreb, whose support and expertness in HGMS was always helpful.

Finally, I wish to express my greatest thanks to my family, who supported me over the years, and to my girlfriend Ellen for her affection and encouragement.

Summary

The current thesis targets on the technical use of Magnetically Enhanced Centrifugation (MEC). Aim is the understanding of the mechanisms of particle transport out of the magnetic field, the development of the equipment and its use for the demonstration of MEC in a large scale. Additionally the analysis of the feasibility and an approach for the design of industrial machines specifically for automatic use including batch-wise and continuous discharge of the machines is important. The use of synthetic magnetic particles with functionalized surface allows the separation of non-magnetic matter. The implementation of MEC for use in protein separation based on synthetic particles is targeted in a scale acceptable for a pilot line.

This work follows the studies of Chen [Chen'09] and Mathias Stolarski [Stolarski'11], who worked out the basics for Magnetically Enhanced Centrifugation (MEC). Stolarski showed experimentally the unloading of a magnetic filter by superposed centrifugation in a lab scale machine. Chen made two-dimensional simulations on particle trajectories and on particle deposit shape.

The investigation of separation using wires of different cross sections was performed by combining a simulation of Computational Fluid Dynamics (CFD) with a magnetic field simulation by the Finite Elements Method (FEM). As a result the influence of different wire cross sections, which cannot be analyzed analytically, could be simulated. Rectangular wires showed to have a superior separation efficiency compared to elliptic wires. Both separated best with a longish shape aligned in field direction. Experiments validate the results of the simulation. The particle agglomeration is investigated by simulation using the Discrete Elements Method (DEM). A custom contact model is implemented based on dipole forces. The magnetic field is simulated by FEM around a wire and then read in the DEM simulation to deduce the magnetic field around the wire and especially at the wire's end under centrifugal forces. The needle-shaped agglomerates observed elsewhere are reproduced by the simulation. The model is set up in a three-dimensional simulation. Furthermore the approach is validated by comparison with photographs of particle deposition on a single wire.

So far no investigations and experience existed for the particle transport out of a magnetic field. The discharge had not yet been performed in an automatic way out of a MEC. The investigation of possibilities and evaluation of the design is a prerequisite for the process. Two different machine concepts are investigated. One is a batch-wise concept discharging by redispersion of the particles, which is as well common in conventional HGMS. The wire filter is used as a stirrer to release particles from the centrifuge wall to a washing liquid. The concept was tested in separation in small and large scale up to a volume flow of 1 m³/h on a machine designed in cooperation with and manufactured by Andritz KMPT. The second

machine concept is the continuous design of a decanter centrifuge, unloading itself by a screw conveyor during application of the magnetic field. Despite the small centrifuge volume of 1.2 l, a volume flow of up to 150 l/h was realized continuously. Both machines are sealed for sterile use. Additionally a permanent magnet arrangement for use with a MEC was developed. This arrangement allows low investment and operating costs and does not risk overheating in contrary to electromagnets. Both centrifugal and magnetic forces influence the structure of the particle deposit during filtering. This was observed directly in the. The exposure of a magnetic field leads to chain-like agglomeration of the particles and enhances the separation by magnetic filtration and centrifugation. The agglomeration represents an important aspect in the process, as colloidal suspensions cannot be separated. It is influenced by the magnetic dipole moment of the particles and depends on the particle concentration.

MEC was tested successfully in bio product recovery on three different products. The first of the three products is the model product ovalbumin, which was separated from hen egg white. The second product is a protein interesting for pharmaceutical use, which was produced by fermentation at the University of Birmingham. It was separated there out of a fermentation broth. The process showed a high separation yield and purity. The third product is BBI, which was separated out of an industrial soy stream at a high volume flow. BBI is interesting as a cancer-preventive food additive and a pharmaceutical and therefore its separation is interesting for medical use. The soy was pretreated by heating and silica and provided by Dupont Solae. The process showed that a high volume flow is possible and large particle amounts can be processed. The individual steps of the purification cycle were performed on each product. The adsorption took place in a stirred tank. Separation, washing and elution were performed inside of the machine. A final washing step was performed to prepare particles for the next cycle. The application experiments demonstrate that the bio product recovery is possible at large volume flow in continuous mode. The choice of a favorable product and a selective particle functionalization is essential for the process though, as salts and different contamination compete for binding ligands and reduce the overall efficiency of the process.

Further investigations should focus on the implementation of the process as alternative to the use of packed beds allowing high volume flow and low cycle times. A successful implementation requires a continuous process, production at large scale and hence low cost particles. For the investigated process only ion exchange functionalization was cheaply available. Careful choice of the product is necessary to select process streams with less contamination prone to bind.

Content

<i>Acknowledgements</i>	<i>1</i>
<i>Summary</i>	<i>3</i>
<i>Content</i>	<i>5</i>
1 Introduction	1
1.1 Initial Situation	1
1.2 Aim of the Work	1
1.3 Overview	3
2 Theory	7
2.1 Magnetism and Magnetic Forces	7
2.1.1 Basic Principles	7
2.1.2 Magnetic Forces	13
2.2 Further Particle Forces	17
2.2.1 Fluid Forces on Particles	17
2.2.2 Surface Forces	19
2.3 Diffusion	24
2.4 Centrifugation	26
2.5 Particle Size Distribution	27
2.6 Modeling and Simulation Basics	27
2.6.1 Computational Fluid Dynamics	27
2.6.2 Magnetic Fields in the Finite Element Method	33
2.6.3 The Discrete Element Method	33
2.7 Biotechnological Downstream Processing	34
2.7.1 Overview over Biotechnological Processes	34
2.7.2 High Gradient Magnetic Fishing	35
2.7.3 Protein Analytics	36
3 Particle Systems	39
3.1 State of the Art of Particle Systems	39
3.2 Target	41
3.3 Materials	41
3.4 Analytic Investigation	44

3.5	Single Particle Contact Force Measurement by Atomic Force Microscopy	46
3.5.1	State of the Art	46
3.5.2	Methods and Materials	47
3.5.3	Results	48
3.6	Bulk Force Measurement by a Magnetic Rheometer	50
3.6.1	State of the Art	50
3.6.2	Methods and Materials	50
3.6.3	Results and Discussion	51
3.7	Influence of Turbulence on Magnetic Separation	54
3.8	Conclusion	55
4	<i>Simulation of Magnetically Induced Particle Agglomeration and Sedimentation</i>	57
4.1	State of the Art	57
4.2	Target of Modeling and Simulation	58
4.3	Simulation Methods in Combining the Discrete Element Method with Magnetic Forces	58
4.3.1	The Finite Element Method	59
4.3.2	Computational Fluid Dynamics	59
4.3.3	The Discrete Element Method	59
4.4	Agglomeration and Agglomerate Porosity	64
4.4.1	Parameter Study	67
4.4.2	Comparison with Different Simulations	70
4.4.3	Experimental Validation	70
4.5	Evaluation of Error Sources	72
4.5.1	Error by Simplification of the Alignment of the Particles	73
4.5.2	Approximation of a Hard Magnetic Sphere by a Hard Magnetic Dipole	73
4.5.3	Mutual Field Enhancement of Weak Magnetic Spheres	75
4.6	Outlook	78
5	<i>Magnetically Enhanced Centrifugation</i>	79
5.1	State of the Art	79
5.1.1	Centrifuge Variants	79
5.1.2	Flow Simulation in High Gradient Magnetic Separation	80
5.1.3	Flow Simulation in Centrifugation	80
5.1.4	Permanent Magnet Arrangements	80
5.1.5	Competing Technologies in High Gradient Magnetic Separation	81
5.1.6	Magnetically Enhanced Centrifugation	83
5.2	Targets	84

5.3	Methods for Experimental Separation and Analysis	85
5.3.1	Separation Methods	85
5.3.2	Concentration Determination	85
5.4	Wire Filter Optimization	87
5.4.1	Materials for Wire Filters	87
5.4.2	Methods for the Simulation of the Fluid Flow around Magnetic Wires	87
5.4.3	Influence of the Cross Section of a Single Wire	88
5.4.4	Matrix Stage Diameter	91
5.4.5	Influence of the Numbers of Wires	92
5.4.6	Wire Arrangement	94
5.5	Computational Fluid Dynamics in Centrifugation	95
5.5.1	Methods for the Simulation of the Large-Scale Centrifuge	95
5.5.2	Results and Improvements	95
5.5.3	Experiments and Validation	97
5.6	Batch-wise Magnetically Enhanced Centrifugation in Pilot Scale	99
5.6.1	Materials and Methods	100
5.6.2	Influencing Parameters	101
5.7	Batch-wise Magnetically Enhanced Centrifugation in Industrial Scale	105
5.7.1	Materials and Methods	105
5.7.2	Results and Discussion	106
5.7.3	Conclusion on Batch-wise Magnetically Enhanced Centrifugation	110
5.8	Continuous Magnetically Enhanced Centrifugation	110
5.8.1	Evaluation of Designs for Automatic Discharge	111
5.8.2	Materials and Methods	112
5.8.3	Particle Tracks after Detachment	115
5.8.4	Start-up Characteristics	115
5.8.5	Parameters Influencing the Separation	116
5.8.6	Parameters Influencing the Transport	118
5.8.7	Summary and Conclusion	119
5.9	Setup of a Longitudinal Permanent Magnet Arrangement for Magnetically Enhanced Centrifugation	120
5.9.1	Materials and Methods	121
5.9.2	Simulation of the Permanent Magnet Arrangement	121
5.9.3	Magnetic Field of a Longitudinal Permanent Magnet Arrangement	122
5.9.4	Magnetically Enhanced Centrifugation Based on a Permanent Magnet Arrangement	123
5.9.5	Magnet Comparison	124
5.10	Selectivity in MEC	125
5.10.1	Materials and Methods	125
5.10.2	Results and Discussion	126

5.11	Calculation Approach for Particle Separation	127
5.11.1	Mathematical Background	128
5.11.2	Application and Validation	129
5.12	Theoretic Comparison of Magnetically Enhanced Centrifugation with Conventional High Gradient Magnetic Separation	130
6	<i>Separation Processes</i>	133
6.1	State of the Art	133
6.1.1	Competing Technologies	133
6.1.2	Ligands	135
6.1.3	Areas of Application	136
6.2	Targets	137
6.3	Simulation of the Adsorption	137
6.3.1	Methods	138
6.3.2	Results and Discussion	140
6.4	Separation of Protein out of Hen Egg White by Magnetically Enhanced Centrifugation	143
6.4.1	Materials and Methods	143
6.4.2	Results and Discussion	146
6.5	Separation out of an Industrial Food Stream	149
6.5.1	Materials and Methods	150
6.5.2	Results and Discussion	152
6.6	Separation out of Fermentation Broth	154
6.6.1	Materials and Methods	154
6.6.2	Results and Discussion	156
6.7	Conclusion and Theoretic Comparison	157
6.8	Outlook: A Completely Continuous Process Based on Magnetically Enhanced Centrifugation	158
7	<i>Conclusion and Outlook</i>	161
7.1	Achievements	161
7.2	Outlook: a Continuous Multi-Stage High Gradient Magnetic Separation Device for Waste-Water-Treatment	164
8	<i>Annex</i>	167
8.1	List of Abbreviations	167
8.2	List of Nature Constants	167

8.3	List of Formula Signs	168
8.4	Further Formulae	171
8.4.1	Brownian Molecular Dynamics	171
8.4.2	Fluid Forces	171
8.5	List of Devices	172
8.5.1	Measurement Devices	172
8.5.2	Demagnetization	173
8.5.3	Data on Electromagnets	173
8.5.4	Overview over Software	173
8.5.5	Adsorption, Washing and Elution Buffer	174
8.5.1	Devices for SDS-Page	174
8.5.2	Buffers and Chemicals for SDS-Page	174
8.5.3	SDS-Page Procedure	175
8.6	Index	176
8.7	Literature	178
8.8	Technical Drawings	187
8.9	Publications	189
8.9.1	Publications	189
8.9.2	Congress Proceedings	189

1 Introduction

1.1 Initial Situation

High Gradient Magnetic Separation (HGMS) is a well-known technology for the separation of magnetic particular systems. HGMS is based on a wire filter implemented in a chamber. The filter is magnetized by an external electro or permanent magnet. It allows the separation of small particles down to nanometer scale and works at high volume flow. For instance, it is not a very wide-spread technology. One of the main reasons is the fact that few systems in nature are magnetic. A new application rising is the use of synthetic particles with magnetic core, which are functionalized on their surface. While the functionalization allows performing reactions such as adsorption, magnetic forces allow an easy control without influencing non-magnetic matter. Additionally, current devices have a low capacity and hence need to be cleaned frequently. They are not continuous, reducing their competitiveness to established technology.

The principle of Magnetically Enhanced Centrifugation (MEC) was patented by Fuchs et al. (US 8012357 B2; US 8075771 B2) at the company Dupont and investigated in experiment by Mathias Stolarski [Stolarski'11] on a lab machine. The experiments allowed the investigation of the behavior of magnetic particles in a centrifuge with a built-in wire filter. Particles on a wire could be discharged partially with most of the particles being freed. The height of the deposit depended on the centrifugal force. The design of the centrifuge set up allowed tests of different wire filters in a batch-wise centrifuge which collected particles. Different aspects of the process like the deposit shape and tracks of particles were simulated by Chen [Chen'09]. In different simulation approaches the shape of the magnetic particles on a wire was investigated in a two-dimensional approach. The radial and axial centrifuge direction was investigated. The magnetic particles flow around wires, which was investigated based on an analytic approximation.

1.2 Aim of the Work

The current work is following up on the investigations of the two PhD theses mentioned above. With the basic principle shown, the target of the current work was the investigation and the setup of devices for use in industrial processes and scale. The new implementation of the principle comprised obligatory automatic discharge. Out of automatically discharging options a continuous discharge was the most attractive option. This design is interesting for industrial use and scale under sterile conditions. It can be used for a continuous implementation in downstream processing of the complete process, if other steps are completely continuous as well. Besides the new discharge, the wire matrix design optimized

for and realizable in a large-scale machine needed to be developed. The matrix design needs to be optimized for separation while still being easily discharged and cheaply produced. Aim was as well the demonstration of selective separation of protein in the process, based on automatic processing and discharge in a pilot machine scale. Finally the realization in the industrial downstream processing targeted on showing the potential of the process.

The first target of simulation was the investigation of particles' tracks around wires of different shape. Additionally the development of a physically correct model for the simulation of more than one wire was targeted. A second target was the three-dimensional simulation of magnetic particle deposit. The focus of the current work is summarized below.

- *Investigation of Magnetically Enhanced Centrifugation*

Phenomenons during MEC were to be investigated experimentally and theoretically with regard to mechanisms on particle scale such as deposition and agglomeration. These are influenced by surface forces and volume forces. Surface forces include the van-der-Waals force and the electrostatic force. Volume forces include magnetic, gravitational and inertia forces. Influences are investigated experimentally indirectly by their effect on the separation, and directly by observation of the deposit build-up. Influences of mechanic particle-particle and particle-wire interaction are investigated theoretically by the simulation of forces in a Discrete Element Model (DEM). A Computational Fluid Dynamics (CFD) simulation allows the investigation of the fluid motion in a centrifugal regime, as well as the investigation of particle motion influenced by fluid forces. Both include the dominating influence of magnetic fields, notably of the wire filter, which is simulated by the Finite Element Method (FEM). The magnetic field leads both to agglomeration and to deposition. Implementation of surface forces summarized in the DLVO theory was done but did not show to have a significant influence. Fluid forces were neglected as they increased the computational effort of the model and did not influence the final deposit shape but only the kinetics.

- *Particle Transport Study, Design and Characteristics Study on Automatically Discharging Magnetically Enhanced Centrifuges*

Different centrifuge designs were investigated and evaluated for their use in the automatic discharge in MEC. Based on a theoretic study on different design possibilities and on experimental pretests, a batch-wise and a continuous approach were chosen and realized in construction and manufacturing. First a centrifuge of 1 l volume was set up allowing automatic discharge and processing of batches of 2 to 200 g of particles. The device was scaled up by Andritz KMPT to set up a machine of 6 l volume, which allowed the processing of up to 700 g of particles at a volume flow up

to 1 m³/h. Finally a continuous device of 1 l volume was set up and tested up to 150 l/h in a cycle.

- *Application of Magnetically Enhanced Centrifugation for Bio Product Recovery*

Different processes were tested to show bio product recovery is possible in large scale by MEC. Processes were exemplary to show the potential of the method for industrial use. A model system was ovalbumin, which was separated selectively from hen egg white. As example for a pharmaceutical product, a process was set up in cooperation with Dr. Mueller and Prof. Thomas at the University of Birmingham, which included fermentation and selective separation of a protein produced by fermentation. As food additive example in cooperation with Solae Denmark, the protein BBI was separated on large scale.

1.3 Overview

Different physical effects influence the process. Additionally it is on different scales by seven orders of magnitude difference. Figure 1-1 shows the different process scales. At a scale of 10⁻¹ m is the centrifuge geometry and the fluid flow in the machine. The wire filter inserted in the machine and the magnetic field distortion created from it is at a scale of 10⁻³ m. It collects particles by magnetic forces and is cleaned from particles simultaneously by centrifugal forces. At the order of magnitude of 10⁻⁶ m, particles agglomerate on the wires influenced by magnetic forces of the wire and by interparticular magnetic forces. The proteins, which adsorb to magnetic particles, are at the order of 10⁻⁸ m.

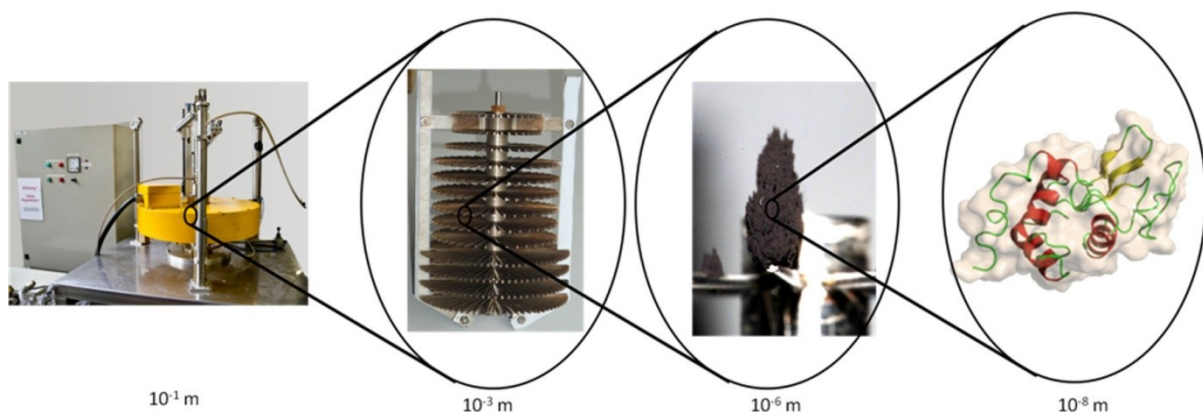


Figure 1-1: the different process scales range from 10⁻¹ m at centrifuge scale to the wire scale of 10⁻³ m, the particle scale of 10⁻⁶ m and down to the product scale of 10⁻⁸ m

In addition to different scales, physical effects are different as well. Figure 1-2 gives an overview over effects and over approaches for their investigation.

- At process scale CFD allows the investigation of the fluid flow in the centrifuge. Experimentally, the flow in the centrifuge could be investigated by color tests. These allowed the validation of the simulation. Chapter 4 shows the investigation by simulation and experiments of the fluid flow and of the centrifuge design.
- Magnetic fields were investigated by FEM. This is necessary for the investigation of the wire shape influence, as well as providing a basis for DEM and CFD. A Hall probe allows the measurement and simulation validation of the magnetic fields. The results for the matrix design and magnet design are as well shown in Chapter 4.
- A force comparison was done by rheology in the magnetic field for the bulk phase and by Atomic Force Microscopy (AFM) for single particle contact. Chapter 3 shows the particle systems and the measurements on their properties. The results were used for the simulation of the magnetic field in discrete element modeling of the particle deposit. The simulation of the dynamic particle behavior in the process is shown in chapter 4.
- The complete process of protein separation out of different feed streams was tested in a micro reactor and transferred to the developed centrifuge. Gel electrophoresis allows the measurement of protein size to conclude on its nature. Optical absorption at 280 nm delivers the protein concentration. The modeling of the process in a microreactor was performed by the Finite Volume Method (FVM), with liquid and protein modeled as continuous phase and functionalized particles modeled as discrete phase (Euler-Euler-Lagrange). The complete separation process, as well as the simulation of adsorption in a μl -reactor, is presented in Chapter 6.

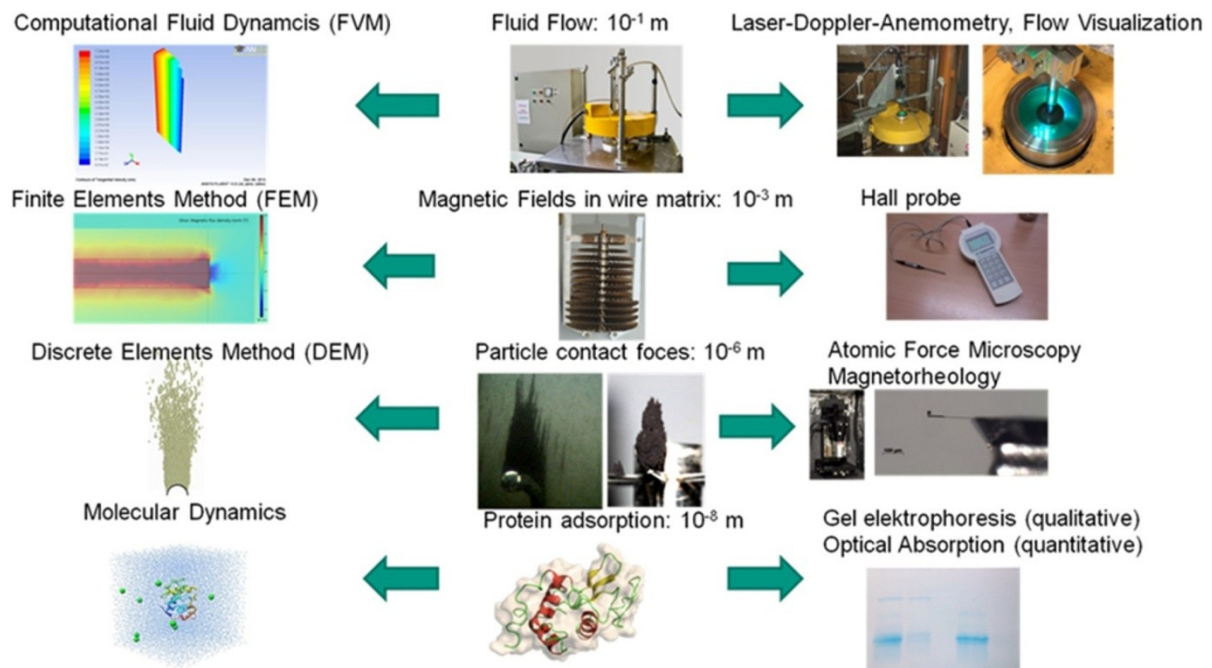


Figure 1-2: the overview over the multi-scale approach in measuring and simulation shows simulation techniques including CFD, FEM and, DEM, as well as the modeling of adsorption in CFD; measuring techniques include color tests, the Hall probe, AFM and gel electrophoresis (or optical absorption measurement)

Different simulation software was used to couple the influence of the physical phenomenon. Figure 1-3 shows the three simulation approaches which were coupled. The FEM was coupled in one way with both CFD and DEM. CFD was as well introduced in DEM, but was not further pursued for not influencing the final deposit shape while significantly increasing the necessary number of time steps.

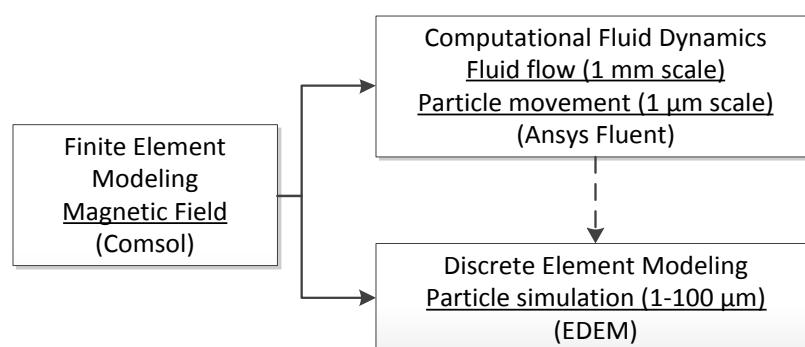


Figure 1-3: links between different simulation methods and scale [Lindner'13]

Along with the investigation of the influences, machines were designed and tested for batch-wise and continuous MEC. The batch-wise approach of MEC did not show to bring a major advantage compared to HGMS, but was important to investigate the complete separation process on particles and feed media available in small scale. The continuous approach is

necessary as an option for industrial use. The core advantage of the complete processes compared to e.g. expanded bed adsorption is the possibility to use it completely continuous at high volume flow. A machine in industrial scale, set up in cooperation with Andritz KMPT and tested with Dupont Solae, showed that the separation in the scale of 1 m³/h is possible. Additionally a permanent magnet arrangement was developed, allowing cost reduction of industrial machines.

2 Theory

This chapter summarizes theoretic background of magnetism, mechanic forces and surface forces acting on particles in a suspension. Because of the abundance of books and theses on HGMS, the theoretic background is presented in a concise form; a detailed description is in corresponding work [Franzreb'03; Svoboda'04; Eichholz'10].

2.1 Magnetism and Magnetic Forces

Magnetism is the underlying driving influence for HGMS and its technical use. Magnetic forces are interesting for technical use, as they are easy to control and can be used without mechanic contact.

2.1.1 Basic Principles

Electric Current and Magnetism

Magnetic fields result in general from the motion of electrons. In case of an electric current I in an infinitely long conductor the magnetic field strength

$$H = \frac{I}{r} \quad (2-1)$$

is created at a distance r as consequence of Ampère's law. In technical applications, this relation is used to describe the magnetic field strength of an electromagnet which is based on a solenoid. The magnetic field strength

$$H = \frac{I * n}{L_{Solenoid}} \quad (2-2)$$

inside of a long and thin solenoid depends on the electric current I , its length $L_{Solenoid}$ and the number of coils n . Electromagnets consist of solenoids, usually out of copper or aluminum, and may be enhanced by a weakly magnetic yoke, concentrating the field to achieve a higher strength. Because of the solenoid resistance lost energy at high currents results in heating of the magnet, which limits the maximum flux density or requires cooling systems. Superconducting magnets consist of special alloys allowing high current density and low resistance at low temperatures below 5 K to achieve more than 20 T field strength. The costs are high, which make it unattractive for HGMS applications.

Quantum Mechanical Description of the Magnetization of Media

The current section is given for completeness without explaining the underlying mathematical description of quantum mechanics, e.g. the Hamilton operator \hat{H} . It is not necessary for the work but is a theoretic approach to magnetism. In case of magnetic matter, a magnetic field is created based on the spin of electrons, more specifically on the intrinsic angular moment of the spin and the orbital angular moment. An electron spinning around the nucleus has got a

magnetic moment, which sums for the whole body to the total magnetic moment. Specifically the outer electron shells strongly influence the magnetic properties. The magnetic moment of the core is neglectably small in comparison. An external magnetic moment influences the orbital angular momentum and hence the moment of the body. The magnetic moment of electrons μ_L always depends on an orbital angular momentum L . The proportionality is given by the gyromagnetic ratio γ . If a body's magnetic field is aligned in the external field direction, the energy is minimal. The change over time of the orbital angular momentum L results hence in the torque T_T [Opel'05] by

$$\begin{aligned}\mu_L &= -|\gamma| \underbrace{L}_{q \times p} \\ \Rightarrow \frac{d\mu_L}{dt} &= -|\gamma| \frac{dL}{dt} = -|\gamma| \underbrace{T_T}_{\mu \times B}.\end{aligned}\quad (2-3)$$

The magnetic moment of an electron of mass m_e turning around the atomic core of a hydrogen atom (as easiest example) was derived and used for the definition (with opposite sign) of the Bohr magneton

$$\mu_B = \underbrace{-\gamma}_{\frac{e}{2m_e}} * \underbrace{\hbar}_{m_e v r} = 9.274 * 10^{-24} \frac{J}{T}.\quad (2-4)$$

The gyromagnetic relation of a hydrogen atom γ is -10^{14}GHz/T . The magnetic moment

$$\mu = \mu_L + \mu_{Sp} = -\frac{\mu_B}{\hbar} (L + g_e S)\quad (2-5)$$

consists of the moment μ_{Sp} resulting from the electron spin S , the Bohr magneton μ_B , the Landé factor g_e (~ 2), the orbital angular momentum of an electron \hbar and the moment μ_L from the kinetic orbital angular momentum L of the electron in the atom shell. The magnetic moment of the core of the atom is negligible. This equation describes paramagnetism. The Quantum mechanical operator of the magnetic moment

$$\hat{\mu} = -\frac{\partial \hat{H}}{\partial B}\quad (2-6)$$

can be defined, under neglectation of terms of order of B^2 , as derivative of the Hamilton-Operator \hat{H} by the magnetic flux density B . In the formula for the hydrogen atom and the electron close to it

$$\hat{H} = \underbrace{\hat{H}_0}_{\text{atom without magnetic field}} + \underbrace{\frac{\mu_B}{\hbar} (L + g_e S) B}_{\hat{H}_{para}} + \underbrace{\frac{e_0^2 B^2}{12m} \sum_{i=1}^Z r_i^2}_{\hat{H}_{dia>0}}.\quad (2-7)$$

there are terms for the atom without magnetic field, the paramagnetic and the diamagnetic field. The term in the middle represents the magnetic moment of the electron shell. A model to describe ferro-, ferri- and antiferromagnetism is the Heisenberg-model. In incomplete

electron shells of ferromagnets, local magnetic moments got an angular momentum which results from the spin. The exchange interaction between magnets results from the spin. It bases on mutual interaction of localized electron spins.

This introduction provides only a theoretical basis, but cannot be used in technical applications. Therefore the quantum mechanical basics of magnetism are not further detailed.

Magnetization of Media by Classic Equations

Magnetic forces can be described and simulated by macroscopic equations. For this purpose the material magnetization is measured and the shape of the magnetic field, which is geometry-dependent, is solved analytically or by FEM simulation. An example for magnetization are permanent magnets, which are usually made out of hard ferrites, AlNiCo or rare earth alloys like NdFeB allowing remanence of up to 1.3 T. An example for the calculation of the magnetic field is a cylindrical magnet. The flux density created on its axis at a radius R and the length L at the distance x can be calculated from

$$B(x) = \frac{B_R}{2} \left(\frac{L+x}{\sqrt{R^2 + (L+x)^2}} - \frac{x}{\sqrt{R^2 + x^2}} \right) \quad (2-8)$$

with a magnet-dependent maximum flux density B_R . A different magnet geometry is approximated by the equivalent pole area.

If magnetizable matter is in an external magnetic field of strength \mathbf{H}_0 , it creates an own local magnetic field. The flux density is defined proportional to the sum of the magnetic field strengths \mathbf{H} and the magnetization \mathbf{M} of the material by the permeability constant μ_0 by

$$\mathbf{B} = \mu_0(\mathbf{H} + \mathbf{M}) = \mu_r \mu_0 \mathbf{H}. \quad (2-9)$$

The field of any weak magnetic body is changed by external field strengths. For a correct physical reproduction, the mutual influence of bodies increasing or decreasing their field needs hence to be introduced. The permeability of the material

$$\mu_r = \frac{\mu_m}{\mu_0} = 1 + \frac{M}{H} = 1 + \kappa \quad (2-10)$$

is defined as the enhancement or reduction of the magnetic field by the material. It is constant in case of paramagnetic material. The permeability μ_m is deduced and the magnetic susceptibility κ is defined as in (2-10). In vacuum μ_r is 1 by definition, the permeability μ_r of water and air is for most purposes approximated by 1.

For paramagnetic matter the magnetization is linear to the field strength (it depends as well on the temperature T and the Curie constant C) and hence κ is constant. In case of ferro- and ferrimagnetic materials, the magnetization

$$\mathbf{M} = \begin{cases} \kappa(\kappa_i, N, \mathbf{H}) * \mathbf{H} & H < H_{Sat} \\ \mathbf{M}_{Sat} & H > H_{Sat} \end{cases} \quad (2-11)$$

is much stronger and converges at a high magnetic field H_{Sat} to a saturation magnetization M_{Sat} . Below saturation, the magnetization depends on the material susceptibility κ_i , on the shape-dependent demagnetization N and the background field H_0 , see (2-11). N consists of a component for each dimension, which sum to 1. The magnetic moment

$$\boldsymbol{\mu} = \int \mathbf{M} \partial V \quad (2-12)$$

of a body depends on its magnetization \mathbf{M} and its volume V . Shape and orientation of the body reduce its magnetization significantly. This demagnetization is defined as

$$N = -\frac{H_{interior}}{M}. \quad (2-13)$$

A longish body oriented in field direction is demagnetized weakly, while a body oriented perpendicular to field direction is demagnetized strongly. The extremes are hence an infinitely long cylinder magnetized in field direction ($N=0$) and a thin disc perpendicular to the field direction ($N=1$), see Figure 2-1 right. A possibility to describe this is by adapting κ , which is hence not only a material constant but shape and orientation dependent. The intrinsic susceptibility κ_i is the material constant ($N=0 \Rightarrow \kappa_i = \kappa$). N is constant (and solved analytically) over the volume for elliptic geometries magnetized parallel to a rotation axis by a homogeneous field. Inside of a body a magnetic field is induced, which is counterdirected to the external magnetic field.

In case of a field strength much stronger than the saturation field strength, the demagnetization is compensated ($\kappa \approx \kappa_i$). For a detailed investigation see [Stoner'45; Franzreb'03; Svoboda'04]. An investigation on the influence of different solids in one particle was done in [Eichholz'10]. For a linear κ this results in

$$\mathbf{H} = \frac{B_0}{\mu_0} - N\mathbf{M} = \frac{B_0}{\mu_0} - N * \kappa_i * \mathbf{H} = \frac{1}{1+N\kappa_i} \frac{B_0}{\mu_0} \quad (2-14)$$

The equation can be rewritten to determine the extrinsic susceptibility κ by

$$\kappa = \frac{\kappa_i}{1+N\kappa_i}. \quad (2-15)$$

Notably there is as well a size influence on the magnetization in case of ferromagnetic (/ferri-) material on κ . While above 100 μm size does not influence susceptibility, it does so below around 100 μm . The susceptibility κ is reduced as the number of Weiss domains diminishes. Notably there is a maximum for one single Weiss domain at around 20 nm, see Figure 2-1 (left) for magnetite. For an even smaller particle κ is small as well.

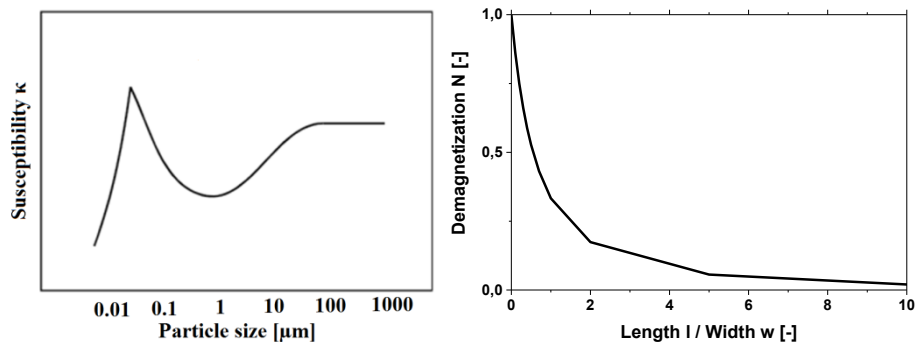


Figure 2-1: Susceptibility in dependence of particle size [Franzreb'03]; Demagnetization n as function of length / width of an ellipsoid [Stoner'45; Franzreb'03; Svoboda'04]

Classification of Magnetic Materials

Diamagnetism is present in all materials and is temperature dependent. Because of completely filled electron shells, magnetic moments compensate each other over the whole body. A circulating current is induced counterdirected to the external field, which results in weakening of the magnetic field inside the body (negative susceptibility). The influence is weak compared to para- and ferromagnetism. Water, noble metals and organic substances show a diamagnetic behavior.

Paramagnetic substances have a low susceptibility. Electron shells are not filled resulting in a magnetic moment of electrons. In a magnetic field moments align parallel to the field and enhance it. By thermal motion this is equally distributed, compensating without external magnetic field strength. The susceptibility is reciprocal proportional to the temperature. At low temperatures saturation is possible (Langevin function), while above the Curie temperature T_C magnetic moments compensate. Examples are alkalimetals.

Ferro-, ferri- and antiferromagnetic material is separated in Weiss domains by Bloch walls, which align in field direction. In contrary to paramagnetic substances, the magnetic moment of different atoms interact. Electron spins align with preferred directions depending on the anisotropic atomic structure. This leads to large values of κ (up to 10^5 for low magnetic field strengths) making the material interesting for technical use. In ferromagnetic material spins align in field direction. In case of antiferromagnetic material, spins are counterdirected and compensate each other. In case of ferrimagnetism, spins are counterdirected but do not compensate. Magnetization is temperature dependent similar to paramagnetic substances. It is separated in magnetically hard and soft material. Hard magnetic material has a high remanence and hence creates high magnetic fields. Its coercive field strength is high at more than 10 000 A/m, i.e. to change its magnetization high fields are necessary. Weak magnetic material has a low coercive field strength (<1000 A/m) and is hence easily remagnetized, with

a low remanence. Superparamagnetism is a property of nanoparticles which are below a size threshold around 20 nm. At this size only one Weiss domain is present, which does not keep magnetization on its own but Brownian motion (thermal energy) is sufficient to reset magnetization. Magnetic particles used in this work are out of magnetite (Fe_2O_3) or maghemite ($\gamma\text{-Fe}_2\text{O}_3$) and hence ferrimagnetic. In this case ferromagnetic moments in subgrids are aligned antiparallel, but have a predominant direction avoiding compensation of the magnetic moment. Several of these particles are superparamagnetic. An overview over the magnetization of different material is presented in Table 2-1.

Table 2-1: Different kinds of magnetism

Effect	Mathematical description $\kappa = \mu_r - 1$	Description	Materials
Diamagnetism	$\kappa < 0$	Non-magnetic for completely filled electron shells; external fields lead to circular current opposing external fields which weaken the external field	All materials
Paramagnetism	$0 < \kappa < 10^{-4}$ $0 < T < T_C$	Partly filled electron shells lead to electron moments which align in an external field and enhance it	Several transition metals
Ferromagnetism	$\kappa(H) \gg 1$ $0 < T < T_C$ $M_R > 0$	Atom moments influence and enhance each other in Weiss domains, remanence at no magnetic field	Fe, Ni, Co, some lanthanoids
Ferrimagnetism	$\kappa(H) \gg 1$ $0 < T < T_C$ $M_R > 0$	Atom moments influence each other in Weiss domains but are rotated in different domains not compensating, spontaneous magnetization is possible;	Magnetite (Fe_3O_4), γ -maghemite ($\gamma\text{-Fe}_2\text{O}_3$)
Antiferromagnetism	$\kappa(H) \gg 1$ $0 < T < T_C$	Atom moments influence each other in Weiss domains but are rotated at same moments in different domains compensating each other	Metal oxides such as Hematite ($\alpha\text{-Fe}_2\text{O}_3$), MnO, FeO, NiO
Superparamagnetism	$\kappa(H) \gg 1$ $T_0 < T < T_C$ $M_R = 0$	Similar to ferro-/ferrimagnetism at particle sizes below 20 - 50 nm, so there exists only one Weiss domain, there is no remanence at temperature above a specific threshold	ferri-/ferromagnetic materials at $d < 20\text{-}50$ nm

Figure 2-2 shows schematic magnetization curves of superparamagnetic (left), weak (middle) and hard magnetic material (right).

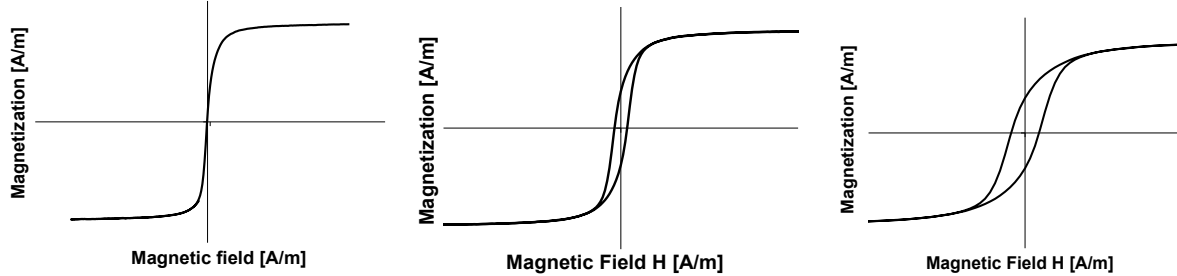


Figure 2-2: examples of the hysteresis curve of superparamagnetic material (left), weak magnetic material (middle) and hard magnetic material (right)

2.1.2 Magnetic Forces

There are two different formalisms, describing the magnetic field \mathbf{H} by a magnetic scalar potential ψ

$$\mathbf{H} = -\nabla\Psi \quad (2-16)$$

or the flux density \mathbf{B} by a magnetic vector potential A_V [Bergmann L.'06]

$$\mathbf{B} = \nabla \times \mathbf{A}_V. \quad (2-17)$$

The magnetic field is free of sources and sinks, hence the divergence of \mathbf{B} is always zero. Two of the four Maxwell equations describe the magnetic field. Ampère's circuital law is simplified here for the case of absence of currents and electric flux density being

$$\nabla \times \mathbf{B} = 0. \quad (2-18)$$

Gauss's law for magnetism is

$$\nabla \cdot \mathbf{B} = 0. \quad (2-19)$$

The energy E of a magnetic field is given by [Bergmann L.'06]

$$\frac{E}{V} = \frac{1}{2}BH = \frac{1}{2} \frac{B^2}{\mu_r}. \quad (2-20)$$

As the influence of μ_r is reciprocal in this equation, the magnetic flux requires less energy in matter of high μ_r compared to vacuum, which is the reason for magnetic attraction. The energy

$$E = -\boldsymbol{\mu} \cdot \mathbf{B} \quad (2-21)$$

of a magnetic moment $\boldsymbol{\mu}$ results from its position and orientation in a magnetic field. In analogy to electric resistance there is as well a magnetic resistance

$$R_M = \frac{l}{\mu_r A}, \quad (2-22)$$

which can be calculated in series and in parallel. Magnetic field lines close hence by the material of highest permeability μ_r and drag matter to reduce the length l and increase the surface area A of the space in the field.

The force on a particle is hence calculated from the energy reduction gained by the lower permeability of the particle compared to the surrounding medium. Another way to look at this is a step of the permeability μ_r at the air – particle interface, so this formula cannot be differentiated. Instead μ_r is replaced by the difference $\Delta\mu_r = \mu_{r,s} - \mu_{r,l}$ between the medium (μ_r is 1 in case of vacuum and close to 1 in air or water) and the particle, resulting in

$$\Delta E = \frac{1}{2} \Delta\mu_r H^2 V. \quad (2-23)$$

This expression is differentiated to deduce the force resulting on a body in vacuum resulting in

$$F = -\nabla(\Delta E) = -\frac{1}{2} V \Delta\mu_r \nabla H^2 = -V \Delta\mu_r H \nabla H = -V \mu_0 \Delta\kappa H \nabla H = -V M \nabla \mu_0 H = -\mu \nabla B. \quad (2-24)$$

In vector notation the force is written as [Rosensweig'97]

$$\mathbf{F}_m = (\boldsymbol{\mu} \cdot \nabla) \mathbf{B} = \mu_0 V_P (\mathbf{M}_P \cdot \nabla) \mathbf{H}. \quad (2-25)$$

Magnetic field and force of a dipole

The vector potential

$$\mathbf{A}_V = \frac{\mu_0 \boldsymbol{\mu} \times \mathbf{r}}{4\pi r^3} \quad (2-26)$$

of a magnetic dipole is analogous to the vector potential of an electric dipole [Bergmann L.'06]. The energy of a dipole results in the torque

$$\mathbf{T}_T = \boldsymbol{\mu} \times \mathbf{B} = \mu_0 V_P \mathbf{M}_P \times \mathbf{H} \quad (2-27)$$

tending to turn the dipole in field direction. \mathbf{M}_P is the magnetization of the particle and V_P its volume. The magnetic field of a dipole in vector coordinates, Cartesian coordinates with the field pointing in z-direction and spherical coordinates [Coey'09] results from (2-17) in

$$\mathbf{H}_{dipole} = \frac{1}{4\pi} \frac{3(\boldsymbol{\mu} \cdot \mathbf{r})\mathbf{r} - r^2 \boldsymbol{\mu}}{r^5} = \frac{1}{4\pi} \frac{\mu}{r^5} \begin{pmatrix} 3xz \\ 3yz \\ 3z^2 - r^2 \end{pmatrix} = \frac{1}{3} M \left(\frac{R}{r}\right)^3 (3\cos^2\theta - 1). \quad (2-28)$$

The magnetic field created by a sphere is hence given by

$$\mathbf{H} = \begin{cases} \frac{1}{3} M \left(\frac{R}{r}\right)^3 (3\cos^2\theta - 1) & r > r_0 \\ -N * \mathbf{M} & r < r_0 \end{cases} \quad (2-29)$$

Figure 2-3 illustrates (2-29). The magnetic field is horizontal. Attracting and repulsing field zones change at $\theta = \arccos\sqrt{1/3} \approx 54.7^\circ$. The repulsing zone surrounds the particle perpendicular to the magnetic field.

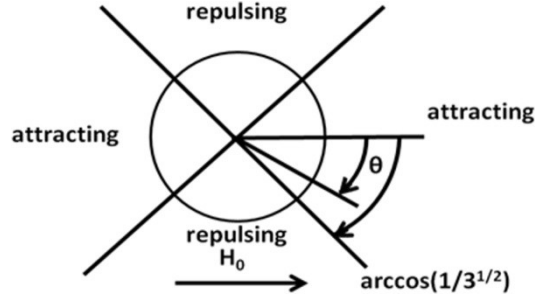


Figure 2-3: the change between attracting and repulsing zones of a dipole or sphere is at 55°

(2-29) can be solved easily. The magnetic field, magnetic flux density and magnetization resulting are shown exemplary in Figure 2-4 by an analytic calculation at $\theta=90^\circ$. The demagnetization leads to a negative magnetic field strength inside of the sphere, while the magnetic flux density is positive.

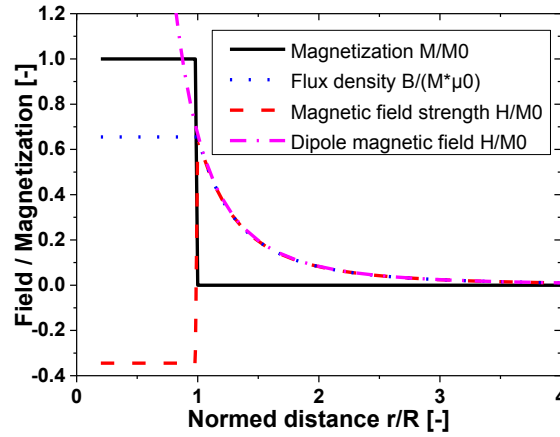


Figure 2-4: the magnetic field strength of a sphere is negative inside by the demagnetization $N=-1/3 M$ and approximated outside by the dipole equation. The flux density is the constant sum of its magnetization and field strength inside, and outside only dependent on the field strength

The energy E of a dipole of the magnetic moment μ_i in the field of dipole μ_j at with the vector \mathbf{r} from i to j is given by combining (2-21) and (2-28) to

$$E = -\boldsymbol{\mu}_i \cdot \mathbf{B}_j = \frac{\mu_0}{4\pi r^3} \left(\boldsymbol{\mu}_i \cdot \boldsymbol{\mu}_j - \frac{3}{r^2} (\boldsymbol{\mu}_i \cdot \mathbf{r})(\boldsymbol{\mu}_j \cdot \mathbf{r}) \right). \quad (2-30)$$

The force \mathbf{F} of one dipole on another dipole is hence deduced easily from its gradient as

$$\mathbf{F} = \nabla(\boldsymbol{\mu}_j \cdot \mathbf{B}_i) = \frac{3\mu_0}{4\pi r^5} \left((\boldsymbol{\mu}_i \cdot \mathbf{r})\boldsymbol{\mu}_j + (\boldsymbol{\mu}_j \cdot \mathbf{r})\boldsymbol{\mu}_i + (\boldsymbol{\mu}_i \cdot \boldsymbol{\mu}_j)\mathbf{r} - \frac{5(\boldsymbol{\mu}_i \cdot \mathbf{r})(\boldsymbol{\mu}_j \cdot \mathbf{r})}{r^2} \mathbf{r} \right). \quad (2-31)$$

In another notation the force

$$\mathbf{F}_{m,ij} = -\frac{3\mu_0\mu_i\mu_j}{4\pi r^4} [-(\mathbf{n}_i * \mathbf{n}_j) + 5(\mathbf{n}_i * \mathbf{t}_{ij})(\mathbf{n}_j * \mathbf{t}_{ij})\mathbf{t}_{ij} - \{(\mathbf{n}_j * \mathbf{t}_{ij})\mathbf{n}_i + (\mathbf{n}_i * \mathbf{t}_{ij})\mathbf{n}_j\}] \quad (2-32)$$

and the torque

$$\mathbf{T}_{m,ij} = -\frac{\mu_0\mu_i\mu_j}{4\pi r^3} \{\mathbf{n}_i \times \mathbf{n}_j - 3(\mathbf{n}_j * \mathbf{t}_{ij})\mathbf{n}_i \times \mathbf{t}_{ij}\} \quad (2-33)$$

were published by Satoh [Satoh'98]. The magnetic moment of the dipoles i and j are μ_i and μ_j , r_{ij} is the dipole distance and \mathbf{n}_i , \mathbf{n}_j is the direction vector of the dipole field strength. The direction vector pointing from dipole i to dipole j is \mathbf{t}_{ij} .

Rheology in Magnetic Suspensions

The interaction between two similar dipoles is important for magnetic suspensions. The Mason number

$$Mn = \frac{Pe}{\lambda} = \frac{54\eta v}{\mu_0 R M^2} \quad (2-34)$$

characterizes whether a particle chain under tension resists, or whether it disrupts or reorganizes by integrating particles [Furst'00]. It is valid for a chain being pulled at its ends. The particle radius is R , the viscosity η and the velocity of outer particles v . The shear stress

$$\tau = F/A = \eta\dot{\gamma} \quad (2-35)$$

is defined as force per area and depends for Newton fluids on the viscosity η and the shear rate $\dot{\gamma}$, see (2-35). The shear rate

$$\dot{\gamma} = v/d \quad (2-36)$$

is defined as velocity v per distance d .

In case of magnetic suspensions needle-shaped agglomerates change the properties. The suspension is similar to a Bingham fluid [Furst'00]. In this case first a flow limit τ_0 needs to be overcome before the material starts to flow as modeled by

$$\tau = \tau_0 + \eta\dot{\gamma}. \quad (2-37)$$

Shulman worked on the viscosity of magnetic suspensions [Shulman'86] and suggested a formula for the breaking of needles to calculate the flow limit by

$$\tau_0 = \frac{\alpha}{2+\kappa} \mu_0 M^2 c_n. \quad (2-38)$$

In this formula c_n is the relative concentration in [g/g] and α is the angle of the particle magnetization to a plane perpendicular to the magnetic field.

Magnetic Field and Force of a Cylinder

The magnetic field around a wire in cylindrical coordinates (r, θ, z) in (2-39) was derived by Stratton [Stratton'41] as

$$\mathbf{H} = M \left(\frac{a}{r}\right)^2 \begin{pmatrix} \cos\varphi \\ \sin\varphi \\ 0 \end{pmatrix}_{(r,\theta,z)} \quad (2-39)$$

The force

$$\mathbf{F}_m = -\mu_0\mu M_W \frac{a^2}{r^3} \begin{pmatrix} \frac{a^2}{r^2} + \cos(2\theta) \\ \sin(2\theta) \\ 0 \end{pmatrix}_{(r,\theta,z)} \quad (2-40)$$

solved for a cylinder of the diameter a and the magnetization M_W on magnetic matter in cylindrical coordinates r and θ was solved analytically [Svoboda'04].

2.2 Further Particle Forces

2.2.1 Fluid Forces on Particles

The Reynolds number

$$Re = \frac{vd}{\nu} \quad (2-41)$$

characterizes the regime of fluid, i.e. whether a laminar or turbulent flow appears. It puts the inertia of fluid in relation with its viscosity ν . In a tube of the equivalent diameter

$$d = \frac{4A}{p} \quad (2-42)$$

(A: cross section area, p: perimeter) the transition between laminar and turbulent flow is at $Re=2300$. In the case of small particles, Reynolds, which depends on the particle diameter d , is small as well.

The fluid resistance force at low Reynolds number ($Re < 0.25$) is in this case given by

$$\mathbf{F}_W = -3\pi\eta d\mathbf{v}. \quad (2-43)$$

In the case of larger particle sizes and hence higher Re numbers ($0.25 < Re < 2 \cdot 10^5$), flow resistance is calculated by the general formula out of c_w according to Kaskas. In case of a needle, the fluid force is different. A formula for both is given in annex 8.4.2.

Out of (2-40) and (2-43) the particle tracks around a wire can be calculated numerically. The particle velocity at each position can be calculated analytically. There is one specific position where fluid force and magnetic force compensate and where particle tracks separate in the

captured and the non-captured particles. Out of this point the capturing radius of a wire can be calculated to (2-45). An example for particle tracks is given in Figure 2-5.

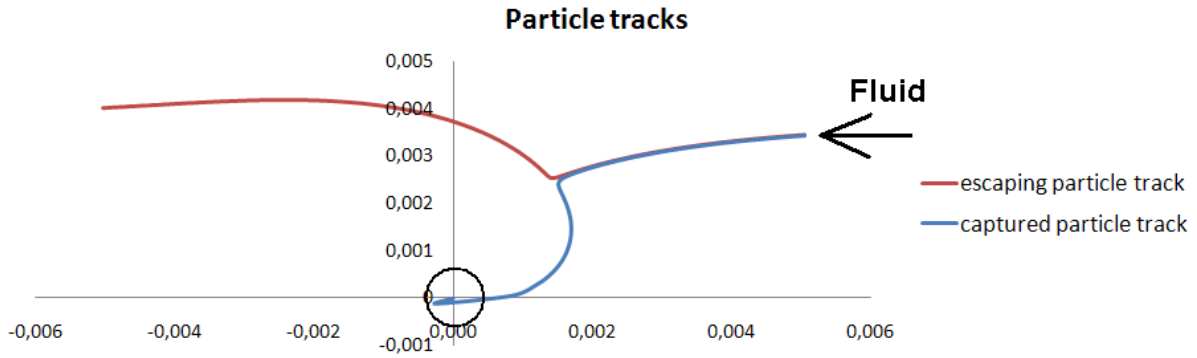


Figure 2-5: example for particle tracks around a wire show a distinct capturing radius, at which the particle track changes in captured and uncaptured

The magnetic velocity

$$v_M = \frac{1}{18} \mu_0 M_W M_P \frac{d_T^2}{a\eta} \quad (2-44)$$

on the surface of a wire in field direction was deduced by equalizing the Stokes resistance of (2-43) and the magnetic wire force [Watson'73]. If particles and wires are not in saturation magnetization, the demagnetization needs to be taken into account in (2-44).

The magnetic field direction is perpendicular to the wire. Flow around a wire is separated in three cases. In the process the longitudinal fluid flow is parallel to the magnetic field. Additionally there is the flow perpendicular to the magnetic field, which is separated in the transversal flow perpendicular to the wire and the axial flow parallel to the wire. The capturing radius normed on the wire radius

$$\frac{Rc}{a} = \left\{ \begin{array}{l} \left[\frac{3}{4} \sqrt{3} \left(\left| \frac{v_m}{v_0} \right| \right)^{1/3} - \left[\frac{\sqrt{3}}{2} - 0.052 * K \right] \left(\frac{v_m}{v_0} \right)^{-1/3} \right. \\ \left. \begin{array}{l} \text{if } \frac{v_m}{v_0} > \frac{2}{\sqrt{1-K}} \text{ and } \frac{v_m}{v_0} > 3 \\ \frac{1}{2} \frac{v_m}{v_0} \left[\sqrt{1-K^2} + K(\pi - \arccos K) \right] \\ \text{if } \frac{v_m}{v_0} < 0.1 \end{array} \right] \end{array} \right\} \quad (2-45)$$

was derived from the magnetic force and the fluid resistance by Uchiyama et al. for the longitudinal arrangement [Uchiyama'78]. Gerber et al. [Gerber'83] and Cowen [Cowen'76] derived similar equations for longitudinal and transversal arrangement. In this formula the parameter $K = M_{S,D}/2H_0$ is important if the wire is below saturation, else $K=1$. The factor 2 is a consequence of the demagnetization $N=0.5$ of a wire. From (2-44) and (2-45) the influence of process parameters on the separation is deduced. The viscosity has a linear reciprocal influence, the magnetization of the wire and particle is linear (but limited by saturation), and the velocity and hence the residence time is exponential depending on the regime but might

be approximated linearly. The influence of the particle size is significant as well and additionally influenced by agglomeration.

Stolarski suggested calculating the separation efficiency

$$E_{sep} = \frac{A_{covered}}{A_{total}} \quad (2-46)$$

of one wire stage from the area covered by the capturing radius around a wire $A_{covered}$ in one stage over the total cross section A_{total} passed by the fluid [Stolarski'11]. The areas result from the geometry of the filter cell and the specific matrix design.

2.2.2 Surface Forces

In addition to magnetic forces, surface forces play an important role. A roundup of surface forces is named for their authors DLVO (Derjaguin, Landau, Verwey, Overbeek), consisting of the van-der-Waals, electrostatic and Born forces. These forces are necessary for a force comparison (see Chapter 3). They include the

- van-der-Waals,
- Coulomb,
- and the Born force.

For ferromagnetic or superparamagnetic particles, magnetic forces additionally appear and cause agglomeration; the influence of the DLVO forces in this case was investigated by Stolarski [Stolarski'07]. Besides the DLVO forces, there are additional influences. The Brownian motion becomes dominant below 10 nm, but might be neglected at the scale of the particle systems considered in this work.

Van-der-Waals-Force

The van-der-Waals force results from short-term charge fluctuations in the electron shell of atoms. This induces dipole moments which in sum create an attractive force. A derivation of the force for two smooth particles was done by Hamaker [Hamaker'37]. The van-der-Waals potential

$$E_{vdw} = \frac{A_H}{12} \left(\frac{d_i d_j}{r^2 - \left(\frac{d_i + d_j}{2}\right)^2} + \frac{d_i d_j}{r^2 - \left(\frac{d_i - d_j}{2}\right)^2} + 2 * \ln \left[\frac{r^2 - \left(\frac{d_i + d_j}{2}\right)^2}{r^2 - \left(\frac{d_i - d_j}{2}\right)^2} \right] \right) \quad (2-47)$$

results from fluctuating charge in the electron shell of atoms [Hamaker'37]. Parameters include the Hamaker constant A_H , based on q atoms with an energy λ ($A_H = \pi^2 q^2 \lambda \sim 3h\omega/2\pi = 3*5 \text{ eV}/2 \pi \sim 10^{-20} \text{ J}$), the particle diameters d_i and d_j , and the distance of the particle centers r . The van-der-Waals force is solved for two particles for $a \ll d_i$ or d_j to

$$F_{vdw,particles} = \frac{A_H}{12} \left(\frac{d_i d_j}{a^2 (d_i + d_j)} \right). \quad (2-48)$$

In case of two particles of the same size d this is further simplified [Hamaker'37]

$$F_{vdw,particles} = \frac{A_H}{24} \left(\frac{d}{a^2} \right). \quad (2-49)$$

For a much different particle size $d_i \ll d_j$ or for a particle in contact with a wall, the force is larger in [Hamaker'37]

$$F_{vdw,wall} = \frac{A_H}{12} \left(\frac{d_i}{a^2} \right). \quad (2-50)$$

Coulomb Force

The electrostatic force is not only important for the agglomeration or repulsion of particles, but as well for the adsorption of protein to an ion exchange functionalized particle surface. Electrostatic forces of dispersed particles in the liquid phase result from different charge of the particles. A charged particle collects oppositely charged ions in its surrounding. In the inner layer ions bind chemically to the particle (chemisorption), while in the outer layer particles are loosely bound by electrostatic forces (physisorption, ion exchange). The charge of particles attracts ions compensating this charge in two different layers. The inner layer, called the Helmholtz layer, is stiff and has the Nernst-Potential in its inner shell and Stern-Potential in its outer shell. The outer layer, called diffuse layer or Gouy-Chapman-double layer, has a shrinking amount of ions. The potential shrinks linearly in the stiff layer and exponentially in the diffuse layer. The diffuse layer moves under tangential stress, with the electric potential at the slipping plane called the zeta-potential. The zeta potential is as well used to characterize the electrostatic force, characteristic is 25 mV, the maximum is about 100 mV. The characteristic thickness is the Debye-length λ . On long range the Stern-double layer compensates the electric force, but for particles being close to each other, electrostatic forces appear at the intersection of the Stern layer of the two particles. Forces are repulsive for particles charged equally and attractive for particles charged oppositely. The different concentration of ions is separated in two regions, called the double layer. The Born force which is sometimes mentioned is for particles sufficiently large and redundant with mechanic forces, i.e. the Hertz force presented above. This work bases in the calculation of DLVO on the same equations as Eichholz [Eichholz'10] who made a similar simulation on magnetic cake filtration.

The Coulomb potential is [Gregory'75; Eichholz'10]

$$E_{Coul} = \frac{32\pi N_A c_{Ion} kT}{\kappa^2} \frac{d_i * d_j}{r} \gamma_i \gamma_j \exp \left(-\kappa_d \left[r - \frac{d_i * d_j}{2} \right] \right). \quad (2-51)$$

Its gradient is the Coulomb force

$$F_{Coul} = -\nabla E_{Coul} = \frac{32\pi N_A c_{Ion} kT d_i * d_j}{\kappa^2} \frac{d_i * d_j}{r} \gamma_i \gamma_j \exp\left(-\kappa_d \left[r - \frac{d_i * d_j}{2}\right]\right) \left(\frac{1}{r} + \kappa\right) \quad (2-52)$$

with the parameter

$$\gamma_{i,j} = \frac{\exp\left(\frac{z_{Ion} e_0 \zeta_{i,j}}{2kT}\right) - 1}{\exp\left(\frac{z_{Ion} e_0 \zeta_{i,j}}{2kT}\right) + 1}. \quad (2-53)$$

The Debye-Hückel-Parameter κ_D and the Debye length λ is given by

$$\lambda = \frac{1}{\kappa_D} = \sqrt{\frac{\epsilon_r \epsilon_0 kT}{e_0^2 N_A \sum c_{Ion} z_{Ion}^2}}. \quad (2-54)$$

The parameters in this equation are the Boltzmann constant k , the temperature T , charge of the ion z , the effective surface potential (ζ -potential) Ψ_0 , the electron charge e and the inverse Debye length κ_D . Figure 2-6 illustrates the distribution and concentration of ions in a particle shell and its influence on the potential.

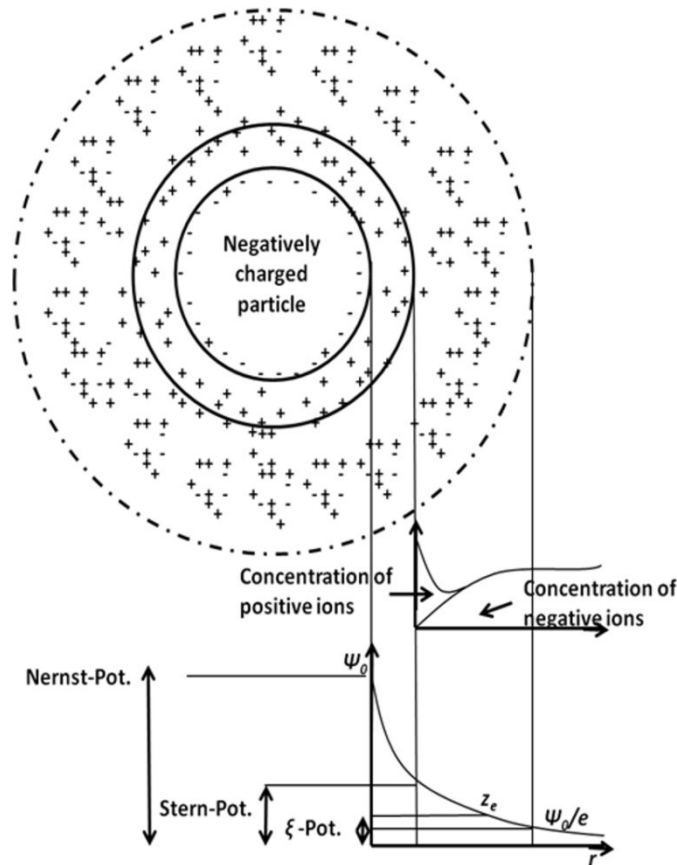


Figure 2-6: the concentration of positive ions around a negatively charged particle rises over distance, being low in the Stern layer and higher in the diffuse double layer

Repulsive forces: Born force

The mechanic force is modeled by two different approaches: in DLVO the Born force is introduced. The Born potential

$$E_{Born} = \frac{A_H R \delta_p^6}{1260(r - 2R)^7} \quad (2-55)$$

results from strong repulsion of molecules in consequence of overlap of their outmost electron shells. It induces forces dominant at low particle distance (<0.1 nm). It is usually modeled as a strong force increasing with an arbitrary exponent, but is not accessible to analytical or experimental investigation. The material constant is $\delta_p=0,5$ nm, R is the particle radius, A_H the Hamaker constant and $r-2R$ the distance of the surfaces [Raveendran'95].

The Born force is

$$F_{Born} = -\nabla E_{Born} = 7 \frac{A_H \frac{d}{2} \delta_p^6}{1260(r-2R)^8}. \quad (2-56)$$

This force has a high gradient, i.e. it changes strongly in case of a small position change, and is hence not stable in simulations based on soft shell models. The Hertz force applies for macroscopic bodies and is more stable in a Discrete Element simulation. Its introduction is as well the theoretic basis of the Discrete Element Method. It requires overlap of particles which is not consistent with equations for other DLVO forces.

Repulsive forces: Macroscopic equations

In case of large particles, the repulsing force increases slowly compared to the Born force, which is better suited for the implementation in a simulation model. The strain of a body, like e.g. a spring, depends linear on the force

$$\mathbf{F} = D_S * \mathbf{x}, \quad (2-57)$$

which depends on the displacement \mathbf{x} and the stiffness D_S . The resonance frequency of a body f is calculated from its stiffness and mass m by

$$2\pi f = \sqrt{\frac{D_S}{m}}. \quad (2-58)$$

In case of two spheres pressed on each other, the relation is not linear. The Hertz normal force [Langston'95; Deen'07] is

$$\mathbf{F}_{n,ij} = k_n \delta^{3/2} \mathbf{n}_{ij} - \eta_{n,ij} * \mathbf{v}_{rel,n,ij}. \quad (2-59)$$

It is based on the virtual overlap δ of two spheres. The tangential force

$$\mathbf{F}_{t,ij} = -\eta_{t,ij} * \mathbf{v}_{rel,t,ij} \quad (2-60)$$

is in this approach limited to a damper, with no spring influence. The parameters $k_{n,ij}$, $\eta_{n,ij}$, $k_{t,ij}$ and $\eta_{t,ij}$ are introduced in (2-61), (2-70), (2-69) and (2-68). The virtual particle overlap δ is defined by

$$\delta = \begin{cases} \frac{d_i+d_j}{2} - r_{ij} & \text{for } r_{ij} < \frac{d_i+d_j}{2} \\ 0 & \text{otherwise} \end{cases} \quad (2-61)$$

The stiffness parameter

$$k_{n,ij} = \frac{\sqrt{2r}E_{eq}}{3(1-\nu^2)} \quad (2-62)$$

is calculated out of the equivalent elasticity modulus E_{eq} and the Poisson ratio ν . The elasticity modulus E_{mod} and the shear modulus

$$G = \frac{E_{mod}}{2(1+\nu)} \quad (2-63)$$

are linked in case of isotropic media. Additional parameters are defined to take into account that parameters might have different properties. The equivalent elasticity modulus

$$E_{eq}^{-1} = \frac{1-\nu_i^2}{E_{mod,i}} + \frac{1-\nu_j^2}{E_{mod,j}} \quad (2-64)$$

is calculated from the modulus of both particles i and j [EDEM_Solutions_Ltd._User's_Guide'10], the equivalent modulus of rigidity

$$G_{eq}^{-1} = \frac{1-\nu_i^2}{G_i} + \frac{1-\nu_j^2}{G_j}, \quad (2-65)$$

the radius

$$R_{eq}^{-1} = R_i^{-1} + R_j^{-1} \quad (2-66)$$

from the particle radii R_i and R_j and the mass

$$m_{eq}^{-1} = m_i^{-1} + m_j^{-1} \quad (2-67)$$

from the particle masses m_i , m_j . A new stiffness parameter

$$k_{n,ij} = \frac{4}{3}\sqrt{R_{eq}}E_{eq} \quad (2-68)$$

is hence introduced based on these parameters. The damper coefficient in normal direction

$$\eta_{n,ij} = 0.3 \sqrt{\frac{9}{2}m_{eq}\sqrt{\delta}k_{n,ij}} \quad (2-69)$$

is important to avoid normal oscillation of particles like a spring and depends on the particle overlap [Chu'08]. The friction coefficient in tangential direction

$$\eta_{t,ij} = 2 \sqrt{\frac{2}{7}m_{eq}k_{t,ij}} \quad (2-70)$$

depends on the tangential stiffness

$$k_{t,ij} = \frac{2\sqrt{2R_{eq}}G_{eq}}{2-\nu}\sqrt{\delta} \quad (2-71)$$

and reduces sliding of particles on each other [Deen'07].

Brownian Motion

Below 10 nm Brownian motion dominates and many suspensions are stable. Colloidal magnetic suspensions at this particle size are called magnetic fluid. Colloidal magnetic suspensions have an interesting behavior which was characterized by Rosensweig [Rosensweig'97]. At the particle sizes above 100 nm investigated in this work, Brownian motion is negligible. The medium quadratic movement of a particle σ^2 was derived by Einstein 1905 (s. annex 8.4.1). The nondimensional parameter

$$\lambda_B = -\frac{E}{kT} = \frac{\mu_0 V_P M^2}{12kT} \quad (2-72)$$

puts magnetic dipole energy and thermal energy into relation to estimate whether magnetic particles form needle-chained agglomerates or a colloidal suspension [Furst'00; de Vicente'11]. In case $\lambda \gg 1$ particles agglomerate.

2.3 Diffusion

The adsorption of protein to a surface, in this case a moving particle with ligands, is influenced by different phenomenon. Driving forces are convection and diffusion. Electrostatic forces do not play a role, as the charge of a particle is compensated in the electrical double layer. Convection is approximated easiest by numerical simulation. The mass transfer to a particle is hence calculated as a function of the relative particle velocity ν by superposed diffusion and convection. The diffusion is described by Fick's law, which is

$$\frac{\partial n}{\partial t} = -D * A * \frac{\partial n}{\partial x}. \quad (2-73)$$

The cross section is A , the concentration c , the time t and the molecule number diffusing is n in [mol].

The diffusion coefficient

$$D = \frac{9.4 * 10^{-15} T}{\eta^3 \sqrt{M_M}} \quad (2-74)$$

is determined by the Polson correlation out of the viscosity η , the molar mass M_M and the temperature T [Ghosh'06]. Another equation for its calculation is the Stokes-Einstein-equation.

Diffusion is superposed with convection as the sphere moves relative to the liquid. The mass transfer is hence calculated by combined diffusion and convection. The Schmidt number

$$Sc = \frac{\nu}{D} \quad (2-75)$$

needs to be calculated out of (2-75). It links fluid viscosity and diffusion, and characterizes hence the transport by convection and diffusion.

The Sherwood number

$$Sh = \frac{\beta * l}{D} \quad (2-76)$$

puts diffusion and the absolute mass transfer into relation and is hence used to calculate convection. The coefficient β characterizes the mass transfer. It may be calculated from (2-76) to replace D in (2-73) to calculate the mass transport. The parameter l is a characteristic length, in this case the particle diameter.

The Sherwood number is calculated by a model. The equations were originally developed for heat transfer, but apply similarly to mass transfer. It depends on a laminar and a turbulent coefficient:

$$Sh = 2 + \sqrt{Sh_{lam}^2 + Sh_{turb}^2}. \quad (2-77)$$

In case velocity and hence the particle Reynolds number Re is small, Sherwood approximates 2 [VDI'06]. The laminar coefficient

$$Sh_{lam} = 0.664 * \sqrt{Re} * Sc^{1/3} \quad (2-78)$$

and the turbulence coefficient

$$Sh_{turb} = \frac{0.037 * Re^{0.8} * Sc}{1 + 2.44 * Re^{-0.1} * (Sc^{2/3} - 1)} \quad (2-79)$$

depend on the Re number and the Sc number.

The model in (2-77) to (2-79) is derived in analogy to heat transfer. Another approach exists for mass transport, but was not implemented in the simulation [Kraume'12]:

$$Sh = \begin{cases} 2 & Re = 0 \\ 0.991 * \sqrt[3]{Re * Sc} & Re < 1 \\ 2 + 0.66 * \left(1 + 0.59 * \sqrt{Sc}\right)^{-1/3} * \frac{(Re * Sc)^{1.7}}{1 + (Re * Sc)^{1.2}} & 1 < Re < 3 * 10^5 \\ \frac{0.037 Re^{0.8} Sc}{1 + 2.44 Re^{-0.1} (Sc^{2/3} - 1)} & Re > 3 * 10^5 \end{cases} \quad (2-80)$$

Additionally diffusion at the surface and in pores is limited by different effects, see Knudsen [Cussler'09] and micropore-diffusion, which is not investigated further in this work. Kinetics can be described by a model of first or second order or the Elovich-equation. A study on the

adsorption kinetics of proteins is in [Lee'74]. A study on the influence of particle size is in [Benguella'02]. There are diverse other studies on the kinetics which mostly found two-step kinetics: after a very fast adsorption of less than a few minutes, a slow adsorption of several hours continued before achieving the maximum adsorption [Chang'05; Li'05; Kabbashi'09]. This may be interpreted as adsorption to the surface and adsorption to inner pores of the particles.

2.4 Centrifugation

The centrifugal force

$$\mathbf{F}_{centrifugal} = -m * \boldsymbol{\omega} \times (\boldsymbol{\omega} \times \mathbf{r}) \quad (2-81)$$

is an inertia force counter directed to the actual centripetal force, it depends on the rotational speed $\boldsymbol{\omega}$, the particle mass m and the rotation radius r .

The centrifugal acceleration is commonly undimensionalized to a value

$$C = \frac{\omega^2 r}{g} \quad (2-82)$$

using the earth gravitation g . The Coriolis force

$$\mathbf{F}_{Coriolis} = -2m \boldsymbol{\omega} \times \mathbf{v} \quad (2-83)$$

is as well an inertia force which influences a bodies' tangential velocity when moving radially in a rotating reference frame. It depends on the body velocity \mathbf{v} in radial direction. In a centrifuge, this force is particularly important at the inlet and outlet.

The waterspout in a centrifuge is calculated from

$$z = \frac{\omega^2 r^2}{2g} + z_s \quad (2-84)$$

by linking the axial position z with the radius r in a centrifuge by its rotational velocity ω and the earth gravitation g [Stolarski'11] with the offset z_s depending on the overflow weir position.

The flow in an overflow centrifuge is not uniform but depends on the radius of the overflow weir. This influences as well the cut size of particles. Different models exist on the velocity distribution of liquid in a centrifuge including a laminar profile and plug flow. Specifically the thickness of the flow region depends on diverse parameters, with different models and no final consensus. According to Reuter [Reuter'67], not the complete fluid in an overflow centrifuge moves, but only a layer at the inside of the device. The thickness

$$\delta_C = \sqrt[5]{\frac{15 L \nu Q}{\pi r_H \omega^2}} \quad (2-85)$$

of the flow layer in a centrifuge is dependent on the volume flow Q , the rotational velocity ω , the centrifuge length L , the medium radius of the flow layer r_H and the viscosity ν .

The cut size of particles in a centrifuge

$$x_p = \sqrt{\frac{18\eta}{(\rho_p - \rho_l)\omega^2 t_0} \ln \frac{R_{dr}}{R}} \quad (2-86)$$

depends on the time t_0 particles need to sediment from their initial diameter R to the outer diameter of the flow layer R_{dr} , the viscosity η and the density difference between particles and liquid $\rho_s - \rho_l$ [Stahl'04].

There are as well several models for the dewatering in decanter centrifuges, which might be applied as well to a magnetic decanter [Stiborski'04].

2.5 Particle Size Distribution

To approximate the particle size distribution by a function, two different approaches showed to be well suited for the used products. The density distribution

$$q(d) = \begin{cases} \frac{1}{\sqrt{2\pi}\sigma d} \exp\left(-\frac{(\ln d - x_{50})^2}{2\sigma_{st}^2}\right) & \text{if } x > 0 \\ 0 & \text{if } x < 0 \end{cases}, \quad (2-87)$$

can well be approximated by a logarithmic cumulative distribution with the cut size d , the medium diameter x_{50} and the standard deviation $\sigma_{st} = \ln(x_{84}/x_{50})$ (x_{84} is the particle diameter where 84% of the particles are smaller).

The sum distribution developed by RRSB (Rosin, Rammler, Sperling, Bennet) is as well a good approximation to calculate the separation from a particle size distribution

$$Q(d) = \exp\left[-\left(\frac{d}{x_{63}}\right)^{n_{RRSB}}\right], \quad (2-88)$$

the size x_{63} at which 63 % are smaller in a mass distribution and the parameter n_{RRSB} [Stieß'09].

2.6 Modeling and Simulation Basics

2.6.1 Computational Fluid Dynamics

Computational Fluid Dynamics (CFD) by the Finite Volume Model (FVM) is well-established and wide-spread for the simulation of fluid. A geometry, in which the fluid flow is to be calculated, is discretized in volumes. In each volume the equations for the conservation

of mass and impulse are solved under compliance of the boundary conditions, i.e. of the flow at the border of the region [Laurien'09]. The method is conservative by definition, which presents an advantage compared to FEM. In case of laminar flow, direct simulation yields acceptable results. The method is e.g. appropriate to determine flow around a single magnetic wire.

Overview

The mass conservation can be derived easily from summing a Finite Volume, resulting in

$$\underbrace{\frac{\partial \rho}{\partial t}}_{\text{change over time}} + \underbrace{\nabla(\rho \cdot \mathbf{v})}_{\text{convection}} = 0. \quad (2-89)$$

It consists of a term of the change of mass per cell volume (density ρ) in the transient case and of the mass conservation including the velocity \mathbf{v} [Hickel'13].

This equation is simplified in case of incompressible media ($\rho = \text{const.}$) or stationary flow. The momentum conservation (as well known as Navier-Stokes equation) sums the energy of a fluid. It consists of the terms for the time change of the impulse and the impulse, a pressure term including the pressure p , a term including the viscosity μ and the external forces \mathbf{F}_V (which is in this case normed on the volume in [N/m^3]) in

$$\underbrace{\rho \frac{\partial \mathbf{v}}{\partial t}}_{\text{change over time}} + \underbrace{\rho(\mathbf{v} \cdot \nabla \mathbf{v})}_{\text{momentum/convection}} = \underbrace{-\nabla p}_{\text{pressure term}} + \underbrace{\mu \cdot \Delta \mathbf{v}}_{\text{viscosity term/diffusion}} + \underbrace{\mathbf{F}_V}_{\text{external forces}}. \quad (2-90)$$

A system of four (2D: 3) unknowns and equations in each cell results, one being the mass conservation, and three the momentum conservation in three dimensions (2D: 2). In case of heat simulation another equation is added for the thermal energy. A pressure-correction method is used, as neither mass nor momentum balance delivers a coupling between pressure and velocity. The numerical solution is done by differentiating schemes, which are usually categorized depending on their order. Lower orders are usually more stable, while higher orders converge faster. This is commonly used by starting a simulation at first order and then changing to a higher order. A matrix results, which is usually sparse and solved directly or iterative. In transient simulations, the solution at a given time is calculated from the solution of the previous time step. The solution methods are separated in explicit (easy to implement, low memory requirements, fast, but unstable at large time steps) and implicit methods (stable but large memory requirements). A combination of the two methods is called predictor-corrector.

Multiphase and Species simulation

Multiphase simulation by Euler-Euler solve, additionally to the conservations equations for the mixture equations for the transport of the volume fraction of one phase, a set of continuity and momentum equations multiplied with the relative concentration of the specific phase. In the case of the simulation of a reaction (e.g. adsorption) simulation, the species are simulated similarly to the Euler-Euler model. The equation

$$\underbrace{\frac{\partial(\rho\alpha_i)}{\partial t}}_{\text{change over time}} + \underbrace{\nabla(\rho\alpha_i\mathbf{v})}_{\text{convection}} = \underbrace{-\nabla \cdot \left(-\rho D \nabla \alpha_i - D_T \frac{\Delta T}{T} \right)}_{\text{diffusion}} + \underbrace{S_j}_{\text{sources}} \quad (2-91)$$

is solved for each species. The local mass fraction of each species is α_i , the sources and sinks including production by reaction are S_i . The simulation of a disperse phase is possible by Euler-Lagrange. In this case the fluid motion is simulated. Then the drag force on a single particle based on the differential velocity of the fluid and the particle motion is calculated from (2-43) or (8-2).

Turbulence

As mentioned above, in case of flow in a tube the regime between turbulent and laminar flow changes at $Re = 2300$. Turbulence cannot be simulated directly as the cell size needs to be small enough to reproduce any flow, i.e. in case of turbulent flow the finest eddies. Kolmogorov scales of turbulent flow show that the necessary number of grid cells rises with $Re^{9/4}$ [Laurien'09], the number of time steps for stability linearly resulting in the computational expense rising with Re^3 . This renders the direct simulation of turbulence in most technical applications impossible. A modeling approach is Reynolds Averaged Navier Stokes (RANS), which bases on the calculation of the average flow velocity while turbulent energy dissipation in smaller scales is modeled. The approach is called eddy viscosity model, based on the turbulent eddy viscosity $\mu_t = \rho \nu_t$ and describes the increase of viscosity by turbulent fluctuations. The approach bases on isotropic turbulence. Turbulence by convection and diffusion is modeled [Laurien'09]. The Reynolds shear tensor

$$\tau_{i,j} = \overline{\rho u_i' u_j'} = -\mu_T \left(\frac{\partial \bar{u}_i}{\partial x_j} + \frac{\partial \bar{u}_j}{\partial x_i} - \frac{2}{3} \frac{\partial \bar{u}_k}{\partial x_k} \delta_{ij} \right) + \frac{2}{3} \rho k \delta_{ij} \quad (2-92)$$

is an additional term in the equation modeling the time-averaged Reynolds shear analogous to Stokes friction. It is approximated by the Boussinesq approach, which models molecular viscosity by shear strain. The shear is induced by turbulence.

This model is wide-spread and several similar approaches were developed to better approximate specific problems.

In the k - ε model, the flow is considered isotropic, reducing the turbulence modeling to two additional equations. They model the transport of the kinetic energy $k = \frac{1}{2}(\overline{u_1'^2} + \overline{u_2'^2} + \overline{u_3'^2})$ and the isotropic dissipation rate $\varepsilon = \nu \frac{\partial \overline{u_i'}}{\partial x_k} \frac{\partial \overline{u_i'}}{\partial x_k}$. The turbulent viscosity $\mu_T = \rho \cdot c_\mu \frac{k^2}{\varepsilon}$ describes the increase of viscosity by increasing turbulent fluctuation. The transport equations are [Wilcox'94; Laurien'09; Ansys_Manual'12]

$$\rho \frac{\partial k}{\partial t} + \rho \overline{u_j} \frac{\partial k}{\partial x_j} = C_\mu \rho \mu_T \left(\frac{\partial \overline{u_i}}{\partial x_j} + \frac{\partial \overline{u_j}}{\partial x_i} \right) - \rho \varepsilon + \frac{\partial}{\partial x_j} \left[\left(\mu + \frac{\mu_t}{\sigma_k} \right) \frac{\partial k}{\partial x_j} \right] \quad (2-93)$$

and

$$\rho \frac{\partial \varepsilon}{\partial t} + \rho \overline{u_j} \frac{\partial \varepsilon}{\partial x_j} = C_{\varepsilon 1} \frac{\varepsilon}{k} \tau_{i,j} \frac{\partial \overline{u_i}}{\partial x_j} - C_{\varepsilon 2} \frac{\varepsilon^2}{k} C_\mu \rho \mu_T \left(\frac{\partial \overline{u_i}}{\partial x_j} + \frac{\partial \overline{u_j}}{\partial x_i} \right) \frac{\partial \overline{u_i}}{\partial x_j} - C_{\varepsilon 2} \frac{\varepsilon^2}{k} + \frac{\partial}{\partial x_j} \left[\left(\mu + \frac{\mu_t}{\sigma_\varepsilon} \right) \frac{\partial \varepsilon}{\partial x_j} \right]. \quad (2-94)$$

The parameters in the model are $C_\mu=0.09$, $C_{\varepsilon 1}=1.44$, $C_{\varepsilon 2}=1.92$, $\sigma_\varepsilon=1.3$ and $\sigma_k=1$.

The k - ε model delivers a good approximation in freestream, i.e. of flow remote from walls. Close to walls the flow is anisotropic though, leading to a bad approximation. The k - ω model was established for flow simulation close to walls. It reduces the characteristic length scale and bases on a transport equation for a characteristic frequency $\omega = 1/C_\mu * \varepsilon/k$ instead of the dissipation rate. The transport equations of k and ω are hence adapted to

$$\rho \frac{\partial k}{\partial t} + \rho \overline{u_j} \frac{\partial k}{\partial x_j} = C_\mu \rho \mu_T \left(\frac{\partial \overline{u_i}}{\partial x_j} + \frac{\partial \overline{u_j}}{\partial x_i} \right) - \beta^* k \rho \omega + \frac{\partial}{\partial x_j} \left[\left(\mu + \sigma^* \mu_t \right) \frac{\partial k}{\partial x_j} \right] \quad (2-95)$$

and

$$\rho \frac{\partial \omega}{\partial t} + \rho \overline{u_j} \frac{\partial \omega}{\partial x_j} = \alpha_t \frac{\omega}{k} C_\mu \rho \mu_T \left(\frac{\partial \overline{u_i}}{\partial x_j} + \frac{\partial \overline{u_j}}{\partial x_i} \right) \frac{\partial \overline{u_i}}{\partial x_j} - \beta \rho \omega^2 + \frac{\partial}{\partial x_j} \left[\left(\mu + \sigma \mu_t \right) \frac{\partial \omega}{\partial x_j} \right]. \quad (2-96)$$

The parameters are according to Wilcox [Wilcox'88] $\alpha_t=5/9$, $\beta=0.075$, $\beta^*=0.09$, $\sigma=0.5$ and $\sigma^*=0.5$. The model k - ω SST is a combination of both k - ε and k - ω models. It was used in this work for the simulation of centrifuges.

A more sophisticated approach mentioned for completeness is the Reynolds Stress Model (RSM). It involves a separate transport equation for the Reynolds stress tensor in each dimension, resulting in a total of at least 6 additional transport equations. This overcomes the problem of eddy viscosity models, which do not deliver good results in bent flow lines or strong twist [Speziale'90] as e.g. in hydrocyclones. Besides numerically more expensive, RSM is less stable, and hence only used if it is indispensable.

Grids

In the grid generation the geometry is discretized to small volumes. The flow from each volume to the neighbouring volumes is calculated, doing a mass balance in every iteration. There are different approaches for the discretization of the geometry, with the most important being summarized in Table 2-2. Grids are classified in structured and unstructured. Structured grids usually deliver better results at the same cell number, especially when the fluid enters the cell perpendicular to the cell face. Hence a structured grid is usually preferred for delivering better results at similar cell numbers compared to unstructured grids. Unstructured grids are usually easy to create in an automatic routine. In case of complex geometries, unstructured grids may be the only option. Several new methods allow as well a better approximation of complex geometries in a structured way like cut-cell, which cuts off structured cells at the boundary of the geometry.

Table 2-2: Overview over grid generation methods

Name	Properties	Advantages / Disadvantages
Structured	- Regular rectangle (2D) or Octaeder (3D) scheme	+ efficient - can only be created in geometries with flat faces
Cooper / Sweep	- Structured 3D scheme which reproduces one face map at specific distances - Hexaeder (in unstructured face map) / Octaeder (in structured face map)	+ structured grid + in many geometries perpendicular to flow direction + easy to create - not possible if the cross section changes qualitatively
Cut-cell	- Rectangular grid which cuts part of a cell off at the border of the domain	+ structured grid in all geometries + completely automatic generation possible - not possible with periodic boundary conditions
Unstructured grid	- Geometry is meshed with a triangle (2D) or tetraeder (3D) scheme	+ completely automatic generation possible + possible in irregular geometries - delivers less exact simulation results than structured grids, needs a larger number of cells for the same quality
Hybrid grid	- Combination of a structured and unstructured grid - In 3D the linking face needs to have structured elements of similar edge length	+ Combines the advantages of structured and unstructured grids - more effort in creation

Grids are for many applications refined in areas of high gradients of the velocity and the pressure. This is usually the case close to the boundaries (hence called “boundary layer”) and is possible for both structured and unstructured grids.

Boundary Conditions

There are two types of boundary conditions. A Dirichlet boundary condition sets a parameter to a specific value ($f(x)=y$). Dirichlet conditions cannot be applied to every boundary in a simulation, as this would for some parameters like fluid velocity create an over determined system. Applying it to specific boundaries is interesting, as it allows the application of experimental process conditions. A Neumann boundary condition does not define a condition itself but its gradient ($f'(x)=y$).

A frequent set of boundary conditions for the in- and outlet is the definition of the velocity or pressure by a Dirichlet condition at the inlet, and of the pressure at the outlet. The respective other condition is set by Neumann.

At walls usually a specific velocity (no slip) or slip (e.g. free slip) is set, in case of a far field the velocity of the surrounding region is usually applied. Turbulence close to a wall needs to be treated separately. One approach common in $k-\epsilon$ models consists in the complete modeling of the flow close to the wall in a layer of one single cell. This approach is well suited for highly turbulent flow and a large velocity difference between fluid and wall, like e.g. in a hydrocyclone. Another approach consists in a special modeling in which the flow in several cells at the wall is resolved in overall velocity.

Symmetry can be used to reduce the geometry which needs to be modeled. There are two different types of symmetry faces. Either the body has a “real” symmetry. In this case a Neumann boundary condition is applied to simulate the same behavior at the opposite side of the face. Or the region is periodic, i.e. liquid leaves the device on one boundary and enters on another boundary. In this case each of the cells of one face is linked to a cell of the other face. Dirichlet conditions apply the negative velocity of one cell as a positive velocity in the linked cell. The pressure is linked directly. An example for a periodic condition is a segment (e.g. a quarter) of a turning centrifuge. This device actually is rotationally symmetric, so both segment faces are linked. Liquid flowing out one face enters on the corresponding other face.

Simulation in rotary flows

Rotary flows are common in engineering applications. The rotation introduces a large radial pressure gradient driving the flow. In mechanical engineering this comprises specifically hydrocyclones and centrifuges. In case of a high swirl like in hydrocyclones, the use of the RSM model is necessary, while for otherwise the (realizable) $k-\epsilon$ model might be sufficient.

Fine meshes are necessary, specifically at high velocity gradients. A general recommendation for the simulation of rotary flows is a specific solver for the pressure discretization (PRESTO!), low underrelaxation factors to enhance the stability and fine meshes [Ansys_Manual'12].

2.6.2 Magnetic Fields in the Finite Element Method

In the Finite Element Method (FEM) the differential equations are solved by integrating them in a domain. The integral is replaced by a sum of single numerical integrals of the elements. A large, linear, sparse system of equations results

$$\mathbf{A}_M \cdot \mathbf{u} = \mathbf{f}, \quad (2-97)$$

(matrix \mathbf{A}_M , vector of unknown functions \mathbf{u} , vector of Neumann boundary conditions \mathbf{f}), which is solved directly (in case of few degrees of freedom) or iteratively. In the current work FEM is used for the simulation of magnetic fields, i.e. the Maxwell equations are the differential equations solved to simulate the magnetic field and its spread in matter and vacuum in a FEM code. In general either a vector potential \mathbf{A} or a scalar potential ψ is determined iteratively. The magnetic field \mathbf{H} is solved by determining a potential ψ satisfying the equations, which can be transformed using (2-9), (2-16) and (2-19), resulting in

$$\nabla \cdot (\mu_0 \nabla \psi - \mu_0 \mathbf{M}) = 0. \quad (2-98)$$

Similarly, Eqs. (2-17) and (2-18) result in

$$\nabla \times (\nabla \times \mathbf{A}_V) = 0. \quad (2-99)$$

2.6.3 The Discrete Element Method

Initially the Discrete Element Method (DEM) served for the simulation of Molecular Dynamics (MD). It was developed by Cundall for discrete interacting bodies [Cundall'88; Hart'88; Cundall'92]. The method is now divided from MD and established for the simulation of particle motion. It bases on the calculation of forces between particles, and deduces motion of multiple particles. Forces introduced usually include Hertz forces. Particles are placed under starting conditions in a geometry or introduced at a boundary. In discrete time steps the position of particles is calculated out of the velocity and interparticular forces. A force

$$\mathbf{F} = m * \frac{d\mathbf{v}}{dt} \quad (2-100)$$

on a body of mass m during a time t changes its velocity \mathbf{v} . Similarly, the torque

$$\mathbf{T}_T = \frac{d\mathbf{L}}{dt} = I_n * \frac{d\boldsymbol{\omega}}{dt} \quad (2-101)$$

on a body changes its rotational speed $\boldsymbol{\omega}$ depending on its moment of inertia I_n , see (2-101), which can be expressed as well as the change of its angular momentum \mathbf{L} .

In this method, the position is calculated at discrete time steps in a cycle. Each time step, the forces are calculated again, and the position and velocity is updated accordingly. A time stepping scheme used in Discrete Element Modeling for calculating the position

$$r_i(t + \Delta t) = r_i(t) + \Delta t v_i(t) + \frac{\Delta t^2}{2m_i} \sum_k F_{i,k}(t) \quad (2-102)$$

and the velocity

$$v_i(t + \Delta t) = v_i(t) + \frac{\Delta t}{m_i} \sum_k F_{i,k}(t) \quad (2-103)$$

[Deen'07] after a time step Δt depends hence on the forces $F_{i,k}$ acting on a body of mass m_i .

There are two different models for the repulsing forces in DEM. A hard sphere model is based on the impulse of two bodies colliding with each other. The rearrangement of particles in an agglomerate is difficult to implement in this approach though. The concept of soft spheres bases on virtual overlapping of the particle shells as introduced in chapter 2.2.2. The repulsing force is a function of the overlapping distance δ of the physical particle radius.

2.7 Biotechnological Downstream Processing

2.7.1 Overview over Biotechnological Processes

Biotechnological processes are in general processes using organisms to fulfill a task. Biotechnology is separated in different areas depending on the application. This might be the production of materials like enzymes in red biotechnology (pharmaceuticals), food additives in green biotechnology (food production) or chemical substances in white biotechnology (chemical production). In grey biotechnology (environmental processes), this includes the elimination of unwanted products by bacteria, e.g. in wastewater treatment plants.

Introduction to Protein Production

Biotechnological production based on fermentation is usually divided in the three steps

- Upstream processing,
- Bioreaction (Fermentation) and
- Downstream processing.

In the upstream processing the actual production is prepared. This includes the pretreatment of materials and bacteria, removing of inhibiting substances and preparation of the reactor, its components and the feed. In the bioreaction the biotechnological step is performed, usually a fermentation. First bacteriae grow in the inoculum, then they are transferred to a reactor. Usually in the first phase bacteria grow without producing a target protein, as the sequence for

separation is under a repressor. After having grown to a specific level, determined by optical density of the broth, an inductor is introduced to inactivate the repressor and start the production of recombinant proteins by expression of clonal genes. In the downstream processing, which this work focuses on, the target product is separated out of fermentation media. The bacteriae need to be disclosed if the product is not produced extracellular. Subsequently the contamination is removed by diverse steps. This is non-trivial, as proteins are small and similar in terms of density and appearance. There are different approaches for the separation in downstream processing. They include:

- Precipitation (supporting further separation by building large agglomerates),
- Centrifugation,
- Membrane Separation and Filtration,
- Electrophoresis,
- Extraction and
- Chromatography.

Precipitation allows the aggregation of proteins. (Ultra-)Filtration, membrane separation and centrifugation separate proteins depending on properties like size and density differences. In the extraction, the protein wanders controlled to one out of multiple phases of an emulsion. Electrophoresis is used to control the wandering of proteins. In size exclusion chromatography the velocity of migration depends on the different distribution in a mobile and a stationary phase. The protein diffuses in porous beads, which is dependent on the protein size. Different proteins are hence collected at different time intervals after insertion. A column is filled with fine material like Silica, in case of high pressure liquid chromatography usually in the range of 20 μm . The flow pattern in a packed bed may not be homogeneous [Moate'09]. Despite high pressure, the volume flow is relatively low [Chmiel'11]. Adsorption chromatography uses specific binding of the proteins to a functionalization. Volume flow in these processes is however limited [Chmiel'11]. In summary there is a multitude of separation approaches available and necessary. Examples of biotechnological products are ethanol, yeast, industrial enzymes or pharmaceutical matter such as antibodies. The cost proportion depends amongst others on the target purity and the chemical similarity of the product with contaminants.

2.7.2 High Gradient Magnetic Fishing

The use of synthetic magnetic particles, which are functionalized to directly separate molecules like proteins, is known as High Gradient Magnetic Fishing (HGMF) and established in analytics. Figure 2-7 shows the principle. Synthetic particles usually consist of a magnetic core (e.g. magnetite), a coating (e.g. a polymer or Silica) and ligands (e.g. an ion

exchange group). They are stirred in a microreactor to adsorb the target product, then particles are separated by magnetic forces. Washing steps might be performed, then particles are redispersed in an elution liquid to release the protein. The process is called High Gradient Magnetic Fishing (HGMF) [Hubbuch 2001].

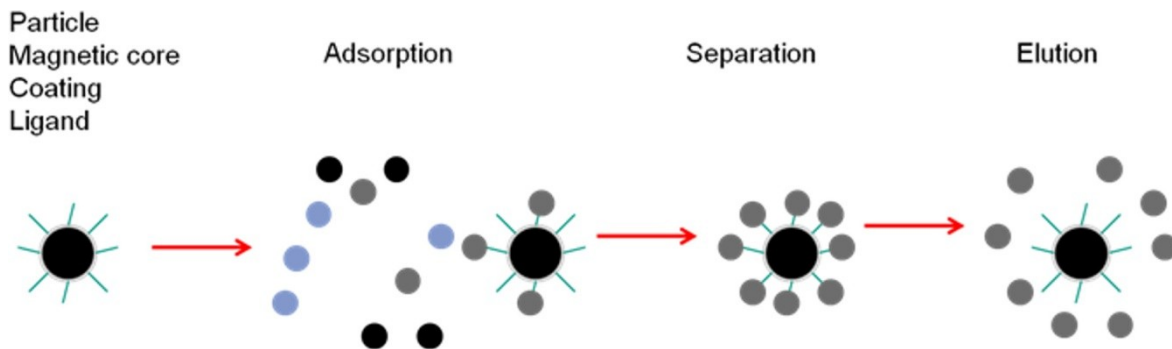


Figure 2-7: Principle of HGMF

As in HGMF particles are synthesized, the separation is usually possible easily even at a high volume flow. The functionalization influences the efficiency of the process by its selectivity. Besides it might influence the surface forces of particles. Particles adhering to tubes and walls render the process inefficient.

Particle contact forces influence the transport. On common HGMS devices, backflushing is done after removing the magnetic field from the cell. This avoids the influence of magnetic forces on the transport. As one of the main targets of the current work is the development of a device transporting particles out of the magnetic field, contact forces were addressed separately. A possibility to investigate contact forces of a single particle is Atomic Force Microscopy (AFM). Bulk contact forces in a suspension are usually investigated by rheometry.

2.7.3 Protein Analytics

Adsorption is the adhesion of molecules from gas, liquid or dissolved solid to a surface. It is quantified by adsorption isotherms. The molecular units which adsorb are called ligands. It is distinguished between physisorption, which bases on the van-der-Waals force (0.8 eV), and chemisorption (8 eV), which bases on a much stronger chemical binding. This work limits to physisorption by ion exchange, which is easier to control and to reverse but less selective. The particle regeneration and the use of the adsorbent is critical in the process. Usually an equilibrium is reached based on charged molecules (ions) in the liquid. A simple change of the pH or the ionic strength, i.e. adding or removing ions by changing the buffer, results in an exchange of the adsorbed substance. Mathematic approaches to describe the adsorption isotherm include the isotherm of Freundlich and of Langmuir [Bathen'01].

Analytical Quantification

The mass balance

$$V_l(c_0 - c) = m(q - q_0) \quad (2-104)$$

of the concentration in liquid and protein load on the particle is sufficient to determine the amount of adsorbed protein. For this purpose the amount of protein in the liquid before and after the adsorption is determined. Assuming a free surface before the test ($q_0=0$), the adsorption isotherm is determined experimentally. Several different theoretical descriptions of adsorption exist. The isotherm of Freundlich

$$q = K_F * c^n \quad (2-105)$$

is a power function with $n < 1$. K_F is the Freundlich sorption coefficient, c the free concentration in the liquid after achieving equilibrium, and q is the amount of protein adsorbed. The Langmuir adsorption isotherm

$$q = \frac{K_L q_{max} c}{1 + K_L c} \quad (2-106)$$

is popular as it is the simplest model on a physical background. It is correct under the assumption of a monomolecular layer, of similar ligands, uniform surface and neglect of interactions between ligands. The maximum capacity is q_{max} and K_L the sorption coefficient.

SDS-Page

SDS-Page is the acronym for Sodium-Dodecyl-Sulfate Poly-Acrylamid-Gel-Electrophoresis. To analyze a product sample in μl range, the sample is given on one side of a gel. The process takes place in a SDS-buffer to equalize the electronegativity of the sample. An electric field is applied to introduce an electrophoretic force proportional to the molecule size. The transport velocity depends on resistance of the gel, making large molecules moving slower. The proteins migrate through the gel by electrophoresis, with the propagation speed depending on its molecular weight and the applied electric field E . Several bands are analyzed in one single run. A marker with defined marks is usually added as additional band, allowing the size determination of the sample bands. The intensity of the band is proportional to the band's amount of protein. Relative protein amounts can be determined of each protein. In case that a defined amount of pure material was added, the absolute protein amount can be determined by image analysis as well. The electrophoretic mobility

$$\mu_e = \frac{v}{E_{el}} = \frac{3\varepsilon_r \varepsilon_0 \zeta}{2\eta} f(R, \dots) \quad (2-107)$$

is defined by the velocity of a particle v in the electric field E_{el} . It is according to the Helmholtz-Smoluchowsky equation proportional to the dielectric constant of the medium ε_r ,

the permittivity of free space ϵ_0 , the ζ -potential, a size dependent factor $f(R, \dots)$ and the viscosity η [Michov'96; Lyklema'03].

In case of spheres instead of proteins the electrophoretic mobility

$$\mu_e = \frac{e_0 * z_e}{6\pi R \eta} \quad (2-108)$$

results from equalizing Stokes resistance and the electric force on a charged particle in an electric field [Schroeder'09].

Optical Measurement

Optical measurement is based on the fact that the aromatic rings in amino acids like proteins absorb light. The absorbance peak is at 280 nm. Determination of a calibration curve allows the exact measurement if the substance is available in pure form. The structure affects the absorbance, so the buffer factors such as pH and ionic strength need to be kept constant to the calibration curve. Another possibility is the optical measurement of the BCA equivalent, which delivers a gram equivalent amount of protein. In this case BCA is added, which binds to proteins and results in a specific color. The method delivers as well values for protein mixtures. A deduction on the purity can of course not be drawn by optical measurement.

The absorption is given by the Lambert-Beer law, characterizing the absorption

$$A_{Abs} = \lg \frac{I_{in}}{I_{out}} = \epsilon_{ex} * c * d_s \quad (2-109)$$

as the logarithmic reduction of the incoming light I_{in} to the outgoing light I_{out} , which depends on the material- and wavelength-dependent specific extinction coefficient ϵ , the concentration c in [g/mol] and the sample thickness d_s .

3 Particle Systems

The particle system is the key to an efficient process. For separation the most important influence is the magnetization of the particles, which is usually low in many substances.

3.1 State of the Art of Particle Systems

Magnetic beads are available on the market for analytic purposes (e.g. Merck, GE), and rarely for different applications like waste water treatment (e.g. Orica MIEX). Particle prices vary strongly depending on the properties and the application area from 10s to 100.000s €. Important properties are:

- Size
- Magnetization
- Remanence
- Specific surface / Activity
- Functionalization (Selectivity, Reversibility)
- Price
- Chemical and mechanical stability

The size of the primary magnetic core influences remanence. Below about 10-20 nm, only one Weiss domain exists, resulting in superparamagnetism and hence low remanence [Svoboda'04]. This is necessary to redisperse particles and avoid building of large agglomerates which reduce potentially adsorption properties. At particle sizes below 10 nm Brownian forces dominate [Rosensweig'97], resulting in a colloidal suspension called magnetic fluid. Magnetic particles still move influenced by the external forces but drag liquid with them, it is no more possible to influence only the disperse phase. Magnetic particles do not agglomerate and do not form a stable deposit, rendering the separation by HGMS impossible. Additionally toxicity and carcinogenic properties are unknown, as nanoparticles pass the cell wall and might influence the DNA building.

A possibility to combine the advantages of small primary cores with large particles is composite particles, i.e. many magnetic cores are packed by coating into one particle. The filling degree is reduced though. The theoretic densest packing of spheres is 74%, with composite particles having a filling degree usually much lower. This results in a lower magnetization. Eichholz reports additional demagnetization effects for a low volume proportion [Eichholz'10]. Magnetization is, together with surface, the most important particle parameter for separation. A possibility of using single magnetic cores is either at the limit of about 25 nm, or using large particles and stabilizing them chemically. Examples for particles based on a single magnetic core with a thin coating are Merck MagPrep (80 Am²/kg), for

many cores combined in one coating are Chemagen (43 Am²/kg) or Evonik MagSilica (up to 69 Am²/kg). Magnetization depends on the proportion of magnetite in the core, which is much higher in a single core covered with a thin layer of coating. The surface is crucial for the amount of functionalization which can be packed on one particle and hence its activity in the process. The specific surface of a sphere is inverse proportional with its diameter, leading to either small particle size or large but porous particles. Porous particles of a size up to 100 μm (e.g. Orica) still achieve high activity and can be separated by simple sedimentation instead of magnetic separation.

The production of magnetic particles is done in several steps. First the magnetic core is produced and coated, then it is functionalized with ligands. Magnetic primary particles are produced mostly from magnetite (Fe₃O₄) or similar compounds like maghemite (Fe₂O₃). A common procedure for the synthesis of the magnetic core is precipitation of nano-scale magnetite. Different processes comprise emulsion polymerization [Hickstein'08], flame pyrolysis [Martelli'00; Morjan'03], emulsion synthesis [Rondeau'10] and spray drying [Rudolph'11]. In a second step the core is coated with polymer (e.g. Polyvinylacetate [Eichholz'10] or Silica (e.g. in Merck MagPrep particles). Then an initiator is immobilized and subsequently the actual ligand is bound by polymerization. Most common are ion exchange ligands, as those are cheaply available and can be used in a broad range of applications. Besides there are chemical ligands which are highly selective yet expensive and need to be adapted to the specific system. Binding needs to be reversible so the product can be eluded and the particle reused. In case of ion exchange particles elution is usually done by shifting the pH or increasing ionic strength and replacing the protein at the surface. In case of chemical binding, different media are added in abundance to displace the protein. This is a critical step, as sometimes toxic substances are necessary [Parekh'11] or as particle recycling is not possible for displacing of the elution substance is difficult. Surface areas of 0.1-7 m²/g particle are common on 3 μm sized particles. While market prices of 80.000 €/kg are not unusual, in production prices below 50 €/kg were reported.

Selective chemical bindings include Protein A, which is a specific antibody for antigens. Specific ligands for BBI were investigated, yet are in price out of range for large-scale applications. In this investigation chemical binding was not tested but focus was put on large-scale applications. A review on protein adsorption is in [Nakanishi'01].

Magnetic suspensions show the characteristic formation of needles. Satoh made simulations of the agglomeration of particles based on dipole forces [Satoh'98]. Vuppu showed that these needles align in the magnetic field and can be rotated together with the magnetic field [Vuppu'03]. Furst showed that the needles rearrange under tension before breaking [Furst'00].

The surface forces of magnetic particles are not different from other particles and are well investigated. Particle contact forces comprise the van-der-Waals force, the electrostatic or Coulomb force and mechanic repulsion which is modeled by Hertz in case of macroscopic bodies and Born in case of overlapping of the electron shell of atoms or molecules in microscopic scale [Stolarski'07]. In contrary to other processes, magnetic forces come into play which completely change the behavior of the magnetic particles. A force comparison with an experimental study was performed before [Chin'01; Stolarski'07]. A study on composite particles was performed by Eichholz [Eichholz'10].

3.2 Target

The target of the investigation of particle properties is the determination of factors influencing the particle deposition and transport in the magnetic field. For this purpose interparticular forces are measured. The measurements are separated in two different aspects, which are the forces between single particles, and the forces in the bulk phase.

1. Non-magnetic surface forces and magnetic forces influence the properties of single particles. The understanding and data on particle contact is necessary for the simulation of magnetic particles in the process in a Discrete Element Method.
2. Bulk forces in magnetic suspensions influence the particle transport, which is one of the main targets of the current work. It is necessary to understand the influences of the magnetic field on particle behavior to develop a machine which transports particles out of the magnetic field. The bulk phase has different properties compared to single particles, as the contact is not perfect and the particle distribution inhomogeneous. This reduces the resistance of particles compared to the theoretic maximum estimation derived from single particle measurements.

The description by formula of the two aspects is as well completely different. While forces for single particles are approximated by dipole equations, the bulk phase is characterized by rheological equations. Interparticular forces change the viscosity of the suspension. The influence is highly isotropic, as the magnetic field direction behaves significantly different to the two dimensions perpendicular.

3.3 Materials

Different particle kinds were used in this work and processed in the centrifuge. They were provided by industrial partners in the project MagPro²LIFE and from outside of the project. A constant limitation to tests of the device was the availability of sufficient amounts of particles, limiting the choice to only a few systems. Table 3-1 gives an overview over important parameters of particle systems used in this study. The particle size was determined by laser

diffraction. Note that the magnetization in this case is normed on the volume instead of its mass:

$$M_V = M/\rho = \frac{\mu}{m}. \quad (3-1)$$

Table 3-1: Overview over particles for performance tests of MEC

	Density ρ [g/cm ³]	BET [m ² /g]	Saturation magnetization M_V [Am ² /kg]	x_{50} [μ m]
017-3/4/5	-	45	47.4	0.8
019/04	-	45	42.1	1.3
018/04	4.32	31	58.6	1.4
Amino	3.46	32	39.44 (Remanence 9.7)	10 (after ultrasonic treatment)

For the separation processes, another set of magnetic particles were used. The data is summarized in Table 3-2. They provide better characteristics but were available in smaller amounts and hence their use was limited to the actual separation processes. These particles were well investigated within the consortium.

Table 3-2: Overview over commercial particles used in the application [Source: MagPro²LIFE Consortium]

	Merck MagPrep TMAP (tri-methyl- ammonium-propyl)	Merck MagPrep SO ₃	Orica MIEX DOC (Methacrylate- DVB)	Orica MIEX HC (not used)
AEX(Anion Exchange)	AEX	CEX	AEX	AEX
CEX(Cation Exchange)				
Density [g/cm ³]	3.25 (theoretic)		1.53	
X 50,3 [μ m]	1.9	3.8	200 (38 after ultrasonic t.)	
Core size [nm]	100			
Particle charge density by titration [ueg/g]	282	950.3	237.4	99.3
Zeta-Potential [mV]	35 mV (pH 7.7)	-43 mV (pH 7.7)	30.8 (pH 5,9)	32.1 (pH 5,9)
BET [m ² /g]	7.21	5.17	3.10	0.87
Magnetization (dry) [emu/g]	66.6	64.3	19	18
Total iron content	52.1	36.9	12.6	7.9

[w%]				
Total magnetite content by AAS [w%]	72.0	51.0	17.4	11.0
Total other content calculated [w%]	28.0	49.0	82.6	89.0
Binding capacity [mg/g]	1150 (BSA)	790 (Lysocyme)	50 (BSA, Lysocyme)	85 (BSA, Lysocyme)

The particle size distribution is usually large over two orders of magnitude, ranging from 300 nm to 30 μm . Particles form agglomerates, which is difficult to measure, as it depends on several parameters such as the medium, the particle age and history and the pretreatment. Two different examples of size distribution measurements of the same sample of Merck MagPrep 100 particles is shown in Figure 3-1 (left). The change of the agglomerate size is significant. Figure 3-1 (right) shows a scanning electron microscopy image the same particle kind. The primary particle size is 100 nm, which is in line with producer specification. Particles form large agglomerates though, which explains the change of size distribution. A consequence is a high variation in the process by the rearrangement of agglomerates. This effect is even stronger in desalinated water, as the pH is in this case not controlled. As a consequence, the curves determined in the performance tests in chapter 5 were mostly done out of one single feed batch and in short time intervals.

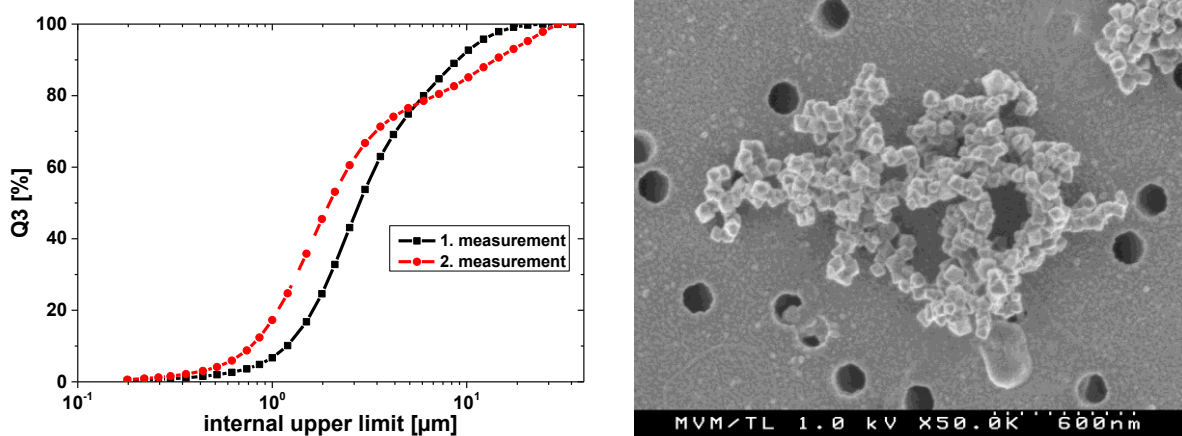


Figure 3-1 left: the particle size distribution of the same Merck Magprep particle sample measured by laser diffraction, the particle size is highly instable with particles rearranging, which is induced by magnetic remanence; right: Scanning electron microscopy of Merck MagPrep 100 particles shows small particles in a size range of 100 nm, but with tendency to build large agglomerates

The magnetization of the different particle kinds was measured by KIT IFG on a MicroMag 2900. The result for different particles is shown in Figure 3-2. Note that a demagnetization factor of $N(5/1)=0.06$ applies in these measurements. Figure 3-2 left shows that, at 100 kA/m (0.13 T), the magnetization of the particles is almost at saturation. Above this field strength,

the magnetization can hence be approximated by the saturation magnetization. κ in contrary is even at saturation magnetization not a constant value, hence the formula description and the implementation in the simulation is easier based on the magnetization. By defining $\kappa = M/\sqrt[4]{H}$, the value seems to be closer to a constant.

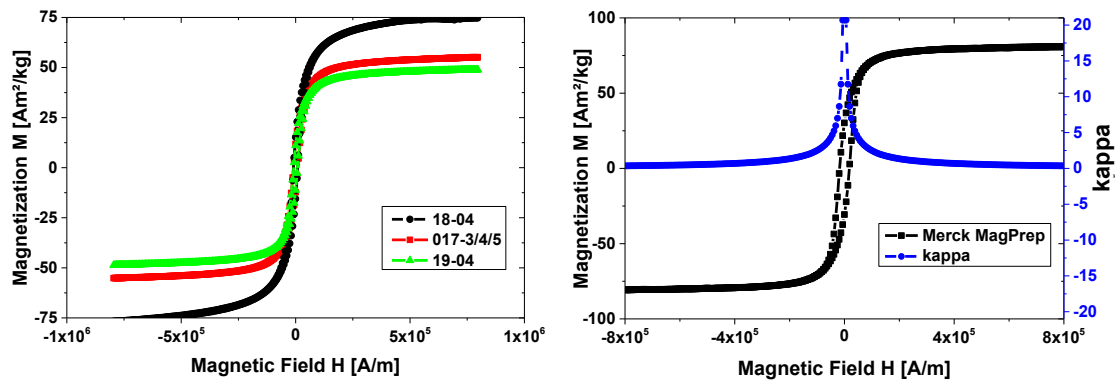


Figure 3-2 left: Merck MagPrep 100 show some remanence; κ is not constant but approximated well by $\kappa = 58532 \cdot H^{-0.88}$; right: Evonik particles show a different saturation magnetization which is different for different batches;

Magnetic particles were not hazardous in the project. Neither the magnetite core nor shell and ligand consisted in this material of toxic substances. To avoid risks of nanomaterials, the particle choice was limited to 100 nm size and larger.

3.4 Analytic Investigation

An analytic calculation of the DLVO potential and magnetic forces reveals that the magnetic forces dominate in this case over DLVO forces. The calculation is as well interesting for comparison with AFM tests. The parameters of particles and medium as well as physical constants used in the graphs are summarized in Table 3-3.

Table 3-3: Parameters used in the DLVO comparison

Parameter	Symbol	value	Unit
Particle diameter	d	1	[μm]
Magnetization	M	80	[Am^2/kg]
Particle density	ρ_P	5.2	[g/cm^3]
Temperature	T	293	[K]
Electrolytic concentration	c_{ion}	3.0	[mM]
Electrolytic valency	z_{ion}	1	[-]
Zeta-Potential	ζ	-5.0	[mV]
Permittivity (Water)	ϵ_r	1.77	-
Hamaker	A_H	1e-20	[J]

Avogadro number	N_A	6.022e23	1/mol
Boltzmann constant	k	1.38e-23	J/K
Electron charge	e_0	1.602e-19	C
Magnetic permeability	μ_0	$4\pi e-7$	Vs/Am
Electric field constant	ϵ_0	8.854e-12	As/Vm

Figure 3-3 shows a comparison of the energy of particles including (left) and excluding magnetism (right). Magnetic forces decline less over distance and hence dominate over a significant distance from the particle surface for a distance 10^{-4} – 1 diameters of the particle. The van-der-Waals force leads only to a very small minimum at around 10^{-4} diameters from the particle. Magnetic forces lead to a very expressed energy minimum, which is not only stronger but especially extends over a distance in the range of a particle diameter. Magnetic forces dominate hence in the process.

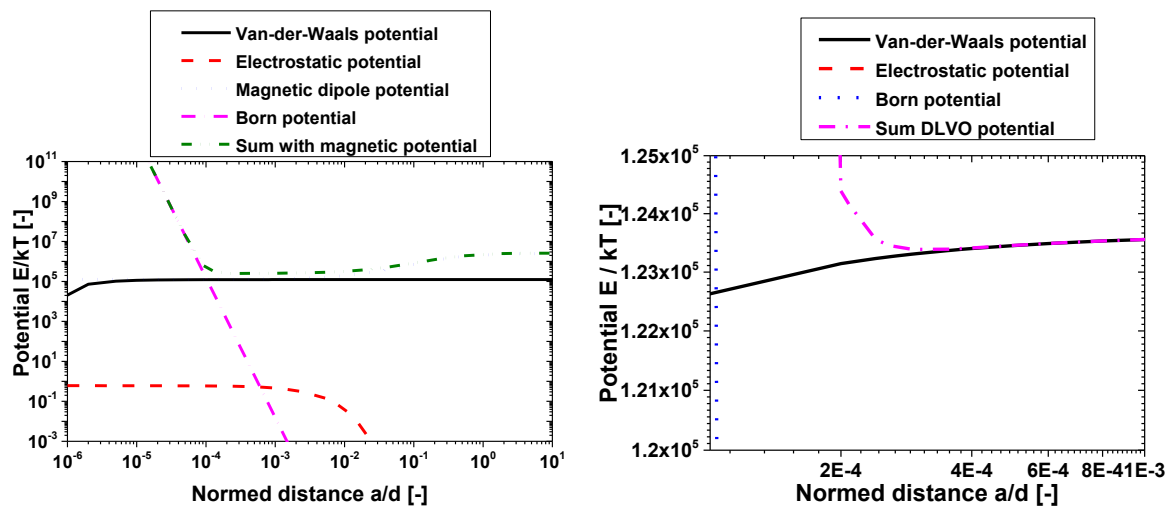


Figure 3-3 left: the DLVO potential over the surface distance (with a positive value added to show negative values of van-der-Waals and magnetic dipole forces) shows a minimum in the potential and hence a stable point where agglomeration occurs; right: the classic DLVO without magnetic forces shows only a very small minimum at a small normal distance in comparison

Forces are shown in Figure 3-4. Interesting is a force of zero showing the equilibrium in which agglomeration appears. Negative values are attractive, positive values are repulsive forces. The magnetic force dominates between 10^{-3} and 1 particle diameter. In this comparison the van-der-Waals force leads only to weak attraction in force at a distance of 10^{-3} m.

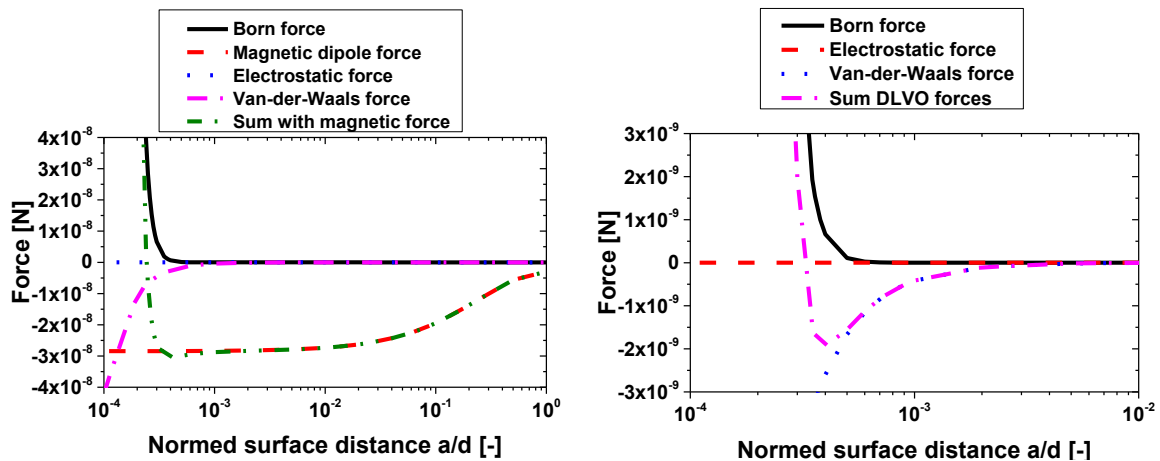


Figure 3-4 left: the force resulting from the DLVO potential shows the agglomeration at zero crossing of the force at 0.24 nm surface distance, the sum of the force results essentially from the Born and dipole force, while the electrostatic and van-der-Waals force may be neglected at the given parameter set; right: the minimum without magnetic force is far less expressed

3.5 Single Particle Contact Force Measurement by Atomic Force Microscopy

The analytic model above is based on general equations and is not specifically adapted to the properties of magnetic particles. To validate the model, Atomic Force Microscopy (AFM) was used to measure the contact force of magnetic particles and to validate the model implemented in the simulation. The AFM measurement was limited to non-magnetic contact surface forces though.

3.5.1 State of the Art

AFM is usually used to measure surface profiles. Atomic force microscopy is based on a cantilever with monoatomic tip, which is moved over a surface. The deflection of the cantilever is measured by a laser, providing after calibration an exact profile of the surface. This is possible in a contact method, touching the surface constantly or in an intermittent mode. In this case the cantilever oscillates, and touches the surface only at the lower end of the oscillation. This usually yields a more exact result. The device needs to be calibrated before measurement.

The methodology to investigate contact forces by AFM is well established and described in literature [Burnham'89; Butt'05; Lyubchenko'11]. Force measurement is possible by fixing a sample on a cantilever tip. Then the cantilever is pressed on a surface and retracted again. During retraction, adhesion force bends the cantilever, which is measured by the laser. The contact force between the sample and the cantilever is proportional to the maximum deflection of the cantilever during removing. The measurement of the contact force F is possible by measuring the deflection x when removing a cantilever from a surface by

(2-57)(2-55). To measure the force between a particle and a support, the particle is glued on a cantilever. The stiffness D_S of the cantilever can be calculated out of its resonance frequency f and mass m in (2-58).

In theory the measurement of weak local magnetic fields is possible as well by measuring the force exerted on a magnetic probe in non-contact mode [Hartmann'99]. The approach was not tested though, as the main interest is the magnetism of particles in the magnetic field, which was not accessible by this measurement method. Superparamagnetic particles in theory do not have remanence, while a deep investigation of the field of remanent particles would go beyond the scope of this investigation.

3.5.2 Methods and Materials

The Cantilever used for contact measurement are SICONA-TL-Cantilever without tip, the cantilevers for 3D imaging are as well from SICONA. The particles glued on the Cantilevers are polystyrene particles (PS-MAG-particles) of the producer microParticles GmbH, which consist of an iron oxide core and a polymer matrix. The product used in centrifuge tests was too undefined and too small to be used for contact force measurement.

AFM was used to measure adhesion forces, more specifically to measure non-magnetic forces of particles on different surfaces and on particles. The AFM used for this purpose is a Q-Scope 250 Nomad of Ambios Technology Corporation. As the mass of the cantilever was unknown, but only the mass of the particle m which is glued, the stiffness D_S was calculated out of its resonance frequency before (f_0) and after (f) gluing the particle by

$$D_S = 4m \frac{(f_0 f \pi)^2}{f_0^2 - f^2} \quad (3-2)$$

from (2-58). The values for the stiffness D_S provided by the producer are not exact enough for force measurement.

Before the measurement a preparation was performed. First, the resonance frequency of the naked cantilever was measured in the AFM. Second, particles of 10, 20 and 40 μm size were glued on cantilever tips. Different adhesives were tested, nail polish showed to deliver better results than a classic adhesive for being better to handle during hardening. The gluing was achieved by using a micromanipulator and a microscope Leica M3C. The cantilever was fixed in the micromanipulator, was then dipped in glue and subsequently moved to a particle. Additionally particles were glued on a support. Figure 3-5 shows images, taken by a microscope, of a single particle glued on a cantilever tip (left) and particles glued on a support (right). Third, the new resonance frequency was determined in the AFM to calculate

the cantilever stiffness. Additionally for testing contact force in between particles, particles were glued on a support.

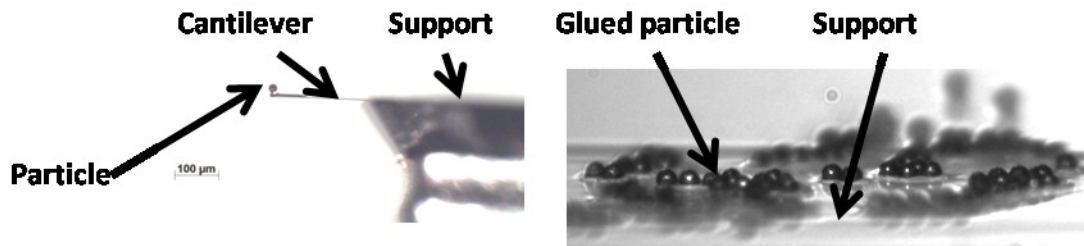


Figure 3-5 left: a particle was successfully glued on an AFM cantilever; right: particles glued on a support

After fixing particles, the force could be measured by touching a surface and removing the cantilever again. Figure 3-6 left shows schematically the force over the distance at different steps during measurement. Figure 3-6 right shows the deflection reported from the AFM over the distance. The principle of measuring the contact force of a cantilever is the measurement of the cantilever deflection during retraction. For this purpose the cantilever is moved to the surface (0->1) and pressed on it (1->2). Then the cantilever is removed (2->3). When removing, contact forces, especially van-der-Waals forces, retain the particle and deflect the cantilever (3->4). The deflection increases until the particle is separated from the surface (4->5). The maximum deflection x of the cantilever (distance 4->5) from its original position correlates with the contact force F by the spring equation (2-57) [Lyubchenko'11]. The contact force measurement was repeated ten times for each data point. This is not enough for a statistically safe analysis, but was limited due to the manual execution.

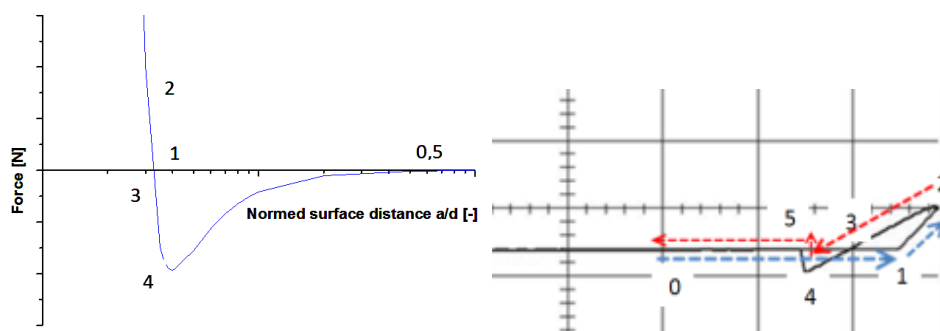


Figure 3-6 left: the schematic contact force over the distance; right: the cantilever deflection over the distance; the test starts at a distance (0), the cantilever approaches (1), then it is pressed against the support resulting in repulsive forces (2); when retracting the particle, adhesive and repulsive forces compensate (3), then adhesive forces appear (4), which reduce suddenly at a specific distance (5); the maximum contact force is calculated from the maximum deflection of the cantilever (4) -> (5)

3.5.3 Results

The contact force of a single particle on another particle and of different surfaces was measured. The force of the three different particle sizes on similar sized particles is shown in

Figure 3-7 (left). Reasons for the high variation might be the variation of humidity, which should be below 40%, the low number of data points and angular particle contact or contact with two particles at the same time, which is difficult to control. It is uncertain whether there are traces of the adhesive influencing the result. The contact force increases significantly for larger particle sizes. Forces on glass, metal and Teflon are shown as well. The adhesion of particles of different sizes shows to be significantly reduced to Teflon compared to glass and metal. The particle size influence is still expressed. Figure 3-7 right shows as well a comparison to a van-der-Waals force calculation at a surface distance of 0.25 nm of differently sized particles. The wall force is in the same order of magnitude, and low particle sizes compare acceptably, but there is a significant discrepancy of the contact force at several particle sizes. The order of magnitude is similar though.

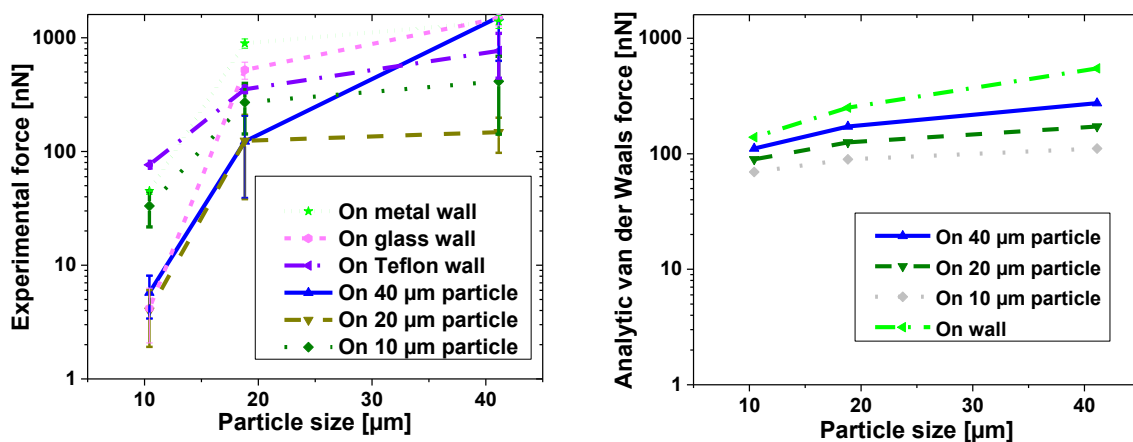


Figure 3-7 left: experimentally determined force of a 10, 20 and 40 μm particle on a 10, 20 and 40 μm particle, a Teflon, glass and metal wall; right: analytical calculation of a the respective particle sizes on particles and on a wall

Comparison with the Calculated Magnetic Force

Magnetic properties of particles may well be calculated analytically from the particle magnetization. Figure 3-8 shows that magnetic forces of the interparticle contact are - at these particle sizes - in a larger order of magnitude. The consequence is that for the investigated particles ranging in size down to 10 μm , magnetic forces dominate over non-magnetic contact forces. The simulation of particles ranging from 1 – 100 μm may hence neglect non-magnetic forces. From measurement a value of about 0.25 nm was deduced for the surface distance. Magnetic forces dominate over adhesion forces. Forces are influenced by particle properties though, limiting the universal validity when using different particles. The experiments were done dry, while the final application is in suspension.

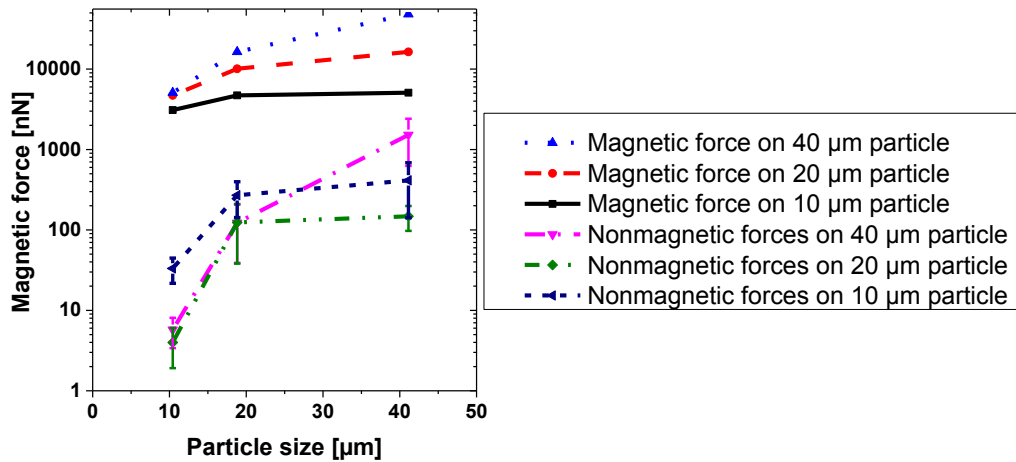


Figure 3-8: Comparison of maximum magnetic force and nonmagnetic contact force

3.6 Bulk Force Measurement by a Magnetic Rheometer

3.6.1 State of the Art

CFD studies on magnetorheological fluids were performed and compared with experiments [Gedik'12; Omidbeygi'12; Omidbeygi'13]. Needle agglomerates were as well simulated directly [Kittipoomwong'05]. Practical studies have been performed before as well for a single particle chain [Furst'00] and for magnetic suspensions [Shulman'86]. A technical use of magnetorheological suspensions is in dampers [Bica'02] or brakes [Bica'04]. A review showing the different regimes of magnetorheological suspensions depending on the shear strain suggested a Bingham-fluid-like behavior for magnetic suspensions [de Vicente'11].

Rheometers of different types are widely used for the investigation of viscosity. Usually they consist of two plates with the sample in between. One plate is fixed, the second moves either horizontally or circular to shear the fluid. Circular rheometers allow applying continuous shear and are therefore important. Different geometries exist, with parallel and conic plates as the most important types. A conic shearing device provides several advantages over parallel plates. In case of parallel plates, the suspension at a high radius influences the torque stronger, which is avoided in a conic plate. Additionally conic plates avoid the moving of particles to the center, which was one challenge in the current measurement. The magnet setup did not allow a conic plate for space restrictions though.

3.6.2 Methods and Materials

The specific target of the current investigation is the flow limit of the particle systems used in the continuous centrifuge. The properties at high concentration and high magnetic field strength are interesting, as these are the conditions which appear in the slurry transported in a decanter. Concentration and magnetic field strength showed in (2-38) the most important

influence. The magnetic rheometer used for tests belongs to the Institute of Functional Interfaces at the KIT Campus Nord. The producer is Anton Paar, the model is MCR 301. The additional magneto-rheological device (MRD 180) was used. It features a water-cooled electromagnet which provides a homogeneous magnetic field up to 1 T at 5 A in the rheometer cell. The volume in the magnetic field is small, so the choice of plates is limited to a plate of 20 mm diameter and a distance plate-to-plate of 1 mm. The particle kind Evonik VT5018 was used for the concentration and flux density study. The particle kind Evonik 18/04 was used for the further tests. A concentration of up to 25 m-% was applied, which is higher than in the feed of the experiments, but is the concentration in the decanter slurry being transported. The suspension was mixed from dry particles and tap water.

To compare equations with an analytical approach, (2-38) is changed. From (2-31) follows an equation for the retaining magnetic force between two spheres in tangential direction. The direction of the magnetic moment is field direction $\boldsymbol{\mu}_{i,j} = (M * V, 0, 0)$ and the direction $\boldsymbol{r} = r * (\cos\theta, \sin\theta, 0)$. The angle giving the strongest force in tangential direction is solved as $\theta = \arctan \sqrt{1/2} = 35.3^\circ$. A correction parameter $C_{needle} < 1$ is introduced which needs to be determined experimentally and which takes into account imperfect building of needle agglomerates, which reduces agglomeration heavily. The particle concentration c_n is in [g/g], the particle radius R , and the center particle distance is $r = 2R$. The minimum particle concentration to create needles and influence the system is c_0 . This results in

$$\begin{aligned} \tau_0 = \frac{F}{A} &= C_{needle} \frac{(c_n - c_0)}{\pi R^2} \frac{3\mu_0}{4\pi r^5} \mu^2 r (-5 * \cos^2\theta * \sin\theta) \\ &= C_{needle} \frac{1}{12} \mu_0 M^2 (c_n - c_0) \left(-5 * \frac{2}{3} * \sqrt{\frac{1}{3}} \right) \\ &= -0.16 \mu_0 M^2 (c_n - c_0) C_{needle} \\ &\quad \text{for } c_n > c_0, \text{ else } 0. \end{aligned} \quad (3-3)$$

3.6.3 Results and Discussion

Figure 3-9 left shows the necessary shear stress to deform a suspension of 12.5 m-% at different flux densities. Applying a defined torque in the measurement resulted in a steady curve without jumps in contrary to applying a constant shear rate. A flow limit of 20 Pa is visible, while viscosity is unchanged and almost linear at high shear rates. The interesting part of the particle behavior is hence at low shear rates. Figure 3-9 right shows the crop of the shear stress at low rates. Obviously a certain yield stress is necessary to break the suspension structure. The highest difference is visible at low magnetic field strengths, while the change

from 0.06 T to 1 T is low from 18 to 20 Pa. The reason is that the magnetization of particles is limited to by saturation, so only a slight gain is then achieved.

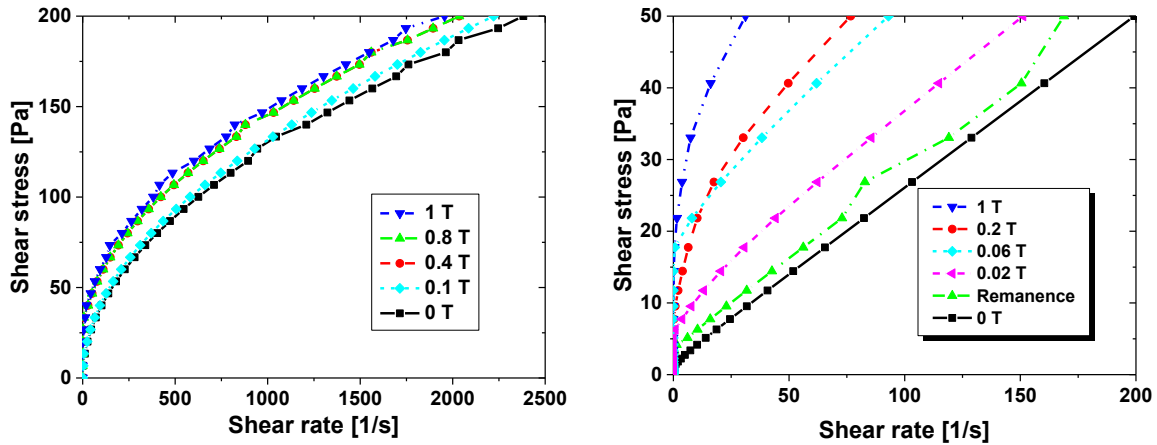


Figure 3-9 left: at a concentration of 12.5% a defined shear stress results in a specific shear rate for magnetic particles which is dependent on the magnetic flux density and showed to increase from 0 T to 1 T; right: a crop of the left diagram to the region 0 – 200 1/s shows an increase in the yield stress from 0 Pa to 20 Pa

Most interestingly, the concentration shows a high influence at a high field strength of 1 T. Notably, at 25 m-% yield stress rises to 120 Pa, and 60 Pa at 12.5 m-%. Notably at a low concentration of 6 m-% and below, there is no flow limit apparent. The reason is probably that there are not enough particles to close needles from the bottom to the top plate. Figure 3-10 left shows the maximum yield stress of 120 Pa.

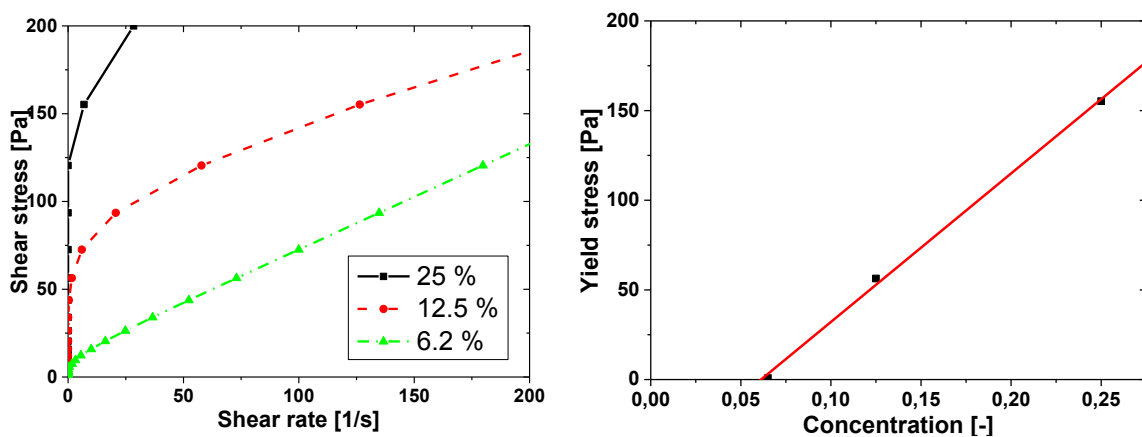


Figure 3-10 left: the concentration influences the yield stress strongly at a flux density of 1 T, rising from 0 Pa to 120 Pa from 6.2 to 25 m-%; right: the yield stress necessary to achieve a shear rate of 1 1/s shows to increase (fit: $-50.7+828 \cdot x$)

This is compared with the analytic equations to deduce on the correction factor C_{needle} . In the experiments C_{needle} is 0.125 at and above 10 V-% particles, while below a flow limit was not detected. Figure 3-10 right shows the yield stress necessary to create a shear rate of 1 1/s for

the three concentrations measured, deduced from Figure 3-10 left. The minimum concentration c_0 is 6 m-%.

Figure 3-11 top left shows a shear stress of about 55 Pa at a flux density of 0.5 T at defined shear rates at a concentration of 12.5 m-%. Figure 3-11 top right shows a creep test. The shear stress over time changes by 20 % over 30 s before reaching a steady state at a shear rate of 1 1/s. Repeating of the experiment showed an oscillation of the shear stress over time. In comparison to a suspension without applying a magnetic field, the shear stress is increased by two orders of magnitude.

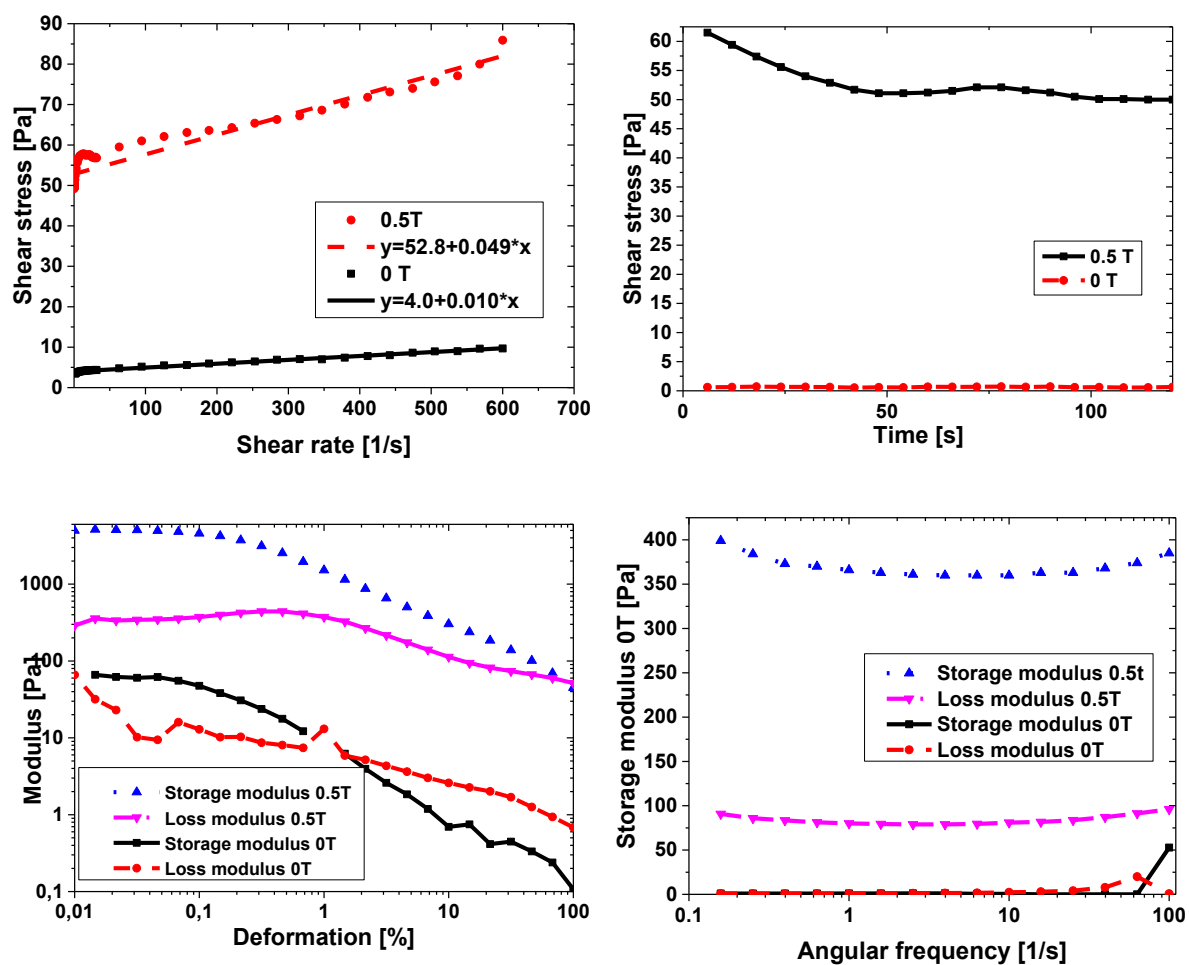


Figure 3-11 top left: the yield stress is 53 Pa, while the viscosity is barely changed at 49 mPa s; there are several orders of magnitude in between viscosity at different magnetic field strength; top right: a creep test on a magnetic suspension shows a decrease of 20 % after 30 s; bottom: the difference between 0 T and 0.5 T results in two orders of magnitude difference; the deformation influence shows no flow limit as the loss modulus tends to 0, at 0.5 T particles are cross-linked with any motion leading to breakage of the structure

The measurement of storage modulus and loss modulus as function of the deformation and the angular frequency in Figure 3-11 bottom left and right shows ductile behavior and a flow

limit of 4 Pa at 0.5 T vs. 0.8 Pa without external magnetic field. The flow limit of the linear visco-elastic region and destruction of cross-linking appears already at 1 % deformation.

Discussion

The shear stress necessary for the motion in a magnetic field in a highly concentrated suspension depends linearly on the concentration and reaches up to 120 Pa at 25 m-%. The magnetization influence is high at low field strengths, but does not increase much when increasing the magnetic field beyond 0.06 T. The shear stress is as well slightly dependent on the time, which is shown by a creep test. The particle viscosity perpendicular to the field direction is highly dependent on the concentration, the magnetic field and the magnetization of the specific particle kind. The viscosity parallel to the field direction is not affected, as in theory repulsive forces in between needles avoid an increase of viscosity.

A consequence is that the setup of a decanter with the field aligned in axial decanter direction is possible, while particle transport perpendicular to the field through valves similar to a disc centrifuge cannot be predicted, as particles form chains and might block valves. These options were hence not further evaluated, but solutions avoiding the need to overcome the yield stress and break particle chains were preferred.

3.7 Influence of Turbulence on Magnetic Separation

While magnetic forces enhance the settling of magnetic particles, turbulence redisperses particles. A magnetic centrifuge hence needs to be optimized to avoid turbulence in settling regions of particles, i.e. in the wire filter and on the centrifuge wall. In a simple experiment leading a hose through an electromagnet at different flow velocities, the settling of particles was determined by measuring the outlet concentration. The tube diameter was 4 mm, the volume flow 5-35 l/h pumped by a peristaltic pump, the maximum field strength of the electromagnet 0.4 T and the concentration 2 g/l. Specifically for Reynolds numbers approaching turbulent regime ($Re = 2300$), the separation completely stopped. The development of magnetic separation devices is hence limited to devices with a laminar flow. This is as well particularly important for MEC, as the Coriolis force creates a differential velocity of fluid and wall and hence shear force. Shear force might be strong enough to actually reduce the separation instead of enhancing it. A consequence is that the preacceleration in a MEC is crucial for the separation of magnetic particles.

It is not possible to enhance turbulent devices like e.g. a hydrocyclone with magnetic forces. Tests on enhancing the separation of a hydrocyclone by permanent magnets of 40 mm edge length revealed similar limits when using magnetite in water. Separation was not enhanced in

a hydrocyclone by magnets added, although a small deposit on the hydrocyclone wall was noticed.

The control of magnetic particles and retaining them in a specific flow layer at the boundary by magnetic forces is not possible; analytic equations suggest rather that magnetic forces increase exponentially from the magnet surface. This results in separation of particles in two fractions: one fraction is too far from the magnet for being influenced significantly by magnetic forces, while the other is close enough to sediment through the boundary layer to the wall.

3.8 Conclusion

From the force comparison of magnetic and non-magnetic surface forces, the first seem to dominate while the latter may be neglected in a simulation. The influence of viscosity on the particle transport is significant. The measurement of the viscosity of the bulk phase delivers data on the yield stress necessary to move a magnetic suspension. The most important influence is down to the magnetization and to the concentration. The resistance of the specific particle system used in the decanter tests showed a flow limit of up to 120 Pa at 25 m-% and 1 T perpendicular to the field direction. Different particle systems, which got a higher magnetization, might cause an even higher resistance yield stress. The particle transport perpendicular to the needle direction is hence difficult to predict.

4 Simulation of Magnetically Induced Particle Agglomeration and Sedimentation

Simulation of HGMS is rather different from the simulation of non-magnetic separation processes due to the characteristic magnetic dipole forces. As mentioned before magnetic suspensions have a highly isotropic behavior. This influences their properties in the process and the possibilities to move them in the magnetic field. This chapter treats the simulation of HMGS and specifically MEC by one-way-coupling of FEM and DEM. The magnetic field of spherical particles can be approximated by dipole equations. It is hence possible to calculate the magnetic forces between particles. Mechanic forces are similar to a conventional DEM simulation. CFD was coupled into the simulation in a first test, but was dropped later. The CFD coupling showed to reduce the kinetics strongly, which became computationally very expensive at the time steps necessary for stable agglomeration simulation. The different simulation software used is summarized in Table 4-1.

Table 4-1: Overview over simulation software

Simulation principle	Physical phenomenon	Producer, Software	Version
Computational fluid dynamics by the Finite Volumes Method	Fluid flow, Navier Stokes	Ansys Fluent	13.0
Finite Element Method	magnetic field, Maxwell equations	Comsol Multiphysics	3.4, 4.2a
Discrete Element Method	Particle motion, Newton / Hertz forces	DEM Solutions, EDEM	2.3

4.1 State of the Art

Needle-shaped agglomeration was reported in literature [Furst'00; Vuppu'03]. Satoh simulated the agglomeration of magnetic particles in a Monte-Carlo study [Satoh'98]. Climent simulated dynamics including Brownian and hydrodynamic interaction [Climent'04]. Magnetic suspensions in between two walls were performed as well [Pappas'05]. Chen simulated particle deposition and agglomeration on magnetic wires by different approaches. One approach included DEM simulation based on interparticular force and wire magnetic force in 2D [Chen'09]. Eichholz investigated HGMS by DEM, yet limited his approach to magnetic filtration [Eichholz'08; Eichholz'12]. Both approaches were limited to a small number of particles.

4.2 Target of Modeling and Simulation

Target of the investigation was the extension of the existing simulation approaches to 3D and to a larger number of particles, to combine the different effects and validate the approach. Additionally the coupling of different simulation approaches was targeted to achieve a comprehensive model, which included a larger number of influences. Then the model was reduced to the effects actually influencing to save computational power. An experimental validation was necessary, as neither Chen nor Eichholz seemed to compare the needle structures to experimental deposition. The simulation approach should be applied to MEC, but as well be universal and reusable for other systems. This was targeted by implementing it in a commercial code which provides interfaces for the import of CAD geometries and for the implementation of different software. In general the use of an existing framework with implemented code allows easier rework than reprogramming custom code. Finally the target was to estimate and evaluate the exactness of the simulation. Major targets are hence summarized below.

1. The interaction between agglomeration and deposition is of major interest.
2. The influence of magnetic forces on the porosity in the process is important, as it limits the capacity of batch-wise centrifuges and influences the transport of particle sediment in a decanter centrifuge.
3. A comparison and validation of the simulation with pictures from real deposit allows estimating the exactness of the model.
4. A theoretic investigation of the errors resulting from the assumptions is necessary. This includes especially the approximation of spherical particles by magnetic dipoles, of the aligning of the particles in the external field direction and of the influence of weak magnetic fields.

4.3 Simulation Methods in Combining the Discrete Element Method with Magnetic Forces

Two different simulation approaches were used additionally to DEM: FEM and CFD were combined to simulate the influence of the wire filter design. FEM data was exported in a vector field and then imported into the DEM simulation. The CFD simulation was not pursued further, as it changed the kinetics of the system and made it overall slower, resulting in a huge increase in the computation time. It was used in Chapter 5.4 for the simulation of flow around magnetic wires.

4.3.1 The Finite Element Method

FEM is well suited for the simulation of magnetic field strength and the magnetization of a body in a magnetic field. In this work it was used specifically for the simulation of the magnetic field created around magnetic wires and particles. This study used the commercial software Comsol Multiphysics with the versions 3.4 and 4.2a. The predefined model “AC/DC no currents” showed to be easy to use for the simulation of particles, wire fields and permanent magnets. A dual core computer with 2.8 GHz, 4 GB Ram, and 32 bit Windows 7 was used. The simulation is based on (2-98) and (2-99). The magnetic field determined by FEM could be exported as vector field and read to the DEM code for the simulation of particle tracks in fluid.

4.3.2 Computational Fluid Dynamics

The fluid flow simulation was performed by the FVM. The software Ansys Fluent version 12 was used for the simulation of fluid flow around a wire and in a centrifuge. The simulation could be coupled in one way by reading a vector field in the DEM simulation. The grid was generated in Gambit and in the Ansys Workbench. The Stokes resistance in (2-43) was implemented for coupling. The differential velocity to the fluid was calculated from a vector field determined by a CFD simulation and implemented as an additional external force. Fluid forces showed to reduce the particle velocity strongly and increase simulation time without changing the final deposition shape. Therefore fluid forces were omitted, and further simulations were performed in vacuum instead. If fluid forces are taken into account, additionally the Stokes resistance needs to be replaced by the resistance of a needle or ellipsoid, which is shown in (8-4) for all particles in one needle. It would be possible in the current simulation approach to calculate the resistance of the needle and assign a proportion to each particle in the needle, as in the simulation approach particles collected in one needle are tracked.

4.3.3 The Discrete Element Method

DEM was used for the simulation of particle agglomeration and deposition. The magnetic field around dipoles had already been solved analytically. It closes in field direction, it is repulsive perpendicular to the magnetic field direction and attractive on top and bottom. This leads to needle-shaped agglomerates. In case of magnetically hard substances, the magnetic field of dipoles can be summed directly. Besides magnetic forces, Hertzian spring and damper forces were implemented. Five assumptions were taken in the model.

1. Spherical magnetic particles may be approximated by a magnetic dipole.
2. The saturation magnetization of the particles is reached.

3. The influence of the hydrodynamic forces changes the kinetics but not the final deposit shape.
4. Surface forces may be neglected.
5. Magnetic particles are always aligned in the external field direction.

Mechanic Model

DEM bases on modeling of the mechanic repulsing forces of the particles. These are in case of molecular forces the Born forces. In case of macroscopic particles, the Born force rises steep at the surface distance a^{-7} , which requires small time steps for stability and therefore cannot be implemented in the model. Instead the Hertz equations are realized in the simulation model, which rise at $\delta^{3/2}$ in normal direction. Additionally damper forces were implemented in the tangential direction from (2-59). In tangential direction only damper forces were implemented from (2-60). Damper forces generally are necessary to avoid oscillation of the particles, changing the potential energy of the attracting and repulsing forces into kinetic energy and vice versa. Increasing damper forces stabilizes the simulation.

Magnetic Dipole Model

Figure 4-1 shows schematically the model implemented in the DEM simulation.

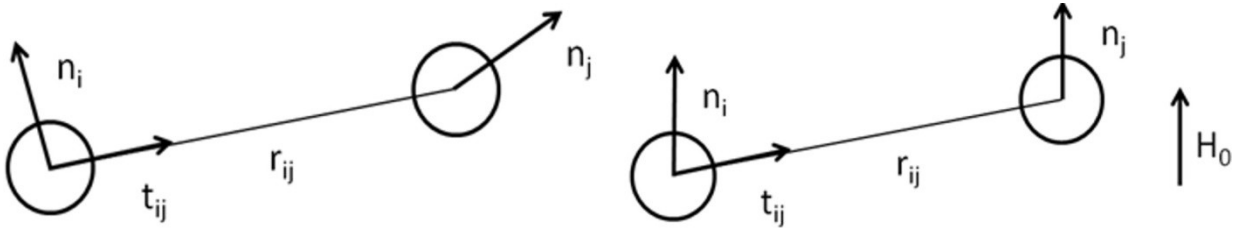


Figure 4-1: schematic particle alignment in the simulation approach; left: particles are not aligned: right: particles are aligned in field direction as implemented in the simulation

While the magnetic moment might point in any direction without an external magnetic field applied (Figure 4-1 left), in the uniform magnetic field H_0 of HGMS particles align in field direction (Figure 4-1 right). The magnetic dipole force in between two particles from (2-32) with the components of the direction vector $\mathbf{t}_{ij} = (t_x, t_y, t_z)$ was simplified to

$$\mathbf{F}_{m,ij} = -\frac{3\mu_0\mu_i\mu_j}{4\pi r^4} \begin{pmatrix} (5t_x^2 - 3)t_x \\ (5t_x^2 - 1)t_y \\ (5t_x^2 - 1)t_z \end{pmatrix}. \quad (4-1)$$

This equation is easy to implement in a DEM simulation. The interaction of magnetic moments is neglected, as the magnetic field of particles is in saturation. The simulation is limited to this case. A mutual interaction below saturation would require coupling a FEM solver with a DEM solver, which is beyond the scope of this work. The magnetic field in

proximity of a magnetic wire is distorted though. A detailed discussion on drawbacks is in Chapter 4.5. The magnetic force only acts below a specific radius, called the contact radius r_c , which is significantly larger than the physical radius of the particle. The restriction of the calculation of interparticular forces to particles below the contact radius reduces calculation power. The parameters in the simulation are summarized in Table 4-2.

Table 4-2: Parameters realized in the simulation

Symbol	Value	Unit	Denotation
M_p	480000	[A/m]	Particle magnetization (except given otherwise)
ν	0.3	[-]	Poisson ratio
E	2e5	[Pa]	Elasticity modulus
ρ_p	2000	[kg/m ³]	Density Particle
R	0.5e-6	[m]	Physical particle radius (mechanic force)
r_c	4e-6	[m]	Contact radius (magnetic force)
v	0.001	[m/s]	Initial velocity
a	5e-4	[m]	Wire radius
b	1e-5	[m]	Particle radius (except given otherwise)
M_w	1.6e6	[A/m]	Wire magnetization

Magnetic Background Field

In OGMS devices, which do not feature wires but only an external magnet, the magnetic background field is the driving force. In HGMS though, the background field is close to homogeneous. Chapter 5.9 shows the magnetic field in the cell, with a gradient of around 0.4 T/m, in comparison to magnetic wires creating field gradients of more than 1.000 T/m. Therefore the background field could be neglected in this simulation. A simulation by FEM and implementation would be easily possible for OGMS devices.

Magnetic Wire Force

The magnetic wire force was implemented in two different ways. First it was implemented for a uniform cylindrical wire based on the analytic model from (2-40). This provides an easy model which is economic in terms of computational power. Subsequently for simulations on the detaching of magnetic particles on the wire end including rotational forces, the magnetic field gradient was simulated based on FEM in Comsol Multiphysics. The simulation approach was already described in Chapter 4.3.1. It was then exported as a vector field and imported in the DEM software. Basing on the field gradient, the force on a particle is calculated from (2-25) as an external force. A magnetic background field of 400 kA/m was set, corresponding to 0.5 T. A wire permeability of 5 was set, corresponding to a magnetization of 1.6 MA/m, as is the case at saturation magnetization in the used steel. This results in magnetic field

gradients retaining particles on the wire end. The field weakens at the wire end, resulting in an important force retaining particles. For the studies on the effect of mutual enhancement between particles, a custom curve based on the experimental values was read to the simulation. An alternative which is more stable is the use of a function approximating experimental values.

DLVO

Van-der-Waals and electrostatic forces were implemented based on (2-49) and (2-52) in a single simulation as additional interparticular forces acting below the contact radius. They did not show to change the result and were therefore omitted in further simulations. The reason is that magnetic forces dominate over a specific distance range in case of strongly magnetic particles, which was explained in detail in Chapter 3.4.

Sequence of the Final Model

The software EDEM Version 2.3.1 from DEM Solutions Ltd. was used as framework for the simulation of particle agglomeration on a quad core computer of 3.14 GHz, 64 bit and 8 GB RAM with Windows XP SP2. The interparticular forces were programmed in User Defined Libraries (UDL). The forces in between particles were approximated by dipole forces [Satoh'98], in an approach similar to the one chosen by Chen. The current simulation approach was extended to simulation in 3D. Figure 4-2 shows a flow scheme of the simulation.

First the geometry is created and imported, in this case in Gambit. The particle properties are defined and the source code is compiled. The time step needs to be chosen adequately to limit the computation time on the one hand and achieve a stable simulation on the other hand. At large time steps particles overlap strongly, which leads to high repulsing forces and velocities undermining simulation stability. In this case the time step was set by the Rayleigh time step, which is

$$\Delta t_{Rayleigh} = \frac{\pi R \sqrt{\frac{\rho}{G}}}{0.1631\nu + 0.8766} \quad (4-2)$$

It is a theoretic time step for a shear wave to propagate through a solid particle. Suggested is a Rayleigh time step of 0.05 - 0.4, which was used as starting value and then adjusted to the needs. In this formula ρ is the density, G the shear modulus and ν the Poisson ratio [EDEM_Solutions_Ltd._User's_Guide'10].

At the beginning of the simulation particles are initialized at a border of the simulation domain at a minimum distance from each other. An initial particle velocity is applied. The external forces, most importantly the magnetic wire force, act from the beginning, attracting

particles. Then for all particle contacts, i.e. all particle pairs below the contact radius, magnetic forces are applied, leading to agglomeration.

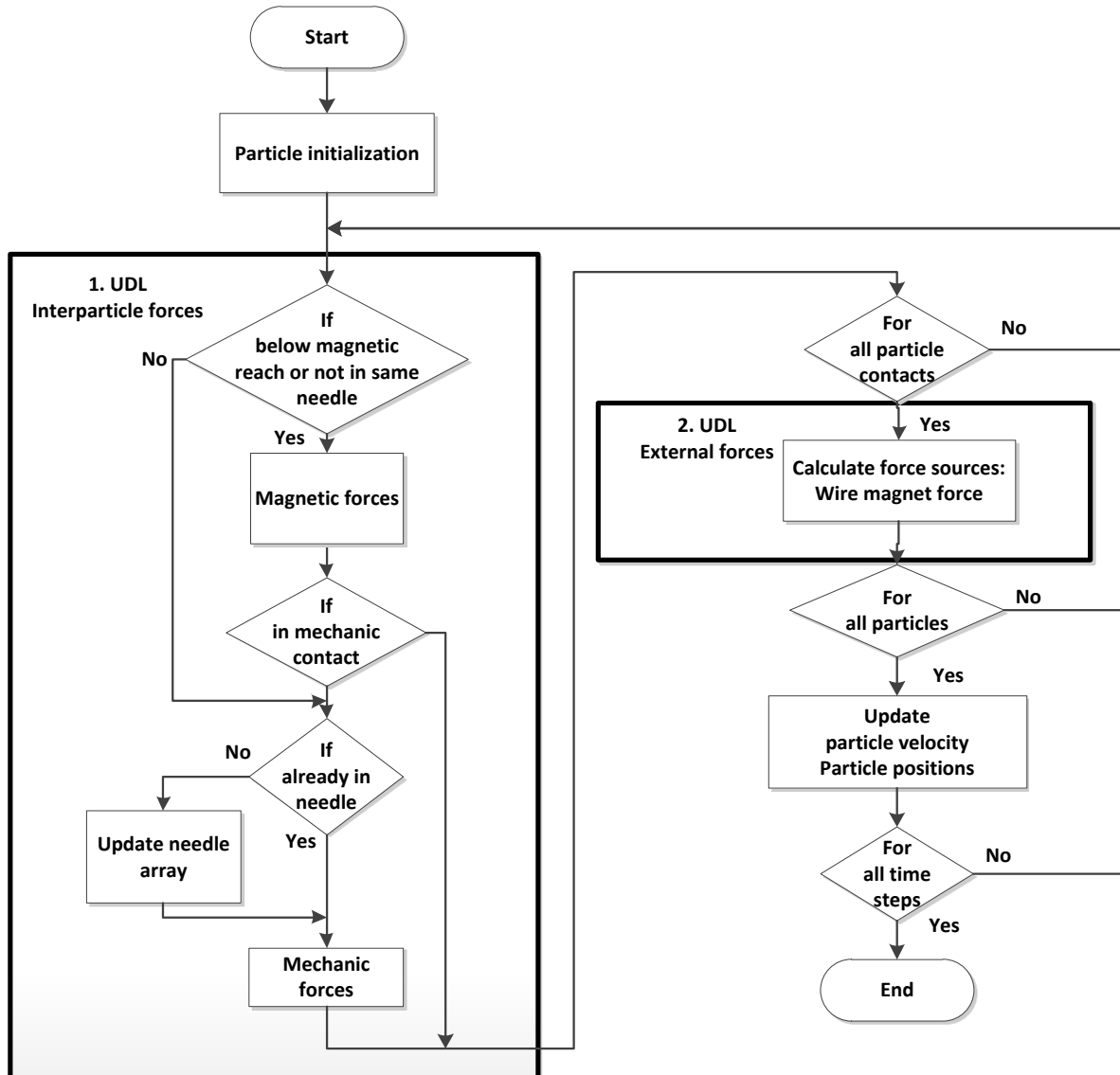


Figure 4-2: Flow scheme of the program with two different UDLs implementing interparticle forces (1. UDL) and external body forces like wire forces (2. UDL)

Magnetic forces act for all particles in contact, i.e. below a particle distance of 4 particle diameters which are not in the same needle. In case of particles which are agglomerated and not in physical contact, the magnetic force is dropped, as it reduces the stability of the simulation. The reason might be the fact that field lines arrange differently in a needle, so the single particles' dipole field is no more valid. This effect was not reported by Eichholz though [Eichholz'12]. Particles collected in one agglomerate are stored in an array. Then the mechanic force is calculated out of the physical contact. This is repeated for all particle pairs. Subsequently the external forces are calculated. This includes mainly the magnetic force

resulting from the wires. First the deduced force was implemented out of (2-40) for the simulation of cylindrical wires without a wire end. Finally the magnetic field was calculated by FEM and read as vector field to enable the simulation of the wire end.

Validation

For validation, two different comparisons were done. The first test was based on a picture taken after separation of a synthetic particle kind in the centrifuge. The wire stage was unmounted and photographed, resulting in a wet deposit. There is no magnetic field while the picture is taken, leading to a weakly magnetic deposition. The second comparison is based on magnetite of Bayferrox (Magnetization 480 kA/m; 2 μm medium particle diameter), which was poured over a wire for a comparison with the simulation. In the simulation 500 particles of 100 μm diameter in a narrow depth of a few particles resulted in a sufficiently large cake.

4.4 Agglomeration and Agglomerate Porosity

Agglomeration of Particles of Different Size

One of the main targets of the simulation is the consequence of interparticular forces for the agglomeration of particles. To control whether the interparticular model works, first a particle was simulated in the magnetic field. Therefore the dipole force of an immobile large particle on small particles was simulated. Figure 4-3 shows the result, i.e. the deposition of small particles on a large particle of 10 times their size and the formation of needle-shaped agglomerates. The directed deposition at one side of the particle and the needle shape is a consequence of attracting and repulsing zones, illustrated in Figure 2-3. The simulation follows the idea of adding large non-functionalized magnetic particles in a process to increase the separation efficiency [Stolarski'11]. The principle enhances separation in the range above 100 nm, where Brownian motion does not dominate (the suspension is not colloidal), but magnetic separation is difficult for the small size of the particles. The simulation shows that the agglomeration of differently sized particles is induced, which is expected to influence the separation.

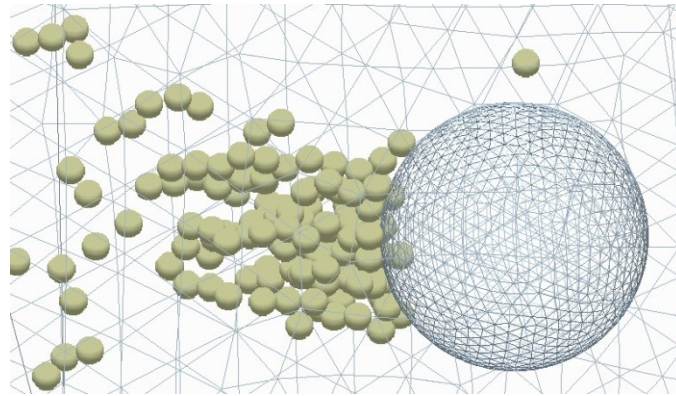


Figure 4-3: Particle agglomeration of 100 μm particles to one 1 mm particle [Lindner'13]

Deposition on a Magnetic Wire in High Gradient Magnetic Separation

Furthermore the deposition of magnetic particles on a magnetic wire is interesting. A similar case with magnetic particles building needles in a magnetic field and being collected on a non-magnetic filter was simulated by Eichholz [Eichholz'10; Eichholz'12]. He suggested a structure of equally spaced needles in a filter cake in theory, although he did not back the assumption by a simulation. A similar structure appears in the simulation of the deposition of particles of the same size on a magnetic wire. The dominating influence seems to be the relation of the magnetization of the wire and of the particles.

The magnetization of particles in this simulation is $4.8 \cdot 10^5$ A/m, while a wire has a magnetization of up to $1.2 \cdot 10^6$ A/m. In a simulation based on this theoretic magnetization of the wire ($M_{particle}/M_{wire} = 0.11$), the particle deposit showed to be dense (Figure 4-4 left). In a second simulation the magnetic wire force was reduced by a factor of 70 compared to the previous simulation ($M_{particle}/M_{wire} = 8.3$), a highly porous deposit resulted on the wire. The distance between particles is large, see Figure 4-4 (middle, right). A consequence is that the porosity of the particle deposit depends on their magnetization. The effect is rather academic though, as it only appears on particles of the same size, and as a displacement of the particle needles by one particle radius leads to attracting forces.

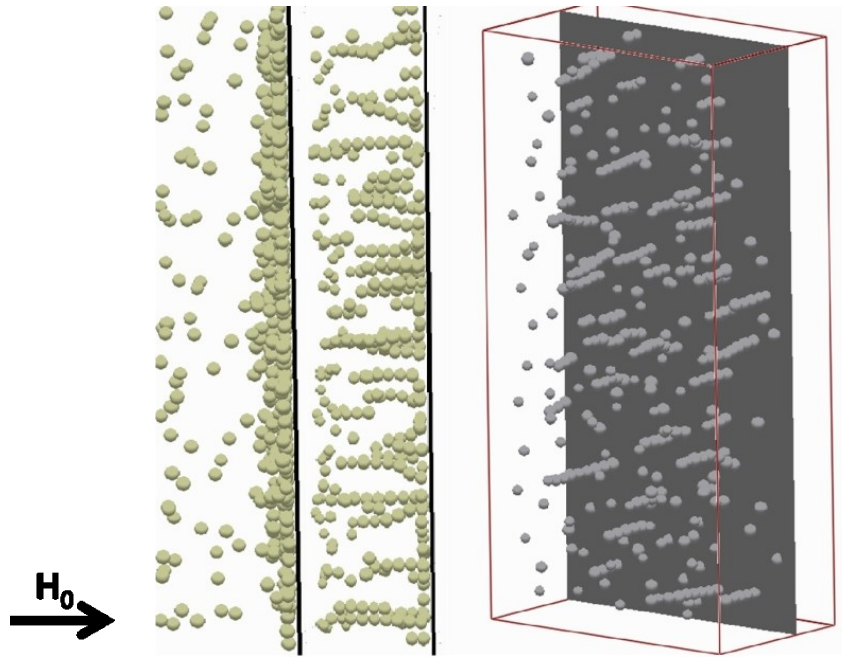


Figure 4-4 left: 1 μm particles build at a strong wire magnetization a dense cake; middle, right: at a weak wire magnetization particles build a highly porous sediment with needle-shaped agglomerates [Lindner'13]

A consequence of this comparison is that in most processes including the current one, a dense cake on the wire results. This is in line with experiments, where a dense bulk was observed. The complete process of deposition could not be visualized based on 2 μm particles on a 1 mm wire for the high computational power which is necessary due to the high particle number. A porous structure only results out of a much higher magnetization of the particles compared to the wires, which is not the case in a common HGMS process.

Analytical Estimation of the Deposit Porosity

Rosensweig puts gravitational energy and magnetic energy into relation to calculate structuring of a particle sediment [Rosensweig'97]. Eichholz used hydrodynamic energy instead of gravitational energy for his case of filtration in the magnetic field [Eichholz'10]. In case of HGMS not gravity but wire force influences the sediment structure. The energy was replaced by the force, as the energy gradient is considered to be actually the basis for comparison. Therefore the particle porosity is estimated as a relation of magnetic wire force and particle wire force. By approximating them with the force of a magnetic cylinder and a magnetic dipole, this results close to the wire for $r_W = a$:

$$\frac{F_{dipole}}{F_{wire}} = \frac{-\frac{3\mu_0\mu_i\mu_j}{4\pi r_p^4} 2}{-\mu_0\mu_i M_W \frac{a^2}{r_W^3} \left(\frac{a^2}{r_W^2} + 1\right)} = \frac{1}{4} \frac{M_P}{M_W} \frac{r_W}{d_P} \frac{r_W^2}{a^2} \frac{1}{\left(\frac{a^2}{r_W^2} + 1\right)} = \frac{1}{8} \frac{M_P}{M_W} \frac{r_W}{d_P} \quad (4-3)$$

$$\begin{cases} \ll 10^2 & \text{dense} \\ \gg 10^2 & \text{porous} \end{cases}$$

A consequence is, that the relation of particle and wire size influences the deposit as well. This results in the value $F_{dipole}/F_{wire} = 14$ for a dense cake and $F_{dipole}/F_{wire} = 1038$ for a porous cake for the simulation above, which suggests a change in the regime at a value of around 10^2 .

4.4.1 Parameter Study

The influence of the particle size for the deposition is important, as the simulation of $2 \mu\text{m}$ sized particles is computationally too expensive. Figure 4-5 shows the deposition of magnetic particles of $10 \mu\text{m}$, $20 \mu\text{m}$ and $100 \mu\text{m}$ size on a magnetic wire. The field direction is horizontal. Obviously, there is no important qualitative difference in the deposition. Particles show a very dense cake at this wire distance. The simulations of large particles allowed the investigation of a much larger deposit, while in small particle sizes the particle number is too high to allow the simulation of the complete deposit.

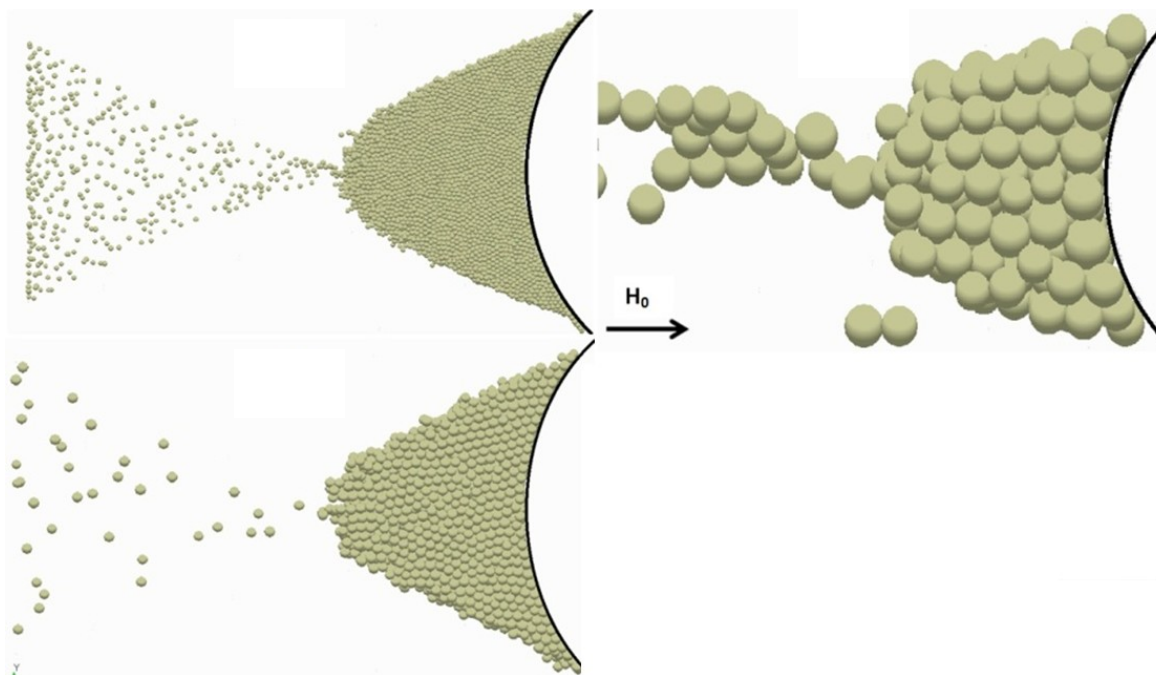


Figure 4-5: Comparison of the deposition shape of particles of $10 \mu\text{m}$ (top left), $20 \mu\text{m}$ (top right) and $100 \mu\text{m}$ (bottom) size results in a similar deposition [Lindner'13]

Process of Particle Deposition on a Wire

The implementation of the magnetic wire force by FEM allows the simulation of particle deposition at the wire end under additional forces. Specifically the centrifugal force is interesting in this simulation. The approach allows the modeling of this important aspect in MEC. Figure 4-6 shows the deposition of magnetic particles on a wire. The deposition starts at the inside (top left), increases (top right), and gets more homogeneous after some time

(bottom left). The building of needles upstream of the wire is well visible. When a centrifugal force is applied, the particles are discharged from the wire, which happens as well in needle-shaped agglomerates. The deposition shows an important accumulation at the end of the wire. At this point a high field gradient retains the particles.

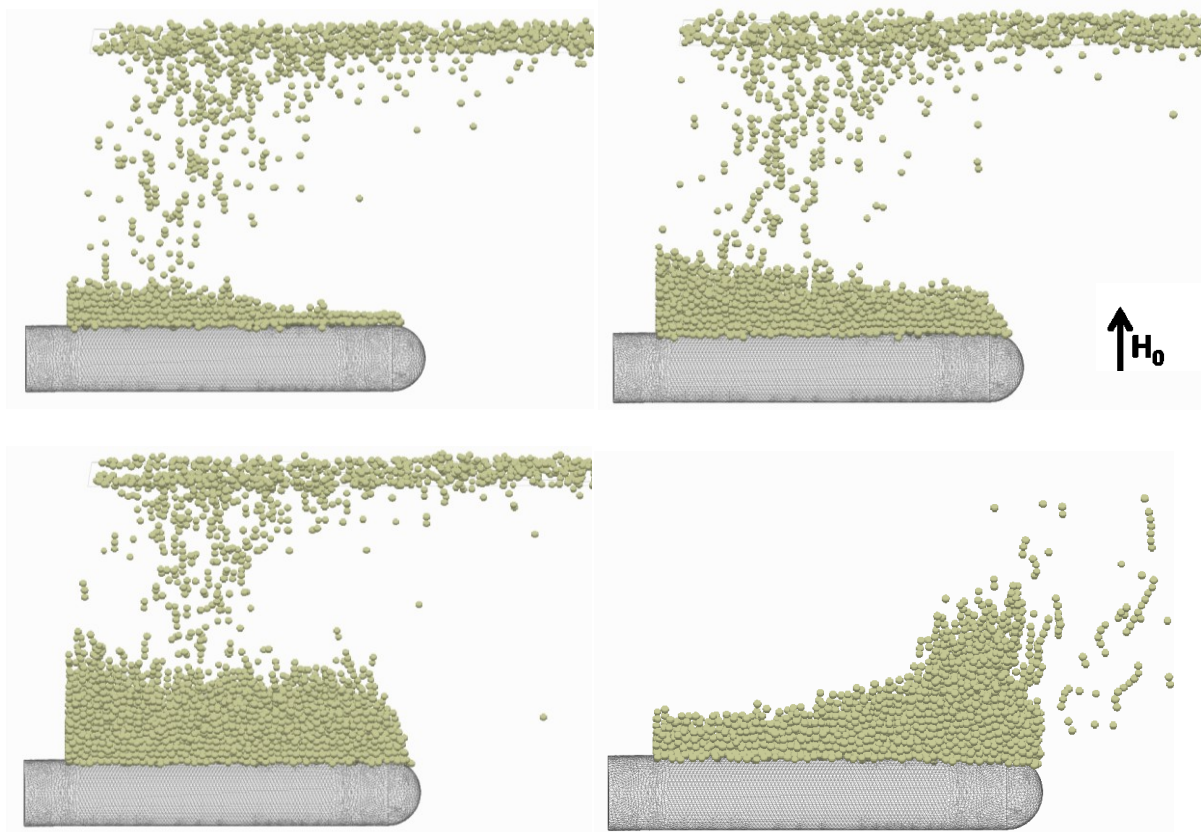


Figure 4-6: the buildup of a deposition of magnetic particles at different times (top left: 0.0274 s; top right: 0.0465 s; bottom left: 0.0753 s) increases steadily without centrifugal field; bottom right: once the centrifugal field is applied, only a small layer of particles stays on the wire with the rest being transported away; needle-shaped agglomeration is well visible before deposition on the wire and for agglomerates detaching from the wire;

Figure 4-7 shows the deposition of magnetic particles on a wire under different accelerations acting in needle direction. The needles are aligned in field direction, as visible at no centrifugal force in Figure 4-7 top left. The particles slide, under centrifugal forces, to the outside of the wire and detach. The centrifugal force corresponds to 0, 10, 60 and 240 g, which is the same range as implemented in the experimental process. Different forces like the Coriolis force are neglected. A centrifugal force leads to detaching of the particles, with the deposit shrinking dependent on the centrifugal force. The deposit cannot be cleaned completely though, as the magnetic force at the end of the wire keeps the particles back. The simulation is similar to experimental investigation, but the friction of the particles on the wire seems to be underestimated.

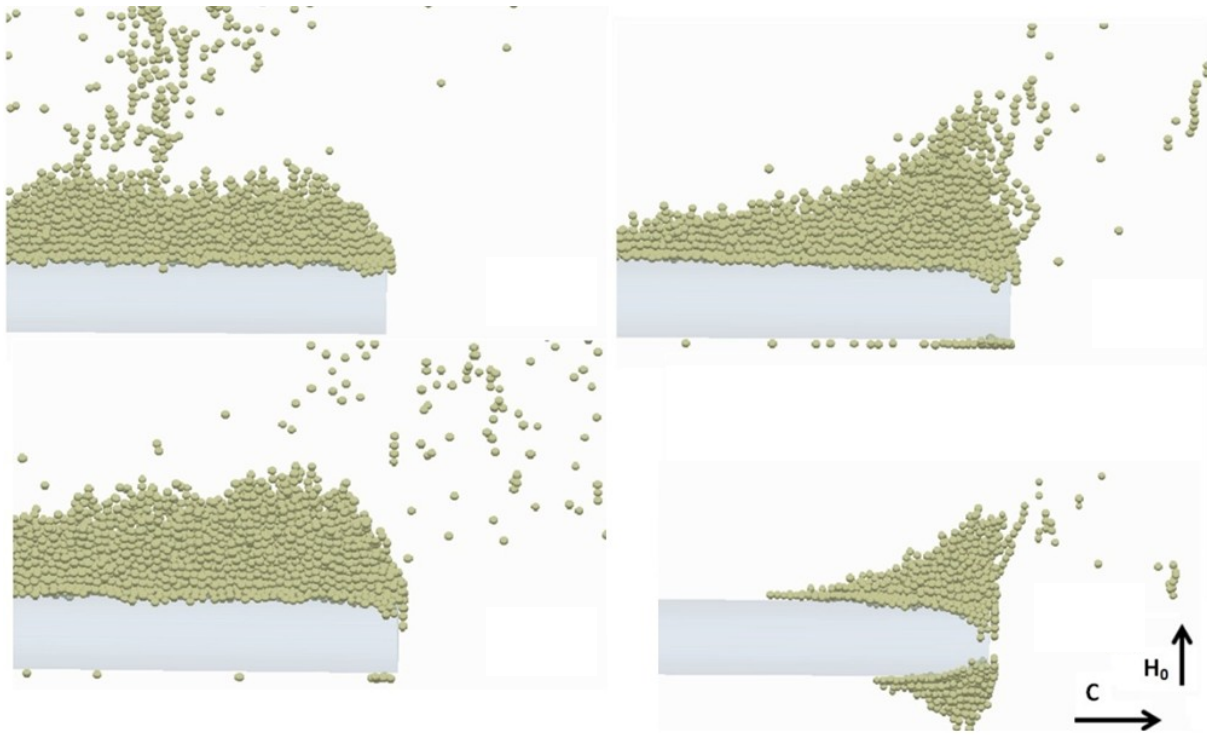


Figure 4-7: Comparison of particle deposition with magnetic field on a wire end; top left: without acceleration a uniform deposition forms; bottom left: at 10 times earth gravitation the deposition is slightly moved to in force direction; top right: at 60 * g the deposition is strongest on the wire end; bottom right: at 240 * g only at the wire end some particle deposition is left [Lindner'13]

The result of the simulation is a shifting of the deposit on the wire to the outside. The length of the wire is 4 mm. This was quantified by determining the center of gravity. Figure 4-8 shows the deposit on magnetic wires for different centrifugal rotational velocities. The position of the gravity center of particles moves from 1.8 mm to 0.3 mm distance from the wire end.

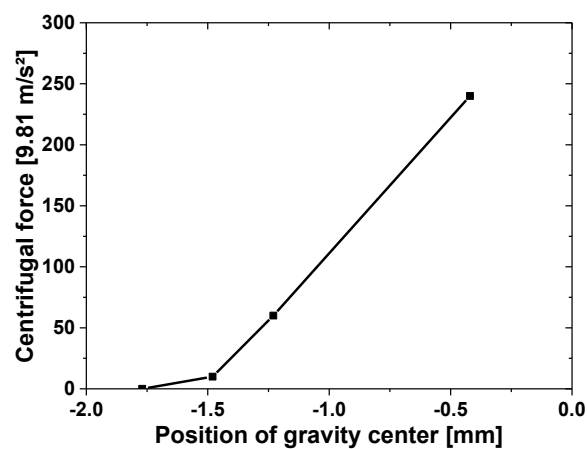


Figure 4-8: at high centrifugal field the centre of gravity shifts towards the wire end [Lindner'13]

In summary, the deposition depends strongly on the magnetization of particles and wires, as well as on the centrifugal force. Especially the high retaining gradients of the wire end reduce the influence of the centrifugation.

4.4.2 Comparison with Different Simulations

The simulation was as well compared to the results of different research groups and validated experimentally. Figure 4-9 shows a comparison of particle deposition with a simulation of Chen [Chen'09]. Chen simulated as well the deposition of magnetic particles on a wire under the influence of centrifugal forces, but limited his approach to two dimensions. The corresponding rotational velocity is 1500 rpm, resulting in 60 g. The basic deposit seems similar in both simulations. The main difference are the forces keeping particles back at the end of the wire, which in the current simulation show a rather sharp stop for particle deposition. In contrary Chen's simulation shows particles being retained beyond the wire, which hints to a different modeling of the magnetic forces.

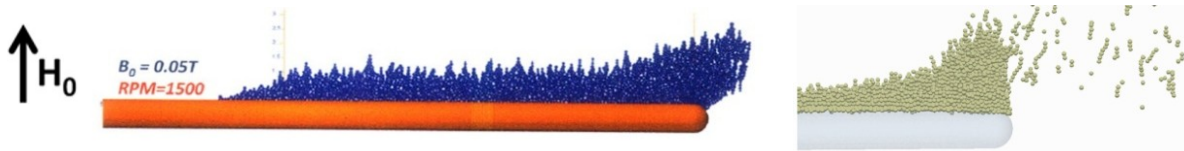


Figure 4-9 left: 2D simulation of Chen [13]; right: a simulation at 60 * g for comparison shows a similar deposition with a difference at the wire end, where retaining magnetic forces lead to a sharper cut in the particle position; the sharp cut seems obvious from the simulation of the magnetic field [Lindner'13]

4.4.3 Experimental Validation

Reducing the particle magnetization while keeping the wire magnetization constant ($M_{\text{dipole}}/M_{\text{wire}} \ll 1$) allows the comparison with deposition after the magnetic field was removed. The reduced particle magnetization seemed not to influence the deposition significantly. The centrifugal force and the wire magnetization were kept unchanged in this simulation. The result is shown in Figure 4-10 left. Figure 4-10 right shows a comparison photograph of magnetic particles on a wire. Particles of 40 Am²/kg magnetization were processed in the centrifuge. Subsequently the matrix was taken out of the centrifuge. The similarity between the simulation and the photograph is obvious, with even the slight elevation of magnetic particles at the wire end being reproduced correctly.



Figure 4-10 left: simulation of the particle deposition of weakly magnetic particles on a magnetic wire; right: deposition of weakly magnetic particles in the MEC and removing from the magnetic field results in a similar deposit compared to the simulation

Finally the deposition of strongly magnetic particles was simulated and compared with the simulation. The deposition achieves a significant height of several times the wire diameter. Figure 4-11 (left) shows a comparison of highly magnetic particles (Bayferrox) poured on a wire in air with a magnet placed underneath. A wire of 1 mm diameter was used as before. Figure 4-11 (second left) shows a wire end filmed during a HGMS process with an endoscope, which was thankfully provided by Menzel. Figure 4-11 (third left) shows the deposition of magnetic particles on a wire. The deposition compares obviously well to both the deposition in air and in process fluid. The most important difference is the less “round” deposition close to the wire between the simulation and the deposition in air. Reason to this is the simplification taken in (4-1). The particles are simulated to always align in direction of the external field. In sum, simulation and experiments compare well though. Figure 4-11 (right) shows a simulation of deposition under neglect of interparticular forces, which shows a rounder deposition and lacks the rough needles on top of the deposition. In this case particles align in direction of the magnetic wire field.

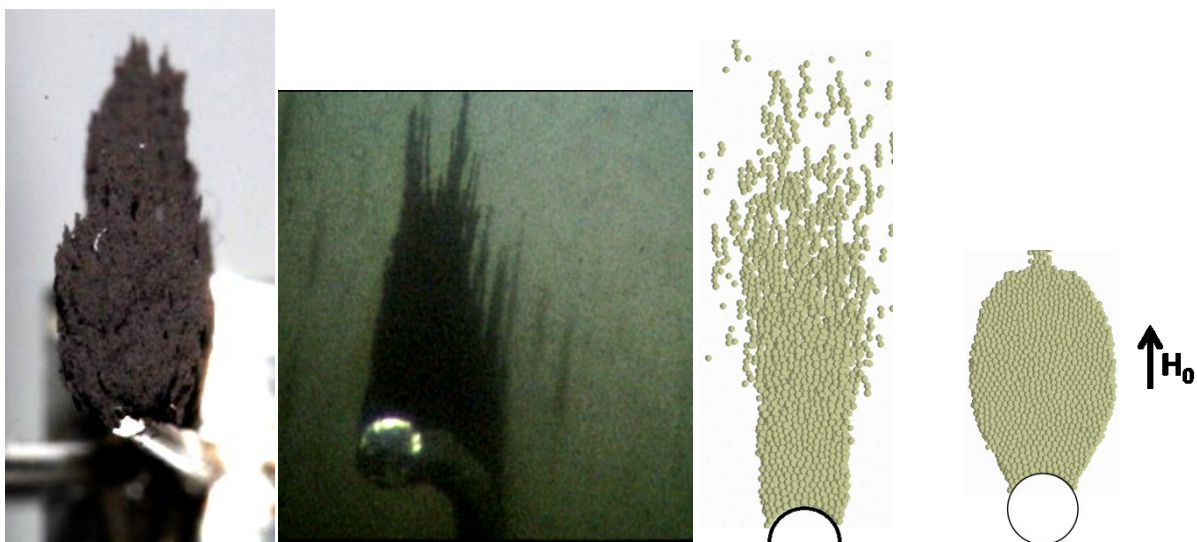


Figure 4-11 left: photograph of magnetite (BayFerrox) on a wire (left) [Lindner'13]; second left: picture from a HGMS process filmed by an endoscope [source: Menzel]; third left: simulation of magnetic

particle deposition on a wire including wire and interparticular forces shows a very similar deposition to the experimental results, with a less round deposition close to the wire in the left photograph [Lindner'13]; right: particle deposition when omitting interparticular forces results in a round deposit

Interesting is as well the distribution of particles on top of the wire. Most of the particles are collected directly on the wire surface; the amount reduces steadily at rising distance from the wire (see Figure 4-11 third from left). A numerical analysis is shown in Figure 4-12. From the wire center the amount of particles decreases almost linearly. Particles are packed more densely close to the wire. The deposition is about 6 mm high in this case of a wire of 1 mm diameter.

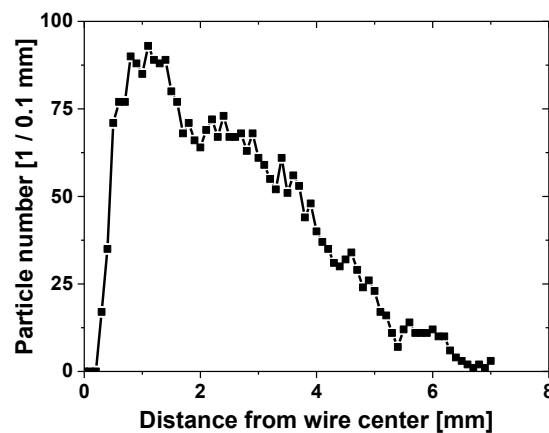


Figure 4-12: the particle number over the distance from the wire in the simulation shows a almost linear decrease of the particle amount

4.5 Evaluation of Error Sources

The modeling approach used here bases, as any simulation, on several assumptions. Their influence is quantified in this chapter. Two of the assumptions showed to be significant: first, magnetic particles are not always aligned in the external field direction, but are turned close to a magnetic wire. Second, the approximation of spheres by dipole equations is only an approximation, which is discussed below. A major drawback of the model is that the dipole force implemented in the simulation showed to produce instabilities which were compensated by neglecting the force of distant particles in agglomerates. This does not provide an exact simulation of forces in between particles. Three different elements reduce the physical exactness of the model.

- The simplification of aligning particles in external field direction is not correct in the direct surroundings of a wire, leading to a different deposition shape close to the wire.

- The simulation is only valid in saturation magnetization. Below saturation, on the one hand demagnetization effects reduce the magnetic field. On the other hand particles reinforce each other's magnetic field, leading to high gradients in between.
- The approximation of spheres by an infinitely small dipole is only an approximation. Mass elements close to each other attract stronger, hence an approximation by the particle center is not justified; in the simulation approach this was compensated by reducing the distant particle's needle force to stabilize the simulation; a new approach should implement the introduced force above as additional magnetic force for particles close to each other.

4.5.1 Error by Simplification of the Alignment of the Particles

As visible from Figure 4-11 left and third left, there is an error of the deposition of magnetic particles close to the wire. The wires bend the magnetic field lines. Initially this was not expected to have an important impact on the simulation. The simulation in Figure 4-11 (right) neglecting interparticular forces showed a round deposit close to the wire, which fits better with the validation experiment. Figure 4-11 (left) illustrates the alignment of particles in the magnetic field direction in this approach. This assumption is justified in the homogeneous field far from wires. A solution would be the calculation of the sum of the field gradients at the particle position and the calculation of the alignment of the dipole.

4.5.2 Approximation of a Hard Magnetic Sphere by a Hard Magnetic Dipole

Initially the approximation of a sphere by a dipole equation seemed to be justified. The norm of the force deduced from (2-32) is

$$F_j = -\frac{3}{2\pi} \mu_0 \mu_j \mu_i \frac{1}{r_j^3}. \quad (4-4)$$

The difference seems low if the magnetic field including the background field is compared, which is shown in Figure 4-13. The flux density and its product with the differential volume of a particle in the field of another particle is shown in Figure 4-13 left. Figure 4-13 right shows a comparison of the field integral with the averaged field in the center. The difference is about 3% in the field itself. Important is the field gradient at the particle position though.

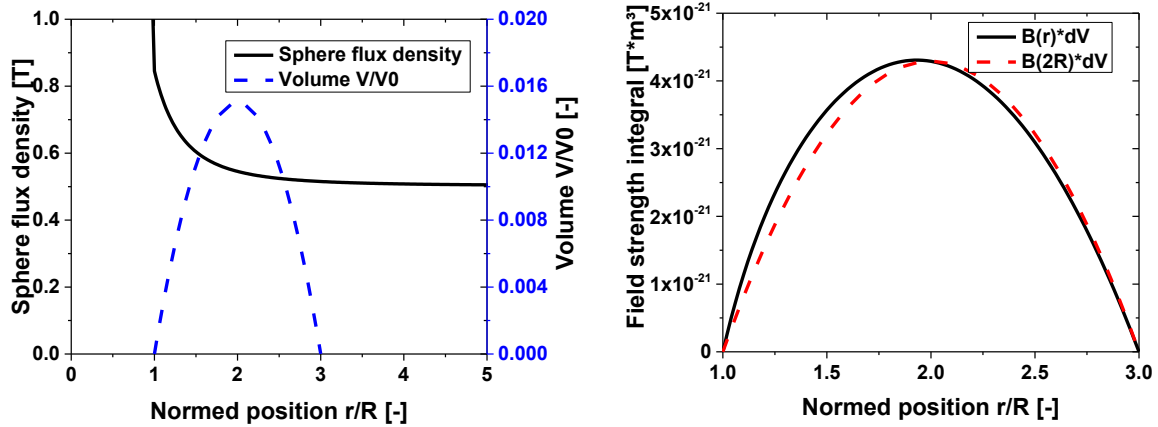


Figure 4-13 left: the magnetic flux density close to a particle and the volume of a particle in field direction; right: the product of the magnetic field in the particle center times the volume element $B(2R) * dV$ and of the field at the place of the volume element $B(r) * dV$ delivers almost the same result (3% difference)

To improve a simulation based on two hard magnetic spheres (or ferromagnetic spheres in saturation), the equation is integrated over the volume of the attracted particle. The field gradient of a dipole in direction of its magnetic moment is from (4-1) given by

$$\nabla H_i = -\frac{3}{2\pi} \frac{\mu_i}{r^4}. \quad (4-5)$$

The integration of a particle volume is in this case done by approximating the sphere by differential cylinders. This is illustrated in Figure 4-14.

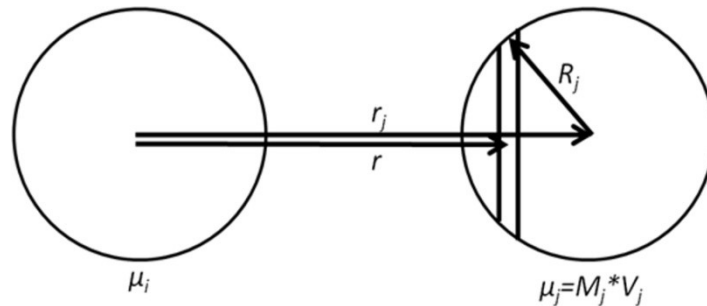


Figure 4-14: the calculation of the force bases on attraction of layers and hence takes into account the reduced distance of a specific part of the next particle

The differential element, a cylinder, is given by

$$dV_j = A(r)dr = \pi (R_j^2 - (r_j - r)^2) dr. \quad (4-6)$$

The field is considered constant all over the differential element. The force hence results as:

$$F_j = -\mu_0 M_j \int_{r_j - R_j}^{r_j + R_j} \nabla H_i(r) dV_j = -\frac{3}{2\pi} \mu_0 \mu_j \mu_i \frac{1}{(r_j^2 - R_j^2)^2}. \quad (4-7)$$

The relation of sphere force over dipole force characterizes the error committed in the simulation:

$$\frac{F_{sphere}}{F_{dipole}} = \frac{\left(\frac{r_j}{R}\right)^4}{\left(\frac{r_j}{R}\right)^4 - 2\left(\frac{r_j}{R}\right)^2 + 1}. \quad (4-8)$$

For $r \gg R$, F_{sphere} / F_{dipole} tends to 1. The field gradient shows an increased force by a factor 1.77 for two agglomerated particles of the same size (i.e. $r = 2R$) and reduces for more distant particles. Figure 4-15 left shows the field gradient multiplied with a volume element, which is significantly higher than the field, compared to Figure 4-15 right, which shows F_{sphere} / F_{dipole} from (4-8).

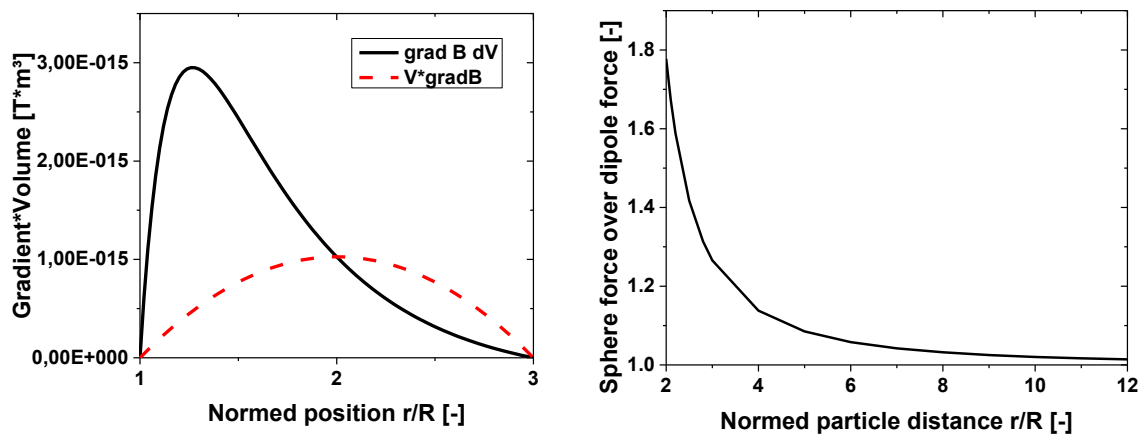


Figure 4-15 left: the field gradient times the volume element $\text{grad } B(r) dV$ delivers a much stronger field than the particle volume times the field gradient in its center $V \cdot \text{grad } B(2R)$; right: the relation for different distances solved analytically

4.5.3 Mutual Field Enhancement of Weak Magnetic Spheres

Calculation of the External Moment of an Agglomerate

In the simulation, magnetic particles and wire were assumed to be in saturation magnetization. The approach is physically correct. Target of this section is to develop a method for the simulation of non-saturated particles in weak magnetic fields. As the susceptibility κ is in this case a function of the magnetic background field H and of the shape and orientation influence N , a derivation is based on the intrinsic susceptibility κ_i . An alternative to this method might be a different definition of κ . In the case of the specific particle system, $\kappa = M/\sqrt{H}$ showed to give an almost constant value of $0.9 \cdot 10^4 - 1.5 \cdot 10^4$ (as mentioned in Chapter 3.3).

The magnetic field of two distinct weak magnetic bodies enhances each other, leading to a stronger attraction. Another way of looking at this is to quantify demagnetization by the agglomerate body's geometry. The demagnetization of a needle can be approximated by that

of a cylinder or ellipsoid. For an agglomerate of two particles, this results in a reduction of the demagnetization factor N from $1/3$ to 0.17 (ellipsoid). As obvious from

$$\frac{\mu_N}{\mu_S} = \frac{\kappa_N V_N}{\kappa_S V_S} = n \frac{1 + N_S \kappa_i}{1 + N_N \kappa_i} \xrightarrow{N_N \kappa_i \gg 1} n \frac{N_S}{N_N}, \quad (4-9)$$

the influence is significant. The number of particles is n , the demagnetization of a sphere N_S and the demagnetization of a needle (approximated by an ellipsoid) N_N .

A FEM simulation of this field enhancement is shown in Figure 4-16. While a single sphere is magnetized weakly, two spheres mutually enhance the magnetic field. Another interpretation is the reduction of the demagnetization by forming a body oriented in field direction.

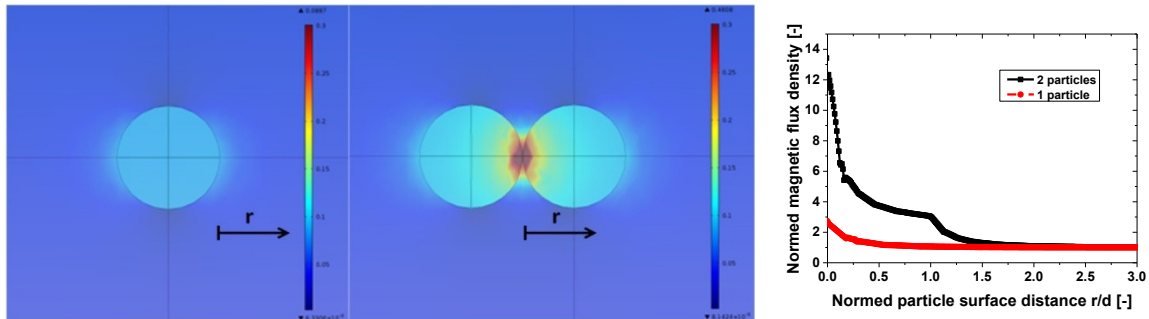


Figure 4-16 left: the magnetic flux density of one particle at $H=25000\text{A/m}$, $\kappa=58532 \cdot H^{-0.88}$; middle: the magnetic flux density of two particles enhancing each other's magnetic field is significantly stronger; right: numerically the magnetic field without background field outside of first particle (i.e. inside of second for two particles) shows to be very strong in the small particle contact region

In case of a simulation, the demagnetization factor would have to be adjusted depending on the length of the needle. An approximation of a needle by an ellipsoid seems sufficient. A simple implementation of the field strength induced by a needle is hence to track the needle length and use an average demagnetization for all particles in the needle of a similar ellipsoid or cylinder calculated by an exponential function (Figure 2-1 right).

In the past N was derived for many different geometries by Fourier-space techniques [Osborn'45; Beleggia'05]. Only elliptic geometries deliver a constant value all over the domain, while most other geometries need to be averaged. An alternative to calculation is the simulation in FEM by the simulation of a hard magnetic body. The demagnetization factor is then calculated out of the interior magnetic field and the body magnetization from (2-13). A validation test lead to an error of 3.5% for an ellipsoid of length/width= 2/1 compared with the analytic value.

Calculation of the Force between Two Particles Mutually Enhancing Each Other

In case of particle needles, a more complex approach is necessary. The force equation can be rewritten for spheres instead of the particles including paramagnetic enhancement of the

spheres. The magnetic field of a dipole i influenced by and influencing an identic dipole j , by introducing the magnetic field from (2-28) in (4-5), is then written as a series:

$$\begin{aligned} H(r) &= H_0 + \frac{1}{2\pi} \frac{V_i \kappa_i}{r^3} \left(H_0 + \frac{1}{2\pi} \frac{V_j \kappa_j}{r^3} (H_0 + H_i) \right) \\ &= H_0 + H_0 \frac{1}{2\pi} \frac{V_i \kappa_i}{r^3} \left(1 + \frac{1}{2\pi} \frac{V_j \kappa_j}{r^3} \left(1 + \frac{1}{2\pi} \frac{V_i \kappa_i}{r^3} (1 + \dots) \right) \right) = H_0 \sum_{k=0}^N \left(\frac{1}{2\pi} \frac{V_i \kappa_i}{r^3} \right)^k. \end{aligned} \quad (4-10)$$

Note that the demagnetization of a single particle needs to be introduced for κ in this approach. Terms are of order $3*k$ or $3*k+1$ for the field gradient, and hence rapidly becoming unimportant at high distance. Close particles increase their field strongly on their surface though (see Figure 4-16 right). Note that (4-5) results as a special case when truncating the field gradient at $k=1$. The series cannot be solved completely, therefore it is truncated. In case of a paramagnetic sphere j being magnetized by a homogeneous background field H_0 and by a dipole i , the agglomeration force is approximated by

$$\begin{aligned} F_j &= -\mu_0 \kappa_j \int_{r_j-R_j}^{r_j+R_j} (H_0 + H_i) \nabla H_i(r) dV_j = \\ &= -\mu_0 \kappa_j \int_{r_j-R_j}^{r_j+R_j} \left(H_0 + \frac{1}{2\pi} \frac{V_i \kappa_i}{r^3} H_0 \right) \left(-\frac{3}{2\pi} \frac{V_i \kappa_i}{r^4} H_0 \right) dV_j. \end{aligned} \quad (4-11)$$

For the force results

$$\begin{aligned} F_j &= \frac{3}{2\pi} \mu_0 \kappa_i V_i H_0 \kappa_j V_j H_0 \left(\frac{1}{(r_j^2 - R_j^2)^2} + \frac{\kappa_i V_i r_j}{\pi (r_j^2 - R_j^2)^5} \left(\frac{1}{2} r_j^2 + \frac{3}{10} R_j^2 \right) \right) \\ &= \frac{3}{2\pi} \mu_0 \kappa_i V_i H_0 \kappa_j V_j H_0 \left(\frac{R_j^{-4}}{(r_j^2/R_j^2 - 1)^2} + \frac{R_j^{-7} \kappa_i V_i r_j}{\pi (r_j^2/R_j^2 - 1)^5} \left(\frac{1}{2} r_j^2/R_j^2 + \frac{3}{10} \right) \right). \end{aligned} \quad (4-12)$$

The term is complex and order increases rapidly, so for high distance the approximation by dipoles is justified. The increase in proximity is significant though. Remember that this is not an exact solution but again only an approximation due to the neglect of terms of higher order. The forces derived are plotted in an example comparison in Figure 4-17 left. In this case at short distance terms of higher order influence attraction strongly. Figure 4-17 right shows the increase compared to a dipole and to a hard magnetic sphere.

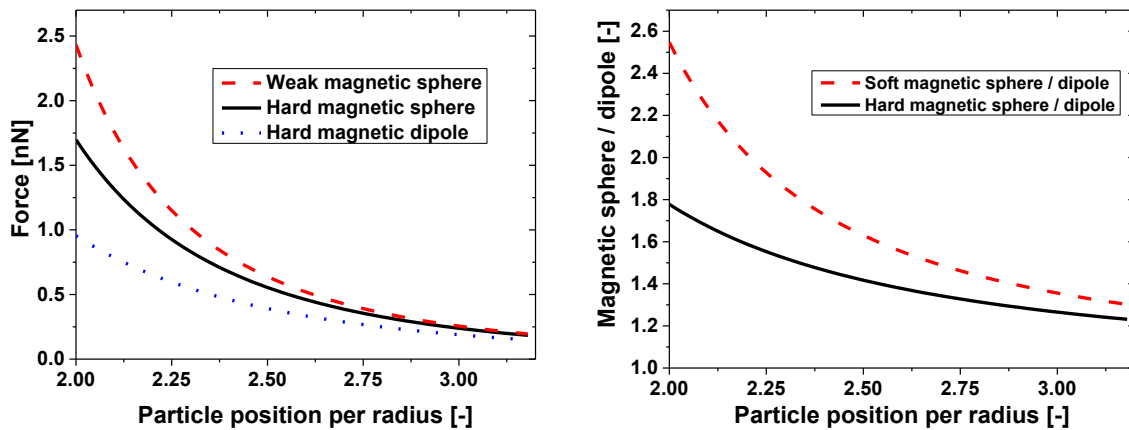


Figure 4-17 left: force comparison of a dipole, hard magnetic sphere and weakly magnetic sphere by a truncated series including the demagnetization influence $\kappa = 1/(1+1/0,33*58532*H^{-0,88})$ at a background field of 40000 A/m; right: the relation for the enhancement is up to 2.5 x for mutual enhancement and reduces over at large particle distance

4.6 Outlook

Analytical Model

To perform the simulation of a complete particle deposit of 1 μm sized particles, the approach may be refined including the sphere difference. A simulation of magnetic spheres not in saturation would be possible by compensating for the lower demagnetization of a needle.

Approximation by a Continuum

The Discrete Element Method is limited in the number of particles which can be calculated. In this approach the simulation was hence limited to 100 μm sized particles. Another possibility is the approximation of particles as a continuum. This might be possible by implementing magnetic forces in FVM or in the Lattice Boltzmann Method. This approach might allow simulation of a complete machine. This is important for understanding the influence of the agglomeration upstream of magnetic wires on the separation of magnetic wires. Additionally the adsorption might be included in the same model by including protein as a continuous phase.

5 Magnetically Enhanced Centrifugation

In MEC centrifugal forces are used for the discharge of a magnetic wire filter. Figure 5-1 shows the principle: magnetic particles are collected on a wire filter, which itself is magnetized by an external magnet similarly to conventional HGMS. In contrary to HGMS though, the wire filter is implemented in a centrifuge and continuously discharged by centrifugal forces. The particles settle on the centrifuge wall where they can be stored or discharged continuously. The electromagnet's axis is arranged on the centrifuge axis.

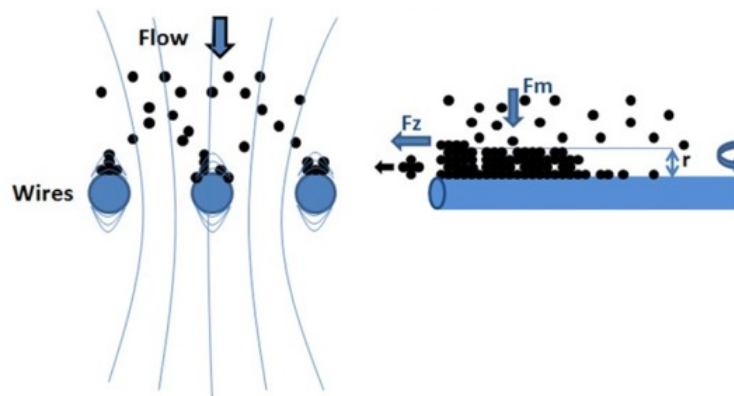


Figure 5-1 left: schematic presentation of the separation of particles to wires in the magnetic field; right: cleaning of particle deposit by centrifugation separates particles from the wire [Lindner'13]

5.1 State of the Art

Centrifugation and HGMS are both well developed. A hybrid method is new though.

5.1.1 Centrifuge Variants

There is a large number of different centrifuge types common in industry and research, an overview is given by Stahl [Stahl'04]. In lab centrifuges a container is placed in a centrifuge on a lever and is centrifugated directly. Industrial centrifuges are separated in weir and filter centrifuges. Centrifuges spinning at high speeds are called ultracentrifuges. Table 5-1 gives an overview over a few important variants.

Table 5-1: Centrifuge variants; B: batch-wise; C: continuous

Name	Description
Weir centrifuges	
Bowl centrifuge (B)	Rotating bowl, with no further mechanics, which either collects the liquid or features an overflow weir while the denser phase is collected
Decanter centrifuge (C)	Completely continuous centrifuge which features a weir for the liquid discharge and a screw to push the solid by a cone over a second weir of lower diameter
Disc separator (C)	Centrifuge design comprising valves at the outside which are opened at discrete times to discharge solid collected at the valves; discs increase the settling surface

Filter centrifuges

Peeler centrifuge (B)	Batch-wise centrifuge type collecting solids inside and containing a peeler knife for discharge
Inverting filter centrifuge (B)	Centrifuge which discharges by inverting the filter cloth and centrifugating the filter cake off
Pusher centrifuge (C)	Centrifuges which creates a cake on a filter and discharges the cake by pushing it over an edge

A sophisticated and important type are the decanter centrifuges. The residence time t_0 depends on the decanter length L_C , the rotational velocity of the screw relative to the wall Δn_r , the pitch L_{lead} and a reducing factor α_d . The transport velocity is hence

$$\frac{L_C}{t_0} = \alpha_d L_{lead} \Delta n_r . \quad (5-1)$$

5.1.2 Flow Simulation in High Gradient Magnetic Separation

Several researchers already simulated flow around the wire filter in HGMS. Okada et al. used CFD simulation to determine the separation efficiency of different wire arrangements [Okada'05]. Hournkumnuard et al. used a Finite Difference Method for the simulation of particle deposition [Hournkumnuard'11], Li et al. simulated elliptic wire shapes and their influence [Li'07]. While analytical approaches were limited to elliptic geometries, FEM allows the simulation of any shape. Hayashi et al. used this method for the simulation of particle trajectories in their specific setup [Hayashi'10].

5.1.3 Flow Simulation in Centrifugation

Diverse work was performed on the simulation of fluid flow in centrifugation, e.g. [Boychyn'01; Jain'05; Romaní Fernández'09; Spelter'10; Symons'11].

5.1.4 Permanent Magnet Arrangements

In HGMS electromagnets are wide-spread. This allows an easy control and fast switching, but requires a significant amount of electricity in long-term use. Superconducting magnets are too expensive for HGMS, and do not provide a major advantage because the magnetization is limited by saturation. Permanent magnets are possible as well [Ebner'07] but usually only allow a rectangular filter cell and a transversal magnetic field, which cannot be used for MEC. Halbach magnet arrangements are interesting in HGMS [Menzel'13], but cannot be used in MEC for the transversal field either. Hugon set up a small permanent magnet arrangement for NMR, which had only a small usable volume and a relatively weak magnetic field, but created an almost homogeneous field in longitudinal direction [Hugon'10]. The design was based on a patent of Aubert [Aubert'93].

5.1.5 Competing Technologies in High Gradient Magnetic Separation

Open Gradient Magnetic Separation (OGMS) devices are not the first choice for the separation of μm -sized particles out of fluids. They are based on an external magnet, which is moved close to a separation cell. Particles are collected at the wall. High Gradient Magnetic Separation (HGMS) was invented in 1937 by Frantz [Svoboda'04]. It adds a magnetizable filter into a cell, which is magnetized by the external magnet. On the surface of the filter high magnetic field gradients appear, resulting in strong forces. This presents a major improvement over OGMS, because the forces are usually several orders of magnitude larger, which allows the separation of smaller particles. The principle has however always been batch-wise, as the magnetic field needs to be removed to flush particles out of the wire filter. A continuous transport is not possible as long as the magnetic field is applied. An exception is a quasi-continuous device set up by Franzreb [Franzreb'01]. There are several different approaches for the use of HGMS.

Permanent Magnet based HGMS

The most basic HGMS device consists of a rectangular chamber filled with steel wool or matrices, inserted in a permanent magnet [Ebner'07]. A lowly inclined inlet and outlet zone avoids swirling from the inlet hose. The device is cost-efficient in investment and operation, light-weight and robust. The specific magnet has field strengths of 0.4 T. It is sealed and efficient for many purposes. The field is applied or removed by moving the permanent magnet to or away from the chamber. The design is cheap, robust and reliable. However flushing back is non-trivial, depending on the gap size between wires. Its main disadvantage is the difficult behavior in flushing back. For this reason many different devices are based on a circular magnetic field. Figure 5-2 shows a photograph of the matrix (left) and the magnet with the filter cell (right).

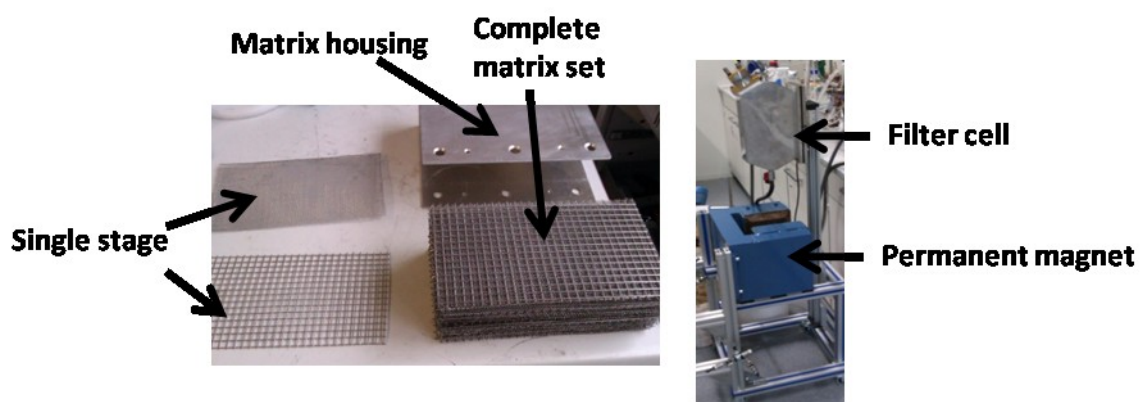


Figure 5-2 left: photograph of the wire structure implemented in a permanent magnet based HGMS; right: photograph of the filter cell on top and blue permanent magnet at the bottom

Rotor-Stator HGMS

A rotor-stator HGMS is on the market, sold by the company Chemagen. It is based on perforated discs in a round chamber. An electromagnet outside of the chamber creates a magnetic field. The discs create local field gradients close to the bore holes. For back-flushing, the discs rotate creating high shear forces between stationary and rotating discs. The device is hence optimized for flushing back. The version sold for industry is completely automatic.

Halbach Magnet Arrangement based HGMS

A recent development is the use of a Halbach magnet arrangement in combination with a magnet filter cell. While the magnetic field at 0.37 T is lower compared to a classic permanent magnet, it has got the advantage of a circular chamber which is easy to stir and hence to empty. Additionally the magnet can be opened for unmounting. The magnet cost and weight is lower than that of a classic permanent magnet for the lower magnet mass which is necessary. Similarly to a classic permanent magnet, the field is in transversal direction, which needs to be taken into account in the design of the wire filter [Menzel'13]. Figure 5-3 shows the Halbach magnet (left) and the filter cell which can be stirred (right).

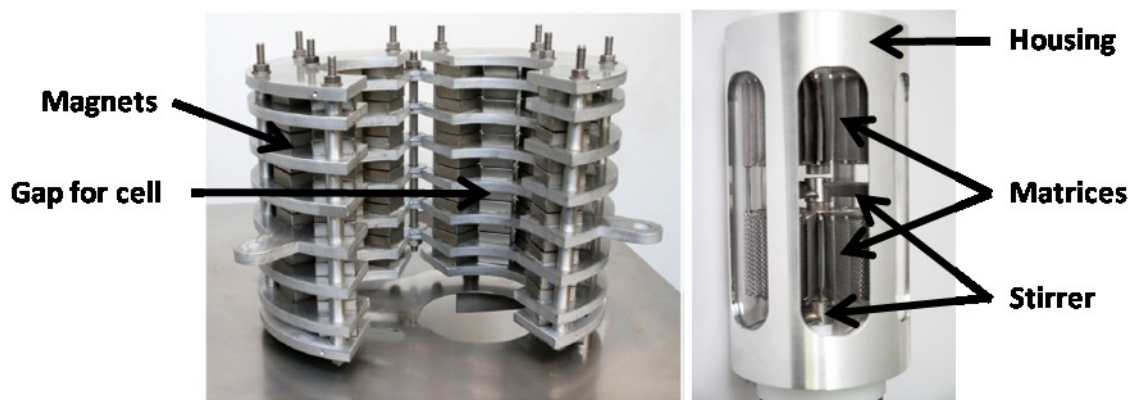


Figure 5-3 left: Halbach magnet arrangement for HGMS [Menzel'13]; right: filter cell implemented in the permanent magnet [source: Menzel, MVM KIT]

HGMS in a Magnetic Carousel

A quasi-continuous HGMS is the magnetic carousel developed by Franzreb [Franzreb'01]. It is built similar to a device known from the mining industry for solid bulk materials but is sealed for the treatment of suspensions. The chambers move in a circle in and out of a magnetic field created by permanent magnets. Three permanent magnets are used in parallel. The chamber is filled with steel wool as magnetic filter. While the chambers are in the magnetic field, the suspension flows through the chambers and magnetic matter is separated to the filter. The chambers are flown through in a counter-current mode. Chambers which moved out of the field are flushed back. The sealing was realized by a Teflon cover flushed

over by the suspension, similar to a drum filter. The concept seems not to have been followed in industrial application. Figure 5-4 shows a photograph of the machine (left) and a technical drawing of the filter cells (right).

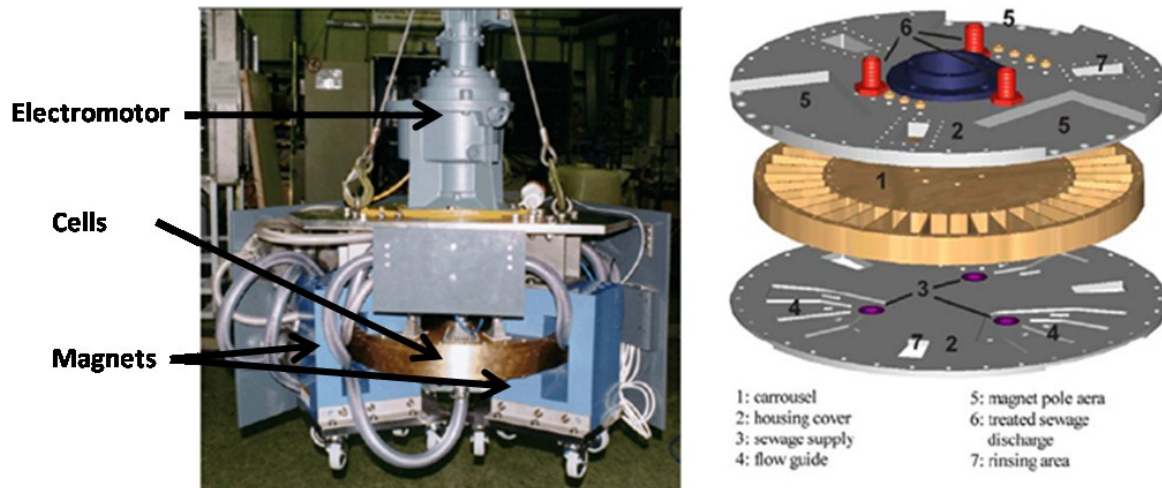


Figure 5-4 left: photograph of the magnetic carousel; right: scheme of the carousel filter cell parts [Franzreb'01]

Magnetically Enhanced Filtration

A non-HGMS approach is magnetically enhanced cake filtration. In cake filtration, the solids are kept on a filter cloth while liquid is separated through the filter. A permanent magnet creates a magnetic field perpendicular to the filter cloth. Magnetic forces influence the structuring of the cake, leading to higher porosity and hence lower filtration times. The magnetic field is not important for separation though. Magnetic forces essentially serve for the structuring of the filter cake, which builds on a classic filter cloth. In the filter cell particles agglomerate in needle shape. Diverse filtration processes were combined with magnetic forces such as press filtration and drum filtration. The process was used as well for the separation of lysocyme on functionalized magnetic particles [Eichholz'10].

5.1.6 Magnetically Enhanced Centrifugation

In 1925 a patent was filed for the classification of matter by opposing magnetic and centrifugal forces [Peck'25]. Different ideas came up later such as a theoretic work of Pitel on the enhancement of the centrifugal force by an additional magnetic force in 1995 [Pitel'95]. The basic idea of combining a centrifuge with magnetic wires was filed for patent by Fuchs in US in 2006 (patent nr. 8075771). Stolarski investigated the influence of different parameters such as the magnetic field strength or the circumferential velocity on the deposit height and the separation. After testing a star-shaped rotor, a lab machine of 0.16 l volume implementing magnetic wires in a centrifuge was developed and investigated by Stolarski [Stolarski'08; Stolarski'11]. The device set up by Stolarski did not allow being discharged other than

manually and had a small length (about 20 mm) and cross section (50 mm diameter) of the magnetic filter. The same machine was used for preliminary tests in this work to prepare the new centrifuge versions. It consisted of an electromagnet produced by Steinert and a custom made centrifuge which allowed implementing a star-shaped magnetic wire filter in its center. The wire filter was welded, and the wires had a cylindrical cross section. Stolarski showed that an increase of volume flow reduces the separation efficiency. An increase of the magnetic flux density increases the separation efficiency. An increase of the centrifugal force showed to reduce the cake height. An increase in the number of wire stages improves the separation efficiency. A differential force of the wire matrix to the centrifuge did not show to be necessary for the discharge of the wire filter. Stolarski showed that, compared to conventional centrifugation, the separation is enhanced by a magnetic field, and implementing a wire matrix enhanced separation further. He showed as well that the deposit height on a magnetic wire depends on the magnetic field and on the circumferential velocity, see Figure 5-5 [Stolarski'08; Stolarski'11].

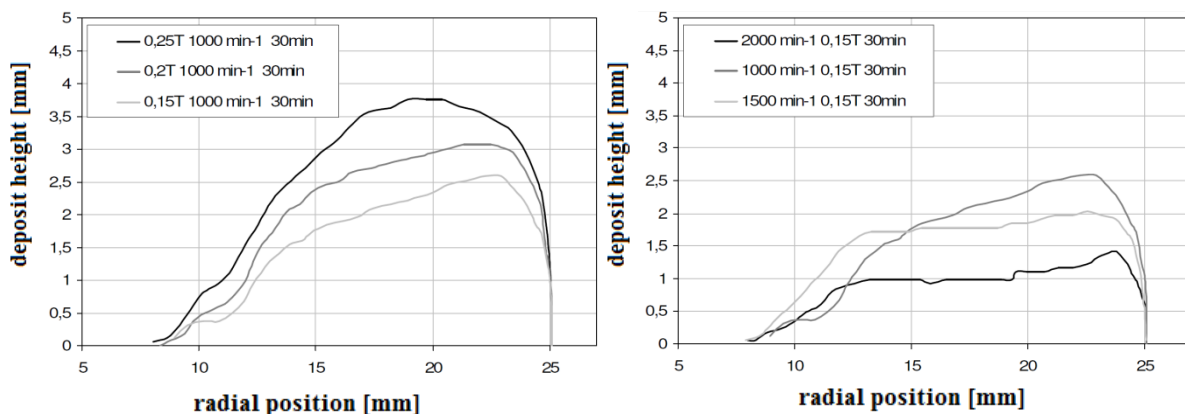


Figure 5-5 left: Stolarski showed that the deposit height depends on the radial position and the magnetic field strength at constant centrifugal force; right: deposition height depends at constant field strength on the rotational velocity [Stolarski'11]

5.2 Targets

The current chapter treats the design and investigation of MEC. The target of the work was to investigate parameters and provide methods to render the principle of MEC possible for industrial use in a large scale.

1. One target is the experimental investigation as well as the simulation of flow around wires of different design. The separation efficiency can be improved by a smart filter development. Especially in MEC the height of the deposition of magnetic particles is strongly dependent on process parameters. The wire filter needs to be created in a way to allow the discharge of the wire filter. Additionally easy manufacturing of the wire filter is important.

2. The investigation of centrifuge parameters is important to optimize the device for industrial use in separation and discharge.
3. The investigation of a method for batch-wise automatic centrifuge discharge and the set up of a MEC is necessary to test the principle on bioseparation.
4. The investigation of particle transport out of the magnetic field is necessary for the discharge in a continuous MEC. The setup of a continuous MEC is an important step for the implementation of the principle in the industry.
5. The design, simulation and set up of a permanent magnet which permits use in MEC is a further important step for the process to be realized in the industry.

The current chapter is hence the core of the work, covering the machine design and investigation for industrial use.

5.3 Methods for Experimental Separation and Analysis

Table 8-4 in the annex gives an overview over parameters and devices which were used for the experimental measurement.

5.3.1 Separation Methods

In each centrifuge test, particles were stirred in a feed tank in desalinated water. Technically, demineralized water is less suited for separation due to a low amount of ions, which stabilizes the suspension. Buffered water or tap water (pH 6.6 at the institute) is better suited for separation and a more predictable particle behavior.

The centrifuge was prefilled with water. Then the suspension was fed into the system at a defined flow rate using a peristaltic pump. A slight change in the particle and media conditions leads to completely different behavior, hence measurements were grouped and similar measurements shown in the same diagram were performed close after each other. Tests were done using Merck MagPrep 100 particles and Evonik research particles of two different types. Chapter 3 summarizes particle data. Tests on particles of lower magnetization than available were performed to have a significant amount of particles unseparated and to be able to measure significant concentrations. Several different batches allowed to test particles with different properties like e.g. high and low magnetization, to perform tests in a different range of separation.

5.3.2 Concentration Determination

From the effluent of the centrifuge, one or three samples were taken at a data point. The separation efficiency E is defined as the amount of particles which was not separated by the

device, i.e. which left the centrifuge. It is calculated out of the effluent volume $V_{Effluent}$ and concentration $c_{Effluent}$, and the feed volume V_{Feed} and concentration c_{Feed} by

$$E = 1 - \frac{V_{Centrate}c_{Centrate}}{V_{Feed}c_{Feed}}. \quad (5-2)$$

In this case the $V_{Effluent}$ is equal to V_{Feed} , simplifying the equation.

Different methods to determine the concentration in the effluent were used. Gravimetry was used in most cases for being reliable and possible over a wide range of concentration. It is laborious though. Turbidity was used specifically for small concentrations, as it showed to be sensitive in this area. It depends on the particle size and on the agglomeration of the suspension, hence regular calibration curves need to be done.

Besides a magnetic reader from the company FZMB with probe 14 06/5/LS was tested. It measures directly magnetized mass in the filter cell, but seems to need superparamagnetic particles. As this is not the case for most of the particle systems, it did not show to be an alternative to gravimetry and turbidity.

Gravimetry

Gravimetry was mostly used in this study. While it is offline and labor-intensive, it is reliable, exact and reproducible. The balance Sartorius LE225D-OCE was used which measures down to 0.01 mg for samples up to 100 g. A concentration range down to 0.01 g/l can be determined at a standard deviation of 0.003 at samples of 30 ml water. It depends slightly on environmental influence like temperature and humidity.

Sample jars were weighed before the tests. During the experiments samples were taken from 3 - 50 ml size. The samples were weighed containing the liquid, subsequently they were dried over night at 40 – 80°C and weighed again. The concentration is then determined from the dried mass and from the mass of the suspension.

Turbidity

A turbidimeter 2100P from Hach was used to determine low concentrations. It determines the transmission of light through a sample. The arbitrary NTU is linked by a calibration curve to the concentration. Concentrations as low as 0.01 g/l can be determined. A disadvantage is the fact that the light absorption depends on the particle size. In case the particle state changes due to e.g. agglomeration, which is common on magnetic particles, or the separation of a large fraction, the calibration curves need to be redone. Additionally the turbidity is limited to low concentrations. The advantage is that it is fast and has a lower concentration limit compared to gravimetry.

5.4 Wire Filter Optimization

The wire filter is the key for the optimization of separation, but it needs to be created in a way allowing its discharge. The two requirements are opposing: while a fine filter creates high gradients and hence enhances the separation of small particles, the formation of bridges between wires in field direction reduces the discharge of particles from the wires. The same restriction applies to conventional HGMS, where a fine wire filter is difficult to flush back although the magnetic field is removed for discharge. To minimize magnetic forces in radial direction, wires were created in star-shape.

5.4.1 Materials for Wire Filters

For the investigation of the wire filter design, the lab scale centrifuge set up and investigated by Stolarski was used for tests. Several wire matrices were produced by laser cutting out of stainless steel (material number 1.4016). While most stainless steels are only weakly magnetizable and suited for other parts of a MEC (1.4301, 1.4404) due to austenitic crystals, the steel 1.4016 (X6Cr17, 6% carbon, 17 % chrome) is ferritic and highly magnetizable. Laser cutting is cheap, accurate and provides a high degree of freedom for the design of filters. The diameter is 50 mm, the wire cross section is 1 mm x 1 mm for most wire sets. One set of wires was produced with a variable diameter from 20 to 50 mm, another set was produced in a different cross section, with a round welded geometry and sizes of 2 mm x 1 mm, 1 mm x 2 mm. The saturation magnetization of the material is 168.44 Am²/kg or 1.32*10⁶ A/m. The wire roughness ranged from 20 nm to 200 nm depending on the sample used. On a wire of $d/L = 0.003$, saturation was reached at a field strength of 25 kA/m.

The used wire filter has a high influence on the separation and backflushing capabilities of the overall device. Fine wires provide a high separation efficiency. A disadvantage of fine wires is the fact that cleaning of the device is difficult. In classic HGMS devices the magnetic field is removed before the filter chamber is backflushed or opened for manual cleaning. In case of fine wires the filter itself needs to be taken apart, which is usually not possible in an automatic approach.

5.4.2 Methods for the Simulation of the Fluid Flow around Magnetic Wires

FEM and CFD was coupled to simulate the particle tracks in a wire filter. Different wire cross sections were simulated, the cross section area was constant at 1 mm² to get comparable results.

Finite Element Modeling of the magnetic field

The simulation method is similar to the procedure described in Chapter 4.3.1. In the investigation of the wire shape influence, a wire permeability of 4.2 at a background field of

400 kA/m (0.5 T) was applied, resulting in the saturation magnetization of the steel of 1.67 MA/m.

Computational Fluid Dynamics

A study was performed on the fluid flow around magnetic wires, which was used for the optimization of the magnetic wire shape in combination with the FEM simulation of the magnetic field. The study was done completely in 2D, as the length of a magnetic wire is large enough to be neglected. Laminar flow dominates in this case, as the Reynolds numbers are around one for the viscosity of water ($10^{-6} \text{ m}^2/\text{s}$), flow velocity around 1 mm/s (which is common in HGMS) and wires of 1 mm diameter. The field gradient of the closest FEM node was read into a User Defined Memory (UDM) of each cell of the CFD simulation in a User Defined Library (UDL). An interpolation was not done as the gain is small in a fine grid. The import procedure was slow, depending on the grid size. Both CFD and FEM grids were refined close to the wire. From the field gradient the local force on a particle can be calculated based on (2-24). The same model was used for the combination with DEM simulation.

5.4.3 Influence of the Cross Section of a Single Wire

The wire influences separation strongly. The attracting force of a single wire depends essentially on

- the intrinsic susceptibility of the material,
- the mass of the wire,
- the demagnetization of the cross section and the
- the local shape of the magnetic field.

The magnetic properties of the material 1.4016 are good with few room for improvement. The mass of the wire cannot be increased as the space in the filter cell is limited. Additionally fine wires create higher gradients while reducing capturing reach, which leads to an improvement at a high number of fine wires. Further improvement depends especially on the demagnetization and the local field shape.

Simulation of the Particle Tracks

The demagnetization of the cross section is influenced mainly by its extension in field direction, see Figure 2-1. This results in a stronger attraction of a longish wire, increasing its separation. The main interest is in rectangular wires, which are implemented in the process and cannot be calculated analytically. To quantify the length influence in HGMS, a simulation was performed by FEM of the magnetic field of a wire. The magnetic field gradient was read into Fluent. The fluid flow around a wire was simulated. Then the tracks of magnetic particles

were calculating out of the fluid drag force and the magnetic force of the wire. Figure 5-6 shows exemplarily the simulation of the magnetic field strength with the external field in the horizontal direction (left), the fluid flow around a wire (middle) and the resulting particle tracks (right). The advantage of the method is the fact any geometry can be investigated, which is not the case in an analytic approach.

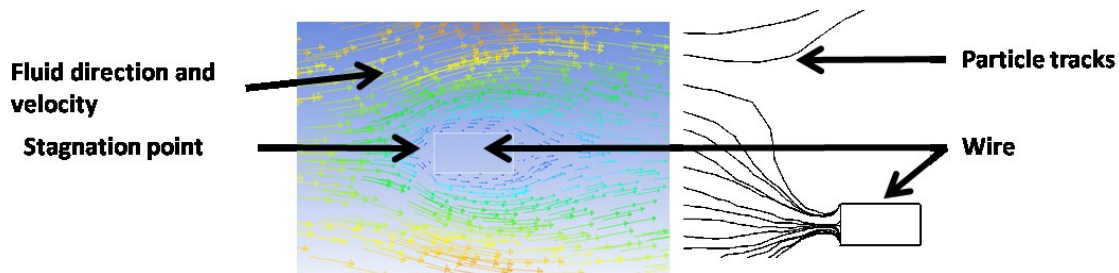


Figure 5-6 left: CFD simulation of horizontal flow around the wire; right: particle tracks resulting from the combination of FEM and CFD in a Euler-Lagrange simulation

The result was normed on the flow around one single cylinder to give a statement independent of the properties like magnetization in the simulation. In case of a cylinder, on which the simulation is normed, the demagnetization is about 0.50 (determined by FEM simulation). Figure 5-7 shows different values for the capturing radius of cylindrical and rectangular wires of different length but of the same area of the cross section.

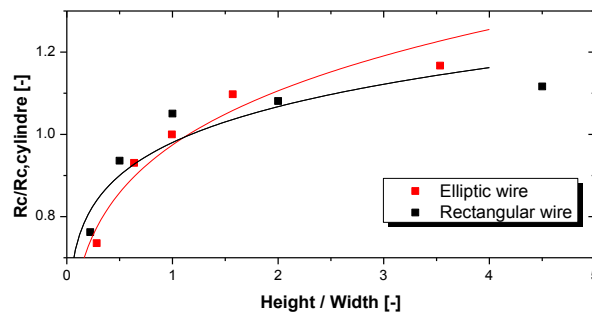


Figure 5-7 left: Capturing radius of different wire shapes normalized to the cylindrical wire's capture radius versus the relation height/width at constant cross section area shows an increase for wires longish in field direction [Lindner'13]

The equations were approximated by the function

$$\frac{R_c}{R_{c,cylinder}} = f * \left(\frac{h}{w}\right)^g, \quad (5-3)$$

which approximates the results sufficiently well.

Table 5-2 shows the parameters suggested for (5-3) for elliptic and rectangular geometries in the current case (i.e. with wires not being in saturation). The equation does not fit perfectly

with the simulated values and overestimates at high relations h/w , but the approximation is still substantially better than not taking the influence into account at all. The capturing radius of a rectangular wire can hence be calculated by calculating the radius of a cylinder of the same cross section by the formula (2-45) and correcting it with formula (5-3). An analytical approximation is the correction by the demagnetization factor $N_{wire} / N_{cylinder}$. A value of $h/w = 2/1$ shows to reduce the demagnetization significantly while keeping the space requirement low.

Table 5-2: Values for f and g [Lindner'13]

	f	g
Ellipse	0.9742	0.1828
Rectangle	0.9802	0.1229

Experimental Investigation

An experimental validation was performed by creating wires of different shape and testing them in the device. The production by laser cutting showed to be easily possible. Wires of 1 mm x 2 mm, 2 mm x w1 mm, 1 mm diameter and 1 mm x 1 mm were created. Note that the cross section area is not constant, hence the wires with 2 mm² cross section are compared with each other and the cylindrical with the quadratic design. Figure 5-8 shows that the simulation result is validated qualitatively by the comparison of wires with 2 mm² cross section. The best separation is delivered by magnetic wires aligned in field direction. A quadratic cross section delivers a high separation compared to a round geometry.

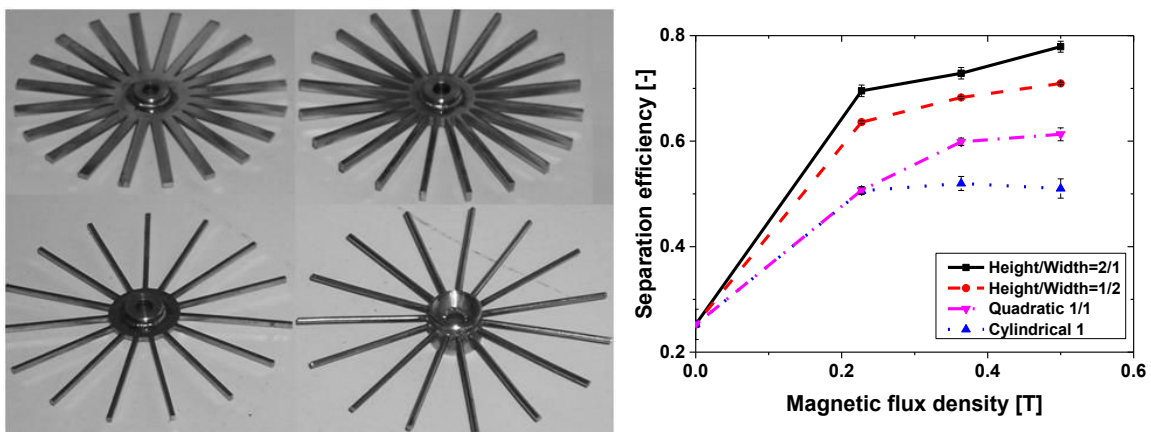


Figure 5-8 left: photograph of different wire geometries produced and tested, 1x2 mm / 2x1 mm; 1x1 mm; 1 mm diameter; right: separation efficiency in MEC of the different wire shapes shows an enhancement for longish geometries [Lindner'10]

Additionally the field shape is different. A cylindrical and a quadratic shape are close in mass and demagnetization, but showed in the experiment a significant difference. The reason are presumably local field gradients. Figure 5-9 hence shows the radial field component normed

by the magnetic field, which results in attractive (blue) and repulsive (red) regions. On a quadratic shape, high gradients appear specifically at the edges, which might additionally increase capturing efficiency. These gradients reduce discharge of the wires though, which is visible in Figure 5-27.

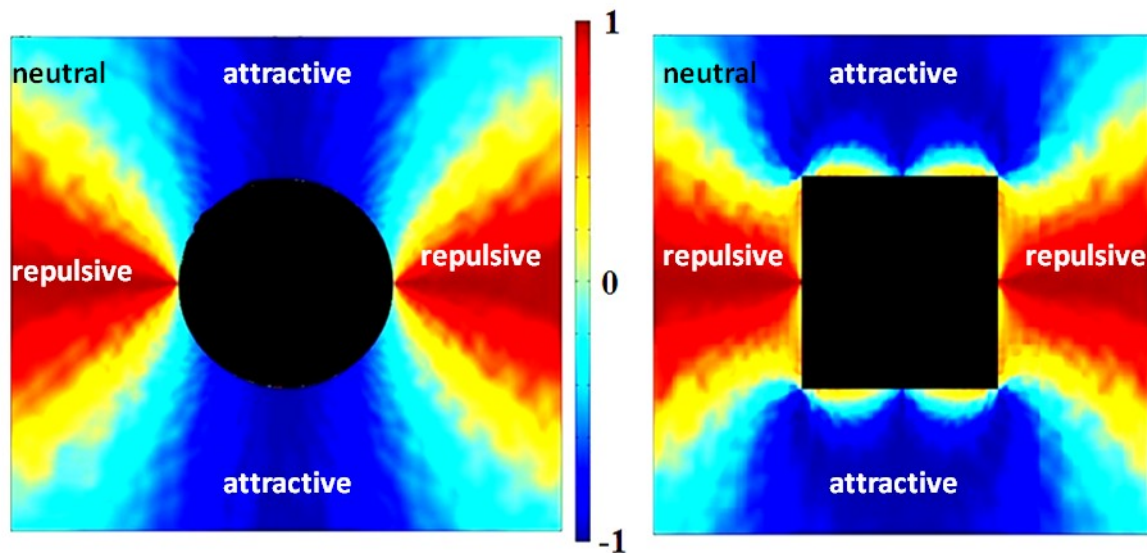


Figure 5-9: the radial field component per normalized field force $F_r/|F|$ for a cylindrical (left) and rectangular (right) wire shape shows a slightly larger angle for the attraction [Lindner'13]

5.4.4 Matrix Stage Diameter

The matrix diameter shows an influence which is less expressed compared to the wire number, but not negligible. Figure 5-10 shows an experimental investigation from matrices of different diameters, covering the range from 25 – 50 mm. There is a significant influence. The influence seems to be limited due to the fact that even wires with small diameter cover most of the flow layer, while long wires only extend into the stagnant sublayer which moves slowly. An analytical approach to calculating the thickness of the flow layer is given by (2-85), which results in this case in a flow layer thickness of 1 mm at a weir diameter of 10 mm radius.

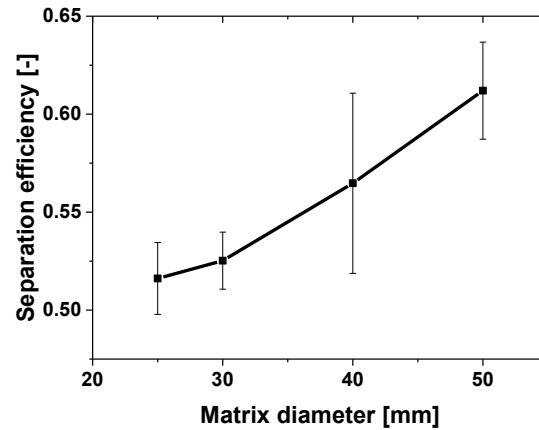


Figure 5-10: the separation efficiency increases slightly for an increased matrix diameter from 25 to 50 mm

5.4.5 Influence of the Numbers of Wires

The overall number of wires is the most important design influence of a wire filter. It can be used to characterize a HGMS device. A different numbers of wires was tested not only in the respect of the separation efficiency, but as well for particle discharge. Figure 5-11 left shows the influence of the number of wires in one stage. Their diameter is 50 mm, and the cross section is quadratic. The increase to the first 20 wires showed to be highest, while a further increase up to 50 wires increased the separation only slightly. A variation of the number of wire stages is shown in Figure 5-11 right. It showed to have a high influence, which was as well reported by Stolarski [Stolarski'11].

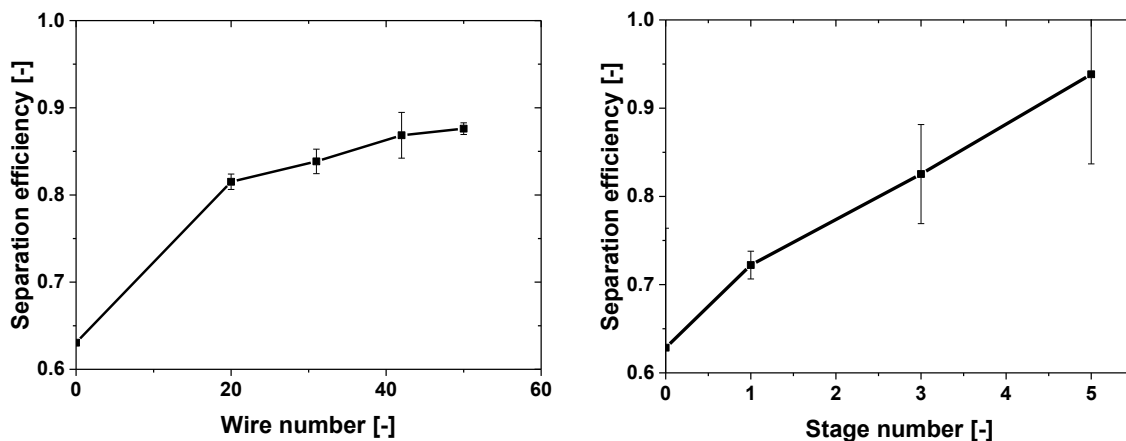


Figure 5-11 left: the separation is enhanced slightly by a larger number of wires at one stage [Lindner'10]; right: an increase in the number of wire stages leads to a strong increase in the separation efficiency

In summary this means that the number of wires needs to be high for efficient separation, which was already known from classic HGMS. Besides enhancing separation, a filter geometry needs to avoid the building of bridges to facilitate discharge by centrifugal forces.

A wire filter which is too dense does not allow being flushed back but risks complete plugging, contradicting the application of many wires in the cell. Implementing fine wires which create high gradients at the cost of capturing radius is hence not wise. In this test the particle kind Evonik 18-04 was used at a concentration of 2 g/l, a centrifuge rotational velocity of 2500 rpm (175 times earth gravitation) and a volume flow of 50 l/h. This results in about 10 g of particles which were collected in the centrifuge. Figure 5-12 shows an unplugged wire filter with particles collected at the wall (left, middle), and a dense, completely plugged cake. Particles form a stable cake, which contradicts the aim of continuous discharge.



Figure 5-12 left: particle cake at a low particle amount from the top; middle: particle cake at low particle amount from the side; right: completely plugged filter at high particle amount

The particle cake which forms gets dense and plugs completely. This does not reduce the separation efficiency, which stays at a constant, very homogeneous level even for a completely covered cross section until the cell is completely filled. This behavior is as well known from conventional HGMS cells. Separation over time is shown in Figure 5-13.

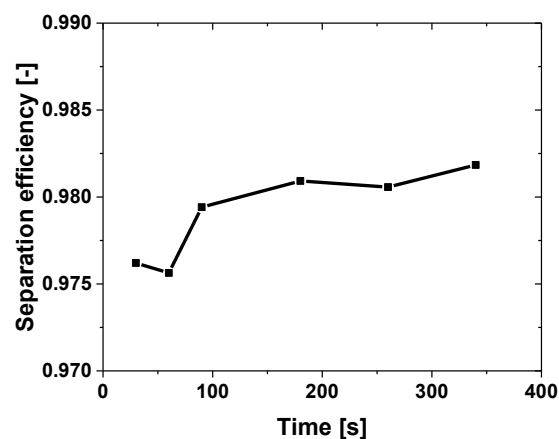


Figure 5-13: separation efficiency is unchanged up to a high load and complete plugging shown in Figure 5-12 right

More important is the capability of cake to be discharged from the wires. Hence an optimum wire distance is chosen which is above the maximum cake height at the target rotational velocity. As a maximum cake height of 4 mm at 63 times earth gravitation was determined, a

wire distance of 8 mm was chosen for the wire filters used in the newly developed centrifuges. This is in line with the data provided by Stolarski in Figure 5-5 [Stolarski'11].

5.4.6 Wire Arrangement

Three specific wire arrangements of cylindric wires were investigated theoretically by Chen [Chen'09], comprising wires arranged in a row and the displacement of every second wire stage. Additionally a variation of the latter was simulated. Different arrangements and magnetic particle motion around wires were calculated by combining simulation of the magnetic field and of the fluid flow. The magnetic field was calculated in Comsol and read as vector field in Fluent. An analytic calculation is not possible, as the wires influence each other and as rectangular wire shapes are investigated. An alternative possibility would have been the calculation of both magnetic field and fluid flow in Comsol. Particle traces were simulated by an Euler-Lagrange approach. Figure 5-14 shows the simulation result. While the worst arrangement is placing a wire in the slipstream of another wire (Figure 5-14 top left), displacing wires in between wires upstream seems sensible (Figure 5-14 top right), which is in line with Chen's results. An optimum arrangement seems to be the placement of wires in the gaps of previous stages (Figure 5-14 bottom left and right). Experimentally tests on displaced arrangements were performed but did not deliver a significant change in the separation. A reason might be that fluid in a centrifuge does not move perfectly accelerated, leading to an angular flow direction. Hence in further tests no specific wire placement was realized.

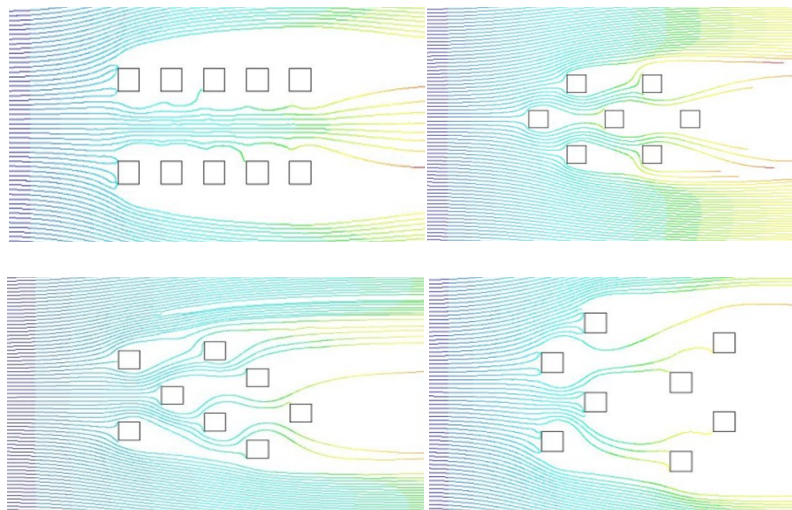


Figure 5-14: the arrangements of rectangular wires in a coupled FEM and CFD simulation delivers particle tracks for different wire arrangements; top left: wire stages in the slipstream of each other does not provide an enhanced separation; top right: wire stages aligned in two different rows increase separation; bottom left and right: slight displacement of wire stages in different schemes aleatory seem to provide the best results; this does not deliver information on the flow in MEC and could not be validated experimentally for the influence of the Coriolis force

5.5 Computational Fluid Dynamics in Centrifugation

The large-scale MEC was optimized by CFD to avoid turbulence in the magnet chamber. As mentioned in Chapter 3.7, turbulence is negative to magnetic separation, which in a bad design reduces the separation of a MEC compared to HGMS. The Coriolis force influences the magnet chamber as well at the inlet as at the outlet. A simulation for the improvement of the accelerating geometry is hence necessary. The centrifuge treated in this chapter is the industry scale device set up in cooperation with Andritz KMPT.

5.5.1 Methods for the Simulation of the Large-Scale Centrifuge

The theory of CFD was presented in Chapter 2.6. Only a small segment of 22.5° was simulated to reduce the computational effort. The segment faces were connected by an axis symmetric periodic condition to simulate the whole centrifuge. A structured grid of 3.7 Mio. cells was set up in the software Gambit, which then was refined in the simulation to 4.3 Mio. cells on places with bad turbulence approximation. The turbulence parameter Y^+ was kept below three. Cells width to length of 1:6 to 1:8 was set as limit. The segments were arranged in a way to implement the inlet and outlet baffles at the segment surface. The simulation was performed on a desktop computer of 64 bit and 8 GB RAM on four cores in parallel. The inlet velocity was set to 0.24 m/s ($1 \text{ m}^3/\text{h}$), at the outlet a ambient constant pressure of 1 bar was assigned. The medium calculated was water (1 mPas). The turbulence model $k-\omega$ SST with fine boundary layers of mostly 20 wires was used, as it provides a good approximation of flow close to a wall and in the freestream, which is expected to be necessary in a centrifuge. The boundary was simulated directly instead of modeling the whole flow at the wall by a turbulence model, as the differential velocity in a centrifuge is low. The boundary condition for the walls did not allow slip. The centrifuge was simulated without wire filter, because the simulation of the flow around wires requires a very fine grid; a simulation of the complete centrifuge including wires is hence not possible. The rotational velocity in the simulation is 1500 rpm.

5.5.2 Results and Improvements

Three different simulations were performed. Initially the centrifuge was simulated while baffles were omitted. When insufficient acceleration of the fluid became apparent, baffles at the inlet were introduced. This simulation was validated with an experiment conducted at Andritz KMPT in Vierkirchen. As a further improvement, baffles at inlet and outlet were modeled in a third simulation.

Simulation without Preacceleration

The first simulation was done on an initial design of the centrifuge which did not feature baffles at the inlet. Besides bad acceleration of the fluid, the simulation did not converge well.

As a result the velocities in the centrifuge are oscillating. There is insufficient acceleration in the fluid over the complete length of the centrifuge. A highly inhomogeneous fluid velocity in both tangential and axial direction results from the simulation. This seems pseudo-turbulent in a simulation which bases on not resolving turbulence, so the simulation result does not approximate reality sufficiently. Basically a high differential velocity seems reasonable though. Figure 5-15 shows the relative tangential flow at two axial positions (left) (bottom left) as well as the axial flow at the same axial positions (right).

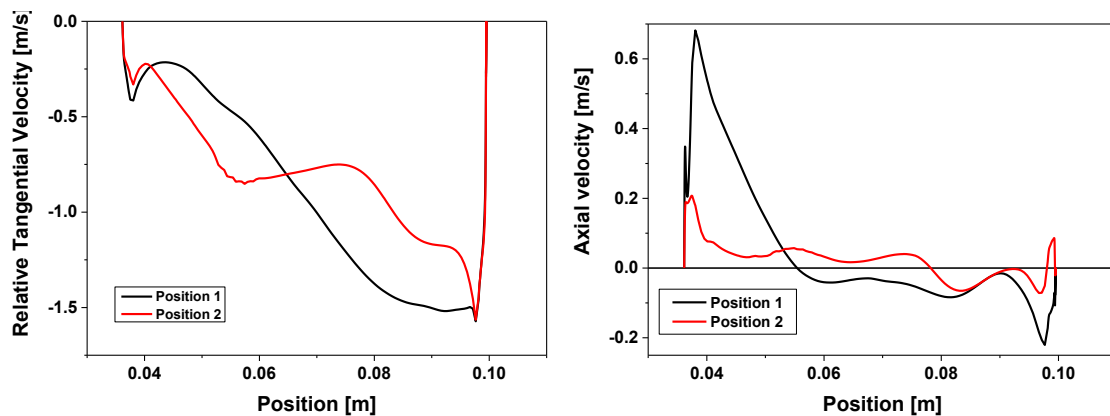


Figure 5-15 left: the tangential velocity in the centrifuge reference frame without preacceleration shows high variation in the numerical values and in the color plot; right: the axial velocity in a centrifuge varies as well strongly in numerical values and color plot

Simulation Including Preacceleration Baffles

Additional baffles for the acceleration of the fluid were implemented in the simulation all over the distribution zone of the machine at the inlet, and showed to influence the flow regime significantly. The result seems as well coherent with the simulation of the axial flow. The validation of the axial flow velocity is shown in the next section. The fluid is now well accelerated, the flow profile is homogeneous, except for the flow close to the outlet. The reason is an insufficient deceleration of the fluid when moving radially inwards to the overflow weir at the centrifuge center. The Coriolis force accelerates the fluid which moves radially inwards in the reference frame of the centrifuge, resulting in a swirl close to the outlet. The swirling influences as well the fluid upstream in the centrifuge. It has as well an influence on the axial flow profile, as it creates a faster flow at the centrifuge inside. A further improvement of the centrifuge contains hence as well deceleration baffles. Figure 5-16 shows relative tangential and axial velocities.

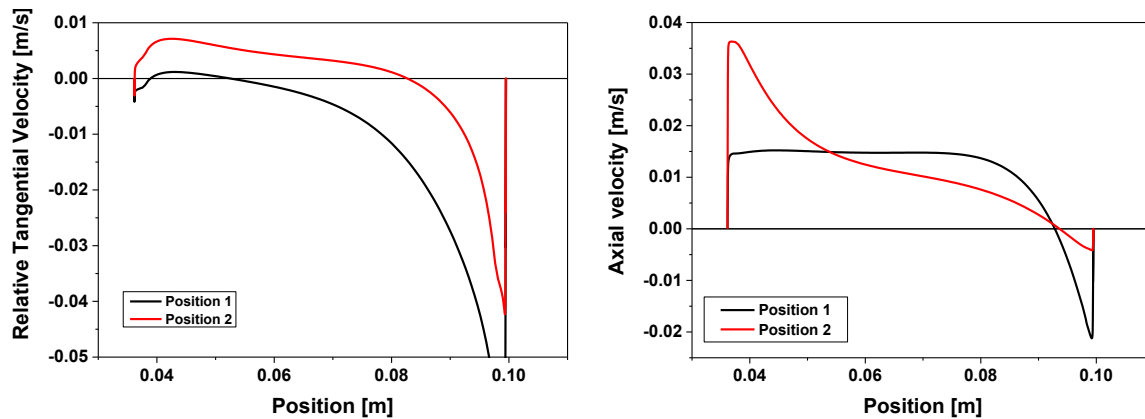


Figure 5-16 left: the flow in centrifuge reference frame with preacceleration delivers an almost perfect except close to the wall in numerical values, the color plot reveals flow ahead of the centrifuge close to the outlet; right: the axial flow is close to homogeneous as well with a faster flow in the center (where the weir is situated) and slower flow at the wall; the simulation seems to be better converging compared to the previous simulation and was validated experimentally as shown in Figure 5-18

Simulation Including Pre- and Postacceleration Baffles

Additional deceleration baffles at the outlet were implemented in a simulation to reduce the tangential swirl at the outlet, and to realize a more homogeneous axial velocity of the centrifuge. The tangential and axial velocities are in this case very homogeneous. The flow layer covers the whole width of the centrifuge, reducing the influence of the Coriolis force strongly. This centrifuge design was finally implemented in Chapter 6.5. By adding the wire matrix, fluid flow is additionally homogenized. Figure 5-17 shows that the tangential and axial velocity is significantly more homogeneous compared to Figure 5-15 and Figure 5-16.

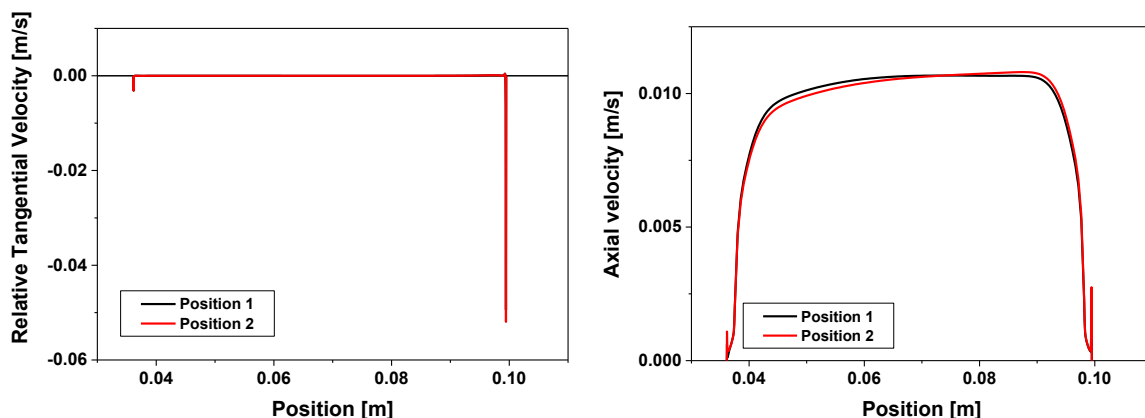


Figure 5-17 left: relative tangential flow in a centrifuge with baffles at the in- and outlet seems to be close to perfect; right: the axial flow profile shows to be homogeneous and close to uniform

5.5.3 Experiments and Validation

The second simulation of the centrifuge, implementing only baffles at the inlet, could be validated by tests on the finally produced centrifuge. The change from water to process

medium (soy whey) was filmed at a sightglass implemented at the top (outlet) of the centrifuge. Note that additionally a wire matrix is implemented in the centrifuge.

Simulation and experiment show both stratified flow first breaking through in the centrifuge center, where the outlet is situated, with slower flow at the outside of the centrifuge. The axial flow in Figure 5-16 right was compared with the film of the experiment of the centrifuge, shown in Figure 5-18 at 0 s, 14 s, and 22 s after start of the feeding. After 14 s, the particles are visible in the center of the centrifuge, showing the faster flow at the inlet predicted by the simulation. After 22 s the outer region shows to get black. A consequence is that the Coriolis force shows its influence at the outside. The wires serve for different process purposes and were not implemented in the simulation for the huge amount of boundary layer they require in a simulation.

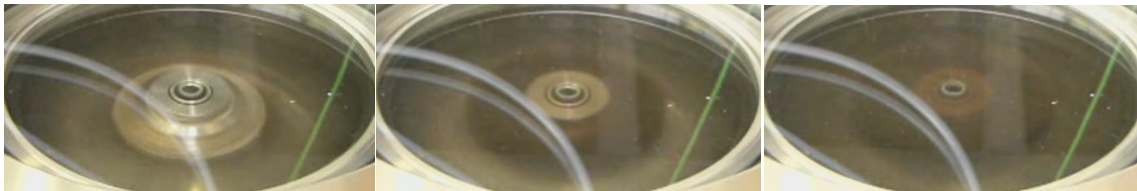


Figure 5-18: Film during a test run while changing feed from pure product to a product suspension containing black particles; 7 s after feeding (left, no change), 14s (middle, product appears in the center), 22s (right, product all over the cross section); first breakthrough is in the middle after 14 s, and the rest of the liquid changes color abruptly after 22 s

Conclusion

The simulation including acceleration delivers the expected result as well for axial flow which showed to be in line with the experiment. The flow with acceleration and deceleration baffles over the entire radius delivered a very homogeneous flow which does not seem to be influenced by the Coriolis force.

To summarize the results, two important elements could be deduced from the simulation.

- It is necessary to implement both acceleration and deceleration components. Acceleration showed to be more important. Simulation was not possible without acceleration baffles but resulted in high velocity gradients, showing that the flow is not sufficiently resolved.
- The inlet area including flights needs to cover the complete radial section of the centrifuge to avoid the Coriolis force influencing the flow when the liquid expands in the radial direction.

Notably, many centrifuges common in industry do usually not provide flights over the whole radius of the outlet zone, i.e. there is a significant potential for improvement.

5.6 Batch-wise Magnetically Enhanced Centrifugation in Pilot Scale

The batch-wise implementation of MEC was necessary to investigate MEC in case that only small particle and media amounts are available. Additionally it allowed to perform washing and elution steps in one single device.

An additional advantage of MEC against HGMS is the fact that the filling of a filter cell is possible from top without prefilling with water. Discontinuous discharge was evaluated as well. Possibilities for the discharge include flushing and the experimentally realized peeler discharge. The principle of magnetic centrifugation is only efficient at continuous transport, though the batch-wise discharge is tested as well. The schematic principle of the batch-wise MEC is shown in Figure 5-19. Outside of the centrifuge the magnet, either permanent or electromagnet, is arranged. It magnetizes the wire filter inside of the machine. The feed containing magnetic and non-magnetic matter enters the centrifuge from the top, with the bigger part being separated on the first couple of wire stages. Non-magnetic matter passes the wire filter unhindered and leaves the centrifuge by the overflow weir at the bottom. Magnetic particles are collected at the centrifuge wall. After stopping the process, magnetic particles are redispersed in liquid by flushing in a cycle and by rotation of the peeler knives attached to the matrix.

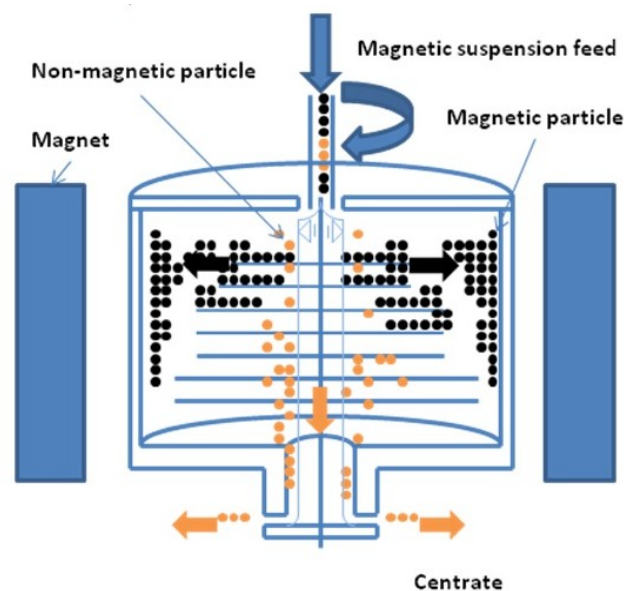


Figure 5-19: schematic principle of a batch-wise MEC shows the storing of particles in the centrifuge [Lindner'13]; after filling the particles are resuspended using the matrix as a stirrer and peeler knives

5.6.1 Materials and Methods

The Device

The batch-wise MEC was set up based on an electromagnet produced by Steinert. Wire matrices were produced by laser cutting in a cross section of 2 mm x 1 mm as deduced in the matrix optimization in Chapter 5.4. The top nine matrix stages had a reduced diameter of 60 mm (2 stages), 70 mm (1 stage) and 85 mm (6 stages). The bottom four matrices have a diameter of 102 mm and are split in two at the end to have a dense matrix set at the outer diameter. The step-wise change in diameter was created to avoid plugging at the inlet and create space for particles. The basket diameter is 105 mm, the length of the zone in the magnetic field is 120 mm. The centrifuge volume is about 1.25 l, out of which 1 l is in the magnetic field. At the outlet at the bottom, where only a small part of particles is separated, a dense wire filter reduces the non-separated particle amount. The inlet geometry consists of four bore holes of 2 mm diameter in radial direction at a diameter of 36 mm. The centrifuge is linked by a belt of ratio 1 to a 2.2 kW electromotor of ABB with a maximum rotational velocity of 2850 rpm. The centrifuge is realized in a cantilever design with two bearings below the process chamber. The motor turning the peeler knives and matrix has a planetary gear head resulting in a maximum torque of 1.75 Nm and a maximum differential velocity of 180 rpm (motor from Faulhaber AG, model 3257G 024CR 38A 25:1). It sits in the centrifuge and is supplied with electricity by a collector ring. The discharge is based on peeler knives, which free the wall from particles and redisperse them. The advantage of the motor implementation inside the centrifuge is that the wire matrix is not moved during separation and that the construction of the centrifuge is cheap relative to the use of a more sophisticated planetary gear. Figure 5-20 shows a picture of the MEC (left) and the wire matrix with peeler knives attached to it (right). Flat jet nozzles were implemented but did not show to be necessary for discharge. The electromagnet was produced by the company Steinert GmbH, it is based on coiled aluminum bands and creates an axial magnetic field of 200 mT flux density at a current of 30 A and 110 V.



Figure 5-20 left: the MEC set up inside the magnet; right: the matrix and peeler knives [Lindner'13]

Methods

Merck MagPrep particles were used for stand time tests and discharge tests, as those particles are easy to separate. Concentration determination needed to be done by turbidity measurement for being more exact at lower concentration. Evonik particles were used for separation tests. Concentration determination was done gravimetrically for being more reliable than different methods.

Particle recovery was done by flushing the centrifuge at 240 l/h in a cycle in three batches at 5 min each with 2.5 l desalinated water, and by simultaneous stirring using the matrix and peeler knives at 120 rpm. Filling the device was done at 600 rpm, before switching the centrifuge off for redispersion.

5.6.2 Influencing Parameters

Several parameters influence the separation of MEC, notably the load, the magnetic field strength, the volume flow and the concentration. The rotational speed showed not to influence the separation at high field strength and is therefore better described in continuous MEC, where it influences the particle transport.

Influence of the Load

The influence of the particle amount is shown in Figure 5-21 based on Merck MagPrep particles. The diagram shows the filling of the centrifuge with 250 g of particles, going to its capacity limit. Particles were reused, which showed to induce preagglomeration. The separation efficiency on this particle kind is high, reaching 99.99% at a concentration of 10

g/l and 80 l/h volume flow. The efficiency drops after filling 200 g of particles, which is hence the capacity limit of the centrifuge.

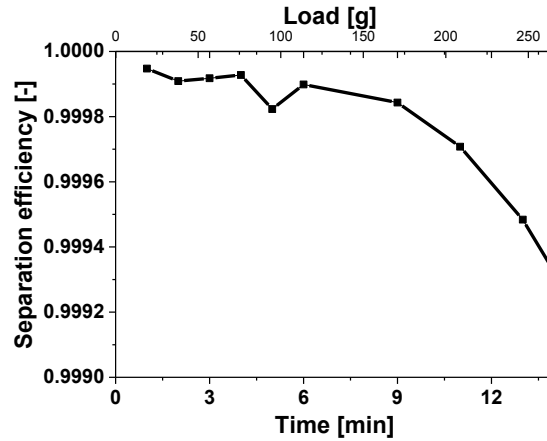


Figure 5-21: the centrifuge can store 200 g of Merck MagPrep particles, with separation dropping slightly above [Lindner'13]

Influence of the Volume Flow

The volume flow is important for separation and seems to influence the separation linearly. Figure 5-22 shows the influence of the volume flow for two different particle kinds. As expected from (2-45), the influence is close to linear. Depending on the particle magnetization, a high separation efficiency is possible at a high volume flow. In this case 150 l/h showed to be possible while the separation was still at a high level of more than 97% for strongly magnetic particles. Separation dropped significantly for particles of low magnetization to below 75%.

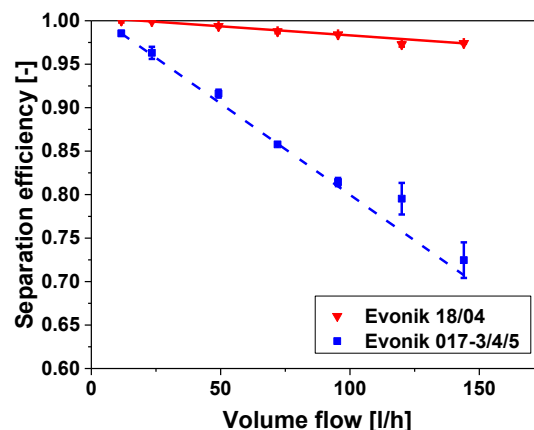


Figure 5-22: two different particle kinds Evonik 18/04 and 017-3/4/5 in the MEC show a linear drop of separation efficiency at increased volume flow from 10 to 150 l/h [Lindner'13]

Influence of the Concentration

The particle concentration is another important parameter. Stolarski suggested a sudden decline when a specific concentration was undercut [Stolarski'11]. The experiments on the batch-wise MEC lead rather to a logarithmic influence. Figure 5-23 (left) shows the influence of the particle concentration on the separation at 54 l/h and 0.23 T. The influence is logarithmic, which is supported by a model based on agglomeration before separation. The model is explained in Chapter 5.11. Low inlet concentration leads hence to a low separation efficiency. Interestingly, plotting the effluent concentration over the inlet concentration (Figure 5-23 right) reveals a maximum concentration in the effluent of 0.2 g/l at an inlet concentration of 4 g/l. At a high inlet concentration, the separation increases by agglomeration, reducing as well the outlet concentration strongly. As a consequence, it seems reasonable to use the process at high particle concentrations. If only small amounts of functionalized particles are necessary, large, cheap non-functionalized particles might be added to increase separation, as simulated in Chapter 4.4.

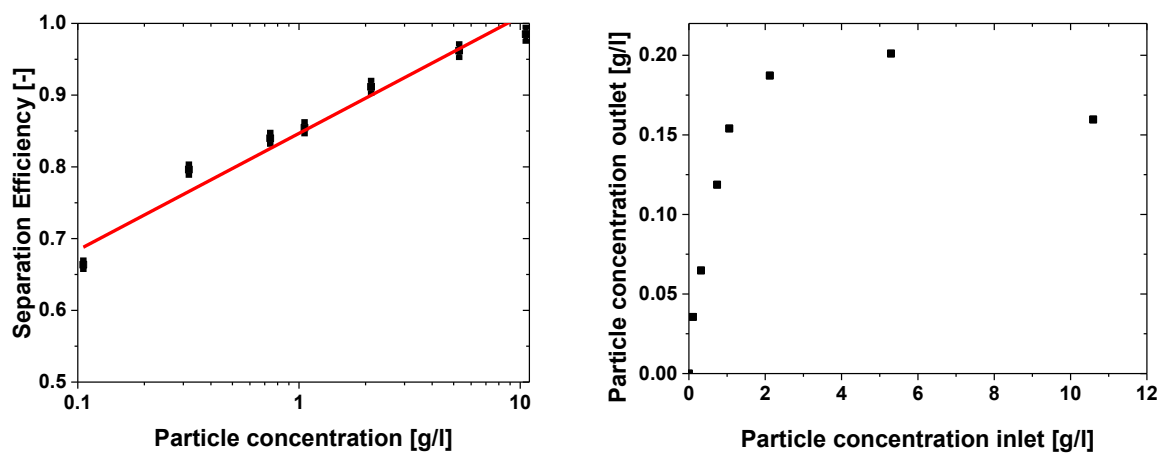


Figure 5-23 left: the particle concentration seems to have a logarithmic influence on the separation efficiency; the concentration in the effluent shows to have a maximum of 0.2 g/l at an inlet concentration of 5 g/l [Lindner'13]

Influence of the Magnetic Field Strength

Figure 5-24 shows the influence of the magnetic field strength on separation. Magnetic forces are the main influence for the separation of magnetic particles. At high field strengths above 200 mT, 99% of magnetic particles could be separated. A further increase beyond 200 mT did not show to improve the separation significantly. The reason is achieving of saturation magnetization of the particles and the wires. The rotational velocity was 1500 rpm as in the previous tests at a volumetric flow rate of 54 l/h and a particle concentration of 2.5 g/l. Without the magnetic field, centrifugal forces separate a proportion of the particles. While magnetic separation is selective and wanted in the process, the centrifugation needs to be

reduced to a minimum to avoid the reduction of selectivity. This is sufficient to separate a significant amount of particles. Particles of high magnetite amount are heavy and highly magnetic, leading to a high separation by both centrifugal and magnetic forces. This explains the differences in particle separation at no magnetic field. When the magnetic field is increased, both particle kinds are separated better, with weaker magnetic particles profiting more of the increased field strength. Separation in a different experiment without the wire matrix showed to result in 38% at 140 l/h and 1500 rpm, while 330 mT increased separation to 74%. The addition of the wire matrix further increased separation to 82%. This is in line with the results of Stolarski [Stolarski'11]. It is interesting as a separation process without wire matrix, in case of media containing fibres which cannot be processed in a wire filter. Particles then agglomerate magnetically induced and are separated by centrifugal forces.

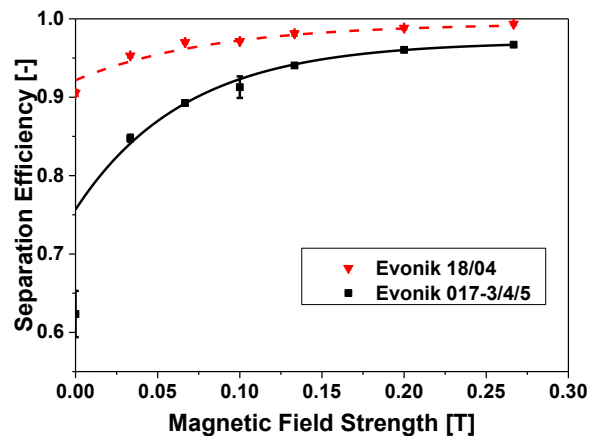


Figure 5-24: the magnetic field strength shows to enhance the separation efficiency at low field strengths, approximating 100% at high field strengths [Lindner'13]

Particle Recovery

The discharge of the MEC is important to use the batch-wise machine in protein separation processes. Figure 5-25 shows the result of different back-flushing strategies. A dense cake is shown (top left). A porosity of 65% was determined for this particle cake, which seems to be process dependent. Successful flushing results in a clear matrix with few particles left, mainly in the center of the device (top right). This is achieved by a high volume flow and by shearing the cake by the peeler knives. Two different ways of failing to discharge particles by flushing the machine were found. Flushing without use of peeler knives results in a discharged centrifuge center with the cake being unharmed at the centrifuge wall (bottom left). Slow volume flow showed not to be efficient but resulted in flushing a center area, but not redispersing particles sufficiently to discharge them.



Figure 5-25 top left: the centrifuge is filled with particles after the test; top right: the effectively cleaned centrifuge shows only few particles left close to the axis ; bottom left: inefficient discharge without use of the peeler knives shows a flushed center but dense cake; bottom right: inefficient discharge using a low volume flow shows a clear center and a cake solved from the wall but not discharged [Lindner'13]

5.7 Batch-wise Magnetically Enhanced Centrifugation in Industrial Scale

An industrial scale MEC was manufactured by Andritz KMPT based on the process design of the academic batch-wise MEC. Main purpose of this device was to show that the principle can be used at high volume flow and in large scale. Similarly to the small MEC it is built on an electromagnet and uses the wire matrix for redispersion.

5.7.1 Materials and Methods

High centrifugal forces were investigated on this machine. Large volume flow on the centrifuge is only possible for a limited time frame until it needs to be flushed back, as the device can hold 700 g of magnetic particles before a significant proportion of the cross section at the inlet is covered. Peeler-knives were not implemented, as the matrix itself creates during rotation high shear force for the redispersion of particles. Figure 5-26 (left) shows the centrifuge itself with the magnet installed, Figure 5-26 (right) shows the matrix implemented in the centrifuge.

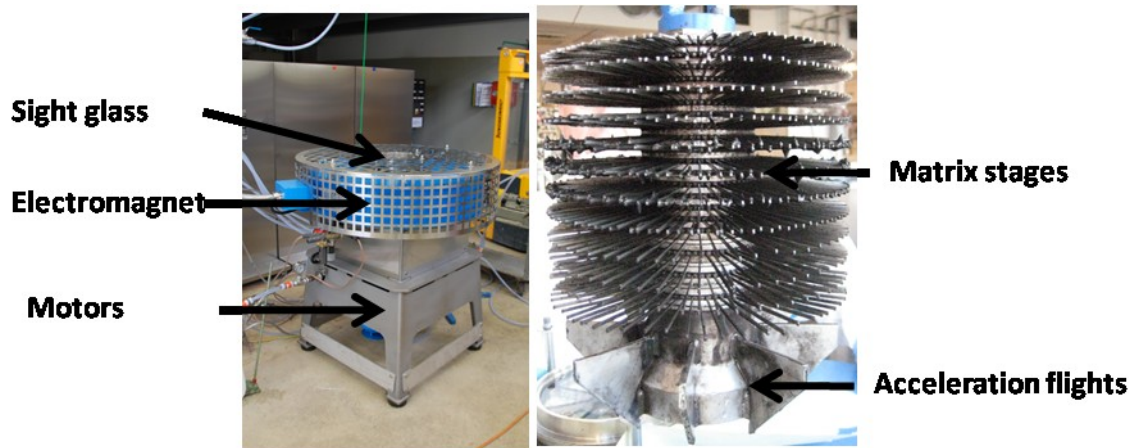


Figure 5-26 left: the industrial-scale MEC with the blue electromagnet installed around the machine by Andritz KMPT; the machine is fed from bottom and discharged on top; a sight glass is installed on top to allow studies of particle deposit; right: the wire matrix is large compared to the small MEC version

Wire Discharge Test

An interesting feature of the centrifuge is the high maximum rotational speed of 4000 rpm and the high maximum magnetic field strength of 0.4 T. A sight glass on top of the cell allows direct observation of the deposit on magnetic wires. Its influence on the cleaning of the wires by centrifugal forces was investigated. To quantify the influence of the wire cleaning, the criterion of a clean line on the top of wires was set to compare the influence of centrifugal and magnetic force. In this tests first wires were covered with magnetic particles by applying the magnetic field for 3 min at a specific magnetic field strength. While the field strength was kept constant, discrete centrifugal forces were tested for a defined time (3 min). The centrifuge was stopped and the wire result documented by photographs. If the criterion was not met, a higher centrifugal force was applied. The test was repeated at several field strengths.

Process parameter influence

The centrifuge characteristics were determined for this centrifuge in cooperation with technicians from Solae Denmark. Merck MagPrep particles were used in the parameter test. A piston pompe was used to move the fluid.

5.7.2 Results and Discussion

Wire Discharge Test

Examples of the deposit of magnetic particles on wires are shown in Figure 5-27. There is a layer of particles covering the top of the wires at 2250 rpm (Figure 5-27 left). In contrast, after increasing the circumferential velocity to 3000 rpm (Figure 5-27 right), the wires show a clean center line.

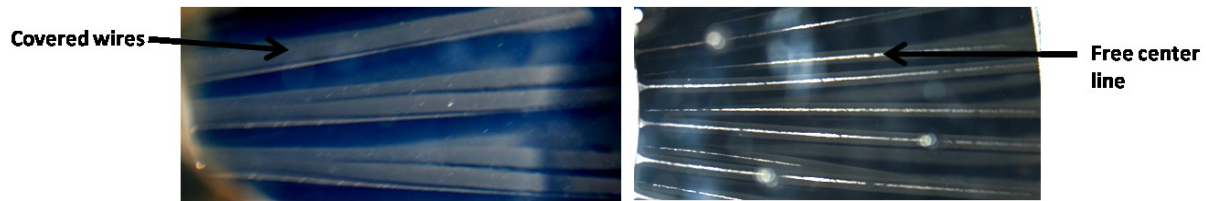


Figure 5-27 left: wires were covered with magnetic particles by magnetic forces, then the centrifugal force was increased to discrete velocities to test the wire discharge, at 240 mT and centrifugation at 2250 rpm the wires are still completely covered; **right:** at 240 mT and 3000 rpm a center line is cleaned while particles still attach to the wire edges;

The result of the tests introduced in Figure 5-27 is shown in Figure 5-28. The influence of the circumferential velocity and magnetic field shows an important influence on the cleaning of wires. A high magnetic field seems to be compensated by high centrifugal forces. In the final process, a specific deposit is tolerated though to keep centrifugal forces low and avoid the sedimentation of contamination. This is important for selectivity.

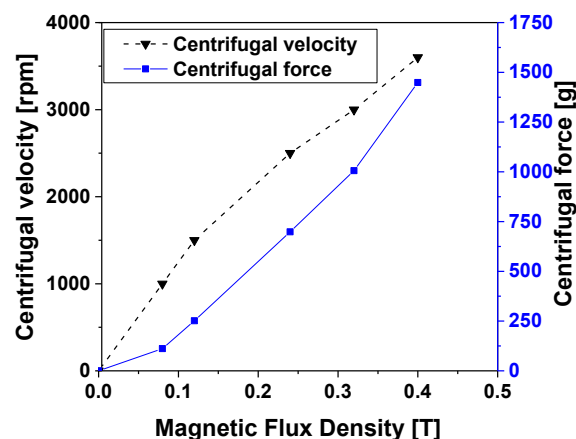


Figure 5-28: cleaning of the filter wires by centrifugal forces until a clean center line appears depends on the magnetic field and the centrifugal acceleration, shown normed on earth gravitation

Process Parameter Influence

The trends identified on the wire stage influence in the lab centrifuge and on the characteristics in the pilot scale centrifuge could be reproduced. Figure 5-29 top left shows the separation efficiency over load for a varying number of wire stages. Obviously 20 wires separate the largest amount of particles. On top, efficiency drops heavily at high load for a reduced wire number and is above 98% up to 700 g load. Separation drops to 92 % for 10 wire stages after charging 700 g of particles. At 6 wires, separation drops quickly and is only at 80% for 700 g load. Separation shows not to be reduced at small load between 0.4 and 0.2 T (Figure 5-29 top right). This was expected as at saturation magnetization of wires and particles, there is no additional gain by a higher centrifugal force. Only after charging 550 g of particles the separation drops at 0.4 T, while this limit seems to be achieved at 450 g for

lower magnetic field strengths. The region close to the discharge hence collected a small amount of particles in case of a stronger magnetic field. Saturation was not reached at 0.14 T, as the separation is lower at 98.3 % compared to 99.7% at 0.4 T. The drop in particle load is at the same load as on 0.2 T. Figure 5-29 bottom left shows the influence of the concentration. Separation at 10 and 20 g/l are close at any load, which is down to the measuring accuracy limited to 0.1%. When reducing the concentration to 0.3 %, separation dropped to 99.7 % at low load and to 98.2 % at 600 g. The maximum processed particle amount was 20 kg/h. Figure 5-29 bottom right shows the influence of the volume flow. At high load the influence drops strongly at 1 m³/h. Tests at 100 and 500 l/h show a high separation. Overall the particle load at a constant wire number seems only to affect above a load of 450 g.

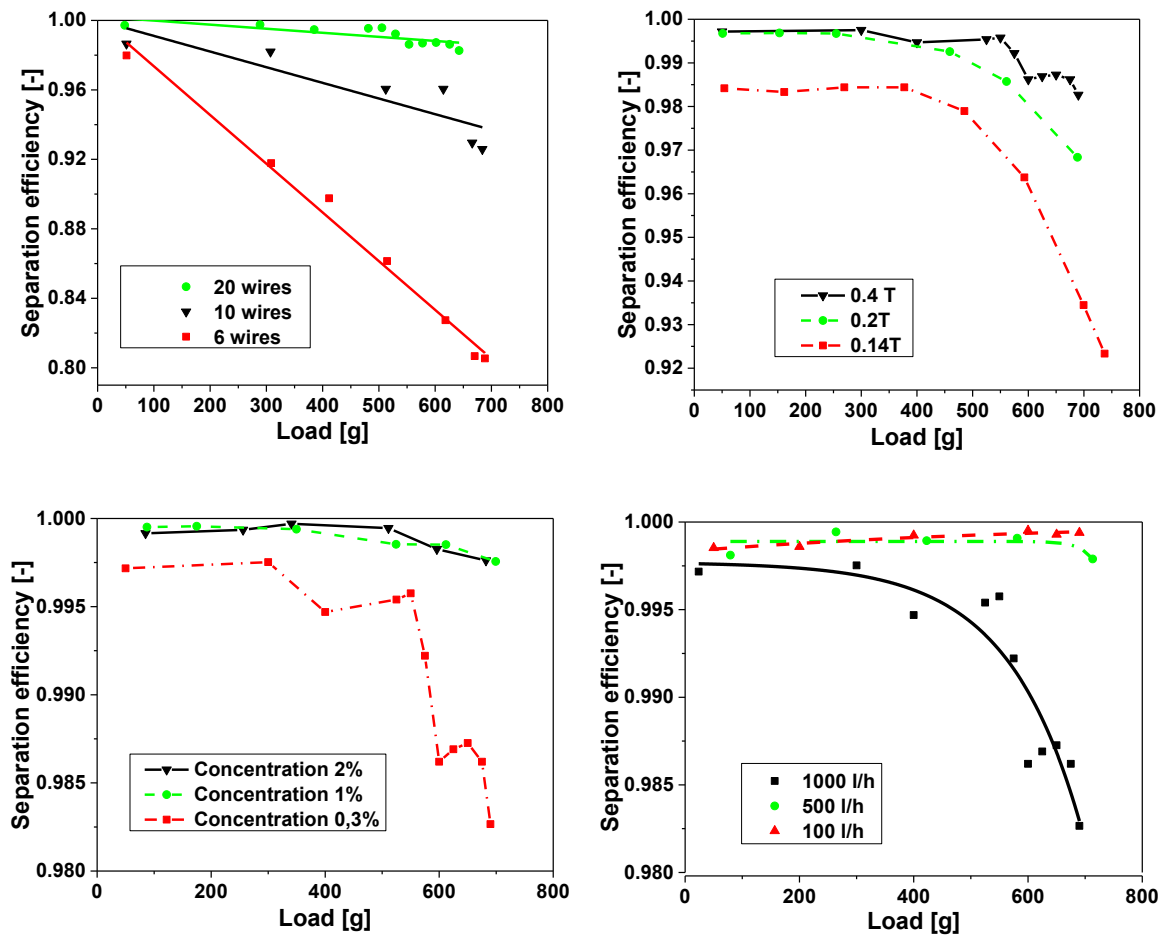


Figure 5-29 top left: a completely filled device with 20 matrix wire stages allows high particle load, while separation is slightly reduced at 10 wires and heavily reduced at 6 wire stages (500 l/h; 1000 rpm; 0.3 wt%; 0.4 T); **top right:** the influence of the magnetic field (1000 l/h; 1000rpm; 0.3 wt%; 20 wire stages in matrix) shows to be significant as well; **bottom left:** a low particle concentration leads to a low separation efficiency (1000 l/h; 1000 rpm; 0.4 T; 20 wire stages); **bottom right:** high volume flow reduces separated particle amount, especially at high load (1000 rpm; 0.4T; 0.3 wt%; 20 wire stages):

The maximum load of the centrifuge in all tests showed to be 600 g. Combined with the centrifuge volume of 6 l and the particle density of around 3 g/cm³, only 0.03 V-% particles can be stored in a MEC before separation dropped below 99%. Compared to the batch-wise MEC storing at least 6 V-% this seems low, but a reason is the different fluid velocity of 9 mm/s vs. 2 mm/s in the test.

The influence of the magnetic field at different volume flow is shown in Figure 5-30 left. A volume flow of 1020 l/h corresponding to a residence time of 21 s showed to give 98.9 % separation at 0.16 T. A volume flow of 720 l/h (30 s residence time) delivers 98.9 % separation efficiency already at 0.12 T. Figure 5-30 right shows the influence of the magnetic field at different numbers of wire stages and volume flow on separation efficiency. At a lower number of wire stages, the magnetic field showed to have a higher influence. The reason is the higher separation by the external magnetic field itself, which is not strongly homogeneous, but is a more expressed influence than initially expected. A variation was as well found while the magnetic field was switched off, as one curve shows higher separation. Strong variation in the separation without magnetic field was observed before and is down to the particle history, which influences agglomeration.

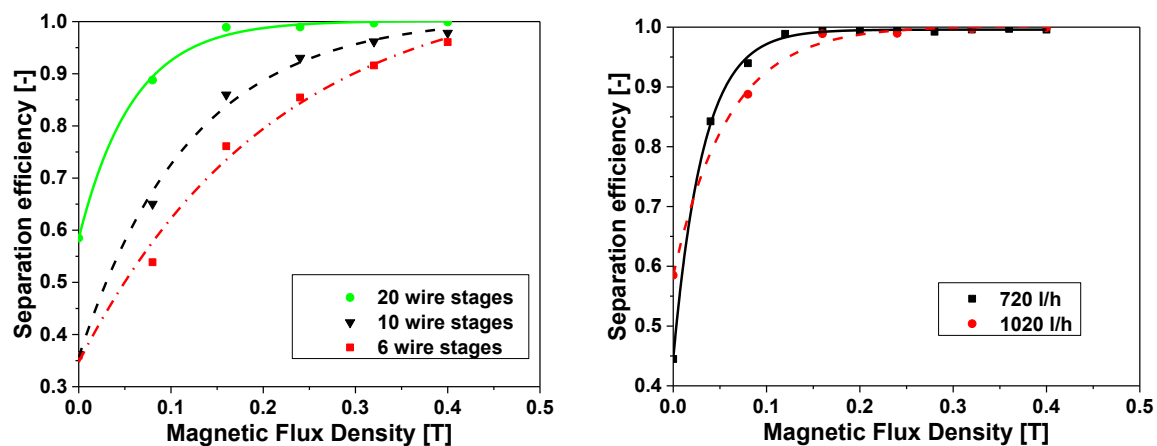


Figure 5-30 left: a low number of wire stages shows to profit stronger from a field increase compared to the better separation of a larger number of wire stages (right; 1000 l/h; 1000 rpm; 0.3 w%); right: the magnetic flux increases the separation to almost 100 % at a volume flow of 1 m³/h already at 0.2 T, with no need to further enhance the field to 0.4 T (1000rpm; 0.3 w%; 20 wire stages) allows high separation efficiency; at low magnetic field strengths, low volume flow increases the separation efficiency;

Discharge

The discharge showed to be critical as well for the large centrifuge. The best performance was achieved by completely draining the chamber after redispersion at 1000 l/h and stirring 5 min. Figure 5-31 shows the discharge in three batches of 10 l liquid, and the manual discharge after unmounting the filter. The first discharge was done by draining the chamber, in the second and third discharge the fluid was displaced from the top. Replacing the draining step by a

displacement step showed to be far less efficient on Merck MagPrep Silica particles. In the separation process in Chapter 6.5, MagPrep TMAP particles showed to be particularly difficult to discharge and to build a particle cake in the center of the wire matrix, with only 25 % of particles being discharged from the centrifuge. The same effect was not reproduced on different particle kinds such as Orica, which showed to be easier to discharge.

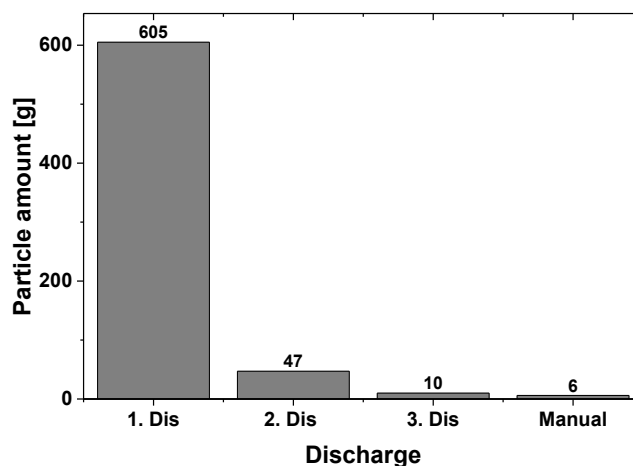


Figure 5-31: particle amounts discharged by redispersing in three batches in 10 l liquid each, with the first batch draining and the 2. and 3. displacement; redispersion was done by pumping in a cycle during 5 min and 5 min matrix stirring; manual discharge by removing filter matrix and flushing manually;

5.7.3 Conclusion on Batch-wise Magnetically Enhanced Centrifugation

While initially an increase of the stand time and the separation efficiency in batch-wise magnetic centrifugation was expected, this was not substantiated in later trials. As discussed later no important advantage of batch-wise centrifugation could be substantiated in experimental trials. It is hence not an option for industrial use.

5.8 Continuous Magnetically Enhanced Centrifugation

Continuous MEC was the original target for this procedure to provide an economic perspective at large scale for the overall process. As mentioned, batch-wise centrifugation does not provide major advantages to conventional HGMS while being more expensive. MEC is more promising as a continuous separation device. Only the magnetic carousel (see Chapter 5.1.5) was a continuous HGMS, but the principle seems to have been dropped. In MEC conventional lip seals are used, which are well established in several processes. An element to keep in mind is the magnetic field, which holds particles back. In case of a smooth decrease of the magnetic field, forces are low, while they might be high in case of high gradients. The target of the investigation is hence the determination of the contact force between non-magnetic particles and magnetic particles in a bulk to estimate the change of particle behavior.

A disadvantage of continuous devices is the fact that a single device is necessary for each process. This rendered the realization of the continuous process in the pilot lines impossible.

5.8.1 Evaluation of Designs for Automatic Discharge

Different designs were evaluated for a continuous discharge of magnetic particles. In continuous discharge, two important possibilities were evaluated. Essentially there are only two centrifuge types with an integrated weir, decanters and valve based disc separators. Both are technically possible in combination with a magnetic filter, but have additional constraints rendering a design complicated.

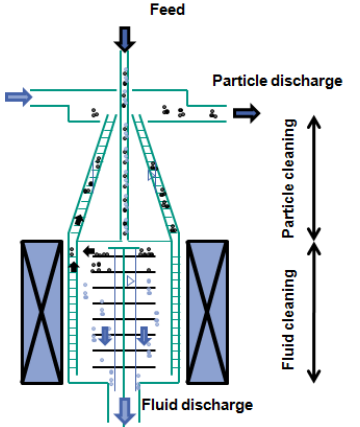
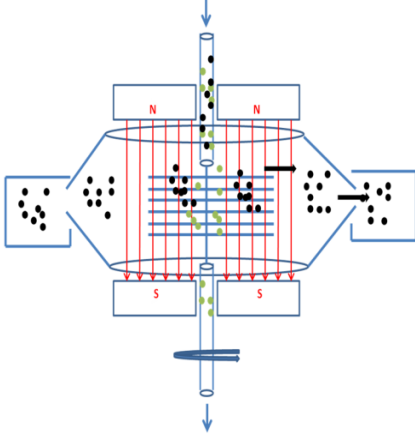
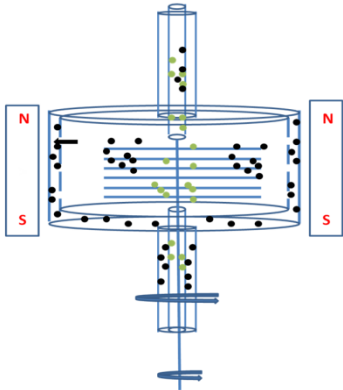
Decanter Approach

A decanter approach seems an obvious choice, as it leaves space radially outside for a magnet, while bearings and rotary feed through are placed on top and bottom as in a conventional decanter (Table 5-3 left). In contrary to a conventional decanter, which usually has a shallow liquid depth to create a short cone, the center of the centrifuge needs to be filled with liquid to use the major part of the magnet area. For this purpose, either the centrifuge possesses a long cone and is used at a low rotational velocity to take profit of the air spout in the center, or the pressure at the particle discharge outlet is increased relative to the fluid discharge. The version finally set up allows both approaches; it was used at a low circumferential velocity.

Valve Based Design

In a design based on valves radially outside of the centrifuge similarly to a disc centrifuge, the position of the magnet needs to be taken into account. A radial position of the magnet complicates a valve approach. Two different concepts avoid this problem: in the first concept a permanent magnet is installed at the top and bottom (Table 5-3 middle). Outside of the device there is space for the implementation of valves similar to a disc centrifuge. The particle transport out of the magnetic field is done by the centrifugal force. This is appealing, as the centrifugal force can be easily controlled. The magnet design in combination with the valve design is complex though. Bearings and other parts need to be installed in a magnet hole. The distance of the magnets, and hence the length of the centrifuge, is limited to keep a strong magnetic field. In the second concept the valves are built in a space saving way (Table 5-3 right). One possibility is the implementation of two rotating baskets with a number of bore holes acting as valves, a design which was developed and designed by Andritz KMPT. The transport in this approach is unpredictable in the direction perpendicular to the magnetic field and to the needle-shaped agglomerate alignment.

Table 5-3: design study for continuous discharge divides in screw transport and valve transport

Screw transport	Valve transport	
Decanter approach	A magnet is situated at top and bottom while a disc centrifuge discharge is realized	Rotating baskets serve as valves combined with a flushing discharge (developed by Andritz KMPT)
		

5.8.2 Materials and Methods

First pretests were performed in the lab scale machine described in chapter 5.4. As an electromotor moved the wire filter at a differential velocity, this could as well be used for pushing of magnetic particles out of the magnetic field by a screw.

The decanter was designed in cooperation with Andritz KMPT. A magnetic centrifuge was set up with a decanter screw inside. Within the decanter screw a wire filter was inserted. The wire filter in the machine consists of 12 stages with 40 wires, at a diameter of 74 mm. All wire stages have the same geometry. The production was similar to the matrices produced for the first matrix versions. It was set up on the basis of the batch-wise MEC, with the same electromagnet and fluid discharge used again. Mechanic parts are based on a similar design with the same electromotor turning the machine. The electromagnet implemented for turning the screw has a stronger gear reduction, resulting in a maximum relative rotational velocity of 24 rpm and a torque of 22 Nm (motor from Faulhaber AG, model 3863 024C 38A 200:1). A high rotational speed is not necessary for the screw, but high torque. The screw itself was produced by rapid prototyping stereolithography out of Polyamid 2200 by Gerg RPT GmbH.

Figure 5-32 shows the decanter scheme (left) next to the decanter screw with the wire matrix implemented (middle) and the complete decanter with electromagnet (right).

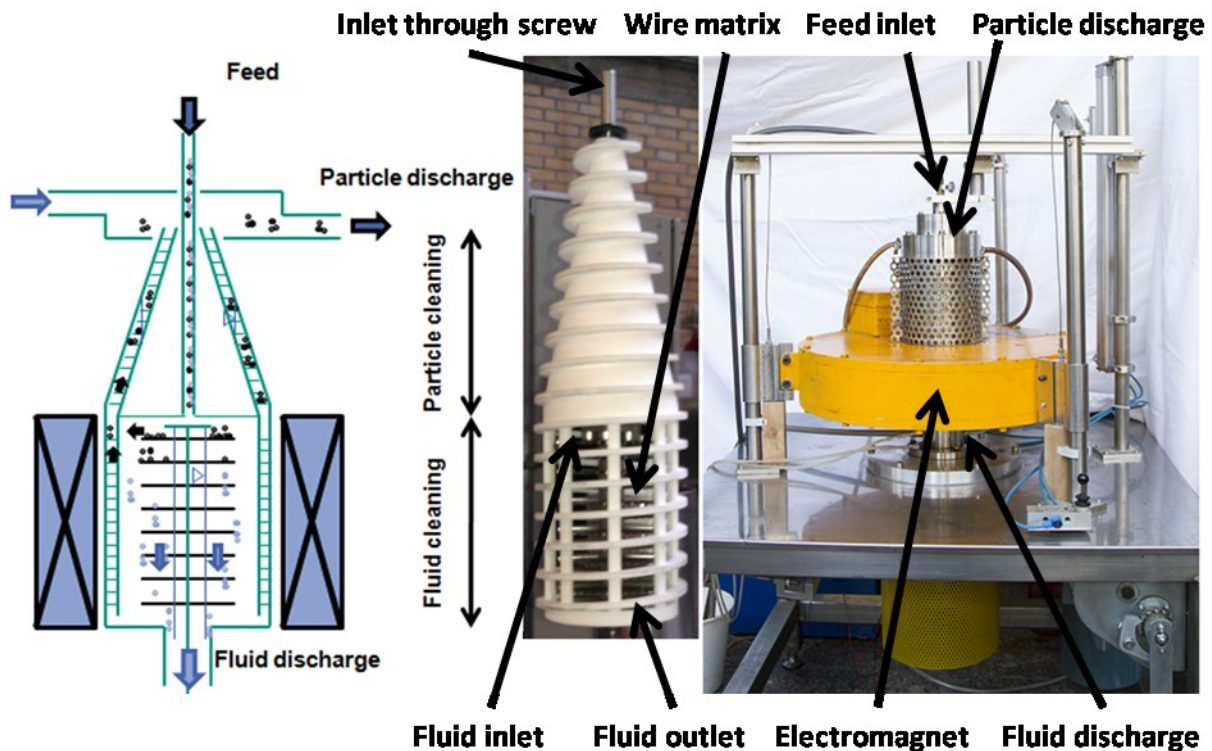


Figure 5-32 left: schematic principle of the decanter centrifuge with the feed inlet from the top by a rotary feedthrough into the filter cell with the wire matrix and the magnet outside, where particles are separated to the filter and discharged to the wall; the liquid flows over a weir at the bottom, while the particles are transported over the cone into a particle discharge cup; middle: the decanter screw is mounted on shaft with the wire filter inside and large windows for the particle transport; right: the magnetic decanter assembled with the yellow magnet, the feed inlet is on top, the particle discharge container below [Lindner'14]

Separation Tests

Before starting separation tests, a stable regime on 3 l of water was established. Then the suspension was fed. High particle amounts up to 20 g/l were applied, as a particle amount of 200 g in the process showed to be necessary for particle transport. The high particle amount limited the batch size to 5 -10 l. In the tests the machine was used in a cycle: the clear effluent of the fluid discharge was used to flush particles from the top container of the machine back into the feed tank.

Start-up Characteristic

The feed tank was stirred. For the test on the start-up characteristic, a stable regime based on pure water was established. At a given time, a suspension was fed. This was kept constant during 30 min. First water from the fluid discharge was collected separately, after 5 min it was fed back to the feed tank. After 30 min the feeding of particles was stopped and clear water was fed. Pretests on Particle Transport

Particle Transport over different cone angles

Before the setup of the decanter started, tests were done on the pilot machine available before. A pusher geometry was implemented, which showed to transport particles a limited way up the cone. The screw is shown in Figure 5-33 with a wire stage in the middle. Different cone angles (7° , 10° and 20°) were tested. Results were ambiguous, so the realization of a 10° cone was decided which limits the length of the decanter compared to 7° but is still conservative and common in industry [Stahl'04].

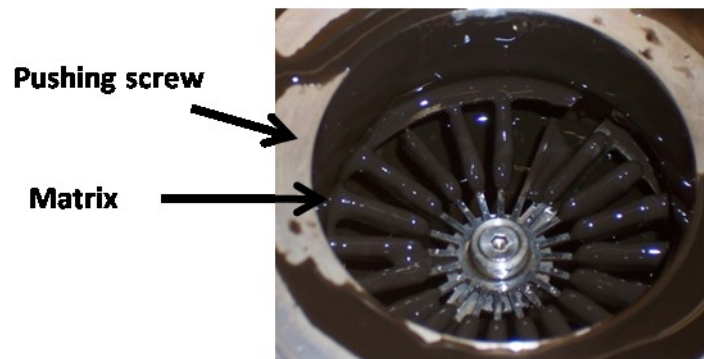


Figure 5-33: in the lab centrifuge a small pushing mechanism was integrated transporting magnetic particles over a cone and one wire in the middle

Determination of the Slope Angle

In the running centrifuge pictures could be taken by a stroboscope at the centrifugal velocity while taking photographs at an exposure time of 1 s through an acrylic glass cover. For this purpose first the suspension was filled in the centrifuge for common centrifugation. Feeding was stopped so particles sedimented and the liquid cleared. This allowed the observation of deposit at the centrifuge wall opposite to the wire end. The slope angle of magnetic particles was determined by measuring the angle in which particles sedimented. A photograph is in Figure 5-34. The cone angle determined is around 25° .

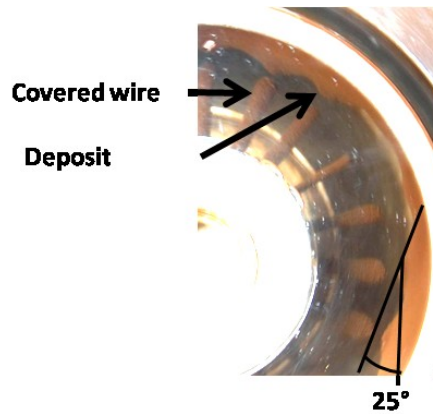


Figure 5-34: photograph of particles during rotation; the slope angle was determined from the angle of the deposit of particles at the centrifuge wall marked in red

5.8.3 Particle Tracks after Detachment

In the process the magnetic particles showed to behave similarly to a batch-wise centrifuge. Particles are collected by magnetic wires. Photographs of the particle deposit are shown in Figure 5-35. Particles form a stable deposit with only upper layers being discharged from the wire. Visible are the particle traces when particles are detached from magnetic wires, following the Coriolis force to the wall (Figure 5-35 left). Figure 5-35 right shows the deposit on the wire and traces of detaching particles on the decanter screw.

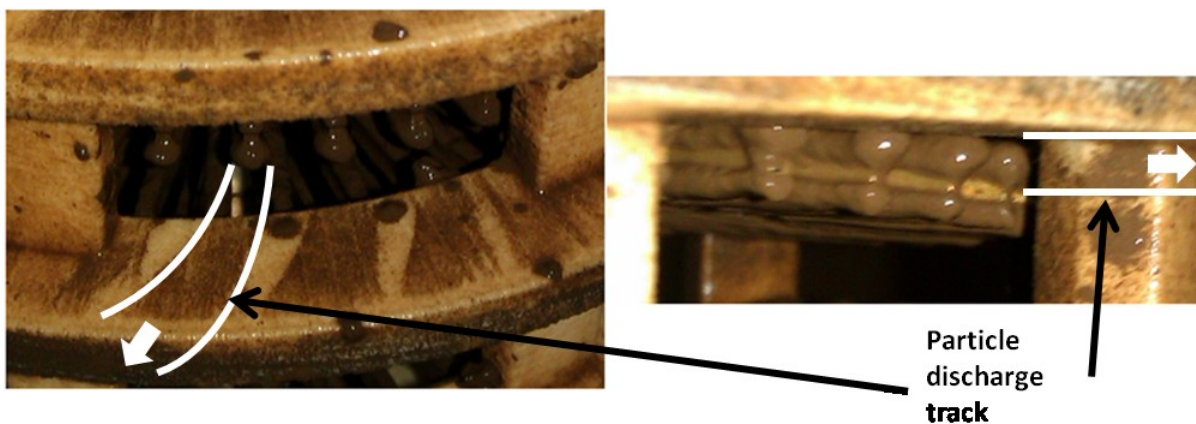


Figure 5-35 left: the particle deposit on wires showed to detach influenced by the Coriolis force and left traces on the screw; right: particles attach at top and bottom of the wires and detach at those positions, which is as well visible on the screw [Lindner'14]

5.8.4 Start-up Characteristics

Interesting is the start-up characteristic of the decanter centrifuge and its behavior over time at constant conditions. A particle amount of at least 100 g showed to be necessary to discharge particles out of the machine. The concentration of particle discharge and fluid discharge are shown in Figure 5-36 during 30 min. The discharge conveyed particles out of the machine 5

min after starting to feed them. The particle discharge concentration is about 20 g/l in average, highly fluctuating around this average. After stopping particle feeding after 30 min, the centrifuge continued discharging the machine for 8 min before it dropped. The separation efficiency is high, with 0.02 g/l left in the fluid discharge at a feed concentration of 10 g/l.

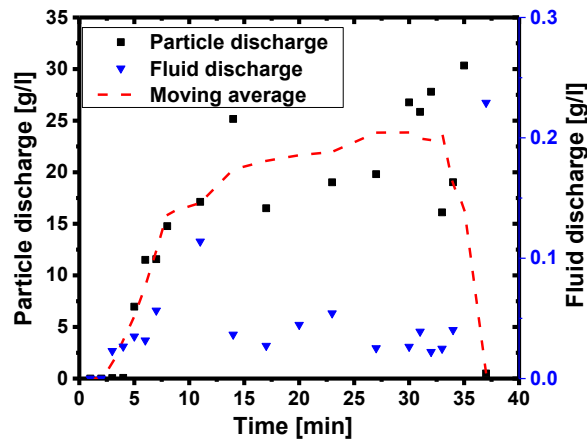


Figure 5-36: the suspension was fed from $t=0$ min to $t=30$ min; particle and fluid discharge over time shows high separation and particle discharge concentration of about 20 g/l with high variation. Discharge starts at $t=5$ min and is at $t=10$ min at constant level; discharge stops 7 min after stopping of particle feeding; (1146 rpm; 51 l/h; 24 g/l; 0.2 T; 22 rpm) [Lindner'14]

5.8.5 Parameters Influencing the Separation

There are several parameters influencing the separation. Notably the centrifugal force only influences at low field strength. Influencing parameters on separation include:

- the magnetic flux density
- the volume flow and
- the particle properties (magnetization, size distribution, surface properties).

Figure 5-37 left shows the influence of the magnetic flux density on the separation efficiency and particle discharge. Similarly to the batch-wise centrifuges, the separation rises steeply at low flux densities. The centrifugal force separates 56 % of magnetic particles while no magnetic field is applied; separation rises up to 97 % at 0.32 T. Notably above 0.13 T no significant increase is achieved by increasing the field strength. The particle discharge oscillated around 10 g/l, the high oscillation was already shown in Figure 5-36.

Figure 5-37 right shows the concentration and separation of particles influenced by the volume flow. As expected the separation drops at high volume flow. While at 27 l/h a separation of 99.9 % is achieved, overall separation decreases to 97 % at a volume flow of 120 l/h, which is still a very high level. This results in a particle separation of 2.4 kg/h, which is more than most current HGMS devices can process. The volume of the backflushing liquid

is increased as well in the experiment to keep steady state, resulting in a constant concentration in the fluid discharge.

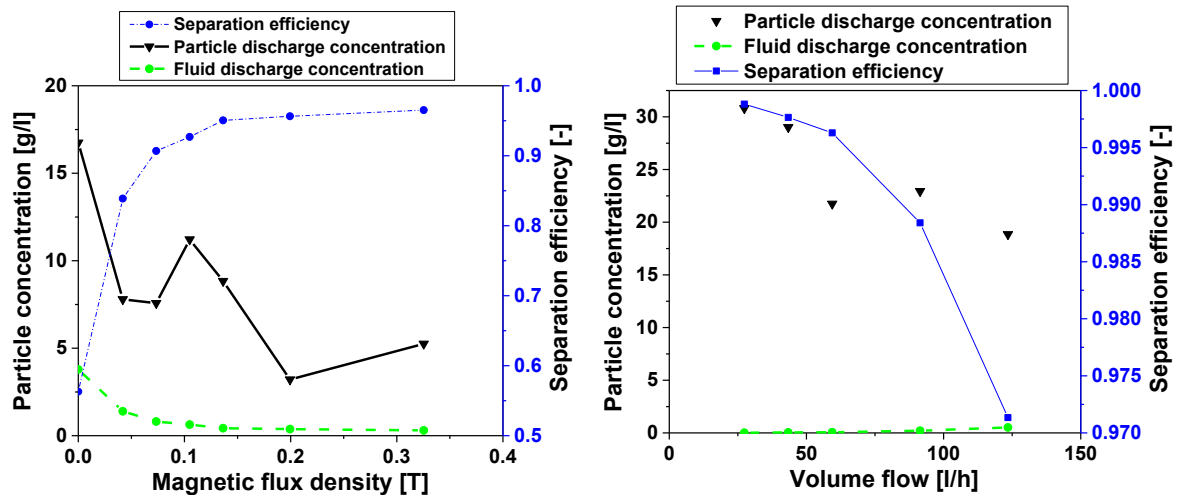


Figure 5-37 left: the separation strongly depends on the magnetic field strength, rising from 56% to 97%; the particle discharge shows an unsteady behavior which is a consequence of the unsteady behavior over time (1649 rpm; 53 l/h; 22 g/l; 22 rpm); **right:** the separation is shown as a function of the volume flow; the particle transport breaks down at a volume flow of 10 l/h in the particle container (1146 rpm; 53 l/h; 20 g/l; 0.2 T; 22 rpm) [Lindner'14]

The influence of the particle age became strongly visible when using magnetic particles in a cycle. Previous tests showed that the magnetic particles changed after reuse. This effect could be investigated by keeping the process running several hours. First a test on the separation efficiency influence of the magnetic field was performed on new particles. Then the particles were kept in the process for several hours before repeating the test. Figure 5-38 left shows the result of the separation efficiency shortly after startup, ranging from below 60 % to 97 % at different flux densities. When the test was repeated, separation was above 99 % at all field strengths. The separation efficiency showed to increase significantly. A reason to this is the agglomeration of particles. The agglomerate size increases by several orders of magnitude. Figure 5-38 right shows the particle size distribution (Q3) of the specific particle kind after the process with and without ultrasonic treatment. The ultrasonic treatment is sufficient to change the medium diameter x_{50} from 75 μm to 10 μm . Particles enter the centrifuge already in an agglomerated state, which leads to better separation.

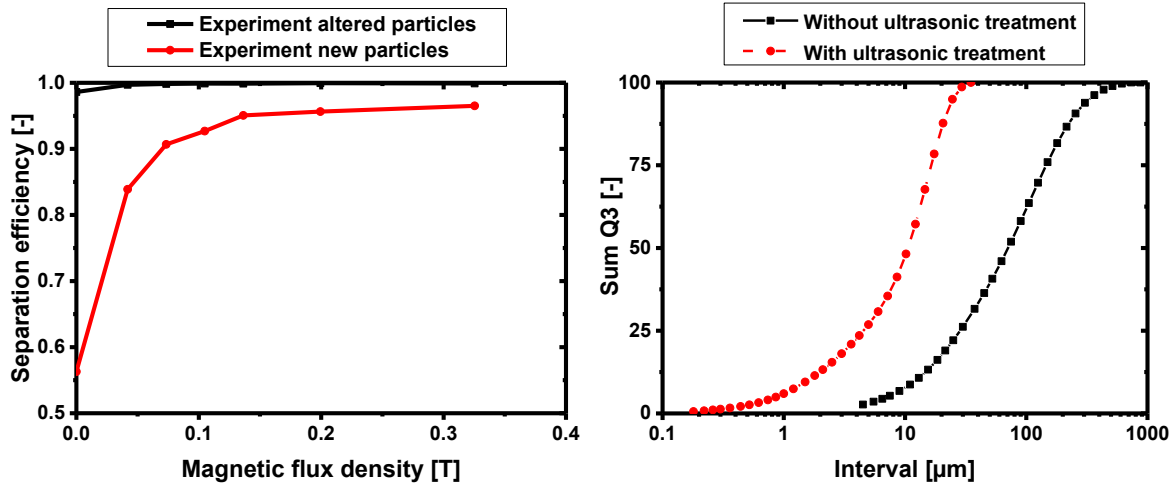


Figure 5-38 left: the magnetic flux density increases separation, but the history of the particles showed to have a strong influence on the separation as well (1694 rpm; 53 l/h; 22 g/l; 22 rpm); right: the particle distribution after the process with and without ultrasonic shows to be changed orders of magnitude [Lindner'14]

5.8.6 Parameters Influencing the Transport

Particle transport out of the magnetic field is critical for MEC. It depends on several parameters. The transport of particles is mostly influenced by

- the screw conveyor velocity,
- the rotational velocity of the centrifuge and
- the amount of water used for flushing the particle container.

Figure 5-39 left shows the influence of the screw conveyor on the particle transport. A minimum conveyor speed of 10 rpm is necessary. Below, the transported amount is reduced which means the centrifuge accumulates particles in the filter cell. Separation efficiency is not affected if the conveyor velocity is reduced for a short time.

The rotational velocity of the centrifuge is shown in Figure 5-39 right. A minimum rotational velocity of the device is necessary for the discharge of about 1100 rpm. At 900 rpm, the particle discharge drops from 30 to less than 5 g/l. The velocity in between 900 and 1100 rpm could not be tested for a resonance frequency at this speed. Interestingly, the centrifuge separation efficiency did not drop below the minimum rotational velocity down to 500 rpm, but instead the centrifuge accumulates particles in its center similar to the batch-wise version. The separation drops below 300 rpm because the waterspout rises and the matrix is no more covered with liquid. Additionally water from the particle discharge tank is flushed down the centrifuge cone below 900 rpm. Above 1650 rpm water from the centrifuge rises up the cone and drowns the particle discharge tank. In between 1150 and 1650 rpm the centrifuge showed

a stable regime which worked reliably. This device seems to be the only decanter centrifuge with separation being decoupled from circumferential velocity.

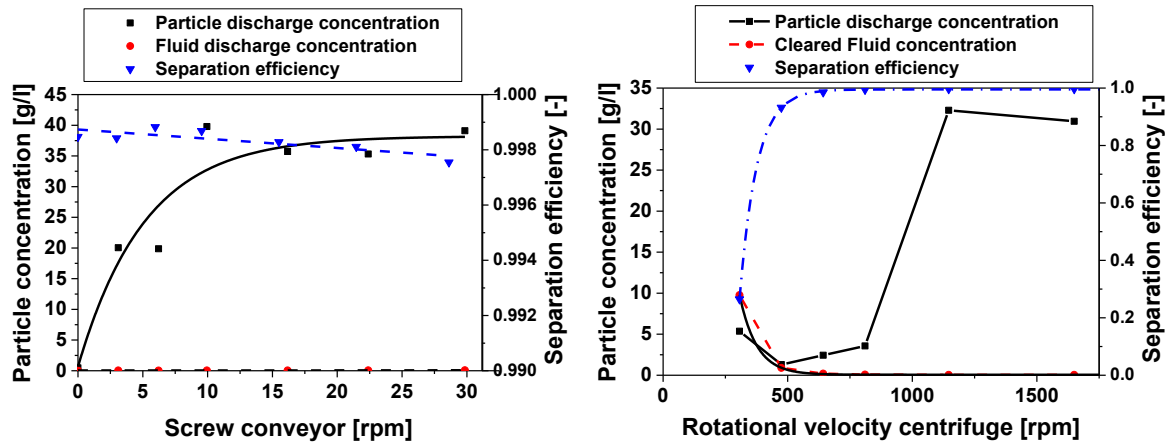


Figure 5-39 left: the transport of the screw conveyor below 10 rpm breaks down with particles being collected in the wire filter, which at first does not reduce separation (1694 rpm; 53 l/h; 22 g/l; 0.2 T); right: the centrifuge speed influence on the discharge and the separation efficiency; below 1000 rpm (56 g) the transport breaks down; Separation efficiency is only reduced below 500 rpm (53 l/h; 22 g/l; 0.2 T; 22 rpm) [Lindner'14]

5.8.7 Summary and Conclusion

In summary several parameters influence either the separation or the particle transport. An overview is given in Table 5-4. While the separation efficiency depends mainly on the magnetic field and the volume flow, the particle transport is influenced by the circumferential speed and the conveyor speed. Magnetic field strength of the electromagnet was set to 30 A corresponding to 0.2 T. A higher current leads to overheating of the device. The particle concentration increases the separation logarithmically, but influences as well the transport. A minimum of 100 - 200 g of particles is necessary on the current centrifuge type. Due to the high amount of particles necessary in the process and high losses when stopping and manually discharging the machine, its use is only promising at industrial process scales. To achieve a stable regime in the centrifuge, a concentration of 20 g/l was used. In a final process the particle concentration would need to be adapted to the process leading to high residence times at low concentrations. The volume flow was set to a medium value of 50 l/h to be able to treat a significant amount of material while maintaining high separation. The circumferential speed influences as well the sedimentation of the contamination, hence it should be kept to the minimum of 48 times earth gravitation. The conveyor speed does not have a negative impact and was set in tests to its maximum of 18 rpm.

Table 5-4: Different parameters influencing the transport and the separation, and their influence in the setup

Parameter	Formula,	Influence
Rotational acceleration	$\omega^2 r / g$	>48 (900 rpm)
Conveyor transport	$\omega * V / \dot{V}$	>2800 (10 rpm)
Reynolds number (necessary for discharging the particle tank)	$Re = u * d_H / \nu$	>350 (10 l/h)
Magnetic Field increase		Asymptotic increase to 100%
Volume flow increase		$E \sim \dot{V}$
Particle age		increase
Concentration influence		$E \sim \ln(c)$ [Lindner'13]

5.9 Setup of a Longitudinal Permanent Magnet Arrangement for Magnetically Enhanced Centrifugation

For an industrial use of MEC, the costs in investment and operation need to be minimized to be competitive to different HGMS processes. A major cost factor is the electromagnet. It is expensive in acquisition, energy-intensive in use and prone to breakdown for overheating or a cooling water spill, which both already occurred on a water-cooled electromagnet used for MEC. Figure 5-40 shows a model with an illustration of the magnetic field lines (left) and a photograph (right) of the magnet arrangement.

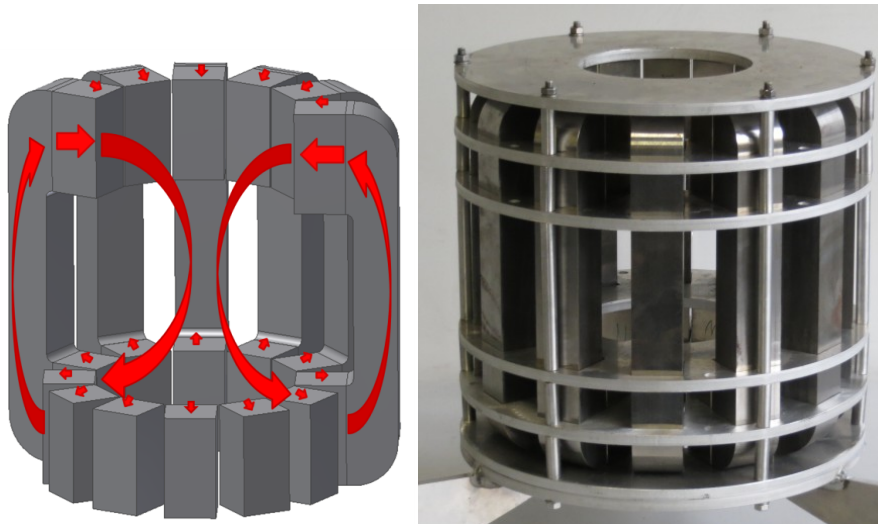


Figure 5-40: Principle (left) and Photograph (right) of the longitudinal permanent magnet arrangement

Classic permanent magnets cannot be used for their horizontal field direction. The wire filter inside of the centrifuge would be magnetized and demagnetized during centrifugation, which

is incompatible with the process. Additionally the rectangular shape is not optimal for combination with the round shape of a centrifuge. An alternative to an electromagnet is the setup of a permanent magnet arrangement. The magnetic field needs to be directed in axial centrifuge direction.

5.9.1 Materials and Methods

Magnetic Field Simulation of the Permanent Magnet

The simulation was done by Comsol Multiphysics, implementing the magnetization of the magnets and simulating the surroundings with the properties of air and the pole yoke as steel with a function for susceptibility values. The permanent magnet was simulated using the same model as in Chapter 4.3.1 and in the wire simulation in Chapter 5.4.2. The iron yoke is modeled as magnetizable steel with a permeability $\mu_r = 10$. The permanent magnets had a magnetization of 900 kA/m (1.13 T) turned towards the centrifuge axis. The outside is simulated as vacuum.

Design and Setup

The permanent magnet assembly was created from laser-cut plates in which the magnets were inserted. In sum 24 magnets of elongated shape were assembled in two circles (35mm x 35 mm x 70 mm magnet length), with north pointing inward on top and outward at the bottom. The longish magnet side is oriented in longitudinal direction. The plates and pole yokes were first assembled without the magnets. Then the magnets were inserted from the top, assisted by assembling aids which only left space vertically for insertion. Only the last few magnets were difficult to assemble for high repulsive forces.

Measurements

A Hall probe was used notably to measure the magnetic field of the electromagnets and the permanent magnet assemblies. The producer is Magnet-Physik Dr. Steingroever GmbH, the model is FH51 Gauss-/ Teslameter.

It could not yet be tested on a continuous machine for design limitations, i.e. the bowl of the decanter is too large. Two magnetic field strengths for the electromagnet were chosen: the electromagnet was set to create the same field strength of 0.23T in the center (34 A) and at the wall (27A). The separation was measured for the permanent magnet and for the two field strengths of the electromagnet at different volume flow from 27 to 127 l/h.

5.9.2 Simulation of the Permanent Magnet Arrangement

The design was optimized by FEM-simulation. Closing of the field lines of the same magnet needs to be avoided to enhance the strength in the magnet center. The magnet placement and

the size was optimized. The field created by cubic magnets of 0.08 T is shown Figure 5-41 left. Elongate magnets (35mm x 35 mm x 70 mm magnet length) showed a significantly higher field than cubic magnets of 0.14 T. To further enhance the field strength, a pole yoke was tested in the simulation. It showed a significant increase of the magnetic field of 57% to 0.2 T. Figure 5-41 right shows the final magnet arrangement. After setup the magnetic field was measured with a Hall probe. It showed a magnetic field of 0.23 T in the center validating the simulation.

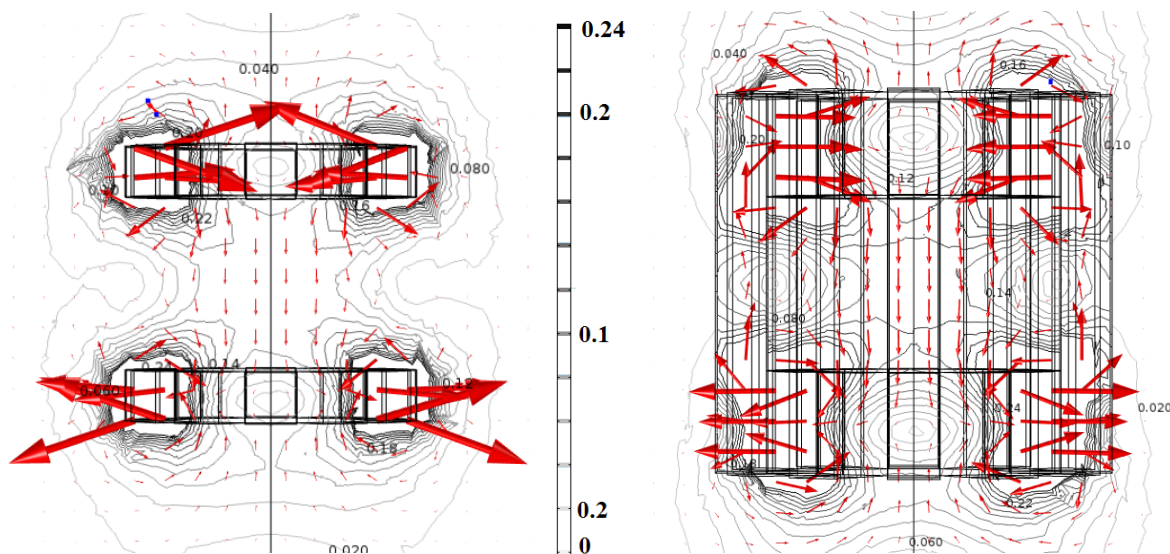


Figure 5-41 left: The FEM simulation of the longitudinal permanent magnet arrangement shows a homogeneous but weak magnetic field around 0.08 T in the center where the process chamber is situated; arrows show the magnetic field direction, colors show the magnetic field strength; right: the longish magnets and the pole yoke increase the field to 0.2 T (right);

5.9.3 Magnetic Field of a Longitudinal Permanent Magnet Arrangement

The measurements of the magnetic flux in its main direction of the different magnets by the Hall probe are shown in Figure 5-42. Figure 5-42 left shows the flux density in the center over the axial position starting from the center of each magnet. Figure 5-42 right shows the flux at the border in axial direction. The longitudinal magnet arrangement was compared with three different magnet setups, which were all used in HGMS devices. A classic permanent magnet [Ebner'07] with yoke shows the strongest field of above 0.4 T. A Halbach magnet arrangement created a significant field of 0.37 T in its center [Menzel'13]. Both created a translational field which was significantly stronger than the longitudinal fields. The electromagnet was used in cake filtration [Eichholz'12] and MEC. For this measurement it was set to the same field strength as the longitudinal magnet arrangement in its center. On water-cooled electromagnets field strengths up to 0.4 T are realistic. The field shape was very homogeneous on the permanent magnet and slightly less homogeneous on the transversal

magnet arrangement (Halbach). The electromagnet had its strongest field close to the magnet wall and is less homogeneous.

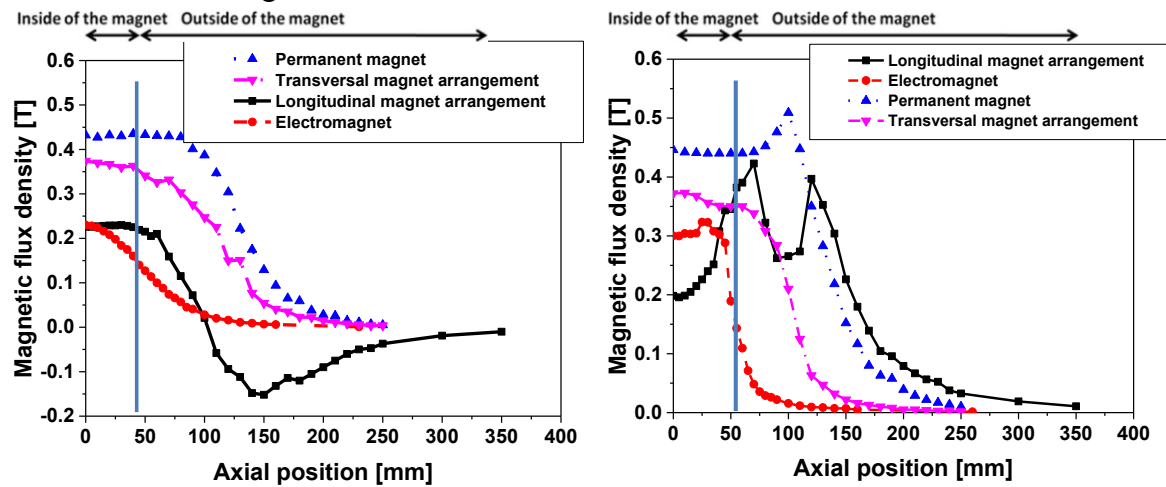


Figure 5-42 left: the flux density in field direction of the longitudinal (axial) magnet arrangement, electromagnet, conventional permanent magnet and transversal (Halbach) magnet arrangement are compared from the center on the axial line to the outside, negative axial positions are symmetrical; the conventional permanent magnet has the strongest and most homogeneous field but in transversal direction, the Halbach magnet is similar; the electromagnet was set to the same field in the center and delivers a less homogeneous field in axial direction; right: the magnetic flux density norm on a line close to the border shows high gradients for the axial magnet arrangement close to the magnets which are not produced by the other magnet types; the position of the cell from -60 to 60 mm is marked with a line

5.9.4 Magnetically Enhanced Centrifugation Based on a Permanent Magnet Arrangement

The permanent magnet was tested on the batch-wise magnetic centrifuge. During separation it was installed around the centrifuge, while for discharge it was pushed to the top (see Figure 5-43 left). The longitudinal magnet arrangement was homogeneous on the center longitudinal line, yet showed high gradients close to the magnet rings. This did not show to impede batch-wise magnetic centrifugation, yet might interfere with particle transport in a decanter MEC. The setup is shown in Figure 5-43 left, the result of batch-wise centrifugation is shown in Figure 5-43 right. The permanent magnet separated similarly to the electromagnet, with separation efficiency being for different volume flows in between the separation of the chosen field strengths. Separation was, hence, comparable with separation of an electromagnet. The backflushing of the centrifuge was more difficult to handle in comparison with an electromagnet, as first the magnet needed to be pushed away before backflushing, and opening the device was difficult without completely removing the permanent magnet. This depended on the specific design.

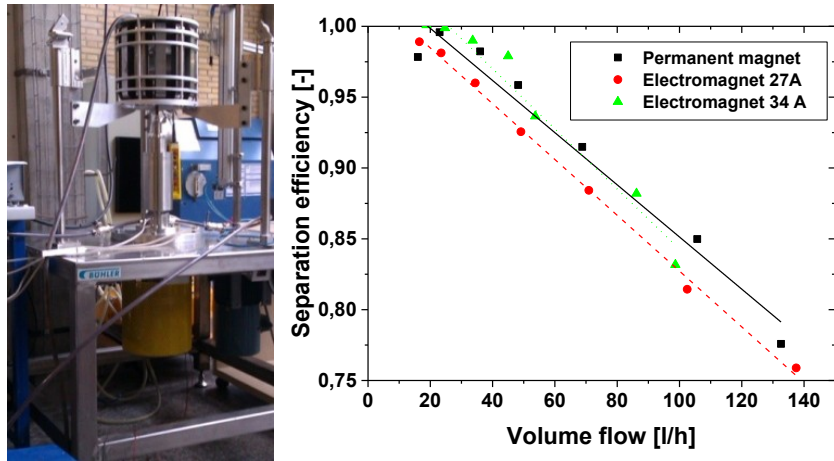


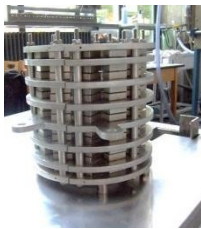




Figure 5-43 left: photograph of the permanent magnet mounted on the batch-wise centrifuge; right: the influence of the volume flow on the separation with an electromagnet at 0.23 T in the center (34 A) and at the wall (27 A) showed that permanent magnet separation was in between the flux densities

5.9.5 Magnet Comparison

As mentioned, the main advantage of the permanent magnet is economic, with low investment and operating cost. Table 5-5 shows a comparison for different economic parameters. Besides the aircooled and watercooled electromagnet, another Halbach arrangement of Menzel [Menzel'13] and a conventional permanent magnet used with a HGMS filter cell is shown. In investment permanent magnets are generally cheaper, at the cases currently investigated by about a factor 5. Electromagnets consume several kW power. Additionally they need to be air- or watercooled and risk overheating when they are used over long periods. Weight of electromagnets is higher by a factor 3 to 5. Additionally a large control cabinet is necessary, which increases the space requirement and the transport effort. As mentioned above, depending on the system the direction of the magnetic field plays an important role. A conventional filter cell is possible based on a transversal magnetic field. A rectangular geometry is as well possible in HGMS, but implementing a stirrer is delicate. Superconducting magnets are not common in HGMS, as they create higher field strengths, but the advantage of their higher field strength is limited by the saturation magnetization of the wires and particles. MEC requires an axial field.

Table 5-5: Comparison of economic parameters of different magnets

	Air-cooled electromagnet	Water-cooled electromagnet	Transversal magnet arrangement (Halbach)	Longitudinal magnet arrangement	Classic permanent magnet
Investment	15 000 €	15 000 €	3 500 € magnet cost 2 860 €	2 000 € magnet cost 1 362 €	3 000 €
Electricity consumption	2.2 kW	5.5 kW	0	0	0
Magnetic Field Strength	0.21 T (on long term at 30 A, 110 V)	0.25 T (on long term at 70 A, 110 V)	0.37 T	0.23 T	0.43 T
Shape	Round	Round	Round	Round	Rectangular
Magnetic field direction	Axial	Axial	Horizontal	Axial	Horizontal
Weight	170 kg + electrical cabinet	240 kg + electrical cabinet	27 kg	47,4 kg	120 kg
Photograph					

5.10 Selectivity in MEC

Selectivity is one of the critical points for the application of MEC in bioseparation. A selective functionalization of particles needs to be combined with devices providing a selective separation of the particles. In case of MEC, selectivity is reduced by the centrifugal force. It depends on the density of the contamination, which is usually low in biofermentation media.

5.10.1 Materials and Methods

For the first experiment on the selectivity of MEC, the small academic centrifuge built by Stolarski was used. Calciumcarbonate (Ulmer Weiss) at a concentration of 4 g/l was used as contamination, which had a density of 2.7 g/cm³ and medium size x_{50} of 6.2 μm . A specific particle kind was used (Evonik 500) at a concentration of 2 g/l, which delivers high separation in comparison with different Evonik particles. The experiment was done by separating magnetic particles and Ulmer Weiss in separate tests at a magnetic field strength of 0.4 T. The experiment was repeated with both materials mixed at 0.5 T. After the test, the samples were washed by sedimenting particles to a magnet at the jar wall and removing the supernatant.

For a test on biomass separation, the small batch-wise centrifuge was used. The separation of the medium provided by Scholz was performed at a centrifugal field from 0 to 60 times earth

gravitation and 200 l/h at different centrifugal forces. The analysis was done by measuring the optical density, which was as well performed by Scholz at the institute of biotechnological process engineering at KIT.

5.10.2 Results and Discussion

Separation from Calciumcarbonate

The results are comparable, which indicates that both materials do not interfere as would be possible by agglomeration or swarm sedimentation. At the applied 1500 rpm, calcium carbonate is separated to a high extent. This is reduced by increasing the volume flow. A reduction of the circumferential velocity further decreased the separated proportion. While it is not possible to completely prevent the separation of heavy contamination, on contamination of lower density and size, like e.g. in a biosuspension, separation can be reduced significantly. Figure 5-44 left shows the distribution sum of Ulmer Weiss, Figure 5-44 right shows the separation efficiency of the calcium carbonate in comparison with magnetic particles.

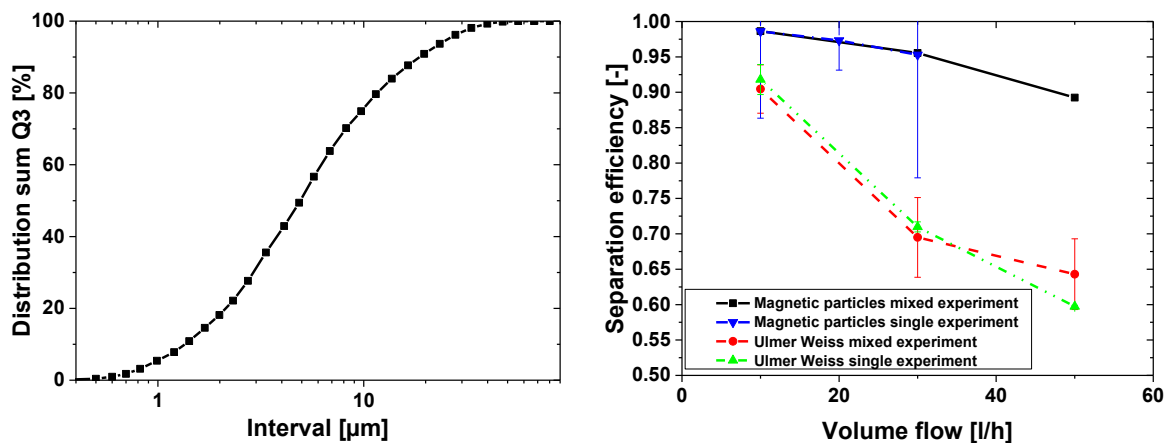


Figure 5-44 left: size distribution of the product Ulmer Weiss, which is large at 6.2 μm and combined with a mass of 2.7 g/cm^3 difficult to exclude from centrifugation; right: Selectivity in lab-MEC; Ulmer Weiss compared with magnetic particles; mixed experiment: 1500 rpm, 0,42 T; single experiments: 1500 rpm, 0,51 T; separation is influenced by volume flow and minimized at high volume flow for highly magnetic particles;

Selectivity for Biomass

Important is as well the separation of biomass by centrifugation. Figure 5-45 shows the biomass separation in the MEC in a test performed on raw fermentation broth. While low volume flow separated a high amount of biomass (not shown), increasing the volume flow to 200 l/h lead to a low biomass separation below 3% at 1000 rpm (corresponding to 60 times earth gravitation).

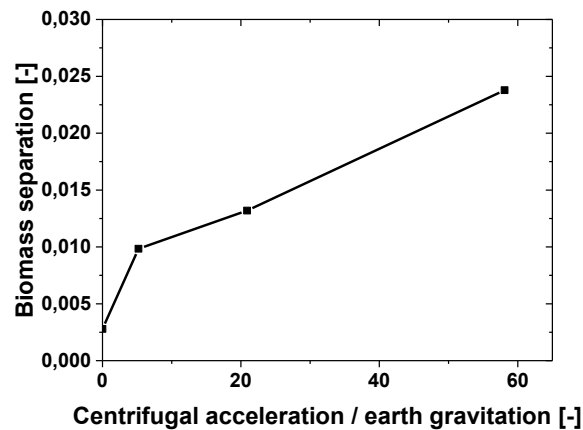


Figure 5-45: the biomass separation out of raw fermentation broth could be reduced below 3% at 1000 rpm and 200 l/h

Selectivity might as well be reduced by the unwanted adsorption of cell fragments to magnetic particles.

5.11 Calculation Approach for Particle Separation

A mathematical approach for the calculation of the separation efficiency is necessary to understand the influences and to optimize the process. A complete approach allows the optimization of the particle system and of the HGMS device. Current calculation approaches like the calculation suggested by Stolarski, see (2-46), do not take into account several influencing parameters. Stolarski presented a method for the calculation of the separation efficiency based on the area passed by flow [Stolarski'11].

- The influence of the centrifugal force needs to be taken into account.
- Particle agglomeration plays an important role (as was shown experimentally); this includes the change in demagnetization, the change in agglomerate mass and needle sedimentation. The influence of the particle diameter is compensated by agglomeration.
- A model for the wire shape of rectangular geometries, as used in this process, is necessary.

Chen suggested a theoretic study on the arrangement of wires in suspension in dependence of two different wire arrangement [Chen'09]. While the arrangement showed to influence the separation in a simulation approach (see Chapter 5.4.6), this could not be reproduced experimentally. Agglomeration influence was not introduced. Therefore the model suggested by Stolarski was extended.

5.11.1 Mathematical Background

The calculation of separation at low concentration

Based on the equations presented in Chapter 2.1.2, an approach was developed to estimate the separation efficiency in a centrifuge based on particle properties. The goal is the description of the correct influence of the parameters. The starting point is the capturing radius of wires given in (2-45). Figure 5-46 illustrates the area separating magnetic particles in a quarter of a centrifuge section.

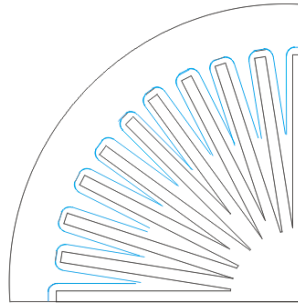


Figure 5-46: Scheme of the covered area in which magnetic particles are separated in a quarter of the centrifuge

If the magnetic field is below the saturation field of particles and wires. The demagnetization of wires and particles needs to be introduced as well. The parameters are for a circular wire $N_{Wire}=0.5$ and for a sphere $N_{Sphere}=1/3$. To calculate the separation of non-cylindric wires like those used in MEC, the different geometries are introduced by calculating the cylinder separation and multiplying with a factor taking flow and demagnetization into account. The cut size is calculated by resolving (2-45) for the particle size, including. The centrifugation is taken into account by calculating its cut size x_P out of (2-85). The flow layer thickness is calculated from (2-86). Then the smaller of the two cut sizes is chosen for the separation. Out of (2-88), the separation of one wire stage is calculated. For an array of N_S wire stages, the separation is calculated out of the joint efficiency by [Lindner'10]

$$E_{total} = 1 - \prod_{i=1}^N (1 - E_i) \xrightarrow{\text{for identic wires}} 1 - (1 - E)^{N_S}. \quad (5-4)$$

Introduction of agglomeration

Additionally to the separation of the wire filter and of centrifugation, agglomeration plays an important role. Magnetic particles tend to agglomerate in a magnetic field, with large agglomerates being easier separated [Svoboda'81]. One approach to take this into account is to calculate an agglomerate size, which is then used for the separation calculation shown above. The agglomeration is based on equalizing the Stokes fluid resistance (2-43) and magnetic dipole forces (4-1). This results in the differential equation

$$\frac{dr}{dt} = \frac{\mu_0 \mu_i \mu_j}{2\pi^2 \eta r^4} \left(\frac{1}{d_i} + \frac{1}{d_j} \right). \quad (5-5)$$

It is solved for r_0 , resulting in

$$r_0 = \left(\frac{1}{t_0} \frac{2\pi^2}{5\mu_0} \frac{\eta}{\mu_i \mu_j \left(\frac{1}{d_i} + \frac{1}{d_j} \right)} \right)^{-1/5}. \quad (5-6)$$

By calculating the new agglomerate diameter d_A out of particles in reach and within a 55° cone, the agglomerate diameter

$$d_A = r_0 \sqrt[3]{\frac{9c}{2\rho} * \frac{2(V_{cone} + V_{calotte})}{V_{sphere}}} = r_0 \sqrt[3]{\frac{9c}{2\rho} * \left(1 - \frac{1}{\sqrt{3}} \right)} \quad (5-7)$$

results. The fluid resistance needs to be calculated from a needle shape and the demagnetization is reduced to that of a cylinder. By calculating the cut size resulting from centrifugation and from magnetic separation on the particle distribution, which may be approximated by RRSB, the separation efficiency is calculated. The advantage of this approach is that it provides an acceptable approximation of the influence of concentration, which in the experiment revealed an increase close logarithmic.

5.11.2 Application and Validation

The process in the continuous MEC is used to validate the calculation approach. In the process the particle behavior showed to change over time. While at the beginning of the process more than 40% particles were separated by centrifugation, after several hours 99.9% were separated at identical process parameters. The agglomeration model above was introduced. The particle size distribution was determined before and after ultrasonic treatment and is shown in Figure 5-47. Particles showed to change by an order of magnitude. In the calculation of the separation of altered particles, the respective size distribution was taken into account. It compares well with the experiments. A consequence is that data on altered particles is necessary for the estimation of the process.

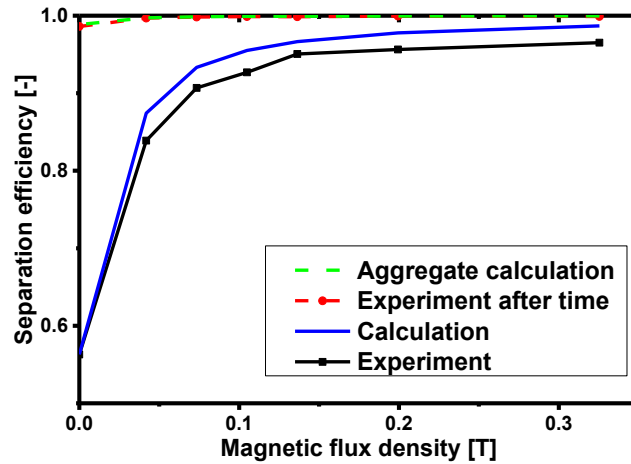


Figure 5-47: to the curve shown in Figure 5-38 a calculated model curve based on the two size distributions was added and shows a good agreement with the final separation

The influence of the volume flow in the model is shown in Figure 5-48 left. The volume flow was adapted to the experiment with an initial particle diameter of 30 μm . The need to is caused by the unknown agglomerate size of the particles before entering the device. The concentration influence is in Figure 5-48 right, appearing linear on a logarithmic scale similar to results shown in Figure 5-23.

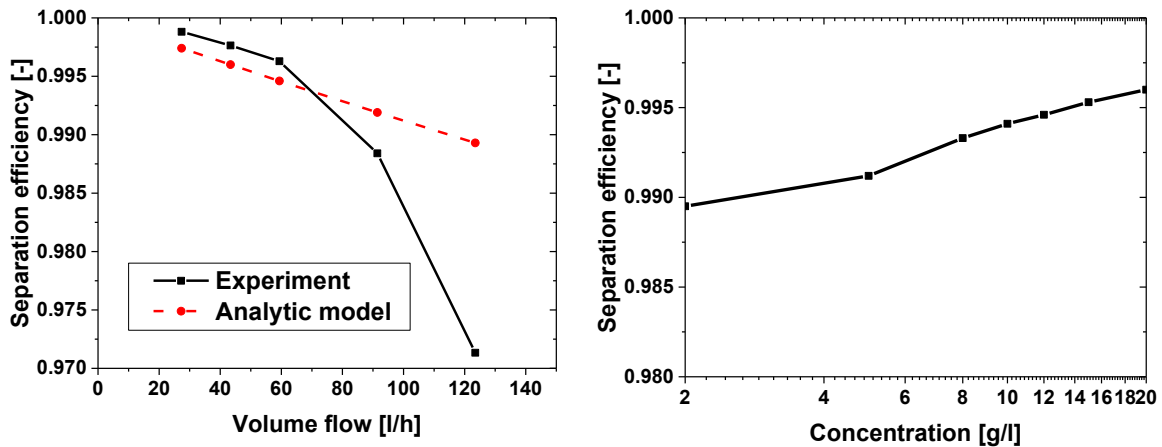


Figure 5-48 left: the calculation for different volume flow needs to be corrected with an additional agglomeration factor (fitted here with 2.5), but then compares acceptably; the concentration calculation shows a logarithmic influence above a certain concentration threshold (same factor 2.5)

5.12 Theoretic Comparison of Magnetically Enhanced Centrifugation with Conventional High Gradient Magnetic Separation

There are several HGMS designs competing with MEC, some of which were presented in Chapter 5.1.5. As both HGMS and MEC have specific advantages, a short comparison is provided. Several factors are important when choosing a system. These include:

- Investment and maintenance cost,
- Selectivity,
- Separation performance,
- Ease of use,
- Batch-wise vs. continuous mode,
- Discharge performance,
- Possibility of performing different operations in one machine and
- GMP conformal use (for some applications).

HGMS in a rotor stator or Halbach-based HGMS device 5.1.5 is a rather simple process which is cheap, easy to realize and easy to adapt for specific needs such as GMP conformity for biotechnological applications. It is more stable and cheaper, and selectivity is not compromised by centrifugal forces. The core advantage of the more sophisticated and expensive MEC is the continuous use and hence the avoiding of dead times, which makes up in several processes for the biggest part of time. A comparison of the financial point of view is as well interesting. Table 5-6 shows a comparison of investment costs, approximate costs of the set up and of the magnetic field strength of MEC and HGMS devices.

Table 5-6: Overview over approximate cost and parameters for different HGMS devices

	MEC	Permanent magnet MEC	Halbach- HGMS	Electromagnet- HGMS	Permanent magnet HGMS
Investment	60 000 €	25 000 €	10 000 €	45 000 €	10 000 €
Electricity consumption	6.6 kW	2.2 kW	0	4.4 kW	0
Magnetic Field Strength	0.2	0.2	0.34	0.2	0.4

An additional advantage of MEC is the fact the wire matrix can be omitted completely. This might enable the separation of particles from suspensions containing fibers which block in a filter. Separation does not break down in MEC without wires implemented, but is still above 60% due to the centrifugal separation of large agglomerates. Table 5-7 shows advantages of MEC over conventional HGMS and vice versa.

Table 5-7: Advantages of MEC and over conventional HGMS

Advantages of MEC	Advantages of HGMS
Separation possibility of media with fibers, which would block a filter, by eliminating the filter based on magnetically induced agglomeration and centrifugation	Low investment and maintenance effort in comparison with MEC, more stable process
Continuous process possible	No Restriction to longitudinal magnets
Volume flow is high due to low dead times	Selectivity is not reduced by sedimentation in a centrifugal field

There are advantages to both systems. Generally MEC is preferable to process high volumes, while HGMS is better suited for batch-wise processing of small amounts including performing subsequent steps in the device.

6 Separation Processes

The application focused on in this work for MEC is the separation of protein in the biotechnological downstream processing.

6.1 State of the Art

The separation of the two steps adsorption and separation allows a more flexible use and high volume flow, as both steps can be optimized separately. It is as well possible to make both steps continuous, which is complicated in adsorption chromatography with moving bed or annular chromatography. Magnetic fishing allows as well In-Situ separation [Kappler'09; Cerff'13; Cerff'13]. This requires that the pretreatment of the fluid before adsorption is not necessary or compatible with the process. This is not evident as bacteria might adsorb to ion exchange particles. Some separation steps might be omitted compared to conventional downstream processing [Franzreb'06]. The process is similar to small scale by using large reactors instead of microreactors, but separation steps are performed by pumping the liquid through an HGMS device. After separating the particle from the elution liquid it is returned in a new process cycle.

6.1.1 Competing Technologies

Besides conventional treatment described in Chapter 2.7.1, there are several selective approaches based on adsorption, which are developed or currently in research such as

- Adsorption chromatography,
- Expanded bed adsorption,
- Travelling cooling zones reactor and
- Continuous magnetic extraction.

These processes are significantly more expensive and more selective than conventional treatment due to chemical ligands. Examples for ligands are given in Chapter 6.1.2. The adsorption-based selective methods are explained shortly to show alternatives to the presented method.

Adsorption Chromatography

Adsorption chromatography is one of the finest and most expensive selective separation processes established in industry. It is based on an adsorbent fixed in a packed bed. The column is flown through by process liquid. Target matter binds selectively to the functionalization. The process allows a highly selective separation. It is however expensive in investment and use. Usually functionalization is expensive, and homogeneous packing of the column is difficult. A large amount of functionalization is necessary and expensive.

Expanded Bed Adsorption (EBA)

In EBA, called as well fluidized bed, a column filling is flown through by a feed stream from bottom to top. The flow velocity is controlled to equalize the resistance force of the fluid on the particles with gravity. This increases the space between particles called expanded or fluidized bed, which allows the cell debris to pass without blocking the bed. In theory it is not necessary to remove particulates before adsorption, and it results in a higher product recovery in a shorter time period. The volume flow is hence higher and the contact is more intense than in a packed bed. The equipment is similar to packed bed chromatography. Particles segregate depending on their size, larger particles are hence found in the bottom part. Particle sizes range from 50 to 400 μm , their density is 1.1-1.3 g/cm^3 . The elution is usually performed in packed bed mode using a downward flow; a continuous process is hence not possible. This seems to be the most direct competitor to HGMF processes yet. It currently seems to lack an industrial break-through. A disadvantage is the fact the particle size needs to be defined and the process well controlled to avoid settling or flushing the bed out [Johansson'96; Hjorth'97; Fernandez-Lahore'99; Chang'00].

Travelling Cooling Zones Reactor (TCZR)

A travelling cooling zones reactor was developed in the EU-Project MagPro²LIFE by Müller at KIT. It essentially is based on media which adsorbs depending on the temperature, but releases the product when cooled. A column is flown through by a feed stream, while target matter adsorbs to the functionalization at a controlled temperature. An external tempering device moves in flow direction slower than the fluid, which cools the column at the specific place. The cooled functionalization releases the target matter, which then flows with the feed stream and is adsorbed downstream again. Each time the cooling zone reaches the outlet of the column, the protein collected on top is discharged and collected separately. The cooling zone is displaced again to the bottom and starts again. The device is currently only in research state and limited by the availability of temperature dependent functionalization [Muller'12]. Figure 6-1 shows a photograph of the TCZR.

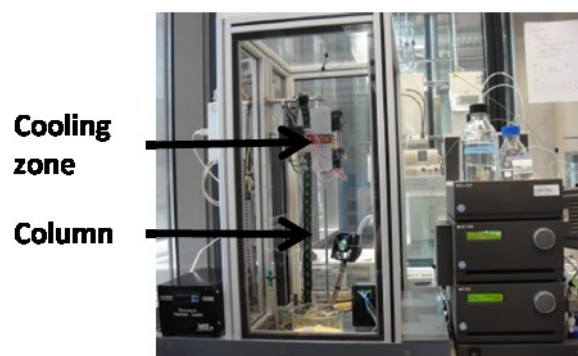


Figure 6-1: Photograph of TCZR [Source: Müller, KIT]

Continuous Magnetic Extraction (CME)

Continuous magnetic extraction bases on the separation of the process liquid to two phases. It was developed as well in the EU-Project MagPro²LIFE. Magnetic forces are not necessary in the process, but enhance the motion of particles to their phase. In downstream processing, proteins adsorb to magnetic particles. Both protein and adsorbed particles are separated to one phase, while different matter stays in the second phase. Subsequently the protein is eluded from the particle. The extraction is repeated with particles again collecting in one phase, while the protein stays in the second phase, being hence separated and eluded. A magnet on top accelerates magnetic particles moving into the top phase. Volume flow is low as chemical phase separation needs to be awaited. As the process is working without the need of a magnet, but based on extraction, the magnetic field gradient is rather low, and technically not even necessary for the process [Becker'08; Fischer'11; Fischer'12a; Fischer'12b]. In contrast to magnetic separation, this process was reported to work well on colloidal particle systems. Figure 6-2 shows a photograph of the two phases separating (left) and of the complete device (right).

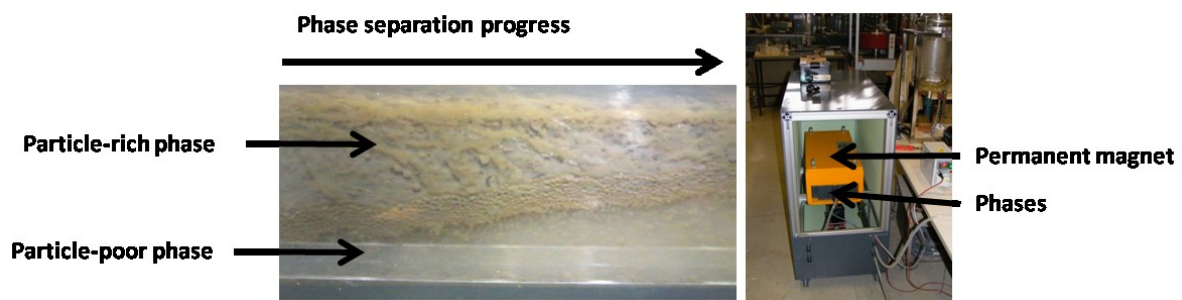


Figure 6-2: Phase separation in CME (left); CME device (right) [Source: Fischer, KIT]

6.1.2 Ligands

Ligands are necessary for selective adsorption as well by magnetic particles as in packed or expanded beds. In general more specialized ligands are more expensive, and elution might be more difficult. While ion exchange ligands are common on the market, prices for more selective functionalization are high. Table 6-1 gives examples of ligands.

Table 6-1: Classification of surface functionalization with target substances [Franzreb'06; Eichholz'10]

Binding	Examples for Ligands	Target substances
Unspecific	Cation exchanger e.g.: -COOH, -SO ₃	Positively charged substances (cations)
	Anion exchanger e.g.: -NH ₂ , DEAE, - N(CH ₂ CH ₃) ₂	Negatively charged substances (anions)

Group specific binding	Cofactors, Cosubstrates, Dyes Metal chelate Streptavidin, Avidin	Encymes His-Tag-Proteins Biotylnlated Proteins
Monospecific bindings	Antigen or Antibodies Hormones or Receptors	Antibodies or Antigen Receptors or Hormones

Ion exchange based adsorption uses electrostatic forces, binding only charged molecules. Figure 6-3 shows the principle for the adsorption of a protein of an isoelectric point of 6 to an ion exchange functionalization. The pH of the medium is increased above the isoelectric point pI of proteins to adsorb it to anion exchange ligands, or below to adsorb to cation exchange ligands.

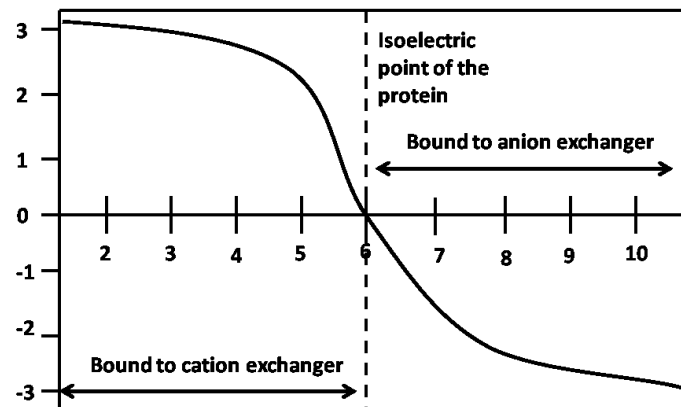


Figure 6-3: adsorption to ion exchange particles as a function of molecule charge depends on the isoelectric point of the protein and the pH; if the product is negatively charged (anion, basic, reduces pH), the pH is increased to bind it to an anion exchanger, a positive cation (acidic, increases pH) the pH is lowered to bind it to a cation exchanger [Silvestre 2009]

6.1.3 Areas of Application

Different application areas are possible for HGMS. It is possible to use HGMS directly to separate wear out of gear oil in case its magnetization is high enough [Menzel'12]. The possibilities by synthetic functionalized particles in HGMP extend the application area. Table 6-2 gives an exemplary overview. Based on functionalized particles, it is possible to perform the downstream processing in biotechnology. Another use is the processing of waste water to either eliminate contents (e.g. mercury), or to recycle components for reuse (e.g. phosphate). The scales of the processes are different, with applications in red biotechnology of a few kg / year to many m³/h in waste water treatment. The budget varies as well significantly from several m€/kg in red biotechnology to a few € / ton in waste water treatment. The particle costs, and usually even more its ligand costs, decide about the process gain. As the unspecific ligand costs are usually not depending on the material, a profitable use of HGMP seems possible.

Table 6-2: Different applications currently in research for HGMS

Area	Feed stream	Target	Particle ligand	Concentration	Viscosity [mPa s]	Selectivity	Price	Process scale
Downstream processing in biotechnology [Franzreb'06]	Fermentation broth	Proteins	Ion exchange, specific functionalization	1-10 g/l	1-10	High	High	Low
Wear from gear oil	Gear oil	Wear: iron compounds	- (Direct separation)		$10^2 - 10^6$	Low	Low	Low
Elimination in Waste water (mercury [Parekh'11]; arsenic [Li'10]; radioactive substances [Ebner'01])	Waste water	e.g. Mercury; radioactive Cesium, Strontium, Arsenic	e.g. dithiocarbamate; Silica	0.1-10 mg/l	1	Low	Low	High
Recycling in waste water [Franzreb'03; Bischoff'13; Shafy'13]		e.g. Phosphate	e.g. Anion exchange (TMAP, COOH)					

6.2 Targets

The current work focuses on the protein separation for red and green biotechnology, i.e. the separation of proteins for pharmaceuticals from fermentation broth, and the separation of proteins from an industrial soy stream as a food additive. Target of the current chapter is the investigation of protein separation by HGMF using MEC. The demonstration of the possibilities of MEC in separation processes

- out of fermentation broth and
- out of an industrial side stream (waste stream of soy whey).

The target of the adsorption modeling was the modeling, implementation, simulation and validation of an approach for the simulation of protein adsorption in HGMF. This is a basis for the process design. It might be integrated in a complete simulation of the process or parts of it. Additionally the feasibility in terms of calculation power was investigated. The target is hence:

- the development of a model for the adsorption of protein to functionalized dispersed particles.

6.3 Simulation of the Adsorption

The simulation was set up to show its feasibility and limits. The system chosen for the simulation is a microreactor, as this is a small device for which limited computational power is necessary. Additionally, the device is common in analytics. The simulation models the

complete process, which is illustrated in Figure 6-4: initially a suspension in a μl -reactor contains a protein; particles are added and moved during a defined time span (Figure 6-4 left). Then the particles are separated by magnetic forces to the wall (Figure 6-4 middle) and the supernatant is withdrawn with a pipette (Figure 6-4 right). Subsequently an elution liquid is added, resolving the protein from the magnetic particles.



Figure 6-4: Treatment of magnetic particles in a μl reactor

6.3.1 Methods

The adsorption process in a μl sized reactor was simulated by implementing protein as a species in Ansys Fluent 13. The grid was created by the Ansys Workbench and had 30.000 cells. Only a quarter of the complete reactor was simulated, with the boundary condition symmetry, to limit the calculation power by taking profit of the symmetry of the system. A laminar simulation was realized. The species model of Ansys Fluent was used for the simulation of protein. Magnetic particles were introduced as a discrete phase. The placement of particles was realized randomly by a User Defined Function (UDF). Adsorption of the species to particles integrated in a Euler-Lagrange approach was realized by programming a UDF in the commercial code Ansys Fluent. The particle motion was realized by a function moving them randomly for a defined time span (20 s). After adsorption, a function for magnetic separation by a cylinder-shaped magnet separated particles to the wall. Then the change to an elution liquid was modeled by an elution function. The mixing function was applied again to model redispersion during elution. Five different UDFs were programmed and linked to the program to introduce magnetic particles as starting condition and to model mixing, adsorption, separation and elution:

- Particle placement was performed by an aleatory function (starting condition).
- Particle mixing was calculated by an aleatory force during adsorption and elution.
- Particle separation was performed by applying the magnetic field of a cylinder-shaped magnet during separation.
- Different models for the adsorption simulation were set up out of which one is presented below based on a linear adsorption isotherm and on mass transfer.

- The elution was performed by reducing the maximum load of the linear adsorption isotherm to model competing adsorption of NaCl to the ligands of the particles.

To limit the computational effort, a single particle of 100 μm size represented a mass equivalent of 1 μm particles. The particles were created hence at 100 x their physical size, reducing their number to 500 instead of $5 \cdot 10^8$. This was compensated by implementing the adsorption kinetics based on a 1 μm particle. In other words, one large particle represents many small particles, while adsorption was kept constant. This approach allows the direct comparison of simulation and experiments, despite the simulation of a smaller number of particles. The approach was inspired by a dense discrete particle model, in which one particle models a cluster. A disadvantage is the fact that less particles result in a less homogeneous distribution and that the particle velocity might be different resulting in a different diffusion speed. The adsorption of 100 μm sized particles, which are as well available, is possible directly with this model.

Adsorption Modeling

An initial concentration of 0.1 g/l was applied. The experimental adsorption isotherm of lysozyme to Merck MagPrep SO_3 (cation exchange) in Figure 6-10 (left) was realized in the simulation. While the first simulation approach was based on a Langmuir adsorption isotherm, the final simulation was based on a linear adsorption isotherm (respectively the special case of a Freundlich isotherm for $n=1$). The linear isotherm in this case fitted well with the experimental model and is easy to implement in a computer code. The maximum particle load determined is 0.77 g/g. The amount of adsorbed protein was calculated from the protein concentration in the cell. Equilibrium is achieved between the amount of protein adsorbed to the particle and present in the fluid. The protein adsorbs in the model hence depending on the overall concentration in the cell. Additionally the adsorption is limited kinetically by diffusion. The protein transport was modeled by convection in CFD based on the model in Chapter 2.3, (2-73) to (2-75). The diffusion is not only necessary for physical correctness, but as well to be independent from grid size. The diffusion coefficient D determined out of (2-74) was $1 \cdot 10^{-10}$ m^2/s . Values which were used in the adsorption simulation are summarized in Table 6-3. Particles moved during adsorption by an aleatory function of a maximum acceleration of the earth gravitation for 1 s. This approximates particle motion when being dispersed or moved by shaking or stirring.

Table 6-3: Values used in the adsorption simulation

Formula sign	Unit	Value	Description
Q_{max}	[g/g]	0.77	Maximum load on a particle
c_{max}	[kg/m ³]	0.1	Maximum concentration at which protein is adsorbed

m_p	[kg]	1.047e-9	Particle mass (100 μm)
D	[m ² /s]	1.162e-10	Diffusion coefficient from Polson Correlation
Sc	[-]	8600	Schmidt number
M_M	[g/mol]	14300	Molar mass of Lysocyme
C_{Salt}	[mol/l]	0.3	Salt concentration

Separation and Elution

After adsorption, the particles were separated to the reactor wall by implementing the force of an external cylindrical permanent magnet. Particles collected on one position at the reactor wall. A DEM model was applied additionally for magnetic separation. After finished separation, a different species model was applied to model the desorption. The function parameters were changed to simulate a high salt content as competitive adsorption. In this approach the salt was modeled as reducing the maximum capacity of particles by concurring adsorption of the same affinity. A 0.3 M salt concentration was applied. Physically, the electronegativity of Na^+ plays an important role, which was neglected as a first approach. Instead of magnetic forces, aleatory mixing was applied again.

Validation

The validation experiment was performed by measuring the adsorption three times each at 5 s, 10 min and 20 min. The adsorption time measured was defined as the time between adding magnetic particles and separating them to the reactor wall. The specified time was set to the collection of the particles at the reactor wall, not the removing of the supernatant. The feed concentration of lysocyme was 0.74 g/l, which was as well set as starting condition in the simulation. MagPrep SO_3 particles were used for the test.

6.3.2 Results and Discussion

The consecutive adsorption, separation and then elution were performed. Figure 6-5 left shows the protein amount in the reactor during the first 20 s of adsorption. The adsorption is fast, being almost finished after the time span with most of the protein bound to the particles. Due to the modeling of the concentration and hence reduced diffusion at low concentrations, the adsorption kinetics drop significantly after 10 s. Figure 6-5 right shows the distribution of the protein load on magnetic particles. The distribution is narrow, being in between 0.6 and 0.755 g/g for all of the particles.

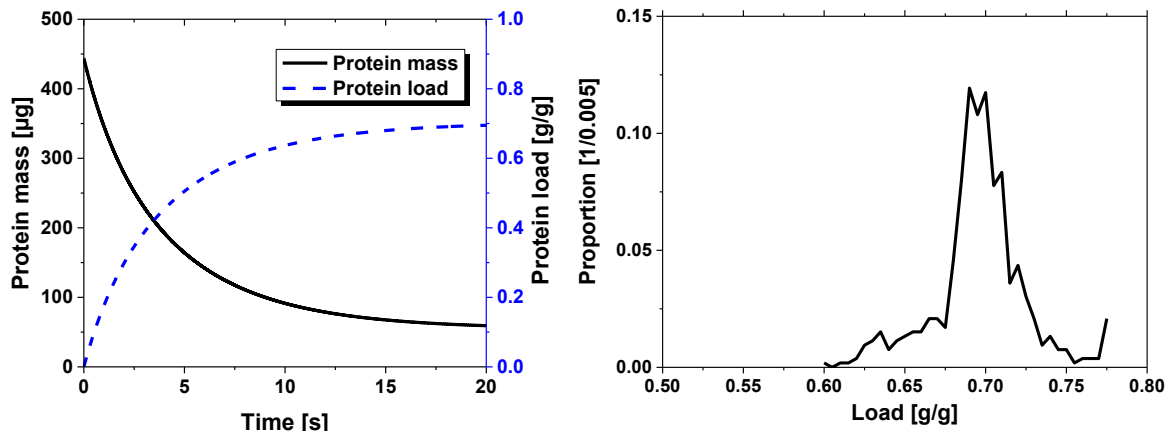


Figure 6-5 left: protein proportion left in a microreactor depending on the time; right: distribution of the load on particles

Figure 6-6 left shows the protein distribution in a quarter of the microreactor and the particles coloured by protein adsorbed at different times. The distribution of protein in the reactor is homogeneous, with a very small change in the concentration at different positions. Figure 6-6 right shows the distribution of magnetic particles in the reactor, and their weight including protein. The distribution of particles in the reactor and of protein on the particle is homogeneous. The weight of a particle without protein is 1.047 μg , resulting in a load up to 0.79 μg corresponding to 0.75 g/g, which is close to the maximum of 0.77 g/g. The simulation was performed for 100 μm particles as mentioned above to be able to simulate a whole reactor segment.

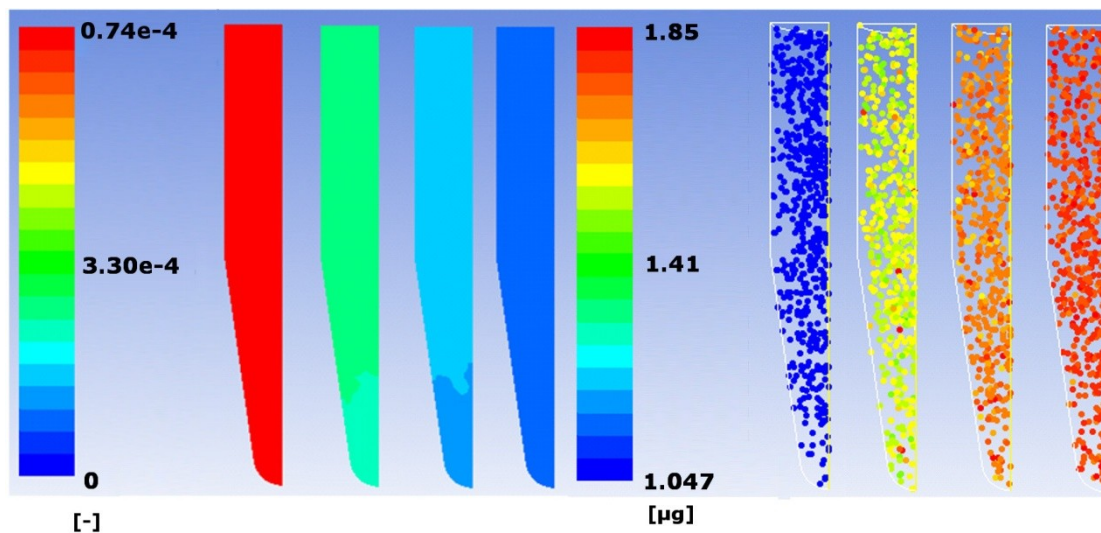


Figure 6-6 left: proportion of protein left in the microreactor (0-0.74 m-%) after 0s, 5, 10 and 20 s; right: particle weight in μg of 100 μm particles including protein at these time steps

Modeling of Magnetic Separation and Elution

Figure 6-7 left shows the amount of protein adsorbed to magnetic particles in the simulation after adsorption is finished and after the particles are separated to a cylindrical magnet. The distribution is equivalent to the distribution in Figure 6-5 left. Figure 6-7 middle shows the distribution of magnetic particles during separation after 0, 2 and 10 ms. Magnetic particles separate to a point close to the magnet, the center of the reactor. The place is similar to the illustration in Figure 6-4 right. Some particles are stuck at the bottom and top of the reactor, which is a problem resulting from the simulation of a quarter of the reactor: particles move in a circular track to the magnet, with the symmetry modeling trapping particles in both distant corners. The track is illustrated by a red arrow. Figure 6-7 right shows the distribution of particles and of protein after elution in the model. Elution showed in this modeling approach to be much faster than redispersion, showing most of the protein is eluded and the particle weight is 1.047 μg after 20 ms of elution. The elution model might not be sophisticated enough, as it assumes perfect salt distribution instead of tracking salt in a species model similar to the protein.

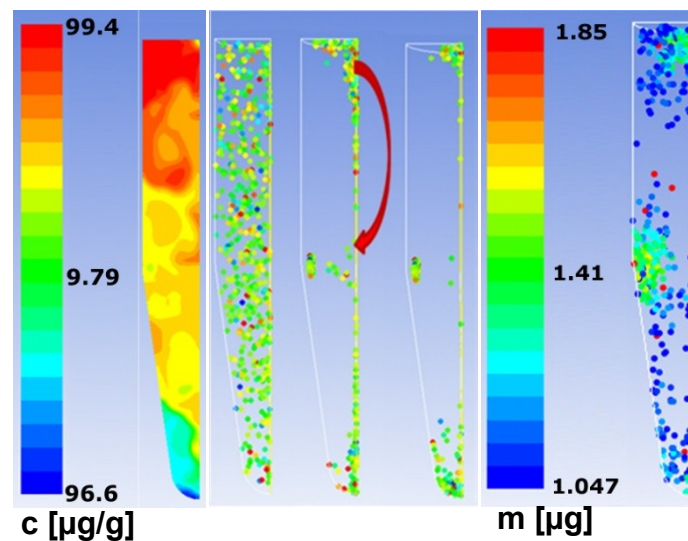


Figure 6-7: the concentration of protein after adsorption in the fluid is shown on the left; the magnetic separation after 0, 2 ms, 10 ms shows quite rapid separation compared to adsorption times based on 100 μm particles (middle); the sum of the particle mass of 1.047 μg and the adsorbed protein is shown: the elution is very fast in the model, showing strong elution 20 ms after adding elution liquid (right);

Validation

A comparison with experimental values is difficult for the high variation. A test was done on the adsorption after 5 s, 10 min and 20 min. It is compared to the simulation over 20 s, which was performed at the same conditions, in Figure 6-8. The experimental and the simulation result delivers a similar result. The variation in the experiment and in the measurements is very high though, resulting in a weak validation. A more sophisticated approach with a higher

number of data points would be necessary for a reliable validation of the experimental adsorption of protein to magnetic particles.

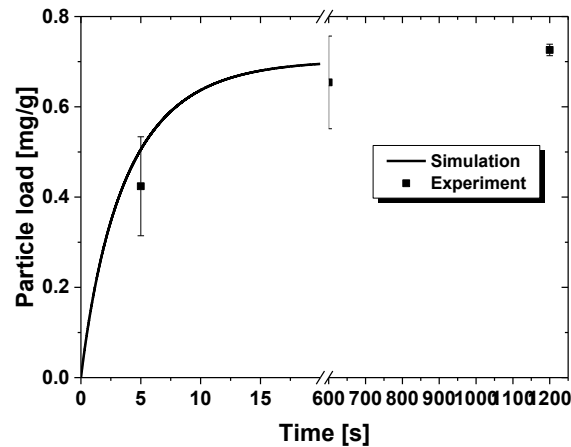


Figure 6-8: the necessary time for adsorption in an experiment compares well with the simulation at 5 s, and 20 s, and shows almost finished separation compared to 600 and 1200 s; note that the standard deviation is high though and validation hence weak

6.4 Separation of Protein out of Hen Egg White by Magnetically Enhanced Centrifugation

6.4.1 Materials and Methods

First tests in lab scale were performed by the model proteins lysozyme and ovalbumin in Hen Egg White (HEW), as this medium is easily available and has good separation properties. By choosing two different substances with a different isoelectric point, it is possible to perform tests on both anion and cation exchange particles. More sophisticated ligands were not available. Lysozyme was separated by a cation exchange particle (MagPrep SO₃) out of pure water (0.1-1 g/l) and out of 30 x diluted hen egg white (33.7 g/l). Its isoelectric point is 10.5 and isolated from other proteins below 7.2, except for Avidin which is only 0.05 % protein. The ovalbumin separation was tested out of hen egg white at 80 x dilution (25 g/2l). Its isoelectric point is 4.8 and hence close to several other proteins. In theory it is possible to separate it from ovotransferrin and ovoglobulin as it has a higher affinity to anion exchange particles for its lower pI, but not from ovomucoid at an even lower pI. The target was the investigation of influencing parameters and optimizing the process before moving to a larger scale in the batch-wise MEC. Table 6-4 gives an overview over the proteins in hen egg white.

Table 6-4: Protein content of hen egg white [Desert'01]

	Protein percentage [%]	Molecular weight [kDa]	Isoelectric point
Ovotransferrin	13	77.7	6.2-7.2
Ovalbumin	54	45	4.75-4.94
Ovomucoid	11	28	3.83-4.41
Avidin	0.05	68.3	10
Lysozym	3.5	14.3	10.5
Ovoglobulin	8	49	5.5-5.8
Other	10.45		

Optical methods and SDS-Page were used in this work for protein analytics. Another very important, yet expensive, method is chromatography. In general the determination of protein amounts is less exact and more error-prone compared to the determination of solids.

Lysozyme Investigation

Different lysozyme concentrations (0.1-1 g/l) were prepared and 1 mg of particles was added. The load of protein on the beads is determined from the protein in the supernatant optically at 280 nm based on a calibration curve. Elution tests were performed by first binding lysozyme to magnetic particles, then adding different concentrations of elution buffer. To determine the influence of particle concentration and pH, hen egg white was prepared, the adsorption was done during 30 min after dilution and rebuffing, then the elution was performed. In this case the evaluation had to be done by an SDS-Page gel. Table 6-5 gives an overview over devices used for analytics.

Table 6-5: Overview over used devices and materials

Method	Device producer	Part	Model
SDS-PAGE	Carl Roth	Cell	Y001.1
		Gel	Roti-Page Precast Gel
		Marker	Roti-Mark 10-150
		Thermo-Mixer	HLC MHR 13
		Power supply	Consort EV243

The Ovalbumin Process

The complete process for the separation of ovalbumin consists of five steps after preparing the hen egg white. 25 g of HEW was dispersed in 2 l of water to dilute it 80 times and to rebuff. The dilution was performed for tests on low protein concentration, but was as well necessary to reduce the viscosity of HEW. The pH was adapted to 6, the buffer was a 20 mM phosphate buffer (see Table 8-8 in Annex 8.5.5). 6 g of particles were washed in the same buffer for use in the process, resulting in a concentration of 3 g/l.

1. As first step the adsorption took place during 20 min in a feed tank.
2. In the next step the magnetic centrifugation was performed at 1500 rpm, a magnetic field strength of 200 mT and a volume flow of 60 l/h. For draining, the magnet was still set at 200 rpm, but air was fed and the centrifuge was stopped.
3. Then a washing step was performed in the centrifuge, i.e. the washing buffer was fed at a circumferential speed of 600 rpm to cover the walls with liquid, while the magnet was switched off. A stirrer speed of 112 rpm was applied for 3 min during washing. Magnetic particles were sedimented by magnetic forces and centrifugation. Then the machine was drained again.
4. The washing step was repeated for elution. This was done at the same conditions as washing during 10 min, but by adding 1 M NaCl to the washing buffer.
5. Subsequently particles were transferred to a buffer of low ionic strength for reuse and discharged. The redispersion was done while pumping 2 l at 240 l/h in a cycle for 5 min with the peeler knives turning at 112 rpm and then discharging particles to prepare them for the next cycle. The complete process is illustrated in Figure 6-9.

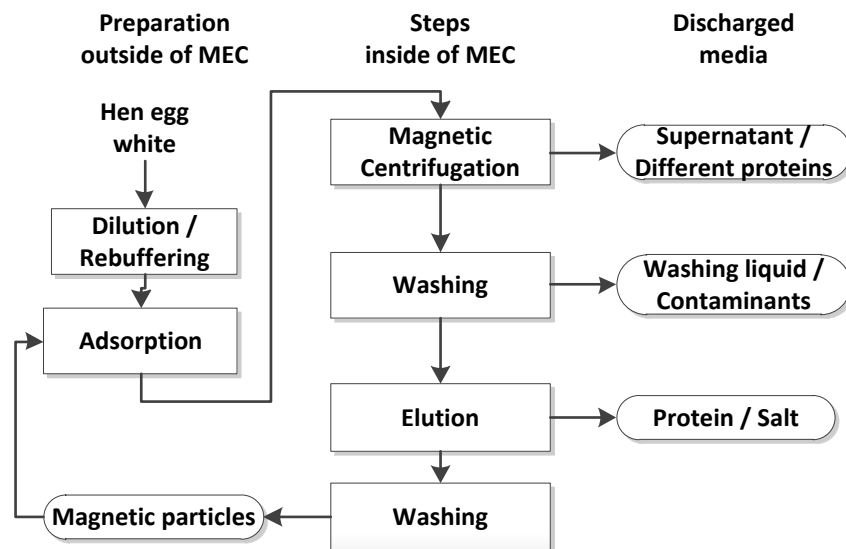


Figure 6-9: Flow chart of the separation of ovalbumin from hen egg white from the preparation, to the separation and to the discharged media

The particle concentration was determined gravimetrically as described in Chapter 5.3.2. For analytics on protein determination by SDS-Page, a commercial gel (Carl Roth, Roti-Page 4-20% gradient) was used. The samples were given on the gel without change of buffer. For the determination of relative protein amounts, the tool ImageJ was used.

6.4.2 Results and Discussion

Lysocyme Separation

The adsorption isotherm was determined, the result was as well used in the modeling to know the maximum protein load on the particles. The result and a Langmuir adsorption isotherm, which was fitted to the experimental values, are shown in Figure 6-10 (left). The maximum protein load on particles is determined as 0.77 g/g, K_D was determined being 0.038 g/l. The result is promising for this particle kind, as particles adsorb almost their own weight in lysocyme.

An interesting option to reduce the non-separated product amount to a minimum with only a small amount of particles is repeated adsorption in a countercurrent process. An outlook of a process taking advantage of this is described in Chapter 0. Figure 6-10 (right) shows repeated separation using unloaded particles. Interesting in case of repeated separation is the low final protein fraction lost and hence high yield which might be achieved in a counter-current process. The protein concentration in the supernatant is determined, before transferring the supernatant to another microreactor containing new particles. After three iterations a very low final protein concentration is achieved, reducing from 0.68 g/l to 0.29, 0.04 and finally 0.02 g/l.

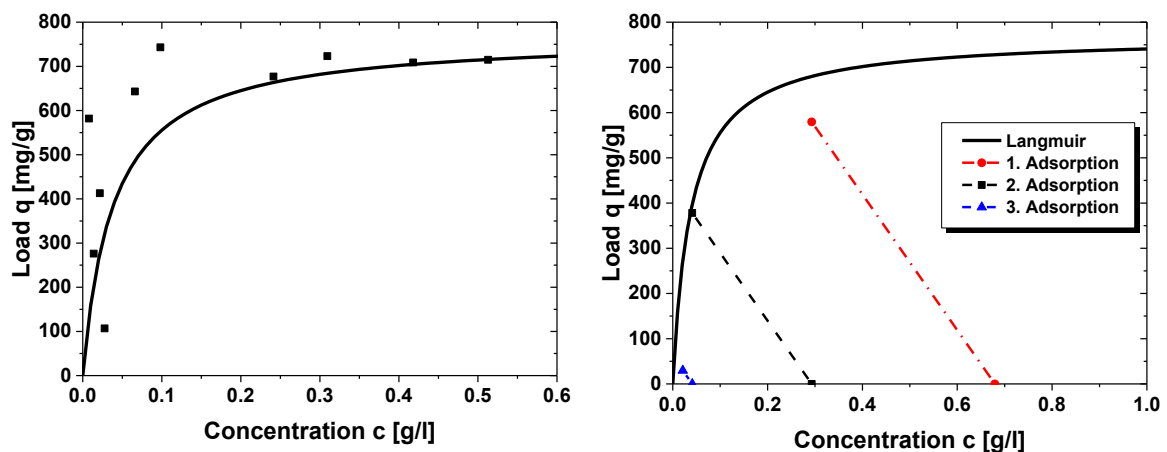


Figure 6-10 left: the separation of lysozyme by MagPrep SO₃ particles with a fitted Langmuir isotherm shows a maximum adsorption of 770 mg/g; right: repeated adsorption in case of a multi-stage process allows to reduce the protein amount to a low concentration by a low particle amount inserted

Elution is the second part of the process which is very important, not only to collect the target protein but as well to reuse particles in the next cycle. Elution was done by transferring particles to a 1 M NaCl buffer to the particles after supernatant is withdrawn. Figure 6-11 shows the hen egg white on the left, the hen egg white after adsorption and the eluded liquid. Interesting is the lysozyme band at 15 kDa, showing that most of the protein is unloaded in

the elution. There is few lysozyme visible in the supernatant but in the elution (0.067 g/l particles SO₃, 33.7 g/l HEW). A quantitative analysis is not possible due to a weak quality of the gel.

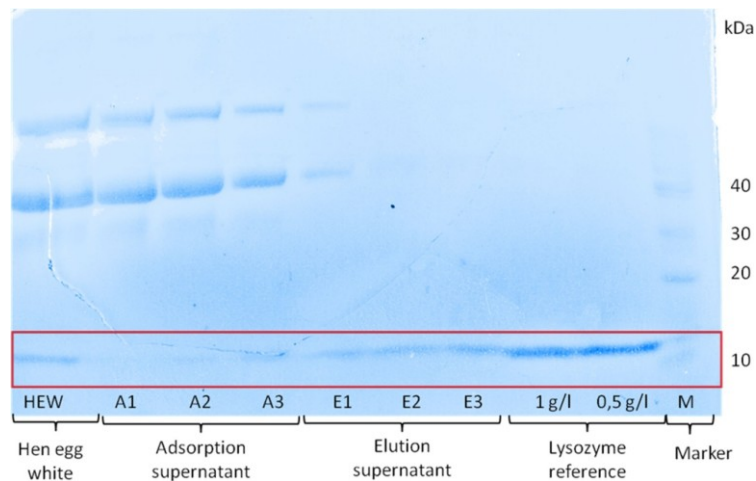


Figure 6-11: adsorption of lysozyme from hen egg white and elution shows that the process works acceptably

Ovalbumin Separation

It is possible to increase the selectivity and yield by adapting the particle concentration and adsorption conditions to the specific system. The ovalbumin separation was performed out of hen egg white combined with SDS-Page analysis, as the selectivity investigation was the main target. Figure 6-12 (left) shows a study on the concentration of hen egg white. It is visible that the concentration can be adjusted for the best yield and purity. In this case the highest separation of ovalbumine out of hen egg white was achieved at a concentration of 3 g/l. Above this concentration an increased separation of contaminants resulted, showing the adsorption of ovotransferrin at 78 kDa and to a lesser extent ovomucoid at 28 kDa in Figure 6-12 left.

A study on different pH values was performed in Figure 6-12 right. A pH of 6 showed to be well suited to exclude separation of contamination. The selectivity is reduced at pH 7, which creates a higher affinity of contaminants with an isoelectric point higher than that of ovalbumin.

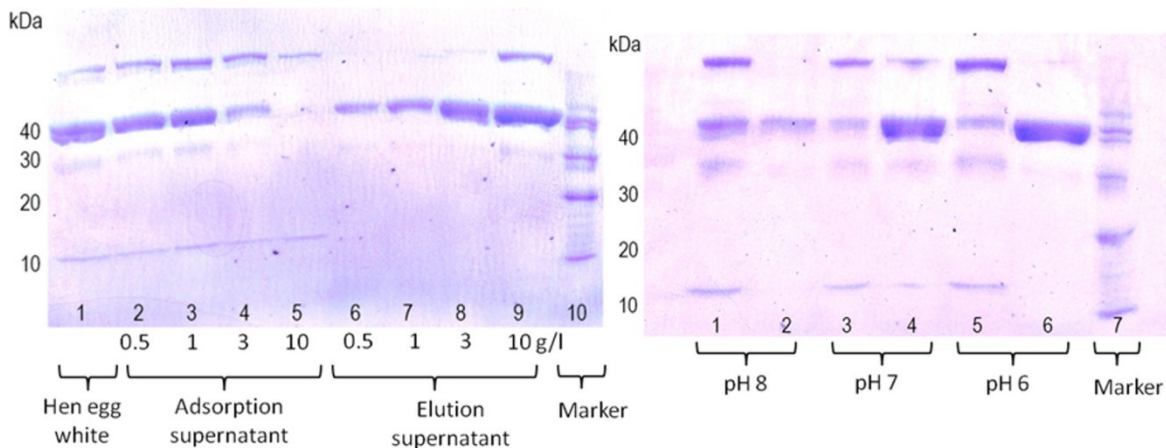


Figure 6-12 left: 1) hen eggwhite solution; 2) adsorption at 0.5 g/l; 3) adsorption at 1 g/l; 4) adsorption at 3 g/l; 5) adsorption at 10 g/l; 6) elution at 0.5 g/l; 7) elution at 1 g/l; 8) elution at 3 g/l; 9) elution at 10 g/l; 10) Marker; the separation of ovalbumin from diluted hen egg white in μ l reactors at pH 8 shows the best performance at 3 g/l with ovalbumin lost below and selectivity reduced by different proteins bound at 10 g/l; **right:** 1) adsorption at pH 8; 2) elution at pH 8; 3) adsorption at pH 7; 4) elution at pH 7; 5) adsorption at pH 6; 6) elution; 7) Marker; at different pHs at 3 g/l the adsorption works best at pH 6 while selectivity is reduced at pH7

The elution was as well tested on a gel shown in Figure 6-13. Different salt contents of 0.1 M, 0.3 M and 1 M were tested for elution. While 0.1 M salt content showed to be too low to completely desorb the protein, a concentration of 0.3 M NaCl showed to be sufficient for the elution. For the process test, 1 M NaCl was realized because no negative effects of a higher salt content were found but even a slight improvement would be welcome.

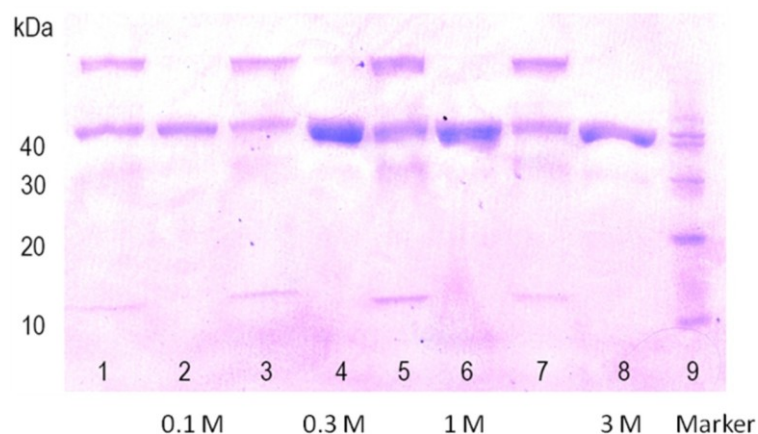


Figure 6-13: 1) adsorption; 2) elution at 0.1 M NaCl; 3) adsorption; 4) elution at 0.3M NaCl; 5) adsorption; 6) elution at 1 M NaCl; elution shows no improvement above 0.3M NaCl

The Process

Cation exchange particles were not available at sufficient scale to realize lysozyme separation in the MEC. A test on the separation of ovalbumin in the MEC was hence performed with a different charge of anion exchange particles after defining parameters in the process condition

test. The separation of ovalbumin from hen egg white is shown in Figure 6-14. The protein content in the original hen egg white diluted to the process conditions (25 g on 2 l) is shown in the first band. The next bands show proteins in the supernatant before and after centrifugation, proteins in the washing step, in the elution step and in the liquid which recovered particles. Obviously a large percentage of the ovalbumin was adsorbed. The ovalbumin was partly recovered in the washing step purely, and in the elution step. The concentration was increased by using a lower elution liquid amount than feed amount. In summary, the process worked well for the purification of ovalbumin.

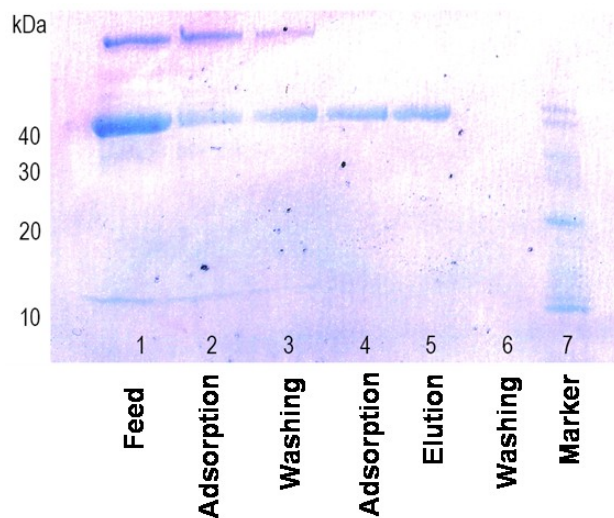


Figure 6-14: 1) 12.7 g/l heng egg white solution; 2) adsorption before centrifuge; 3) adsorption after centrifuge; 4) washing step ; 5) elution; 6) washing and discharge; 7) Marker; separation of ovalbumin from hen egg white by MEC using anion exchange particles; [Lindner'13]

After the process, the particles were discharged from the centrifuge. The discharge showed to be compromised by the low particle amount of 6 g available. In the first discharge only 43% particles were recovered, in the total over three discharges 65% were recovered. This represents 2 g of particles left in the machine. Previous tests showed that this amount is left in the centrifuge independent of the initial particle amount, which means that a higher proportion of particles is discharged in case of larger initial particle amounts. A particle amount of 6 g showed to be too low for an efficient use of batch-wise MEC.

6.5 Separation out of an Industrial Food Stream

As an industrial process for the use of HGMF by a MEC at large scale, the separation of BBI was tested. The initial feed stream was produced out of a industrial waste stream of soy by Dupont Solae in Aarhus, Denmark.

6.5.1 Materials and Methods

The separation of BBI was tested in two different devices. The small batch-wise MEC was used for the separation at the KIT. The large industry-scale MEC was tested at the company Solae in Aarhus for larger amounts of particles and soy whey. Tests in Aarhus were conducted in cooperation with technicians of Dupont Solae.

Separation in the Small Batch-Wise Magnetically Enhanced Centrifuge

The process liquid showed to be less suited for separation compared to hen egg white for a higher salt content and a larger amount of contaminating proteins at similar pI as the target protein. The stream was therefore pretreated by Solae with adsorption to Silica and a heat treatment to eliminate competing proteins. The feed broth contains the BBI, showing up around 12 kDa, and only one contamination at around 28 kDa. The target of the process is hence the increase in concentration and the transfer of the protein to another liquid, while selective separation from different proteins does not play a role. Two different anion exchange particle kinds were tested, Merck MagPrep TMAP and Orica MIEX. The soy sample was freeze-dried for storing. The small batch-wise machine was used for this test. The target of the test is the increase of concentration and the transfer to controlled media only containing water and salt. For separation particles are first washed in desalinated water to reduce ethanol, in which particles are stored. Then 25 g of MagPrep particles are added to 1.25 l of soy whey in a first test. In the second test, 50 g of Orica particles were added to 2.5 l soy whey. The particles are stirred for 10 min for adsorption. Then they are separated in the centrifuge, the supernatant is discharged and the particles are kept in the centrifuge. Particles are washed (0.7 l, 20 mM NaPh, pH 7), then the protein is eluted (0.7 l, 20 mM NaPh, pH 7, 1 M NaCl), then the particles are washed again. The process is similar to the Ovalbumin process presented in Chapter 6.4.1.

Separation in the industrial scale Magnetically Enhanced Centrifuge

Besides protein separation in a small centrifuge, separation was performed in the industry device set up by Andritz KMPT at Solae Dupont. Gels could not be done on place, because no factory acceptance test was conducted. Samples were shipped to KIT for analysis, but showed to be harmed during the transport. An analysis was performed by Solae Ltd. though, which is presented below. The basic process was similar to the realization in the small MEC.

As washing buffer 20 mM NaH_2PO_4 was used, the pH is set to 7 by HCl and NaOH, the conductivity was 2 mS/cm. The elution buffer is similar to the washing buffer with 0.5 M Na_2SO_4 resulting in a conductivity of 50 mS/cm. Particles were washed before the process in a washing buffer. Between processes particles were washed first in a washing buffer, then in an elution buffer, and finally again in a washing buffer.

For an exchange of the liquids, a displacement was performed from top to bottom. The elution liquid was displaced bottom to top to avoid mixing of the less dense salt suspension. The resuspension was done at a volume flow of 240 l/h, while stirring in both directions with the matrix for 5 min. A valve system was used to feed the centrifuge forward or backward.

An amount of 300 g particles were used to process 15 l of soy whey, corresponding to a concentration of 20 g/l. The concentration was high, which was necessary for the low activity of particles in the specific system. This reduced the amount of soy whey processed strongly, as the amount of particles was limited to an amount which can be stored in the MEC without influencing separation. A completely continuous process would require several continuous MECs, which were not available. The process was hence simulated batch-wise.

Before starting the process, the particles were trapped in the centrifuge, washed, eluted and washed again.

1. First the adsorption was done. For this purpose, the magnetic field was applied and the liquid in the centrifuge displaced with soy whey from bottom to top at a volume flow of 60 l/h. Then the liquid was pumped at 240 l/h in a cycle for 5 min, while the matrix was used as a stirrer to redisperse the magnetic particles. No circumferential velocity was applied in this step.
2. The washing liquid in the centrifuge was replaced by soy whey and the particles were redispersed for 5 min similar to step 1.
3. An elution step was performed, again doing the displacement. This was performed from top to bottom. Subsequently the redispersion was performed again from bottom to top at 240 l/h.
4. Finally a washing step was done while the elution liquid containing the protein was collected. To make sure that the displacement was efficient, the conductivity was measured and the displacement was continued until the conductivity of the effluent undercut 3 mS/cm.

The whole process was repeated several times. In contrary to the small MEC, the liquid was not drained but displaced, as the draining showed to be difficult in the specific setup. The complete process is shown in Figure 6-15.

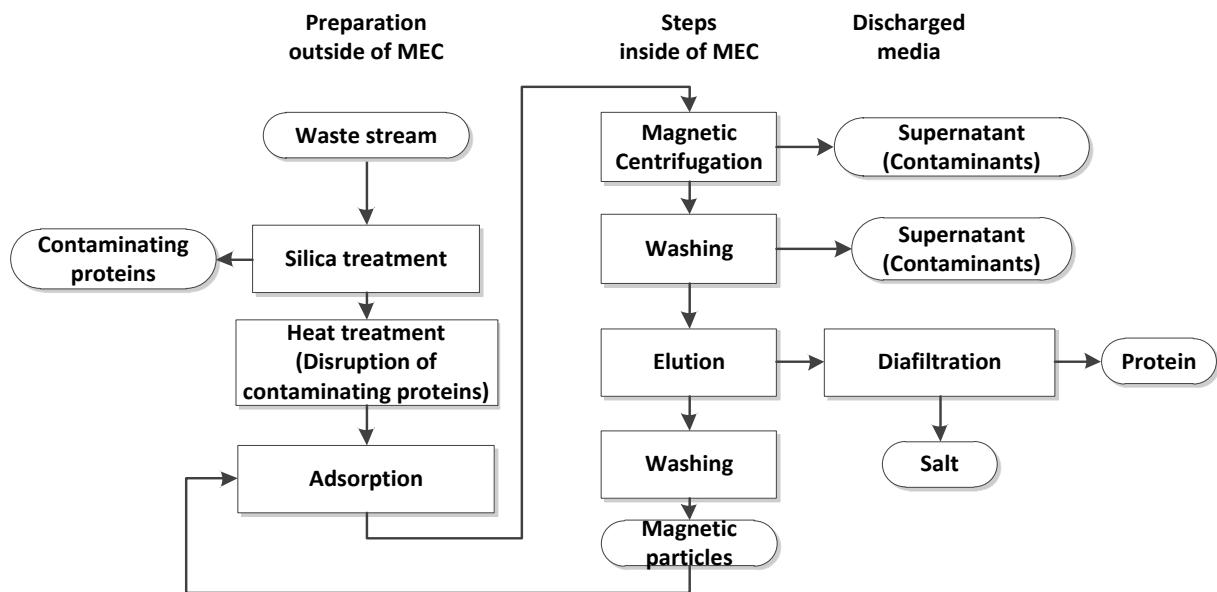


Figure 6-15: flow scheme of the BBI separation process shows the preparation steps outside of the MEC, the steps inside of the batch-wise MEC and lists the discharged media

The particles were discharged after the adsorption tests. The particles were redispersed in water, flushed out of the centrifuge and collected separately. For preservation 0.05 % of Proclin was used. Then the machine was unmounted, the matrix taken out and flushed separately. The separated BBI was, after the process, 0.2 μm filtered, concentrated 20x, diafiltered 7x to a concentration of more than 1000x, freeze dried and analyzed by technicians of Solae.

6.5.2 Results and Discussion

Separation in the Small Batch-Wise Magnetically Enhanced Centrifuge

Separation in the small batch-wise centrifuge showed that the process is possible based on the treated soy whey. The gels in Figure 6-16 show a high purity of the final product. In the gel a good performance of Orica MIEX (Figure 6-16 left) is visible concerning the separated amount of BBI, with few BBI visible in the supernatant. Figure 6-16 right shows the separation of MagPrep particles. In the eluate both systems showed high selectivity with a contamination at 28 kDa being undetectable. The washing liquid is in both steps clean from protein.

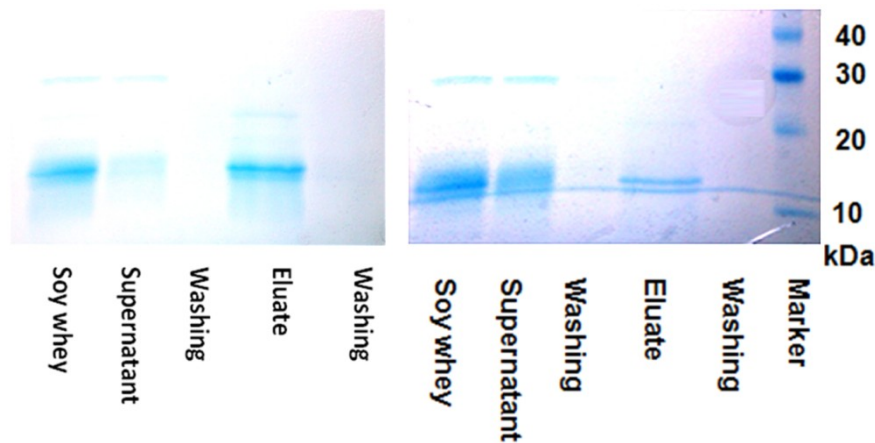


Figure 6-16 left: separation of BBI from an industrial stream using Orica MIEX particles (50 g/ 2.5l whey); right: BBI separation by Merck MagPrep TMAP 100 nm particles (25 g / 1.25 l whey)

Separation in the Industrial-Scale Magnetically Enhanced Centrifuge

This batch of MagPrep particles showed to be difficult to unload from the centrifuge, with 92 % collected in the center of the centrifuge. Hence in the process only 8 % of the particles were really active. This behavior was only found on this specific particle kind and might be prevented by shifting the pH during discharge to create a colloidal suspension. The nine cycles of Merck particles resulted in 22 g powder, with 47.6 % of BBI, the rest being sugar and other substances with 102.7 u/g. From an activity of 63585 Ci, the eluate only had 4745 Ci and the powder 2280 u/g, resulting in 7.5 % eluded and finally 3.6 % purified protein. The average binding capacity was 9 mg/g, the average produced protein in each cycle was 2.4 g. The low activity and yield is due to several reasons:

- The selectivity of the particle system is low. This results in a low adsorption of the target protein for the competing adsorption of sugar to the anion exchange particles. A high particle concentration was hence necessary while the yield was still reduced and the amount of product being processed in one cycle limited. Additionally heavy pretreatment was performed to reduce the amount of contaminating protein, and it would have to be extended to eliminate sugar.
- The high volume flow technically possible in the principle was not advantageous as the dead times for the change of liquid dominated. In combination with the batch-wise process this resulted in a low overall process efficiency.

In summary the process was not efficient for the separation. Two drawbacks need to be overcome.

- A more selective functionalization is necessary to avoid pretreatment steps and to increase the activity for the target protein by excluding competing adsorption. This

reduces the need of high particle amounts and allows the treatment of larger amounts of soy whey.

- The separation was possible at a volume flow of 1000 l/h, processing 15 l of soy whey in less than one minute. Washing and elution steps required more than 10 min each, resulting in a dead time 30 times higher than the separation time.

The setup of a continuous process based on several HGMS devices is hence necessary to actually make the process interesting for this kind of application. While the yield does not need to be large to generate profit from a waste stream, the process showed to be too laborious and dead times too significant. A continuous process would allow the process to compete with different - and even cheap - protein separation approaches.

6.6 Separation out of Fermentation Broth

A high-cost and hence interesting application of HGMF is the separation of proteins out of fermentation broth in a pharmaceutical production process. Such a process was tested in cooperation with the group of Prof. Thomas, notably Dr. Mueller, at the University of Birmingham. Fermentation was set up in l-scale. A pharmaceutically interesting protein was produced and separated by HGMF using a MEC.

6.6.1 Materials and Methods

Materials

The particles used are Merck MagPrep 100 nm SO₃, which are functionalized cation exchange particles. They are similar to Merck MagPrep Silica or TMAP, with the main difference being a different ligand. Preparation, fermentation and cell harvest was completely performed by Dr. Mueller from the University of Birmingham. The whole production process was performed in three steps:

1. Upstream processing: Preparation
2. Inoculation, Fermentation
3. Downstream Processing
 - a. Cell Harvest
 - b. Removal of cell debris
 - c. HGMF

Technically MEC is only suited for much larger product amounts than available in this process. The fermentation was performed by Dr. Müller. The recombinant protein was expressed in E.Coli and periplasmatically targeted. In the fermentation first bacteria grow until a specific optical density is reached, then IPTG (Isopropyl-β-D-thiogalactopyranosid) is induced to start the production of the target protein. After fermentation cells are harvested,

and opened up by a heat shock to release the protein. The cell debris is removed by an intermittent centrifugation step; this is necessary as cell fragments adsorb to particles. The steps are necessary for the use of cation exchange (-SO₃) particles instead of more specific ligands. Analytics were performed by SDS-Page and by detection of the BCA equivalent. Table 6-6 shows the information on the used Kit.

Table 6-6: Materials used for the detection of the BCA equivalent

Method	Device producer	Part	Model
Optical measurement	Jenway		Genova
BCA	Thermo Scientific	Kit	Pierce Protein Assay Kit #23228

Methods

The process was performed in the small batch-wise MEC, which allows the treatment of low product amounts. There are seven separation steps necessary in the separation:

1. Dilution

To reduce the conductivity of the fermentation broth and to allow the adsorption of the protein to the particle, the feed is diluted 10x from 330 ml to 3.3 l with a 20 mM sodium phosphate buffer (6.61 g NaH₂PO₄; 0.68 g Na₂HPO₄ on 3 l demineralized water) to achieve a conductivity of around 1 mS/cm. The pH is in this step adjusted to 6.

2. Adsorption

The overall particle amount is limited due to the fermentation batch size, while the MEC can handle significantly higher particle and broth amounts. The actual adsorption is performed with 6 g of particles corresponding to a concentration of 1.76 g/l in 3.4 l of liquid. The suspension is stirred for 20 min to achieve a complete adsorption of the target protein.

3. Magnetic Separation

The magnetic separation is the key separation step in which the particles and the protein adsorbed to the particles are separated selectively from the fermentation broth. The magnetic field strength is 200 mT, the centrifugal force is 1500 rpm and volume flow during separation is 40 l/h. Then the centrifuge is switched off and the machine is drained while the magnetic field is still applied to keep magnetic particles in the centrifuge.

4. Washing

The washing step is necessary to make sure there are no contaminants left (0.9 l; 20 mM; 0.8 mS/cm).

5. Elution

Finally in the elution step which is performed as well in the centrifuge (1 l; 0.3 M NaCl; 6 mS/cm), the protein is released again.

6. Washing

The washing step is performed to clean the particles from salt rests and reduce the ionic strength (0.9 l). This is necessary to prepare the particles for the next separation cycle.

7. Particle Discharge

Finally the particles are discharged from the centrifuge in another liquid and stored. Technically they can as well be reused.

The complete process is shown in Figure 6-17.

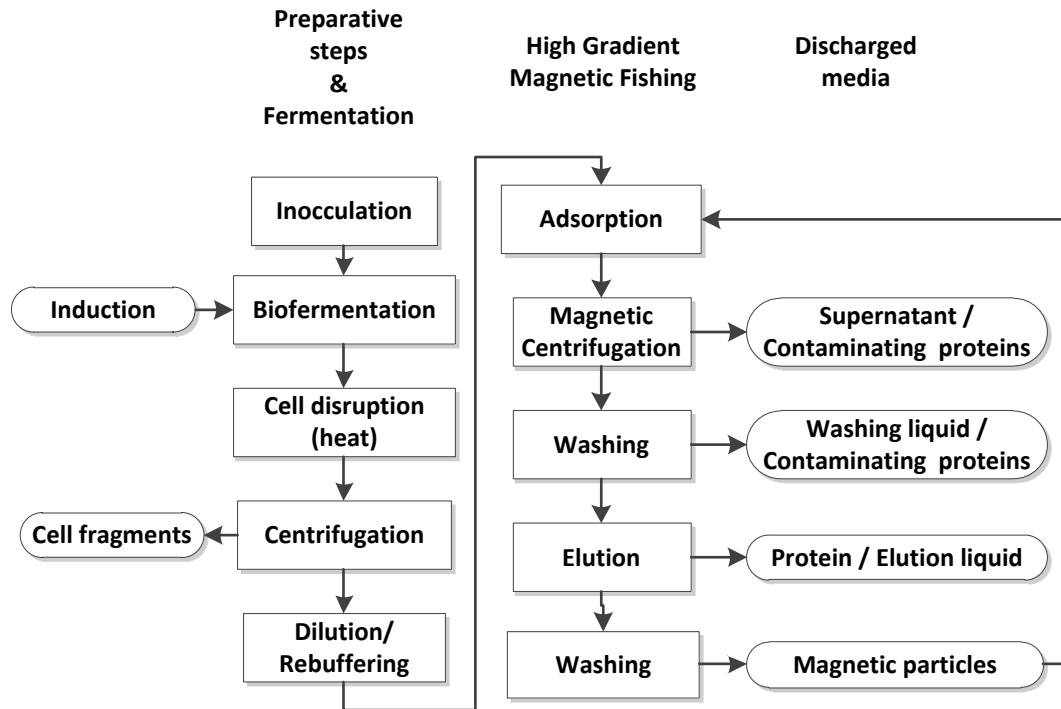


Figure 6-17: flow chart of a biofermentation process including fermentation, HGMF and a list of the discharged media

6.6.2 Results and Discussion

Figure 6-18 shows a SDS-Page gel of the separation of the target protein after fermentation by MEC. The protein amount is given in BCA equivalent which was determined along with the SDS-Page. The feed after removal of cell debris is shown in the first band, and after dilution in the second band. The supernatant leaving the centrifuge is shown in the third band. Then washing and draining is performed in the centrifuge without contamination visible in the fourth band. Elution is shown in the fifth band, and the final washing step without protein loss in the sixth band. The seventh band shows the marker. Figure 6-18 shows as well protein amounts determined as BCA equivalent. The target protein yield is 69%, the purity 98%, and the purification factor 8.3x. Particle loss during separation is less than 1% and hence not detectable; note though that about 1% particles are collected separately in each washing step before discharging the rest of the whey.

The selectivity and yield of the separation showed to be high. The fermenter size limited the batch size. With 250 g of particles available, both the increase of the process scale seems hence possible easily up to at least 20 x.

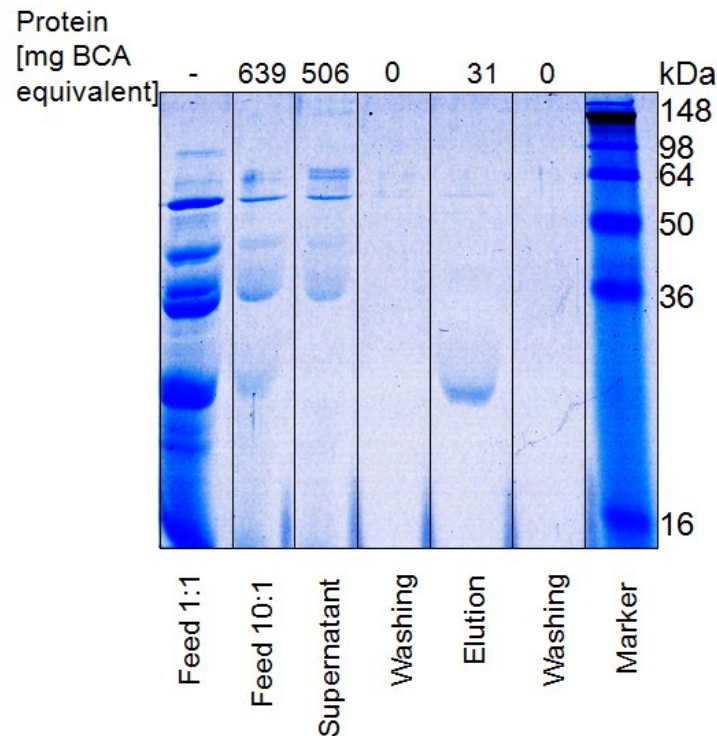


Figure 6-18: the SDS-Page gel of the separation of the target protein after fermentation by MEC; 1. feed undiluted; 2. feed diluted 10x; 3. supernatant after adsorption without target protein; 4. Washing liquid does not show contamination; 5. Elution liquid shows the target protein with increased concentration and high purity; 6. Washing liquid does not show any protein left; 7. A marker was given for comparison

6.7 Conclusion and Theoretic Comparison

MEC in downstream processing is promising as long as the process scale is high. It did not show to bring important advantages compared to other HGMS devices when it was performed batch-wise, but at a low amount of product different approaches such as Halbach-HGMS seem to be more efficient in costs. Still the principle allows even batch-wise a procedure for handling and redispersing magnetic particles. The main advantages of MEC in comparison is the option for continuous operation and volume flow.

Comparison to Adsorption Chromatography

Advantages of the system compared to adsorption chromatography comprise the high volume flow per functionalization and the possibility for a continuous process (which otherwise would only be possible by a simulated moving bed). Additionally the size of contamination is irrelevant, which might lead to a reduction of pretreatment steps.

Comparison to an Expanded Bed Adsorption

The process provides in some respects similar advantages as an expanded bed, with the size of contamination being irrelevant and a high volume flow compared to a packed bed. While a packed bed needs to be controlled to the fluidization point to avoid sedimenting of large particles and flushing out of small particles, this is no issue in HGMS. Additionally a continuous process is possible, while EBA needs to be stopped for elution.

The main drawback, which applies to EBA and packed bed adsorption as well, is the high device investment. Additionally to find an adsorbent fitted to the system is not obvious in many cases. Competing adsorption appeared in one of the pilot lines. Less selective ligands, specifically anion exchanger, require heavy pretreatment to eliminate contamination which otherwise makes the process inefficient. Table 6-7 summarizes theoretic advantages of HGMF over a packed bed and over EBA.

Table 6-7: Overview over theoretic advantages of HGMF to a packed bed and EBA

	Advantages of HGMF to a packed bed	Advantages of HGMF to EBA
Volume flow	High volume flow per functionalization	Continuous process possible
Process control	Size of contamination irrelevant, reduction of pretreatment steps possible	Easy to control (compared to finding a fluidization point)

Necessities for the use of HGMF in industrial processes comprise:

- a system with fitting adsorbent avoiding competing adsorption of contaminants with the product for binding spots,
- the medium properties such as a low viscosity play an important role; HGMS is less prone to viscosity issues compared to chromatography though;
- diverse particle properties influence the separation, with the most important being magnetization and the affinity of particles to agglomerate. Particles forming colloidal suspensions (e.g. below 10 nm or stabilized chemically in the specific medium) cannot be separated.

6.8 Outlook: A Completely Continuous Process Based on Magnetically Enhanced Centrifugation

A far more interesting and promising use of MEC is a completely continuous process, which was not yet implemented as one MEC would be necessary for each process step. A single MEC is enough for a catalysis process based on magnetic particles. For a separation process two to four MECs are necessary depending on the number of washing steps. Figure 6-19

shows a process scheme for an adsorption process omitting washing steps. This allows taking profit of the high volume flow at high separation efficiency possible in MEC.

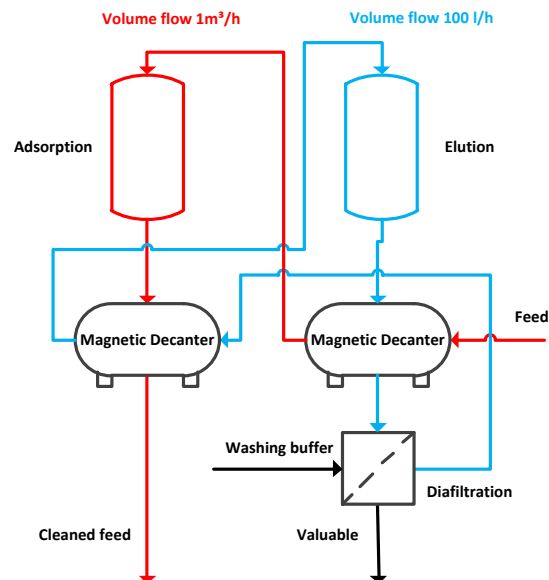


Figure 6-19: Flow chart of a completely continuous process for separation omitting washing steps

7 Conclusion and Outlook

7.1 Achievements

The work advances engineering in two respects: firstly, the understanding and modeling of magnetic suspensions are advanced by work on models, simulation and their comparison with experiments; secondly, it advances engineering applications in the economic utilization of magnetic particles by providing a new continuous device for their separation at high volume flow.

1. Magnetic Forces Induce Agglomeration and Strongly Influence the Separation, Agglomerate Shape and Porosity in Magnetically Enhanced Centrifugation

Properties of the particle systems used in the work are summarized and results of the investigations are shown. AFM experiments confirmed that the magnetic forces dominate over electrostatic and van-der-Waals forces for particles down to at least 10 μm . Rheometer experiments allowed to measure the influence of different parameters on the viscosity. The concentration and magnetic field strength influence the yield stress heavily. Exceeding a minimum concentration, the yield stress increases significantly at high concentration and magnetic field strength. This is particularly important for the transport of particles inside and out of the magnetic field, and hence the technical use of the process. Specifically the yield stress, which needs to be overcome before particles can be transported perpendicular to the field direction, is an important factor.

The MEC experiments allow measuring the effects of agglomeration on the separation. There is a significant increase of the separation at high concentrations. Current models for the separation prediction, basing on the capturing radius of a single wire, do not include this effect.

A strong influence of the concentration is visible in the simulation as well, which provides an insight into the process. A model on the magnetic forces and for magnetically induced agglomeration was developed. Different simulation approaches show the different aspects of magnetic separation. The flow and particle motion in proximity of magnetic wires, the magnetically induced agglomeration, and the deposition of particles on magnetic wires was investigated by DEM. A thorough study on drawbacks of the particle model evaluates the exactness and provides solutions for future simulations. The DEM simulations, coupled with the FEM simulation of the wire filter, show the mechanisms influencing the deposit shape. The needle-building of agglomerates at a distance has a strong influence. It enhances the separation, while the shape of the deposit on a wire is rough. The porosity of the deposition

depends on the relation of the magnetization of the filter wire and the magnetic particle, replacing a dense deposit by a highly porous one for decreasing wire magnetization. Photographs of the deposit on a wire in the air confirm a dense cake on the wire and a rough deposit at a distance.

In summary, the interparticular magnetic forces change the behavior of magnetic suspensions completely. They have a high impact on agglomeration, separation and on the particle transport. This influences the design of a continuous MEC, as it is difficult to move particles perpendicular to the magnetic field. The separation of magnetic particles from media is highly dependent on interparticular forces.

As an outlook on a decrease of the simulated particle size, a different simulation approach is necessary. A granular model or a dense discrete phase model would allow a simulation of particles closer in size to the experimental particles.

2. Magnetically Enhanced Centrifugation is Possible in Continuous Mode at High Volume Flow

A batch-wise concept, realized and tested experimentally in two different sizes, allows automatic discharge and separation. Classic HGMS devices base on removing the magnetic field from the filter chamber, either by switching off an electromagnet or by moving the magnet away from the cell. A decanter design was realized and showed that the particle separation and transport were uncoupled. The separation of magnetic particles depended on the magnetic field strength, while the transport was influenced mainly by the circumferential velocity. The performance tests showed that a high volume flow at high separation efficiency is possible in a cycle. An analytical model was suggested for the separation of magnetic particles from a suspension.

Wire optimization allowed an increase of the volume flow. A coupled FEM and CFD study enabled the optimization of the magnetic wire structure to the process. Performance tests on diverse wire parameters show their influence on the separation. A CFD study allowed the simulation and improvement of the industry-scale centrifuge.

In the current thesis a design study was performed to show promising principles for continuous discharge of magnetic particles. One concept was realized, a magnetically enhanced decanter effectively separated and transported magnetic particles. Even the small pilot machine implemented for test purposes separated up to 2.4 kg/h of magnetic particles out of 120 l/h feed in a continuous mode, exceeding the capabilities of current HGMS devices by a huge margin. As MEC bases on removing particles out of the filter and allows the discharge out of the magnetic field, dead times are avoided.

MEC was as well realized in an industry scale machine, which was developed in cooperation with Andritz KMPT. This machine allowed the batch-wise processing of magnetic suspensions. Its usable volume was 6 l, resulting in volume flows up to 1 m³/h fluid and 20 kg/h of particles, not counting dead times. The scale-up was hence successful and an implementation in an industrial pilot line possible.

The principle can be realized basing on permanent magnets as well as electromagnets. Both show important advantages. The core advantage of the electromagnet, which is the easy applying and to disabling of the magnetic field, is not important in a continuous centrifuge. For this reason a permanent magnet assembly was developed, which showed to be comparable in the process to the electromagnet but was much cheaper in investment and use. The magnet can be scaled linearly. An upscale of the centrifuge and of the permanent magnet is hence possible, resulting in a process interesting for industrial use.

3. Use of Magnetically Enhanced Centrifugation is possible in High Gradient Magnetic Filtration at high volume flow in bioprocessing

The potential of HGMF in bioseparation had been shown already before in analytical scale. The simulation of the adsorption in HGMF in a μ l-reactor was successful, based on the physical model of a protein diffusing through the surface layer of a particle. It showed that adsorption kinetics are fast, which is interesting in a continuous process. Currently HGMF was mostly limited to a small scale, while the maximum volume flow of MEC is on a much larger scale. The pilot line tests were limited to a batch-wise mode due to the availability of only one device.

The first model system is the separation of ovalbumin from hen egg white in MEC. The test was performed at the KIT and showed the basic possibility of selective separation. It was used to determine methods which could then be used on different processes.

The second system was the separation of a target protein interesting for pharmaceutical use from fermentation broth in cooperation with the university of Birmingham. Fermentation is becoming increasingly important for the production of pharmaceuticals, a process allowing the continuous separation is hence interesting. The separation of the protein was possible in a highly selective way. The scale of the experiment was limited only by the fermentation batch size. As an outlook, an interesting option is in-Situ separation of protein; i.e. the target protein is separated from the fermentation broth, then the fermentation broth is fed back to the bioreactor to continue the fermentation.

The third system was the separation of protein from an industrial waste stream. The protein is lowly concentrated, hence it is an interesting example for industrial use. The separation was

basically successful, but showed as well necessary prerequisites for industrially efficient use. The particle functionalization showed not to be selective enough, separating as well sugar and hence reducing the selectivity of the process tremendously. Additionally the batch-wise realization showed to be not efficient. The separation of the suspension was possible at high volume flow, while the backflushing of the device, washing and elution steps required a 30 times larger amount of time.

In summary the pilot line tests show that the principle is not limited to the use in μ l-reactors, but is actually possible in a huge production size. A process based on several continuous machines would allow the treatment of large amounts of product. A technical use of the system now depends on the availability of cheap, selective particles and an interesting target system.

7.2 Outlook: a Continuous Multi-Stage High Gradient Magnetic Separation Device for Waste-Water-Treatment

HGMS is an interesting process which still did not have a breakthrough in industry. The main reason is the fact that few substances are magnetic by themselves. Synthetic matter, as investigated in this work, is only now getting cheap enough for common use. Production costs down to 50 €/kg of magnetic particles and below were reported.

A large drawback in HGMS is the lack of a countercurrent process, while a packed bed is consecutively filled, leading to the last part of the bed which is unloaded and serves for the separation of small protein concentrations. A concept was developed for a cooperation with the Hatton group at the MIT for waste water treatment. Specifically the separation of mercury out of waste water was targeted. A particle functionalization had been produced by the Hatton group which serves for adsorption of mercury to magnetic particles with a selective functionalization. The concept was not developed further, as the measurement at the low target concentration was not possible and the project was not financed. In theory, a multi-stage process allows high reduction of the final concentration even at low concentration in countercurrent. This requires either parallel HGMS or a multi-stage device.

A continuous alternative to a MEC allowing parallel multi-stage separation is a carousel separator. A countercurrent design was already set up for fluid by Franzreb [Franzreb'01] (see Chapter 5.1.5). One of the disadvantages is sealing technology, which was realized by Teflon seals similar to drum filters. A possibility to avoid the sealing by Teflon is the use of valves. Additionally the main advantage of the layout is the fact this machine provides different chambers in a continuous process. This allows a multi-step process in a single machine. The machine developed consists of nine chambers, out of which three are backflushed while 3 x 2

are used for separation in counter-current mode. During changing of the chamber, Figure 7-1 shows a drawing from top of magnets and chambers.

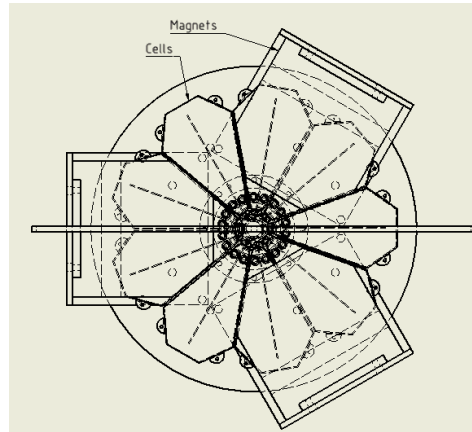


Figure 7-1: carousel arrangement as technical drawing from the top with 9 chambers, out of which 6 are in 3 magnets and separate, while 3 are flushed back; during chamber changing only 3 cells separate

8 Annex

8.1 List of Abbreviations

Table 8-1: list of abbreviations

2D	two-dimensional	LDA	Laser Doppler Anemometry
3D	three-dimensional	MEC	Magnetically Enhanced Centrifugation
AEX	Anion EXchanger		
AFM	Atomic Force Microscopy	SDS-	Sodium-Dodecylsulfate
BSA	Bovine Serum Albumin	Page	Polyacrylamid Gelelectrophoresis
CEX	Cation EXchanger	UDF	User Defined Function, Method to program in Ansys Fluent
CFD	Computational Fluid Dynamics		
DEM	Discrete Element Modeling	UDM	User Defined Memory, memory in each cell of a Ansys Fluent grid, its use is defined by the user
FEM	Finite Element Modeling		
HGMS	High Gradient Magnetic Separation	UDL	User Defined Library, Method to program in EDEM
HGMF	High Gradient Magnetic Filtration		

8.2 List of Nature Constants

Table 8-2: list of universal constants

Symbol	Value	Unit	Denotation
A_H	(6.5 e-20)	[J]	Hamaker constant
e_0	1.602177e-19	[C]	Elementary charge
g	9.81	[m/s ²]	Earth gravity
g_e	2.00231930	[-]	Landé factor for electron
$\hbar(= h/2\pi)$	1.054571726*10 ⁻³⁴	[Js]	Reduced Planck'constant
k	1,38066e-23	[J/K]	Boltzmann constant
N_A	6.02214e23	[1/mol]	Avogadro constant
ϵ_0	8.85419e-12	[C ² /Jm]	Dielectricity constant
μ_B	9.27400968*10 ⁻²⁴	[J/T]	Bohr magneton
μ_0	4 π e-7	[Vs/Am]	Permeability constant
π	3.141592	[-]	

8.3 List of Formula Signs

Table 8-3: list of formula signs

	Unit	Denotation			
			E_{el}	[V/m]	Electric field strength
a	[m]	wire radius (common: 0.5 e-3)	E_m	[W]	Magnetic energy
A	[m ²]	area	E_{vdW}	[W]	Van-der-Waals energy
A_{abs}	[-]	Absorption	E_{mod}	[Pa]	Elasticity Modulus
A_V		Vector potential	E_{eq}	[Pa]	Equivalent Elasticity Modulus
A_M		matrix	E_{sep}	[-]	Separation efficiency
B	[T]	magnetic flux density	e_r, e_θ	[-]	unity vectors in cylindrical coordinates
B_0	[T]	Magnetic background flux density	F	[N]	force
b	[m]	particle radius	F_m	[N]	magnetic force
C_μ	[-]	Turbulence parameter: 0.09	f	[Hz]	Resonance frequency
$C_{\epsilon 1}$	[-]	Turbulence parameter: 1.44	$f(...)$	[-]	function
$C_{\epsilon 2}$	[-]	Turbulence parameter: 1.92	f_0	[Hz]	Initial cantilever resonance frequency
c	[mol/l]	concentration	G	[Pa]	Shear modulus
c_0	[g/g]	Minimum concentration	G_{eq}	[Pa]	Equivalent shear modulus
$C_{Effluent}$	[g/l]	Effluent Concentration	H	[A/m]	magnetic field
C_{Feed}	[g/l]	Feed Concentration	\hat{H}	-	Hamilton operator
C_n	[g/g]	Relative concentration	H_0	[A/m]	magnetic background field (4,00E+05)
D	[m ² /s]	Diffusion coefficient	I	[A]	current
D_S	[m/N]	Spring stiffness	I_{in}	[W/m ²]	Intensity of the incoming light
D_T	[m ² /s]	Temperature diffusion coefficient	I_{out}	[W/m ²]	Intensity of the outgoing light
d	[m]	Particle diameter	I_n		inertia
d_A	[m]	Agglomerate diameter	J_i	[kg m ²]	inertia tensor
d_i, d_j	[m]	Diameter of particle i,j	K	[-]	auxiliary quantity
d_S	[m]	Thickness of optical cell	K_F	[l/mol]	Adsorption coefficient
E	[W]	Energy	k	[kg/s]	Energy term in turbulence model
E_{Born}	[W]	Born energy	$k_{n,ij}$	[Pa m ^{1/2}]	Normal stiffness parameter
E_{Coul}	[W]	Coulomb energy	$k_{t,ij}$	[Pa m]	Tangential stiffness

L	[kg m ² /s]	parameter Angular momentum	Re R_i	[-] [m]	Reynolds number Initial radial position
L_C	[m]	Centrifuge length	R_{dr}	[m]	Outer diameter of the flow layer
L_{coil}	[m]	Coil length			
L_{lead}	[m]	Pitch, lead	R_m	[V s/Am ²]	Magnetic resistance
l	[m]	Characteristic length	R_0	[m]	Hydrodynamic radius
M	[A/m]	magnetization			
M_M	[g/mol= Da]	Molar mass	r	[m]	distance vector, cylindrical coordinate
M_p	[A/m]	Magnetization particle	r_c	[m]	Contact radius
M_W	[A/m]	magnetization wire (susceptibility of iron: 1.7e6)	r_{eq} r_H	[m] [m]	Equivalent radius Medium of the flow layer radius
m	[kg]	mass of particle	r_x, r_y, r_z	[-]	components of the distance vector
\hat{m}		Quantum mechanical operator of the magnetic moment	S Sc Sh	[-] [-] [-]	Spin Schmidt Number Sherwood number
m_{eq}	[kg]	Equivalent mass	Sh_{lam}	[-]	Laminar Sherwood number
N	[-]	Demagnetization factor	Sh_{turb}	[-]	Turbulent Sherwood number
N_{wire}	[-]	Demagnetization factor of a wire (cylinder: 0.5)	T T_T	[K] [Nm]	temperature torque
N_{sphere}	[-]	Demagnetization factor of a sphere (0.33)	t_0 t_{ij}	[s] [-]	Residence time Direction vector body i to body j
N_S	[-]	Number of wire stages	u_i, u_j, u_k	[m/s]	Velocity in turbulence model
n	[mol]	Molecule number	$\bar{u}_i, \bar{u}_j, \bar{u}_k$		Time average of velocities
n_i, n_j	[-]	Magnetic field direction vector	$\overline{u'_i}, \overline{u'_j}, \overline{u'_k}$		Time average of Reynolds shear velocity
n_r	[1/min]	Rotational velocity	\mathbf{v}	[m]	Relative normal particle velocity
n_{RRSB}	[-]	Parameter in RRSB	$\mathbf{v}_{rel,n,ij}$	[m/s]	Relative tangential particle velocity
n_{ij}	[-]	Normal vector			
p	[m]	Perimeter			
Q	[-]	Sum distribution function	$\mathbf{v}_{rel,t,ij}$	[m/s]	fluid velocity
q	[1/m]	Density distribution function	v_0 v_m	[m/s] [m/s]	velocity of magnetic particle next to the wire
R	[m]	Particle radius			
Rc	[m]	capturing radius			

V	[m ³]	volume	γ	[1/Ts]	Gyromagnetic ratio
$V_{Effluent}$	[m ³]	Effluent volume	κ	[-]	susceptibility
V_{Feed}	[m ³]	Feed volume	κ_d	[1/m]	inverse Debye length (2,00E+08)
V_N	[m ³]	Needle volume			
V_P	[m ³]	particle volume	κ_i	[-]	Intrinsic susceptibility
V_S	[m ³]	Sphere volume			
x	[m]	Cartesian coordinate, distance	κ_N	[-]	Susceptibility of a needle
			κ_S	[-]	Susceptibility of a sphere
x_{50}	[m]	Medium size			
x_{63}	[m]	Particle size with 63% / 84% smaller	λ		Radius ion cloud
x_{84}			λ_B	[-]	Number for agglomeration
y	[-]	Cartesian coordinate	μ	[A m ²]	magnetic moment
z	[-]	Cartesian coordinate	μ_i	[A m ²]	Magnetic moment of particle i
z_e	[-]	Number of electrons	μ_j	[A m ²]	Magnetic moment of particle j
α_t	[-]	Turbulence parameter: 5/9	μ_L	[A m ²]	Magnetic moment from orbital momentum
α_d	[-]	Decanter transport parameter	μ_N	[A m ²]	Magnetic moment of a needle
β	[m/s]	Mass transfer coefficient	μ_S	[A m ²]	Magnetic moment of a sphere
β	[-]	Turbulence parameter: 3/40	μ_{Sp}	[A m ²]	Magnetic moment from electron spin
β^*	[-]	Turbulence parameter: 9/100	μ_m	[Vs /Am]	$\mu^*\mu_0$
δ	[m]	Particle overlap	μ_r	[-]	specific permeability (vacuum: 1)
δ_C	[m]	Centrifuge flow layer thickness			
δ_{ij}	[-]	Kronecker delta	μ_T	[kg/m s ²]	Turbulent viscosity
δ_P	[-]	Material constant of Born potential	ψ	[A]	Magnetic scalar potential
ε	[m ² /s ³]	Dissipation	ρ_L	[kg/m ³]	liquid density (water: 1000)
ε_{ex}	[m ² /mol]	Extinction coefficient	ρ_P	[kg/m ³]	particle density (common: 2000 - 4000)
ε_r	[-]	specific permittivity (vacuum: 1)			
η	[kg/m s]	dynamic viscosity (water: 1000)	σ	[-]	Turbulence parameter: 0.5
$\eta_{n,ij}$	[kg/s]	Normal damper coefficient	σ_{st}	[-]	Standard deviation
			σ^*	[-]	Turbulence parameter: 0.5
$\eta_{t,ij}$	[kg/s]	Tangential damper coefficient	σ_k	[-]	Turbulence

σ_ε	[-]	parameter: 1 Turbulence	τ_0	[N/m ²]	Yield stress
		parameter: 1.3	ν	[m ² /s]	kinematic viscosity (water: 1e-6)
θ	[-]	angle, cylindrical coordinate	ν_i, ν_j	[-]	Poisson number
θ_c	[-]	Attractive angle	ω	[1/s]	circumferential velocity
τ	[N/m ²]	Shear stress	ζ		ζ -potential
$\tau_{i,j}$	[Pa]	Reynolds shear tensor			

8.4 Further Formulae

8.4.1 Brownian Molecular Dynamics

The medium quadratic movement σ^2 of a particle is in (8-1).

$$\sigma^2 = \frac{RT}{3\pi N_A \eta r} \quad (8-1)$$

8.4.2 Fluid Forces

Further fluid forces which were not implemented, but are important are the flow resistance of a needle and swarm sedimentation. The flow resistance for a force at $Re > 0.25$ is in (8-2).

$$F_W = \pi \frac{d^2}{4} c_W(Re) \frac{\rho_f}{2} v^2 \quad (8-2)$$

The formula of Kaskas (8-3) for the drag coefficient c_W allows the calculation for $Re < 10^5$.

$$c_W(Re) = \frac{24}{Re} + \frac{4}{\sqrt{Re}} + 0.4 \quad (8-3)$$

The flow resistance of a circular needle in (8-4) was derived by Batchelor [Batchelor'06]. It allows the calculation of the fluid resistance of a needle with $\varepsilon = (\log(L/d))^{-1}$, with needle length L and needle diameter d . In case of a needle composed out of particles this is $d = d_p$.

$$F_W = 2\pi\eta Lv \left(\frac{\varepsilon + 0.307\varepsilon^2}{1 - 0.5\varepsilon} + 0.4255\varepsilon^3 \right) \quad (8-4)$$

The sedimentation velocity can only for low particle concentrations be approximated by the Stokes resistance. In case of high particle concentrations the formula (8-5) of Richardson and Zaki is used to calculate the sedimentation velocity.

$$u(c) = u_\infty (1 - c)^{n(Re)} \quad (8-5)$$

8.5 List of Devices

8.5.1 Measurement Devices

Table 8-4 gives an overview over commercial measurement devices which were used.

Table 8-4: Overview over measurement devices

Parameter		Device / Physical principle	Producer	Model	Sensitivity
Magnetic flux		Hall probe	Magnet-Physik Dr. Steingroever GmbH	FH51 Gauss-/Teslameter	> 1 mT
Concentration determination		Gravimetry	Sartorius	LE225D-OCE	>0,01 g up to 100 g
		Turbidimeter	Hach	2100 P	1000-0,01 NTU
		Magnetic field variation: Magnetic Reader	FZMB	probe 14 06/5/LS	
Particle properties	Size distribution	Laser diffraction	Sympathec	Helos	400µm-400 nm
		Disc centrifuge	CPS Instruments Inc.	DC24000	
	Magnetization	Magnetization measurement	Princeton Measurements Corporation	MicroMag™ 2900	10 nemu = 10 pAm ²
	Particle shape and size distribution	Microscopy	Leica	Microscope WILD M 420 Macroscope M3C	XXX 10 µm and less
	Density	Pycnometer		MP 1305	
Suspension viscosity		Magnetic rheometer	Anton Paar	MCR 301 with MRD 180	1mPas – 50 Pas
Particle Contact force 3D Surface		Atomic Force Microscopy	Ambios Technology Corporation	Q-Scope 250 Nomad	>10 nN 10nm- 20µm
Particle / Fluid velocity		Laser-Doppler-Anemometer	Dantec Dynamics	BSA Flow Software	

8.5.2 Demagnetization

The demagnetization is done by a magnetic field changing in direction with steadily decreasing amplitude. The device available is from the producer Tiede, the type ETT.

Table 8-5: Demagnetization device

Magnetization	Demagnetization	Tiede	Typ ETT
---------------	-----------------	-------	---------

8.5.3 Data on Electromagnets

Table 8-6: data of the permanent magnets

	Cooled/uncooled magnet
Coil material	Aluminum
Housing	Steel 1.0036
Bore hole diameter	123 mm
Housing diameter	618 mm
Height	121/154
Band thickness	0.3/0.35 mm
Number of coils	680/618
Voltage	65/110 V
Maximum current	65/150A
Time for maximum current	22.5%/25%
Magnetic flux density at max. current	0.4/0.68T
Cooling power	-/5.5 kW

8.5.4 Overview over Software

Different commercial software was used for the simulation. An overview is given in Table 8-7.

Table 8-7: Overview over important used software

Physical phenomenon / purpose	Method	Producer	Software	Version
Computational Fluid Dynamics	Finite Volume Method (FVM)	Ansys	Fluent	6.0; 12.0; 13.0
Magnetic Field simulation	Finite Element Method (FEM)	Comsol	Comsol Multiphysics	3.4; 4.0a; 4.2a
Particle motion / agglomeration	Discrete Element Method	DEM Solutions	EDEM	
Machine design	3D Computer Aided Design	Autodesk	Inventor	2010

8.5.5 Adsorption, Washing and Elution Buffer

Table 8-8: 1l 20 mM Sodiumphosphate Binding and washing buffer for the separation out of hen egg white

pH	NaH ₂ PO ₄ [mol]	NaH ₂ PO ₄ [g]	Na ₂ HPO ₄ [mol]	Na ₂ HPO ₄ [g]
6	0.0181	2,4976	0.0018	0.255
7	0.0119	1.6424	0.008	1.335
8	0.0025	0.3449	0.0175	2.4796

The elution buffer was similar but 1 M NaCl was added.

8.5.1 Devices for SDS-Page

Table 8-9: Overview over devices for protein analysis

Parameter	Device / Physical principle	Producer	Model
pH		WTW GmbH	PH/Cond 340i/SET
Thermo-mixer		HLC Biotech	MHR 13
Gel electrophorese unit		Carl-Roth GmbH	
Centrifuge for µl-reactor	Micro Centrifuge	Carl Roth GmbH	
Photometer	Light absorption	Genova MK3 LIFE Science Analyser With UV cuvettes 1.5 micro	Landgraf Laborsysteme GmbH

8.5.2 Buffers and Chemicals for SDS-Page

Table 8-10: Running buffer

	Balance [g]	Value
TRIS base	3,3	25 mM
Glycin	16,9	200 mM
SDS Pellets	1,1	0,1%
VE-Wasser	ad 1,1 l	

Table 8-11: Fixing and Coloring buffer

	Volume [ml]	Balance [g]	Value
Methanol	50	-	50%
Essigsäure	10	-	10%
Coomassie-Blue G250	-	0,1	0,1%
VE-Wasser	ad 100 ml	-	

Table 8-12: Uncoloring buffer

	Volumen [ml]	Value
Essigsäure	25	10V%
VE-Wasser	ad 250 ml	

Table 8-13: Chemicals ready for use

Description	Name	Producer	Nr.
Denaturing	Roti-Load 1 reducing 4 x concentrated	Roth	K929.1
Marker	Roti-Mark 10-150	Roth	T850.1
Gel	Roti-PAGW Gradient (4-20%)	Roth	2843.1

8.5.3 SDS-Page Procedure

Sample treatment

- 20 µl sample treatment with 7 µl Roti-Load (1:4-dilution)
- 5 min in thermomixer at 95 Grad
- Cooling in ice
- 5 min in microcentrifuge
- Cooling in ice

Sample adding

- 10 µl of sample per row

Running the gel

- 125V (limiting)
- 16 W
- 32 mA
- 2:15h

Fixing

- Wash 2x in water before
- 10 min on mixer

Coloring

- Wash 2x in water before
- 30 min. on mixer

Uncoloring

- Wash 2x in water before
- 18 h on mixer
- Change buffer 1-2x

8.6 Index

A		F	
Adsorption Chromatography	156	Ferromagnetism	10
B		Fick's law	23
Biofermentation process	155	Finite Element Method	31, 57
Born force	21	flow layer thickness	25
Boundary conditions	30	flow resistance	
Brownian Molecular Dynamics		needle	168
medium quadratic movement	168	swarm sedimentation	168
number	23	fluid resistance	
C		single particle laminar	16
capturing radius	17	single particle turbulent	168
Chromatography	34	G	
Computational Fluid Dynamics	26, 58	Gauss's law for magnetism	12
Cone angle	113	Grid	29
Coriolis force	25	I	
Coulomb Force	19	Industrial separation process	151
cut size centrifugation	25	Inertia	32
Cylinder Magnetic Field	16	ion exchange	
D		theory	19
deposit		Ion exchange	
height	83	Ligands	135
porosity	64	Ionic strength	147
Diamagnetism	10	L	
diffusion coefficient	23	Ligands	134
Discrete Element Method	58	M	
DLVO	18, 43	Magnet	
E		Conventional Permanent	80
electromagnet	6	electro-	98
Elution	145	Halbach Arrangement	81
energy		longitudinal arrangement	120
Born	20	magnetic	
Coulomb	19	field strength	8
magnetic field	12	moment	9
magnetic moment	12	scalar potential	12
van der Waals	18	vector potential	12
Euler-Euler	27	velocity	17
Euler-Lagrange	28	magnetic carousel	81, 162
Expanded Bed Adsorption	156	magnetic dipole	
		implementation	59

theory	13
magnetization	8
magnetorheology	
experimental	49
theory	15
Mason number	15
multi stage adsorption	162
Multiphase simulation	27

N

number	
colloidal suspension	23
Mason	15
Reynolds	16
Schmidt	23
Sherwood	24

P

Paramagnetism	10
Particle detachment	114
particle size distribution	26
particle tracks	16, 87, 93
permeability	8
Polson correlation	23
Protein analytics	
Optical Measurement	36
SDS-Page	36

Q

Quantum mechanics	6
-------------------------	---

R

Reynolds number	16
-----------------------	----

S

Schmidt number	23
Selectivity	
Centrifuge	124
separation efficiency	
agglomeration	127
multiple wire stages	127
single wire stage	18
Sherwood number	24
Slope angle	113
Stern-double	19
stiffness	46

T

The Discrete Element Method	32
Turbulence	
Magnetic Separation	54

V

Van-der-Waals Force	18
---------------------------	----

W

waterspout	25
------------------	----

Z

zeta-potential	19
----------------------	----

8.7 Literature

- Ansys_Manual (2012). Fluent User's Guide V14.5.
- Aubert, G. (1993). Permanent magnet for nuclear magnetic resonance imaging equipment US Patent.
- Batchelor, G. K. (2006). "Slender-body theory for particles of arbitrary cross-section in Stokes flow." Journal of Fluid Mechanics **44**(03): 419.
- Bathen, D. and M. Breitbach (2001). Adsorptionstechnik, Springer.
- Becker, J., S. Raffelt and M. Franzreb (2008). "Untersuchungen zur Proteinseparation mittels magnetischer Mikrosorbentien in Kombination mit wässrigen Zweiphasen-Systemen." Chemie Ingenieur Technik **80**(6): 847-853.
- Beleggia, M., M. D. Graef, Y. T. Millev, D. A. Goode and G. Rowlands (2005). "Demagnetization factors for elliptic cylinders." Journal of Physics D: Applied Physics **38**(18): 3333-3342.
- Benguella, B. (2002). "Cadmium removal from aqueous solutions by chitin: kinetic and equilibrium studies." Water Res **36**(10): 2463-2474.
- Bergmann L., S. C. (2006). Elektromagnetismus, de Gruyter.
- Bica, I. (2002). "Damper with magnetorheological suspension." Journal of Magnetism and Magnetic Materials **241**(2-3): 196-200.
- Bica, I. (2004). "Magnetorheological suspension electromagnetic brake." Journal of Magnetism and Magnetic Materials **270**(3): 321-326.
- Bischoff, R. (2013). Die Phosphat-Fischer. Bild der Wissenschaft Plus.
- Boychyn, M., S. S. S. Yim, P. Ayazi Shamlou, M. Bulmer, J. More, et al. (2001). "Characterization of flow intensity in continuous centrifuges for the development of laboratory mimics." Chemical Engineering Science **56**(16): 4759-4770.
- Burnham, N. A. (1989). "Measuring the nanomechanical properties and surface forces of materials using an atomic force microscope." Journal of Vacuum Science & Technology A: Vacuum, Surfaces, and Films **7**(4): 2906.
- Butt, H.-J., B. Cappella and M. Kappl (2005). "Force measurements with the atomic force microscope: Technique, interpretation and applications." Surface Science Reports **59**(1-6): 1-152.
- Cerff, M., A. Scholz, M. Franzreb, I. L. Batalha, A. C. Roque, et al. (2013). "In situ magnetic separation of antibody fragments from Escherichia coli in complex media." BMC Biotechnol **13**(1): 44.
- Cerff, M., A. Scholz, T. Kappler, K. E. Ottow, T. J. Hobley, et al. (2013). "Semi-continuous in situ magnetic separation for enhanced extracellular protease production-modeling and experimental validation." Biotechnol Bioeng **110**(8): 2161-2172.

- Chang, Y. C. and D. H. Chen (2005). "Adsorption kinetics and thermodynamics of acid dyes on a carboxymethylated chitosan-conjugated magnetic nano-adsorbent." Macromol Biosci **5**(3): 254-261.
- Chang, Y. K. and H. A. Chase (2000). "Development of operating conditions for protein purification using expanded bed techniques: The effect of the degree of bed expansion on adsorption performance." Biotechnol Bioeng **49**(5): 512-526.
- Chen, F. (2009). "Magnetically Enhanced Centrifugation for Continuous Biopharmaceutical Processing." Massachusetts Institute of Technology.
- Chin, C.-J., S. Yiaccoumi and C. Tsouris (2001). "Probing DLVO Forces Using Interparticle Magnetic Forces: Transition from Secondary-Minimum to Primary-Minimum Aggregation." Langmuir **17**(20): 6065-6071.
- Chmiel, H. (2011). Bioprozesstechnik, Springer.
- Chu, K. W. and A. B. Yu (2008). "Numerical simulation of complex particle-fluid flows." Powder Technology **179**(3): 104-114.
- Clement, E., M. R. Maxey and G. E. Karniadakis (2004). "Dynamics of Self-Assembled Chaining in Magnetorheological Fluids." Langmuir **20**(2): 507-513.
- Coey, J. M. D. (2009). Magnetism and magnetic materials. Cambridge, Cambridge University Press.
- Cowen, C., F. Friedlaender and R. Jaluria (1976). "Single wire model of high gradient magnetic separation processes I." IEEE Transactions on Magnetics **12**(5): 466-470.
- Cundall, P. A. (1988). "Formulation of a three-dimensional distinct element model—Part I. A scheme to detect and represent contacts in a system composed of many polyhedral blocks." International Journal of Rock Mechanics and Mining Sciences & Geomechanics Abstracts **25**(3): 107-116.
- Cundall, P. A. and R. D. Hart (1992). "Numerical Modelling of Discontinua." Engineering Computations **9**(2): 101-113.
- Cussler, E. L. (2009). Diffusion: Mass Transfer in Fluid Systems, Cambridge University Press.
- de Vicente, J., D. J. Klingenberg and R. Hidalgo-Alvarez (2011). "Magnetorheological fluids: a review." Soft Matter **7**(8): 3701.
- Deen, N. G., M. Van Sint Annaland, M. A. Van der Hoef and J. A. M. Kuipers (2007). "Review of discrete particle modeling of fluidized beds." Chemical Engineering Science **62**(1-2): 28-44.

- Desert, C., C. Guérin-Dubiard, F. Nau, G. Jan, F. Val, et al. (2001). "Comparison of Different Electrophoretic Separations of Hen Egg White Proteins." Journal of Agricultural and Food Chemistry **49**(10): 4553-4561.
- Ebner, A. D., J. A. Ritter and J. D. Navratil (2001). "Adsorption of Cesium, Strontium, and Cobalt Ions on Magnetite and a Magnetite–Silica Composite." Industrial & Engineering Chemistry Research **40**(7): 1615-1623.
- Ebner, N. A., C. S. G. Gomes, T. J. Hobley, O. R. T. Thomas and M. Franzreb (2007). "Filter Capacity Predictions for the Capture of Magnetic Microparticles by High-Gradient Magnetic Separation." IEEE Transactions on Magnetics **43**(5): 1941-1949.
- EDEM_Solutions_Ltd._User's_Guide (2010).
- Eichholz, C. (2010). Zur magnetfeldinduzierten Strukturierung von Filterkuchen, Karlsruhe Institute of Technology.
- Eichholz, C., H. Nirschl, F. Chen and T. A. Hatton (2012). "DEM-simulation of the magnetic field enhanced cake filtration." AIChE Journal **58**(12): 3633-3644.
- Eichholz, C., M. Stolarski, V. Goertz and H. Nirschl (2008). "Magnetic field enhanced cake filtration of superparamagnetic PVAc-particles." Chemical Engineering Science **63**(12): 3193-3200.
- Fernandez-Lahore, H. M., R. Kleef, M. R. Kula and J. Thoemmes (1999). "The influence of complex biological feedstock on the fluidization and bed stability in expanded bed adsorption." Biotechnol Bioeng **64**(4): 484-496.
- Fischer, I. and M. Franzreb (2011). "Direct determination of the composition of aqueous micellar two-phase systems (AMTPS) using potentiometric titration—A rapid tool for detergent-based bioseparation." Colloids and Surfaces A: Physicochemical and Engineering Aspects **377**(1-3): 97-102.
- Fischer, I. and M. Franzreb (2012a). "Nanoparticle Mediated Protein Separation in Aqueous Micellar Two-Phase Systems." Solvent Extraction and Ion Exchange **30**(1): 1-16.
- Fischer, I., C. Morhardt, S. Heissler and M. Franzreb (2012b). "Partitioning behavior of silica-coated nanoparticles in aqueous micellar two-phase systems: evidence for an adsorption-driven mechanism from QCM-D and ATR-FTIR measurements." Langmuir **28**(45): 15789-15796.
- Franzreb, M. (2001). "New Design of High-Gradient Magnetic Separators Using Permanent Magnets." Proceeding 6th Chem Eng World Congress.

- Franzreb, M. (2003). "Magnetetechnologie in der Verfahrenstechnik waessriger Medien." Forschungszentrum Karlsruhe GmbH.
- Franzreb, M., M. Siemann-Herzberg, T. J. Hobley and O. R. Thomas (2006). "Protein purification using magnetic adsorbent particles." Appl Microbiol Biotechnol **70**(5): 505-516.
- Furst, E. and A. Gast (2000). "Micromechanics of magnetorheological suspensions." Physical Review E **61**(6): 6732-6739.
- Gedik, E., H. Kurt, Z. Recebli and C. Balan (2012). "Two-dimensional CFD simulation of magnetorheological fluid between two fixed parallel plates applied external magnetic field." Computers & Fluids **63**: 128-134.
- Gerber, R. and R. R. Birss (1983). "High Gradient Magnetic Separation." Research Studies Press.
- Ghosh, R. (2006). Principles of Bioseparations Engineering.
- Gregory, J. (1975). "Interaction of unequal double layers at constant charge." J Colloid Interface Sci **51**(1): 44-51.
- Hamaker, H. C. (1937). "The London—van der Waals attraction between spherical particles." Physica **4**(10): 1058-1072.
- Hart, R., P. A. Cundall and J. Lemos (1988). "Formulation of a three-dimensional distinct element model—Part II. Mechanical calculations for motion and interaction of a system composed of many polyhedral blocks." International Journal of Rock Mechanics and Mining Sciences & Geomechanics Abstracts **25**(3): 117-125.
- Hartmann, U. (1999). "Magnetic Force Microscopy." Annu. Rev. Mater. Sci.(29): 53-87.
- Hayashi, S., F. Mishima, Y. Akiyama and S. Nishijima (2010). "Development of High Gradient Magnetic Separation System for a Highly Viscous Fluid." IEEE Transactions on Applied Superconductivity **20**(3): 945-948.
- Hickel, S. (2013). Angewandte Strömungssimulation. Lecture notes, Technical University Munich.
- Hickstein, B. and U. A. Peuker (2008). "Characterization of protein capacity of nanocation exchanger particles as filling material for functional magnetic beads for bioseparation purposes." Biotechnol Prog **24**(2): 409-416.
- Hjorth, R. (1997). "Expanded-bed adsorption in industrial bioprocessing: Recent developments." Trends in Biotechnology **15**(6): 230-235.
- Hournkumnuard, K. and C. Chantrapornchai (2011). "Parallel simulation of concentration dynamics of nano-particles in High Gradient Magnetic

- Separation." Simulation Modelling Practice and Theory **19**(2): 847-871.
- Hugon, C., F. D'Amico, G. Aubert and D. Sakellariou (2010). "Design of arbitrarily homogeneous permanent magnet systems for NMR and MRI: theory and experimental developments of a simple portable magnet." J Magn Reson **205**(1): 75-85.
- Jain, M., M. Paranandi, D. Roush, K. Göklen and W. J. Kelly (2005). "Using CFD To Understand How Flow Patterns Affect Retention of Cell-Sized Particles in a Tubular Bowl Centrifuge." Industrial & Engineering Chemistry Research **44**(20): 7876-7884.
- Johansson, H. J., C. Jägersten and J. Shiloach (1996). "Large scale recovery and purification of periplasmic recombinant protein from E. coli using expanded bed adsorption chromatography followed by new ion exchange media." Journal of Biotechnology **48**(1-2): 9-14.
- Kabbashi, N. A., M. A. Atieh, A. Al-Mamun, M. E. S. Mirghami, M. D. Z. Alam, et al. (2009). "Kinetic adsorption of application of carbon nanotubes for Pb(II) removal from aqueous solution." Journal of Environmental Sciences **21**(4): 539-544.
- Kappler, T., M. Cerff, K. Ottow, T. Hobley and C. Posten (2009). "In situ magnetic separation for extracellular protein production." Biotechnol Bioeng **102**(2): 535-545.
- Kittipoomwong, D., D. J. Klingenberg and J. C. Ulicny (2005). "Dynamic yield stress enhancement in bidisperse magnetorheological fluids." Journal of Rheology **49**(6): 1521.
- Kraume, M. (2012). Transportvorgänge in der Verfahrenstechnik.
- Langston, P. A., U. Tüzün and D. M. Heyes (1995). "Discrete element simulation of granular flow in 2D and 3D hoppers: Dependence of discharge rate and wall stress on particle interactions." Chemical Engineering Science **50**(6): 967-987.
- Laurien, E. and H. Oertel (2009). Numerische Strömungsmechanik, Vieweg + Teubner.
- Lee, R. G. and S. W. Kim (1974). "Adsorption of proteins onto hydrophobic polymer surfaces: adsorption isotherms and kinetics." J Biomed Mater Res **8**(5): 251-259.
- Li, X. L., K. L. Yao, H. R. Liu and Z. L. Liu (2007). "The investigation of capture behaviors of different shape magnetic sources in the high-gradient magnetic field." Journal of Magnetism and Magnetic Materials **311**(2): 481-488.

- Li, Y., J. Wang, Y. Zhao and Z. Luan (2010). "Research on magnetic seeding flocculation for arsenic removal by superconducting magnetic separation." Separation and Purification Technology **73**(2): 264-270.
- Li, Y. H., Z. Di, J. Ding, D. Wu, Z. Luan, et al. (2005). "Adsorption thermodynamic, kinetic and desorption studies of Pb²⁺ on carbon nanotubes." Water Res **39**(4): 605-609.
- Lindner, J., K. Menzel and H. Nirschl (2013). "Parameters influencing magnetically enhanced centrifugation for protein separation." Chemical Engineering Science **97**: 385-393.
- Lindner, J., K. Menzel and H. Nirschl (2013). "Simulation of magnetic suspensions for HGMS using CFD, FEM and DEM modeling." Computers & Chemical Engineering **54**: 111-121.
- Lindner, J. and H. Nirschl (2014). "A hybrid method for combining High-Gradient Magnetic Separation and Centrifugation for a Continuous Process." Separation and Purification Technology.
- Lindner, J., K. Wagner, C. Eichholz and H. Nirschl (2010). "Efficiency Optimization and Prediction in High-Gradient Magnetic Centrifugation." Chemical Engineering & Technology **33**(8): 1315-1320.
- Lyklema, J. (2003). "Electrokinetics after Smoluchowski." Colloids and Surfaces A: Physicochemical and Engineering Aspects **222**(1-3): 5-14.
- Lyubchenko, Y. L. (2011). "Preparation of DNA and nucleoprotein samples for AFM imaging." Micron **42**(2): 196-206.
- Martelli, S., A. Mancini, R. Giorgi, R. Alexandrescu, S. Cojocar, et al. (2000). "Production of iron-oxide nanoparticles by laser-induced pyrolysis of gaseous precursors." Applied Surface Science **154-155**: 353-359.
- Menzel, K., J. Lindner and H. Nirschl (2012). "Removal of magnetite particles and lubricant contamination from viscous oil by High-Gradient Magnetic Separation technique." Separation and Purification Technology **92**: 122-128.
- Menzel, K., C. W. Windt, J. A. Lindner, A. Michel and H. Nirschl (2013). "Dipolar openable Halbach magnet design for High-Gradient Magnetic Filtration." Separation and Purification Technology **105**: 114-120.
- Michov, B. (1996). Elektrophorese: Theorie und Praxis, Walter de Gruyter.
- Moate, J. R. and M. D. LeVan (2009). "Fixed-bed adsorption with nonplug flow: Perturbation solution for constant pattern behavior." Chemical Engineering Science **64**(6): 1178-1184.
- Morjan, I., I. Voicu, F. Dumitrache, I. Sandu, I. Soare, et al. (2003). "Carbon nanopowders from the continuous-wave CO₂ laser-induced pyrolysis of ethylene." Carbon **41**(15): 2913-2921.

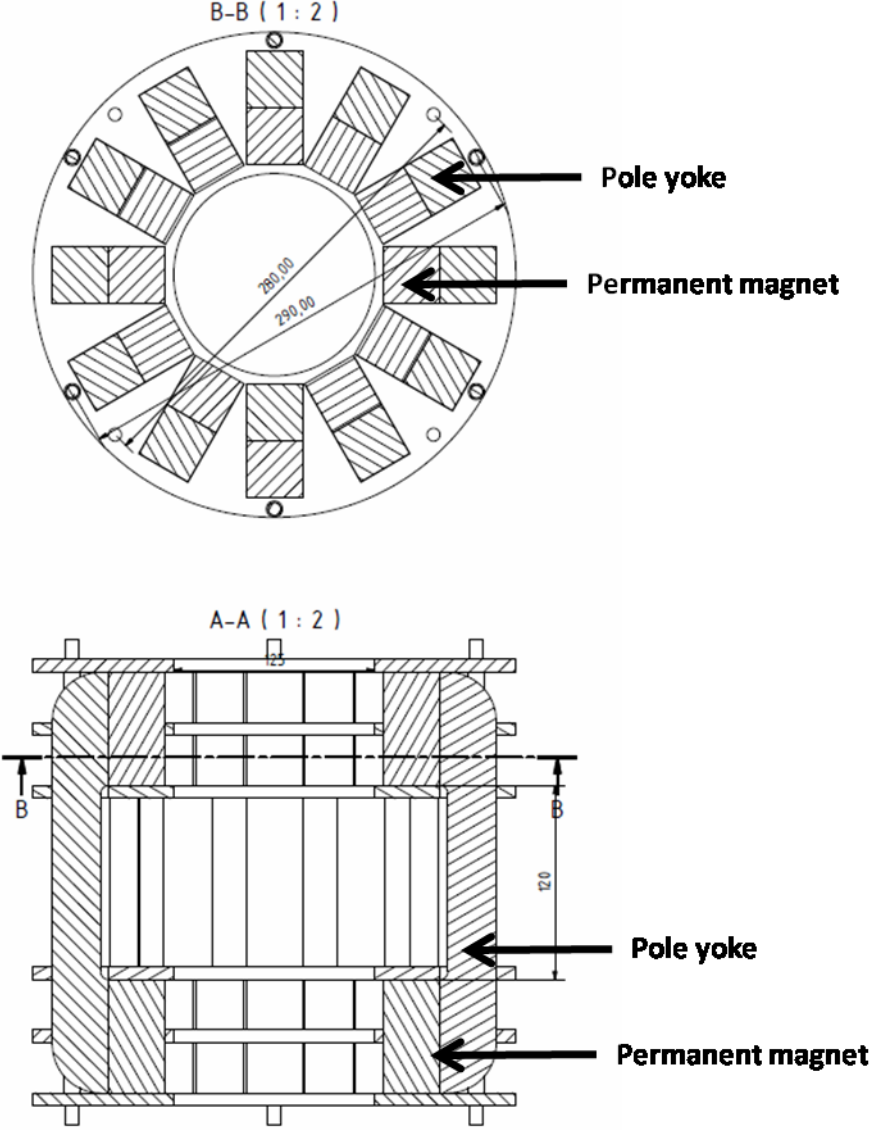
- Muller, T. K. and M. Franzreb (2012). "Suitability of commercial hydrophobic interaction sorbents for temperature-controlled protein liquid chromatography under low salt conditions." J Chromatogr A **1260**: 88-96.
- Nakanishi, K., T. Sakiyama and K. Imamura (2001). "On the adsorption of proteins on solid surfaces, a common but very complicated phenomenon." J Biosci Bioeng **91**(3): 233-244.
- Okada, H., K. Mitsuhashi, T. Ohara, E. R. Whitby and H. Wada (2005). "Computational Fluid Dynamics Simulation of High Gradient Magnetic Separation." Separation Science and Technology **40**(7): 1567-1584.
- Omidbeygi, F. and S. H. Hashemabadi (2012). "Experimental study and CFD simulation of rotational eccentric cylinder in a magnetorheological fluid." Journal of Magnetism and Magnetic Materials **324**(13): 2062-2069.
- Omidbeygi, F. and S. H. Hashemabadi (2013). "Exact solution and CFD simulation of magnetorheological fluid purely tangential flow within an eccentric annulus." International Journal of Mechanical Sciences **75**: 26-33.
- Opel, M. (2005). Lecture notes on "Magnetism". Walther-Meißner-Institut (WMI), Bayerische Akademie der Wissenschaften
- Chair for Technical Physics (E23), Technische Universität München.
- Osborn, J. (1945). "Demagnetizing Factors of the General Ellipsoid." Physical Review **67**(11-12): 351-357.
- Pappas, Y. and D. J. Klingenberg (2005). "Simulations of magnetorheological suspensions in Poiseuille flow." Rheologica Acta **45**(5): 621-629.
- Parekh, A. (2011). Magnetic nanoparticles and their applications in environmental remediation, Massachusetts Institute of Technology.
- Peck, O. B. (1925). Magnetic centrifugal separator. <http://www.freepatentsonline.com/1527070.pdf>. u. s. p. office. USA.
- Pitel, J. (1995). "Theoretical analysis of the motion of spherical particles in a Magnetic Centrifuge and the Design of its force field as a solution of an inverse problem." Department of Metallurgical Engineering, University of Utah.
- Raveendran, P. and A. Amirtharajah (1995). "Role of Short-Range Forces in Particle Detachment during Filter Backwashing." Journal of Environmental Engineering **121**(12): 860-868.
- Reuter, H. (1967). "Sedimentation in der Überlaufzentrifuge." Chemie-Ing.-Techn. **39**(9/10): 548-553.

- Romaní Fernández, X. and H. Nirschl (2009). "Multiphase CFD Simulation of a Solid Bowl Centrifuge." Chemical Engineering & Technology **32**(5): 719-725.
- Rondeau, E., S. Holzapfel, P. Fischer and E. Windhab (2010). An integrated microfluidic device for the preparation and evaluation of magneto-responsive composite particles. 14 th International conference on Miniaturized Systems for Chemistry and Life Sciences, Groningen.
- Rosensweig, R. E. (1997). "Ferrohydrodynamics." Courier Dover Publications.
- Rudolph, M. and U. A. Peuker (2011). "Coagulation and stabilization of sterically functionalized magnetite nanoparticles in an organic solvent with different technical polymers." J Colloid Interface Sci **357**(2): 292-299.
- Satoh, A., R. W. Chantrell, G. N. Coverdale and S. Kamiyama (1998). "Stokesian Dynamics Simulations of Ferromagnetic Colloidal Dispersions in a Simple Shear Flow." J Colloid Interface Sci **203**(2): 233-248.
- Schroeder, S. (2009). Praezision in der Gelelektrophorese für die Pharmazeutische Qualitaetskontrolle. PhD, TU Braunschweig.
- Shafy, S. (2013). Gold aus Gülle und Knochen. Der Spiegel **37**: 122-123.
- Shulman, Z. P., V. I. Kordonsky, E. A. Zaltsgendler, I. V. Prokhorov, B. M. Khusid, et al. (1986). "Structure, physical properties and dynamics of magnetorheological suspensions." International Journal of Multiphase Flow **12**(6): 935-955.
- Spelter, L. E. and H. Nirschl (2010). "Classification of Fine Particles in High-Speed Centrifuges." Chemical Engineering & Technology **33**(8): 1276-1282.
- Speziale, C. G. (1990). "Analytical Methods for the Development of Reynolds Stress Closures in Turbulence." INSTITUTE FOR COMPUTER APPLICATIONS IN SCIENCE AND ENGINEERING HAMPTON VA.
- Stahl, H. W. (2004). "Industrie-Zentrifugen." DrM Press.
- Stiborski, M. (2004). Numerische Simulation der Entfeuchtung körniger Feststoffe in Dekantierzentrifugen. PhD, Universitaet Fridericiana zu Karlsruhe.
- Stieß, M. (2009). "Mechanische Verfahrenstechnik 1."
- Stolarski, M. (2011). "Die magnetfeldüberlagerte Zentrifugation; ein neues hybrides Trennverfahren zur Selektiven Bioseparation."
- Stolarski, M., C. Eichholz, B. Fuchs and H. Nirschl (2007). "Sedimentation acceleration of remanent iron oxide by magnetic flocculation." China Particuology **5**(1-2): 145-150.

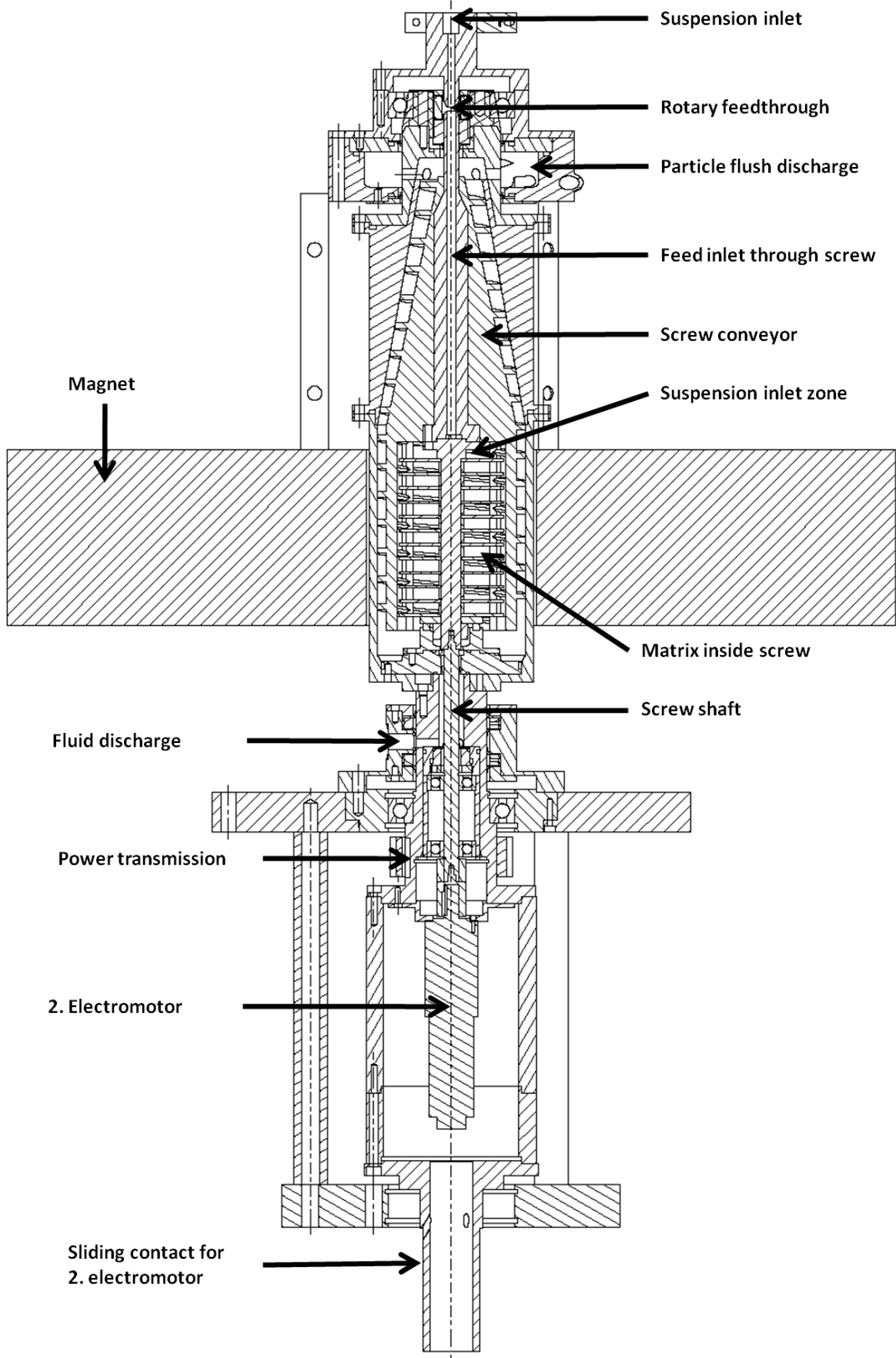
- Stolarski, M. K., K.; Eichholz, C.; Fuchs, B.; Nirschl, H. (2008). "Continuous Selective High Gradient Magnetic Bio Separation Using Novel Rotating Matrix Centrifugation." American Filtration Society Conference.
- Stoner, E. C. (1945). "The Demagnetization Factors for Ellipsoids." Philosophical Magazine Ser. 7, Voil. 36, No.263-Dec 1945.
- Straton, J. A. (1941). Electromagnetic Theory.
- Svoboda, J. (1981). "A theoretical approach to the magnetic flocculation of weakly magnetic minerals." International Journal of Mineral Processing **8**(4): 377-390.
- Svoboda, J. (2004). Magnetic Techniques for the Treatment of Materials, Kluwer Academic Publishers.
- Symons, D. D. (2011). "Integral methods for flow in a conical centrifuge." Chemical Engineering Science **66**(13): 3020-3029.
- Uchiyama, S., Hayashi, K. (1978). "Analytical theory of magnetic particle capture process and capture radius in high gradient magnetic separation." Industrial applications of magnetic separation: Proceedings of an International Conference, Rindge(IEEE: 78CH1447-2).
- VDI (2006). VDI - Waermeatlas, Verein deutscher Ingenieure; GVC: Fe₃.
- Vuppu, A. K., A. A. Garcia and M. A. Hayes (2003). "Video Microscopy of Dynamically Aggregated Paramagnetic Particle Chains in an Applied Rotating Magnetic Field." Langmuir **19**(21): 8646-8653.
- Watson, J. H. P. (1973). "Magnetic filtration." Journal of Applied Physics **44**(9): 4209.
- Wilcox, D. A. (1994). "Simulation of Transition with a Two-Equation Turbulence Model." AIAA Journal **32**(2): 247-255.
- Wilcox, D. C. (1988). "Reassessment of the scale-determining equation for advanced turbulence models." AIAA Journal **26**(11): 1299-1310.

8.8 Technical Drawings

1. Permanent magnet



2. Continuous magnetically enhanced centrifuge



8.9 Publications

8.9.1 Publications

Lindner, J.; Menzel, K.; Nirschl, H.: *Influencing Parameters in Magnetically Enhanced Centrifugation*; **2013**; DOI: 10.1016/j.compchemeng.2013.03.012

Lindner, J.; Menzel, K.; Nirschl, H.: *Simulation of magnetic suspensions for HGMS using CFD, FEM and DEM modeling*; **2013**; Computers and Chemical Engineering; DOI: 10.1016/j.compchemeng.2013.03.012

Lindner, J.; Wagner, K.; Eichholz, C.; Nirschl, H.: *Efficiency Optimisation and Prediction in High-Gradient Magnetic Centrifugation*; **2010**; Chemical Engineering and Technology; DOI: 10.1002/ceat.201000112

Lindner, J.; Nirschl, H.: *A hybrid method for combining High-Gradient Magnetic Separation and Centrifugation for a Continuous Process*; **2014**; Separation and Purification Technology; DOI: 10.1016/j.seppur.2014.04.019

Lindner, J.; Keller, K.; Grim, G. ; Feller, J.; Nielsen, C.; Dalgaard, N.; Nirschl, H.: *Magnetically Enhanced Centrifugation for industrial use*; **2014**; Book chapter in: Upscaling of Bio-Nano-Processes; Springer; ISBN 978-3-662-43898-5

8.9.2 Congress Proceedings

Surface functionalized particles in Magnetic Field enhanced Centrifugation, International Congress on Particle Technology (Partec), Nürnberg, 23.-25.4.2013

Protein Separation by Surface Functionalized Magnetic Particles in Magnetically Enhanced Centrifugation, European Society of Biochemical Engineering Sciences (ESBES), Istanbul, 24.-26.09.2012

Simulation in Magnetic Field Enhanced Centrifugation, World Filtration Congress 11, Graz, 16.-20.4.2011

Selective Separation of Magnetic Particles by Magnetic Field Enhanced Centrifugation, FILTECH 2011, Wiesbaden, 22.-24.03.2011

Magnetically Enhanced Centrifugation with a longitudinal permanent magnet, FILTECH 2013, Wiesbaden, 22.-24.10.2013